

ABSTRACT

LOSEY, BRADLEY POWELL. Understanding Solvation: A Case Study in Zinc Chloride Dissolution. (Under the direction of James D. Martin).

The crystalline and liquid structures of the zinc chloride hydrate system were explored across a wide compositional range utilizing synchrotron and single crystal X-ray diffraction and variable temperature neutron diffraction, attenuated total reflectance infrared (ATR-IR) and Raman spectroscopy, proton nuclear magnetic resonance (^1H NMR) spectroscopy, differential scanning calorimetry (DSC) and reverse Monte Carlo (RMC) modelling. It was found by previous group members from DSC measurements in the vicinity of the 75 mol % water composition that a pure crystalline hydrate phase exists. Single crystal X-ray diffraction confirmed the structure to consist of a pseudo-CsCl packing of the molecular ions $[\text{Zn}(\text{H}_2\text{O})_6][\text{ZnCl}_4]$. Subsequent analysis showed that these ions do persist upon melting of the trihydrate as confirmed by low frequency Raman spectroscopy which show evidence of the symmetric stretching modes of the ions as well as analysis of the pair distribution functions (PDFs) obtained from diffraction measurements which show persistence the intramolecular ion distances.

A broader concentration range was examined utilizing the same techniques to determine if there were any additional crystalline hydrate phases and if the molecular ions observed in the trihydrate persisted upon dilution. As in the trihydrate system the symmetric stretching modes as well as the intramolecular pair correlations of the ions are seen to persist upon dilution. In addition, pair correlations corresponding to the Zn-O_{II} distance of the second hydration shell are also observed. A compositional ZnCl₂/H₂O phase diagram was constructed from DSC data and it is observed that an "amorphous chasm" exists in the region of $4 < R < 10$ in which no crystallization is observed. It is proposed here that the inability of the system to phase segregate

in this region is due to the strong hydrogen bonding between waters of the first and second hydration shells.

Analysis of the structure factor ($S(Q)$) data of both X-ray and neutron diffraction of the $R = 3$ combined with RMC modelling confirmed that the CsCl-type packing of the ions persists into the liquid state. Additionally, utilizing idealized models and RMC the packing motif could also be applied to more dilute solutions at the $R = 9$ and $R = 21$ compositions in which it is found that intermediate range order (IRO) exists in the zinc chloride hydrate system to at least a composition of $R = 21$. Furthermore, it is found that the idealized CsCl-type packing best describes both the $R = 9$ and $R = 21$ solutions.

Two-state models, assuming solvated and bulk water in the system, were applied to the ^1H NMR and vibrational spectroscopy data. The zinc chloride hydrate system was ideal for investigating the two-state model due to the unique ability to experimentally measure the spectrum of solvated water. However, in each case it was found that to properly fit the data additional hydration shells needed to be included in the system thus expanding the two-state model to include multiple water environments.

Lastly, the aqueous zinc chloride system was utilized as a probe to better understand the vibrational spectrum of pure water by examining the evolution of water vibrational modes from the $R = 3$ hydrate, where the hydrogen bonding network of pure water does not exist, to that of pure water. Evidence suggests that the molecular modes of water are observed at $\sim 1600\text{ cm}^{-1}$ for the bending mode along with a combination peak of the symmetric and asymmetric stretching modes at $\sim 3450\text{ cm}^{-1}$ while the peaks observed at 3200 and 3600 cm^{-1} primarily correspond to the hydrogen bonding network of the system, although some intensity of the 3200 cm^{-1} peak is due to the bending overtone.

© Copyright 2018 Bradley Losey

All Rights Reserved

Understanding Solvation: A Case Study in Zinc Chloride Dissolution

by
Bradley Powell Losey

A dissertation submitted to the Graduate Faculty of
North Carolina State University
in partial fulfillment of the
requirements for the degree of
Doctor of Philosophy

Chemistry

Raleigh, North Carolina

2018

APPROVED BY:

James D. Martin
Committee Chair

David A. Shultz

Walter W. Weare

Paul A. Maggard

DEDICATION

This work is dedicated to my wonderful family and my amazing wife for their continued love and support throughout my graduate career. I would also like to dedicate this work to the memory of Dr. Richard Kopp who reignited my passion for chemistry as a freshman at East Tennessee State University.

BIOGRAPHY

Bradley Losey was born August 24th, 1981 in Little Rock, Arkansas to parents Steve and Jana Losey. He moved with his family to Arlington, Texas in 1988 and then to Johnson City, Tennessee in 1994. He graduated from Science Hill High School in 2000 where he had participated in the National Beta Club and JROTC. He began studies at East Tennessee State University in January 2007 to pursue a degree in Chemistry. While at ETSU he began working under the advisement of Dr. Aleksey Vasiliev as an undergraduate researcher in the spring of 2010. After obtaining his Bachelor of Science degree in May 2011 he went to North Carolina State University to pursue a graduate degree in Inorganic Chemistry with Dr. James Martin.

ACKNOWLEDGMENTS

I would like to first and foremost acknowledge my graduate advisor, Dr. James Martin for support and guidance throughout my time at NC State. In addition, I would like to thank Dr. Jaap Folmer for all of his help and insight during my graduate work, especially when it came to data processing and statistical analysis. I would also like to give my appreciation to many of the past and present members of the Martin group, including Eric Dill for all of his wisdom and mentorship as the senior graduate student when I first joined the group. Feier Hou for her friendship and guidance, especially on all things DSC. And, Rob Wilcox for the amazing research into the zinc chloride hydrate system which laid the ground work for my entire graduate career. I also want to acknowledge Mick Williams, Elijah Gordon, James Weng and Daniel Rosoff who were of great help for many of the neutron diffraction experiments. And finally, Berkley Hillis, Josh Rickard, Olivia Burns and Brittany Crouse who have been of great assistance during the writing process; I wish all of you the best in the remainder of your time at NC State. I would also like to acknowledge many of my fellow graduate students in the chemistry department for their friendship and encouragement during my time at NC State, especially Kushal Shrestha, Jonathan Boltersdorf, Ian Sullivan, Judah High and David Bowmen.

I would like to express my sincere gratitude to Dr. Paul Maggard for giving me the amazing opportunity to do research with his group during the summer before I began as a graduate student at NC State during which time I learned a great deal about solid state synthesis and X-ray diffraction. Additionally, I would like to acknowledge Dr. Stefan Franzen, Dr. Evgeny Danilov and Dr. David Shultz for helping me to better understand chemical spectroscopy, which would be of great importance to my graduate research. Furthermore, I would like to thank Dr. Roger Sommer and Dr. Joerg Neufeind for their wealth of knowledge

on X-ray and neutron diffraction. I would also like to acknowledge Dr. Elena Jakubikova for introducing me to Gaussian 09 and helping me to better understand computational and quantum chemistry.

Lastly, I would like to acknowledge the support of my graduate committee members (Dr. David Shultz, Dr. Walter Weare, Dr. Paul Maggard and Dr. Dimitris Argyropoulos) as well as all of the faculty and staff of the NC State chemistry department for all of their help.

TABLE OF CONTENTS

LIST OF TABLES	ix
LIST OF FIGURES	x
CHAPTER 1 General Introduction	1
1.1 Motivation.....	1
1.2 Monatomic liquid structure	2
1.3 Water and aqueous solution structure.....	3
1.4 Reasons for using zinc chloride	6
1.5 Outline.....	7
1.6 References	10
CHAPTER 2 Crystalline and Liquid Structure of Zinc Chloride Tri-hydrate: A unique ionic liquid.....	14
2.1 Introduction.....	14
2.2 Experimental Methods	17
2.2.1 Materials and synthesis	17
2.2.2 Single crystal structure.....	18
2.2.3 Synchrotron XRD of liquid	19
2.2.4 Neutron diffraction	20
2.2.5 ATR-IR	21
2.2.6 Raman	22
2.2.7 Computational methods	22
2.3 Results	23
2.3.1 (H/D) ₂ O:ZnCl ₂ phase diagram.....	23
2.3.2 Structure of [Zn(O(H/D) ₂) ₆][ZnCl ₄], <i>I_H</i> and <i>I_D</i>	25
2.3.3 Diffraction of the molten hydrate	30
2.3.4 Raman spectroscopy of the molten salt hydrate	33
2.3.5 ATR-IR spectroscopy of the water of hydration.....	34
2.4 Discussion.....	36
2.4.1 Crystalline structure of <i>I</i>	36
2.4.2 Structure of the molten salt hydrate	39
2.4.3 Reverse Monte Carlo modeling (RMC)	46
2.4.4 Understanding the water of hydration.....	49

2.5 Conclusion	51
2.6 References	53
CHAPTER 3 Liquid Structure of $\text{ZnCl}_2 \cdot n\text{H}_2\text{O}$ from $n = 3$ to $n = 250$.....	58
3.1 Introduction.....	58
3.2 Experimental Methods	63
3.2.1 Materials and synthesis	63
3.2.2 Synchrotron XRD of liquid.....	64
3.2.3 Neutron diffraction	64
3.2.4 Raman	65
3.2.5 Computational methods	66
3.3 Results	67
3.3.1 $\text{ZnCl}_2\text{:H}_2\text{O}$ phase diagram	67
3.3.2 Liquid phase diffraction of ZnCl_2 dilution series	78
3.3.3 Raman spectroscopy of the dilution series.....	85
3.4 Discussion.....	92
3.4.1 DSC and phase change behavior	92
3.4.2 Local order of the dilution series	97
3.4.3 Intermediate range order in the system.....	105
3.4.4 RMC modelling of the system.....	109
3.5 Conclusion	113
3.6 References.....	115
CHAPTER 4 Nuclear Magnetic Resonance Studies of the Concentration Dependence of Hydrogen Bonding Interactions in Aqueous Zinc Chloride Solutions	123
4.1 Introduction.....	123
4.2 Experimental Methods	126
4.2.1 Sample preparation	126
4.2.2 ^1H NMR measurements	126
4.2.3 Hartree-Fock calculations.....	126
4.3 Results	127
4.3.1 Concentration dependent ^1H NMR of zinc chloride solutions.....	127
4.3.2 Measurements of different salts.....	129
4.3.3 Temperature dependent ^1H NMR of aqueous ZnCl_2	133
4.4 Discussion.....	136
4.4.1 Temperature dependence of the ^1H NMR spectra of aqueous ZnCl_2	136

4.4.2 Two-state model fit of concentration dependent ^1H NMR data from aqueous ZnCl_2 solutions.....	137
4.4.3 Multi-state model fit of concentration dependent ^1H NMR data from aqueous ZnCl_2 solutions.....	140
4.4.4 Multi-State fitting model applied to the ^1H NMR data of additional ionic salt solutions	148
4.5 Conclusion	152
4.6 References.....	153
CHAPTER 5 Analysis of the Waters of Hydration in Aqueous Zinc Chloride Solutions Via Vibrational Spectroscopy	157
5.1 Introduction.....	157
5.2 Experimental Methods	160
5.2.1 Materials and synthesis	160
5.2.2 Raman spectroscopy	161
5.2.3 Infrared spectroscopy	161
5.3 Results	162
5.3.1 Examination of the 2800 to 4000 cm^{-1} spectral region.....	162
5.3.2 Examination of the 1500 to 1800 cm^{-1} spectral region.....	168
5.4 Discussion.....	175
5.4.1 Application of the two-state fitting model to vibrational spectroscopic data	175
5.4.2 Utilization of multi-shell fitting models to vibrational spectroscopic data	179
5.4.3 Insight into the nature of pure water gained though the study of aqueous ZnCl_2	185
5.5 Conclusion	189
5.6 References.....	190
CHAPTER 6 Conclusion.....	198
APPENDICES.....	200
Appendix A	201

LIST OF TABLES

Table 2.1	Single Crystal Data and Refinement Parameters for $[\text{Zn}(\text{O}(\text{H}/\text{D})_2)_6][\text{ZnCl}_4]$	25
Table 2.2	Selected Bond Distances observed for $[\text{Zn}(\text{OH}_2)_6][\text{ZnCl}_4]$ at 208 K.....	29
Table 2.3	Nearest intermolecular ion Cl--O and O--O contacts in Å observed for $[\text{Zn}(\text{OH}_2)_6][\text{ZnCl}_4]$ at 208 K.	29
Table 4.1	Values for the solubility of the salts examined in the aqueous solutions.....	130
Table 4.2	Values for the ionic radii given in angstroms and calculated charge density of the examined ions. Ref. 26 ^a	132
Table 4.3	Calculated fixed chemical shift values fo the higher hydration shells along with the average experimentally measured chemical shift of the R = 3 hydrate.....	142
Table 4.4	Calculated parameters for the exponential fit equations of the first four hydration shells.	147
Table 4.5	The number of hydration shells that were necessary to sufficiently fit each of the additional salts examined.....	151
Table 5.1	Equations used to calculate the mole fraction of waters in each hydration shell based on the solution concentration given in R (α) and mole fraction (α').	180
Table A.1	Determined fitting parameters for the additional salt solutions investigated via ¹ H HMR and fit with the multi-shell exponential model.	201

LIST OF FIGURES

Figure 2.1	Water: zinc chloride phase diagram in the vicinity of the R = 3 composition. Data for H ₂ O are plotted in blue and data for D ₂ O are plotted in red.....	24
Figure 2.2	Temperature dependence of the volume of I_H and I_D	26
Figure 2.3	GSAS refinement using time of flight data collected on the NOMAD-SNS on an in-situ grown sample of of I_D . While this is a polycrystalline sample, it is not a powdered sample, thus preferred orientation of the limited number of crystallites results in an intensity profile that limits the structural refinement.	28
Figure 2.4	ORTEP drawing of R = 3, [Zn(OH ₂) ₆][ZnCl ₄] showing the crystallographic labeling scheme.....	30
Figure 2.5	Structure factor plots of (a) the X-ray scattering of the room temperature molten hydrates R = 3 (purple), R = 1.7 (green), water (blue), and molten ZnCl ₂ at 320 °C (red), X-ray synchrotron; and (b) the neutron scattering of the room temperature R = 3 molten hydrate (purple), 233 R = 3 crystalline (dark purple), D ₂ O (blue), and amorphous ZnCl ₂ (red), neutron.	31
Figure 2.6	Structure factor plot of the variable temperature (255 to 280 K) diffraction of the R = 3 zinc chloride hydrate.....	32
Figure 2.7	Raman spectra of the R = 3 and R = 2.3 zinc chloride hydrates. Because of the strong luminescence of the lower hydrates, the R = 2.3 spectrum is plotted at 50% the scale as the R = 3 spectrum.	34
Figure 2.8	ATR-IR spectra of the R = 3 (purple) and R = 2 zinc chloride hydrates (green), compared with that of 18 MΩ H ₂ O (blue). Insets emphasize the splitting of the band at ~ 2100 cm ⁻¹ band, and the shift of the H-O-H bend, respectively. * indicates a trace of CO ₂ in the spectrometer's beam path.	36
Figure 2.9	Slices of the four pseudo-close packed ligand planes, viewed parallel and perpendicular to each of the four Zn-Cl bond vectors. Light blue lines provide visual guides to the ligand close packing.	38
Figure 2.10	Pair distribution function plots of (a) the X-ray scattering of the room temperature molten hydrates R = 3.03 (purple), R = 1.72 (green), 18 MΩ H ₂ O (blue), and molten anhydrous ZnCl ₂ at 320 °C (red); and (b) the neutron scattering of the room temperature R = 3 molten hydrate (purple), 233 R = 3 crystals (dark purple), D ₂ O (blue), and amorphous ZnCl ₂ (red). Yellow arrows denote pair correlations previously assigned to zinc chloride oligomers, but are instead include O-O pair correlations.....	41

Figure 2.11	Calculated partial pair correlations from the crystal structure of I for (a) X-ray and (b) neutron scattering.....	42
Figure 2.12	Low Q portion of the experimental neutron and X-ray structure factor plots for the R = 3 room temperature liquid (black) compared with the respective calculated crystalline powder patterns for I_D neutron and I_H X-ray scattering for the CsCl-type (red) and LCCP-type (blue) lattices expanded to match the experimental liquid density.	45
Figure 2.13	(a) Structure factor and (b) PDF plots comparing the experimental neutron scattering data for the R = 3 hydrate (black) with the RMC modeling of 5184-atom boxes based on the expanded triclinic (aqua), CsCl (red) and ligand cubic close packed (LCCP) model structures. Inset in (a) is an expanded view of the low-Q peak. Inset in (b) is a 2 × expanded view of the low r PDF.	47
Figure 2.14	Ball and stick drawing of the RMC simulation box resultant from the LCCP model.....	48
Figure 3.1	Phase diagram reported by Mylius and Dietz in 1905. ¹⁴	68
Figure 3.2	DSC plots of the R = 3 (75% water) ZnCl ₂ hydrate for H ₂ O (blue) cycled from -50 to 25 °C at a rate of 0.5 °C/min and D ₂ O (red) cycled from -80 to 50 °C at a rate of 1.0 °C/min.....	70
Figure 3.3	Stack plots of the DSC cycling of ZnCl ₂ :D ₂ O samples of a) R = 2.61 (72.3% water), b) R = 2.73 (73.2% water), and c) R = 2.83 (73.9% water). All samples were cycled four times from -80 to 50 °C at a rate of 1.0 °C/min and are shown as cycle 1 (green), cycle 2 (blue), cycle 3 (orange) and cycle 4 (red). Insets for each composition show an expansion of the melting regions.	72
Figure 3.4	Stack plots of the DSC cycling of ZnCl ₂ :D ₂ O samples of a) R = 3.23 (76.4 % water), b) R = 3.27 (76.6% water), c) R = 3.41 (77% water), and d) R = 3.61 (78% water). All samples were cycled from -80 to 50 °C at a rate of 1.0 °C/min and are shown as cycle 1 (green), cycle 2 (blue), cycle 3 (orange) and cycle 4 (red). Insets for each composition show an expansion of the melting regions.....	73
Figure 3.5	Water:ZnCl ₂ phase diagram for both H ₂ O (blue) and D ₂ O (red) in the compositional region between R = 1.3 (57% water) and pure water. Squares represent eutectic points and circles represent melting points (liquidous curve).	76

Figure 3.6	Neutron diffraction structure factors of $\text{ZnCl}_2:\text{D}_2\text{O}$ solutions of $R = 3$ (black) at 223 K, $R = 4$ (light green) at 213 K, $R = 9$ (red) at 213 K, $R = 21$ (purple) at 213 K and pure D_2O (dark blue) at 193 K.....	78
Figure 3.7	Structure factor plots of select X-ray diffraction patterns for molten anhydrous ZnCl_2 at 320 °C (blue), $R = 2.9$ (green), $R = 9$ (red), $R = 21$ (purple), $R = 30$ (gray), $R = 50$ (orange), $R = 100$ (dark red), pure H_2O (dark blue).....	79
Figure 3.8	Structure factor plots of data collection of the neutron diffraction patterns for glassy ZnCl_2 (black) as well as room temperature ZnCl_2 aqueous solutions of $R = 3$ (red), $R = 5$ (blue), $R = 7$ (gray), $R = 9$ (dark red), $R = 13$ (green), $R = 18$ (purple), $R = 21$ (orange), $R = 45$ (dark green), $R = 93$ (light blue), $R = 175$ (teal) and pure D_2O (dark blue).....	80
Figure 3.9	a) Position of the low-Q X-ray diffraction peak as a function of zinc chloride concentration from $R = 2.07$ (67% water) to $R = 100$ (99% water), b) the 2.09 \AA^{-1} peak and c) Shift in the 3.59 \AA^{-1} peak from molten zinc chloride to pure water as a function of mole percent H_2O	82
Figure 3.10	Position of the low-Q neutron diffraction peak as a function of percent water.....	84
Figure 3.11	Shift in the neutron diffraction principal peak as a function of zinc chloride concentration.....	85
Figure 3.13	Rotated SVD basis vectors of (a) \mathbf{u}_1' , (b) \mathbf{u}_2' , (c) \mathbf{v}_1' , and (d) \mathbf{v}_2' . Dilution series are represented as D1 (red), D2 (gray) and D3 (blue).....	89
Figure 3.14	Peak intensities of the Raman peaks at 283 cm^{-1} (circles) and 400 cm^{-1} (squares) for aqueous zinc chloride as a function of percent water for the dilution series D1 (red), D2 (gray) and D3 (blue).....	91
Figure 3.15	Frequency of the ZnCl_4^{2-} totally symmetric stretching mode as a function of concentration for dilution series D1 (red), D2 (gray) and D3 (blue).....	92
Figure 3.16	X-ray diffraction PDFs for molten anhydrous ZnCl_2 at 320 °C (blue) as well as room temperature aqueous zinc chloride solutions of concentration $R = 2.9$ (green), $R = 9$ (red), $R = 21$ (purple), $R = 30$ (gray), $R = 50$ (orange), $R = 100$ (dark red) and pure H_2O (dark blue).....	99
Figure 3.17	Neutron diffraction PDFs for room temperature aqueous zinc chloride solutions of composition $R = 3$ (yellow), $R = 9$ (red), $R = 21$ (purple), $R = 45$ (light blue), $R = 93$ (blue-gray), $R = 150$ (black), $R = 275$ (gold) and pure D_2O (dark blue).....	100

Figure 3.18	Concentration dependent shift in the combination peak corresponding to the Zn-O/Zn-Cl pair correlations of the ZnCl_4^{2-} and $\text{Zn}(\text{H}_2\text{O})_6^{2+}$ ions observed from neutron (blue) and X-ray (red) diffraction.....	102
Figure 3.19	Experimental neutron and X-ray structure factor plots of the R = 9 aqueous zinc chloride (black) compared with the calculated powder diffraction patterns of the idealized CsCl- (blue) and NaCl-type (red) packing structures.....	108
Figure 3.20	Experimental neutron and X-ray structure factor plots of the R = 21 aqueous zinc chloride (black) compared with the calculated powder diffraction patterns of the idealized CsCl- (blue) and NaCl-type (red) packing structures.	109
Figure 3.21	Pair distribution functions of the R = 9 zinc chloride solution obtained by neutron diffraction measurements (black) and RMC modelling of the idealized CsCl- (red) and NaCl-type (blue) supercells.....	111
Figure 3.22	Structure factor plots of the R = 9 zinc chloride solution obtained by neutron diffraction measurements (black) and RMC modelling of the idealized CsCl- (red) and NaCl-type (blue) supercells.....	112
Figure 3.23	Ball-and-stick representation of the RMC simulation box of the idealized CsCl model of the R = 9 ZnCl_2 solution.	113
Figure 4.1	Concentration dependent ^1H NMR chemical shift of the zinc chloride aqueous solutions from R = 3 to R = 9 (squares), R = 9 to R = 100 (triangles), and R = 100 to pure water (circles).	128
Figure 4.2	Peak intensities of the Raman peaks at 283 cm^{-1} (orange) and 400 cm^{-1} (blue) for aqueous zinc chloride as a function of percent water.	129
Figure 4.3	^1H NMR chemical shifts reported relative to the chemical shift of pure water for aqueous solutions of AlCl_3 (red), $\text{Al}_2(\text{SO}_4)_3$ (blue), MgSO_4 (green), ZnSO_4 (orange), MgCl_2 (purple), CaCl_2 (gray), NaCl (dark blue), and a 1:1 mixture of $\text{MgCl}_2/\text{ZnCl}_2$ (light green) as well as measurements of ZnCl_2 (dark red) taken at 296 K.	131
Figure 4.4	The calculated proton chemical shifts of sodium (purple), calcium (orange), zinc (green), magnesium (blue) and aluminum (red) ions hydrated by six water molecules.	133
Figure 4.5	Variable temperature measurements for the R = 21 zinc chloride hydrate at 304 (blue), 300 (red), 297 (gray), 293 (orange), 290 (green), 284 (purple), 279 (teal), 273 (brown), 267 (light green), 262 (navy), 256 (dark red), 250 (light blue), and 245 (black) Kelvin.....	134

Figure 4.6	Temperature dependence of the ^1H NMR chemical shift of R = 3 (orange), R = 9 (red), R = 21 (green) aqueous zinc chloride solutions and pure water (blue) relative to ^6d -acetone.	135
Figure 4.7	Dependence of the temperature variation as a function of % water in the aqueous zinc chloride solutions.	136
Figure 4.8	Fit of the ^1H NMR experimental data (blue) using the two-state model (red) along with the fit residuals (gray).	139
Figure 4.9	Fit of the ^1H NMR experimental data (blue) using the multi-state model with fixed chemical shift values (red) along with the fit residuals (gray).	142
Figure 4.10	Simple concentric circular model displaying the increasing shell idea with the first hydration shell in red, second in blue and third in green.	145
Figure 4.11	Plot of the exponential function $1 - e^{-kx}$ where $k = 1$	146
Figure 4.12	Fit of the ^1H NMR experimental data (blue) using the multi-state model with exponentially varying chemical shift values (red) along with the fit residuals (gray).	148
Figure 4.13	The calculated chemical shift (black) obtained from the application of the multi-state fitting model to the experimental data (orange) of a) $\text{Zn}(\text{SO}_4)$, b) $\text{Mg}(\text{SO}_4)$, c) AlCl_3 and d) $\text{Al}_2(\text{SO}_4)$ along with the fit residuals (gray).	150
Figure 4.14	The calculated chemical shift (black) obtained from the application of the multi-state fitting model to the experimental data (orange) of a) CaCl_2 , b) NaCl , c) MgCl_2 and d) 1:1 mixture of $\text{ZnCl}_2/\text{MgCl}_2$ along with the fit residuals (gray).	151
Figure 5.1	Isotropic Raman spectra of aqueous zinc chloride solutions of composition R = 3 (red), R = 6 (blue), R = 9 (green), R = 15 (purple), R = 21 (dark red), R = 35 (orange), R = 45 (dark blue), R = 60 (brown), R = 80 (gray), R = 100 (dark green) and pure water (black).	164
Figure 5.2	Concentration dependence of the main spectroscopic feature for dataset D1 (red) and D2 (blue).	165
Figure 5.3	ATR-IR spectra of aqueous zinc chloride solutions of composition R = 2.03 (red), R = 3.09 (blue), R = 5.99 (green), R = 9.96 (purple), R = 14.63 (dark red), R = 20.69 (orange), R = 37.71 (dark blue), R = 57.58 (brown), R = 87.01 (gray), R = 120.67 (dark green), R = 229.38 (yellow) and pure water (black).	166
Figure 5.4	Concentration dependence of the main spectroscopic peak in the IR data for A1 (red) and A2 (blue).	167

Figure 5.5	Polarized Raman spectra of pure water. Parallel alignment (red) and perpendicular alignment (blue).	168
Figure 5.6	Raman spectra of the zinc chloride hydrates for dilution series D1 R = 3 (blue), R = 6 (orange), R = 9 (gray), R = 12 (red), R = 15 (purple), R = 21 (light blue), R = 40 (green), R = 60 (dark red), R = 80 (blue-gray), R = 100 (brown), R = 175 (dark blue), R = 250 (light green), and pure H ₂ O (black).	170
Figure 5.7	SVD of the Raman data in the water bending mode region for a) u_1 , b) u_2 , c) v_1 and d) v_2 . Dilution series are represented as B1 (blue), B2 (red) and B3 (gray).	172
Figure 5.8	ATR-IR spectra of the water bending mode in aqueous zinc chloride solutions of composition R = 2.03 (red), R = 3.09 (blue), R = 5.99 (green), R = 9.96 (purple), R = 14.63 (dark red), R = 20.69 (orange), R = 37.71 (dark blue), R = 57.58 (brown), R = 87.01 (gray), R = 120.67 (dark green), R = 229.38 (yellow) and pure water (black).	173
Figure 5.9	Concentration dependence of the frequency of the water bending peak in the IR data for A1 (red) and A2 (blue).	174
Figure 5.10	Concentration dependence of the full width at half maximum (FWHM) water bending peak in the IR data for A1 (red) and A2 (blue).	175
Figure 5.11	Raman spectra from data series (D1) for compositions of a) R = 6, b) R = 35, c) R = 70 and d) R = 100. The experimental data (red) are shown along with the two-state fitting model (black) and residuals (gray) for each composition.	177
Figure 5.12	ATR-IR spectra from data series (A1) for compositions of a) R = 6, b) R = 27, c) R = 58 and d) R = 229. The experimental data (red) are shown along with the two-state fitting model (black) and residuals (gray) for each composition.	178
Figure 5.13	The measured spectrum of the R = 3 hydrate (black) corresponding to the first hydration shell plus the calculated spectra of the second (blue), third (red), fourth (gray) and fifth (green) hydration shells.	181
Figure 5.14	The measured spectrum of the R = 3 hydrate (black) corresponding to the first hydration shell plus the calculated spectra of the second (blue), third (red), fourth (gray) and fifth (green) hydration shells.	182
Figure 5.15	Raman spectra from data series (D1) for compositions of a) R = 6, b) R = 35, c) R = 70 and d) R = 100. The experimental data (red) are shown along with the multi-shell fitting model utilizing five hydration shells (black) and residuals (gray) for each composition.	184

Figure 5.16 ATR-IR spectra from data series (A1) for compositions of a) $R = 6$, b) $R = 27$, c) $R = 58$ and d) $R = 229$. The experimental data (red) are shown along with the multi-shell fitting model utilizing five hydration shells (black) and residuals (gray) for each composition..... 185

CHAPTER 1

General Introduction

1.1 Motivation

Solutions are important due to their ubiquitous role in nature as well as industry. Biologically solutions are found in regions such as the cytoplasm of cells where many vital chemical processes of organisms occur. Geologically, solutions are found from the oceans to deep in the earth's crust. In industrial applications solutions are very good media in which to conduct reactions because of the ability to control the concentration as well as additional solution properties such as pH, conductivity, melting point, boiling point, viscosity, ionic strength, and buffering. Additionally, the fluidity of solutions means that they can be efficiently pumped from one place to another. However, because the properties of solutions can be so drastically varied, it is important to understand solutions at the molecular level which will ultimately lead to better control over their properties. At the most fundamental level understanding solutions requires knowledge of solute/solvent, solute/solute and solvent/solvent interactions combined with general structural features of liquids.

Understanding the connection between the local and intermediate range order with the observed bulk properties of solutions could allow for much more accurate engineering of the liquid properties and fine tuning for numerous applications. For example, the introduction of Bragg's Law¹ which allows for the determination of the structure of crystalline solids through the use of diffraction methods resulted in a much deeper understanding of the relationship between crystalline structure and bulk properties. This understanding has allowed for the advancement of areas such as solid-state electronics over the past several decades. The same degree of usefulness could be applied to liquids and solutions if their structural features could be accurately

determined. However, in liquids the structural order is on the local and intermediate range and the system is far more dynamic than that of crystalline solids. The lack of long range translational symmetry in liquids means that it is ultimately very difficult to determine structural features which has resulted in much research with very little to show in the way of understanding their structure. However, a common example of applied structure in solution is that of liquid crystals. When first discovered, these were nothing more than a scientific curiosity, but over time as more was learned about the ordering present in liquid crystals and how to control that order they found uses in areas such as liquid crystal displays. While liquid crystals are traditionally comprised solely of anisotropic organic compounds, there have been reports of metallotropic liquid crystals which incorporate inorganic compounds such as $ZnCl_2$ into organic liquid crystalline phases.² If other types of solutions, such as those of aqueous salts, could be understood in the context of intermediate range ordering they too could lead to new areas of technology.

1.2 Monatomic liquid structure

To a first approximation, simple monatomic liquids have been studied as model systems for understanding liquid structure for nearly a hundred years. Over this time multiple interpretations have been proposed which include cell theory, first popularized by Lennard-Jones and Devonshire,³⁻⁴ in which a liquid is viewed as a slightly disordered crystal. However, this ultimately results in too much long-range order in the liquid model. Hole theory proposed by Frenkel⁵, Hirschfelder⁶ and Eyring⁷ utilizes statistical mechanics and proposes that the difference between a liquid and a solid is that, in a liquid, the energy for a particle to move from one position to a hole is on the order of $k_B T$. Since the introduction of these theories they have been modified in various ways including to combine the two theories by addition of holes into

the lattice theory to introduce more disorder into the system.⁸ Kinetic multiple molecular contact theory also utilizes statistical mechanics but views a liquid as a condensed gas.⁹⁻¹¹ Lastly, Bernal¹²⁻¹³ proposed that monatomic liquids should be thought of as “irregular assemblages” in which the order could be represented by the statistical average of particles around each other utilizing what he called “statistical geometry”. This idea relates closely to the technique of Voronoi tessellation commonly employed in computational simulations to determine an average coordination number.¹⁴ While each of these theories falls short of providing a truly accurate description of liquid structure, they do each provide evidence for a certain degree of intermediate range order in liquid systems.

1.3 Water and aqueous solution structure

Solutions have been studied for well over a hundred years, over which time many different experimental and computational methods have been utilized resulting in the development of multiple theories as to the true nature of aqueous solutions. A major leap forward in the understanding of solutions came from Arrhenius with the proposal of solutions consisting of positive and negative ions surrounded by solvent for which he was awarded the 1903 Nobel Prize.¹⁵ In 1923, Debye and Hückel¹⁶ proposed a theory which introduced the concept of the activity coefficient to correct for non-ideality in solutions by taking into account the interactions between ions. However, this theory did not account for the formation of ion pairs or any interaction of the ions with the solvent. Additionally, this theory is only valid for dilute solutions. To move beyond Debye-Hückel, attempts were made to relate microscopic structural features of solutions to bulk properties resulting in what is known as the Kirkwood-Buff theory which utilizes partial pair correlations of a solution to determine thermodynamic properties such as the partial molar volume, isothermal compressibility and osmotic pressure.¹⁷

Later, Ben-Naim developed the Inverse Kirkwood-Buff theory that allowed for the calculation of partial pair correlations from the measured thermodynamic parameters.¹⁸ However, the drawback of the Kirkwood-Buff theory is that it primarily works for two-component systems such as liquid/liquid mixtures, beyond that the math begins to become too complex thus making the application of this theory to aqueous salt solutions very difficult. Expanding the scope of aqueous salt solutions to include higher concentrations, Braunstein classified these solutions into five distinct regions defined by the mole fraction of water. The approximate ranges were as follows: (I) Debye-Hückel limiting ($1 - > 0.99$); (II) extended Debye-Hückel theory ($0.99 - 0.9$); (III) hydrate melts ($0.9 - 0.75$); (IV) incomplete hydration sheaths ($0.75 - 0.01$); (V) gas solubility (< 0.01).¹⁹

An important solvent for solutions, both in nature and in applications, is water. Water is particularly unique amongst molecular liquids which can be observed by comparison of its physical properties to other similar compounds such as its unusually high melting/boiling points and observed increase in density upon melting. Part of what makes water so unique is the strength of the hydrogen bonding in the liquid state.²⁰⁻²¹ Early in the days of X-ray crystallography Bernal et al. began to consider the structure of liquid water and how it could be described by diffraction, it was proposed that liquid water has a disordered tetrahedral network similar to that of ice.²²⁻²⁴ However, this was contradicted by Pauling who proposed that water consists of icosahedral clusters.²⁵ The debate as to which of these ideas is correct still remains today. The presence of ions in aqueous solutions has been shown to have a dramatic effect on the hydrogen bonding structure of water. In 1888, Hofmeister showed that ions had an effect on the solubility of egg white proteins in aqueous solutions as follows ($\text{SO}_4^{2-} > \text{HPO}_4^{2-} > \text{C}_2\text{H}_3\text{O}_2^- > \text{Cl}^- > \text{NO}_3^-$) and ($\text{Mg}^{2+} > \text{Li}^+ > \text{Na}^+, \text{K}^+ > \text{NH}_4^+$).²⁶ Subsequently Hofmeister's observation led to

the concept of ions being classified as those that either increase (structure making, ex. Mg^{2+} and SO_4^{2-}) or decrease (structure breaking, ex. NH_4^+ and NO_3^-) the degree of hydrogen bonding when added to pure water.²⁷⁻²⁸ Like Debye-Hückel, this idea typically only applies to dilute solutions as at very high concentrations water becomes part of hydration shells and the tetrahedral network is undoubtedly broken apart as reported by Kabisch who found that at salt concentrations higher than $R = 9$ (90 % water) the water structure is completely broken, no matter the identity of the ions present.²⁹

In addition to predicting bulk properties of solutions and examining the effects of ions on the hydrogen bonding network of pure water, there has also been much research in an attempt to understand how ions are hydrated in aqueous solutions. Much experimental evidence of the first hydration shell around Zn^{2+} containing six waters has been provided, for example, by X-ray diffraction and EXAFS measurements of aqueous $\text{Zn}(\text{NO}_3)_2$ and ZnSO_4 solutions.³⁰⁻³¹ Additionally, molecular dynamics as well as ab initio HF-SCF and MP2 calculations of Zn^{2+} have shown the existence of a stable first hydration shell of octahedral geometry.³²⁻³⁴ While it is well established that a first hydration shell exists, the nature of hydration beyond the first shell is still hotly debated in the scientific literature. Ab initio molecular dynamics of the hydration of Mg^{2+} and Al^{3+} as well as Zn^{2+} have shown the existence of a second hydration shell but also report that beyond the second shell the tetrahedral structure of bulk water returns.³⁵⁻³⁶ Experimental evidence in the form of EXAFS measurements of the hydration of Cr^{3+} and Zn^{2+} in $\text{Cr}(\text{NO}_3)_3$ and $\text{Zn}(\text{NO}_3)_2$ solutions,³⁷ as well as X-ray diffraction measurements of divalent metal nitrate solutions have reported the existence of a second hydration shell consisting of 12 waters with an M-O distance of approx. 4.2 Å.³⁸ Additionally, vibrational spectroscopic studies from both IR and Raman measurements have proposed the existence of a second hydration shell in

aqueous solutions of alkali salts and transition metal ions.³⁹⁻⁴⁰ However, there have been contradictory reports based on EXAFS measurements of Zn^{2+} , Ni^{2+} and Co^{2+} which reported no detection of a second shell.⁴¹ Additionally, hydrogen isotope substitution neutron diffraction measurements combined with empirical potential structure refinement (EPSR) provided evidence of a first hydration shell around both cations and anions in potassium halide solutions but claimed that beyond the first shell water was unaffected.⁴²

Lastly, there have been reports of crystalline type packing in aqueous solutions such as those of Neilson et al⁴³ in which it is argued that the low-Q peak at approximately 1.0 \AA^{-1} in the neutron scattering data of concentrated NiCl_2 solutions is indicative of “quasi-lattice” ordering. Additionally, X-ray diffraction studies of concentrated CaCl_2 solutions have also shown the existence of a low-Q peak in the structure factor data that was interpreted as evidence of positional correlations beyond the nearest neighbor contacts in solution.⁴⁴ The importance of the crystalline type packing combined with the hydration shells and the effects on water structure begin to give the microscopic picture necessary to gain a deeper understanding of aqueous solutions and the factors that give rise to their observed bulk properties.

1.4 Reasons for using zinc chloride

Aqueous solutions of zinc chloride have been studied for many decades. There have been studies of physical properties such as the activity coefficients⁴⁵⁻⁴⁶ as well as conductivity and viscosity.⁴⁷⁻⁴⁸ Additionally, the concentration dependent phase diagram of aqueous zinc chloride has been investigated⁴⁹ along with the reporting of the crystal structures of several hydrate phases.⁵⁰⁻⁵² Furthermore, the hydration and coordination of Zn^{2+} in aqueous zinc chloride solutions has been investigated via X-ray⁵³⁻⁵⁵ and neutron⁵⁶ diffraction as well as Raman spectroscopy^{54, 57-58} and computational techniques.⁵⁹ This is partly because of the high solubility

of zinc chloride (432 g/100 mL of H₂O at 25 °C). There has been much discussion in the literature about the ion association and hydration nature of species in the high concentration region. It is the purpose of this thesis to examine zinc chloride solutions over a wide concentration range in an attempt to understand the structural features as a function of concentration. In this present study, we have utilized X-ray and neutron diffraction to analyze the structure factors $S(Q)$ and pair distribution functions (PDFs) with respect to concentration. Attenuated total reflectance infrared (ATR-IR) and Raman spectra were taken to examine the variation in the Zn-O and Zn-Cl stretching modes as well as the change in the water bending and stretching modes as a function of concentration. Lastly, proton nuclear magnetic resonance (¹H-NMR) measurements were taken to examine the variation in the chemical shift (i.e. electron density on the water hydrogen) as a function of concentration. In the limit of infinite dilution, it is expected that the structure would be that of pure water. On the more concentrated side however, we will show that there is an ionic liquid nature to the system in which water does not act as a solvent but rather as a ligand. Furthermore, it is shown that the R = 3 composition forms a pure crystalline phase of which the structural features are maintained into the liquid state. Knowledge of the nature of the system at these two concentration regimes allows for two important starting points when analyzing and interpreting the concentration dependent data.

1.5 Outline

In this work, the aqueous zinc chloride system has been examined across a wide concentration and temperature range through the use of differential scanning calorimetry (DSC), synchrotron X-ray diffraction (XRD), neutron diffraction as well as infrared (IR), Raman and ¹H NMR spectroscopy. Ultimately it is shown that there is the formation of strong complexes, Zn(H₂O)₆²⁺ and ZnCl₄²⁻, persisting to high dilutions as well as a strong ordering/directing of the

waters around the cation to form multiple hydration shells upon dilution. Additionally, it is shown that crystalline type packing persists into the liquid state.

In Chapter 2, examination of the $R = 3$ zinc chloride hydrate found it to be a congruently melting phase of the $\text{ZnCl}_2/\text{H}_2\text{O}$ system for which the crystal structure was solved. It was found to have a $P\bar{1}$ unit cell with pseudo-CsCl type packing of the molecular ions $\text{Zn}(\text{H}_2\text{O})_6^{2+}$ and ZnCl_4^{2-} . An investigation was begun to determine if the crystalline order persisted into the liquid state. Neutron and X-ray diffraction measurements as well as structural refinements and reverse Monte Carlo modelling were employed to determine if the observed crystalline structure was maintained to some extent into the liquid state. Single crystal X-ray and neutron diffraction measurements were taken of the deuterated $R = 3$ zinc chloride hydrate. Following structural refinement, it was determined that the peak profile of the liquid diffraction pattern corresponded to the Bragg peaks observed in the crystal pattern. Modelling was performed and confirmed this. It was ultimately found that the $R = 3$ hydrate has a pseudo CsCl-type packing in the liquid state and that the molecular ions persist upon melting.

Chapter 3 continues the diffraction work, examining the structures that occur in the aqueous zinc chloride system upon dilution of the $R = 3$ hydrate. The goal of this chapter was to determine if any intermediate range order persisted in the system upon the addition of water, if there are any liquid/liquid phase transitions occurring in the system as a function of concentration and, if the ions observed in the $R = 3$ phase persisted upon dilution. The structure factor data and the pair distribution functions (PDFs) for both X-ray and neutron diffraction over a range of concentrations were examined. The full compositional phase diagram was produced from DSC measurements and it was found that there is a region in which no crystallization

occurs. Raman measurements were taken in the low frequency region of the $\text{Zn}(\text{H}_2\text{O})_6^{2+}$ and ZnCl_4^{2-} stretching modes and it was found that the ions persist upon dilution.

In Chapter 4, ^1H NMR was utilized to determine the various proton environments in the zinc chloride solutions as a function of temperature and concentration. It was anticipated that the various hydration shell environments could be observed via this method in order to gain deeper insight into the degree of hydration of the zinc ion. Initially low temperature measurements were taken in an attempt to slow down the proton dynamics in the system to the extent that the hydration shells could be observed. Upon the failure of this attempt an extensive effort was begun to fit the room temperature chemical shift data as a function of concentration and develop a model that accounted for the degree of hydration in the system. It was found that utilizing an exponential fit to describe the change of the different water environments as they not only interact with the ion but also with waters in higher hydration shells, a piecewise function gave the best fit in which the individual pieces correspond to the specific hydration shells of the zinc cation and the parameters of the exponential fit have physical meaning with respect to the system. From this it was found that five hydration shells are needed to accurately describe the data.

Lastly, in Chapter 5 the water bending and stretching mode regions were examined as a function of zinc chloride concentration via IR and Raman spectroscopy. A two-state model was applied to the data from which it was discovered that in fact multiple water environments were necessary to describe the data. As with the ^1H NMR fitting of Chapter 4, it was found that five hydration shells are necessary to fully describe the experimental data.

1.6 References

1. Bragg, W. H.; Bragg, W. L., The reflection of X-rays by crystals. *Proceedings of the Royal Society of London. Series A, Containing Papers of a Mathematical and Physical Character* **1913**, 88 (605), 428-438.
2. Martin, J. D.; Keary, C. L.; Thornton, T. A.; Novotnak, M. P.; Knutson, J. W.; Folmer, J. C., Metallotropic liquid crystals formed by surfactant templating of molten metal halides. *Nature materials* **2006**, 5 (4), 271-275.
3. Barker, J. A., *Lattice theories of the liquid state*. Pergamon Press: 1963; Vol. 1.
4. Rowlinson, J.; Curtiss, C., Lattice theories of the liquid state. *The Journal of Chemical Physics* **1951**, 19 (12), 1519-1529.
5. Frank, F. In *Supercooling of liquids*, Proc. R. Soc. Lond. A, The Royal Society: 1952; pp 43-46.
6. Hirschfelder, J.; Stevenson, D.; Eyring, H., A theory of liquid structure. *The Journal of Chemical Physics* **1937**, 5 (11), 896-912.
7. Eyring, H., H. Eyring, J. Chem. Phys. 4, 283 (1936). *J. Chem. Phys.* **1936**, 4, 283.
8. Peek, H. M.; Hill, T. L., On Lattice Theories of the Liquid State. *The Journal of Chemical Physics* **1950**, 18 (9), 1252-1255.
9. Green, H. In *A general kinetic theory of liquids I. The molecular distribution functions*, Proc. R. Soc. Lond. A, The Royal Society: 1946; pp 10-18.
10. Kirkwood, J. G., Molecular distribution in liquids. *The Journal of Chemical Physics* **1939**, 7 (10), 919-925.
11. Kirkwood, J. G., The statistical mechanical theory of transport processes I. General theory. *The Journal of Chemical Physics* **1946**, 14 (3), 180-201.
12. Bernal, J., An attempt at a molecular theory of liquid structure. *Transactions of the Faraday Society* **1937**, 33, 27-40.
13. Bernal, J. D., A geometrical approach to the structure of liquids. *Nature* **1959**, 183 (4655), 141.
14. Naberukhin, Y. I.; Voloshin, V.; Medvedev, N., Geometrical analysis of the structure of simple liquids: percolation approach. *Molecular Physics* **1991**, 73 (4), 917-936.
15. Arrhenius, S., Development of the theory of electrolytic dissociation. *Nobel Lecture* **1903**.

16. Hückel, E.; Debye, P., The theory of electrolytes: I. lowering of freezing point and related phenomena. *Phys. Z* **1923**, *24*, 185-206.
17. Kirkwood, J. G.; Buff, F. P., The statistical mechanical theory of solutions. I. *The Journal of Chemical Physics* **1951**, *19* (6), 774-777.
18. Ben-Naim, A., Inversion of the Kirkwood–Buff theory of solutions: application to the water–ethanol system. *The Journal of Chemical Physics* **1977**, *67* (11), 4884-4890.
19. Braunstein, J., Some aspects of solution chemistry in liquid mixtures of inorganic salts with water. *Inorganica Chimica Acta Reviews* **1968**, *2*, 19-30.
20. Bernal, J. D., The Bakerian lecture, 1962. The structure of liquids. *Proceedings of the Royal Society of London. Series A, Mathematical and Physical Sciences* **1964**, *280* (1382), 299-322.
21. Bernal, J.; Fowler, R., A theory of water and ionic solution, with particular reference to hydrogen and hydroxyl ions. *The Journal of Chemical Physics* **1933**, *1* (8), 515-548.
22. Finney, J. L. In *Bernal and the structure of water*, Journal of Physics: Conference Series, IOP Publishing: 2007; p 40.
23. Pauling, L., The structure of water. In *Hydrogen Bonding*, Elsevier: 1959; pp 1-6.
24. Hofmeister, F., About the science of the effects of salts: About the water withdrawing effect of the salts. *Arch. Exp. Pathol. Pharmacol.* **1888**, *24*, 247-260.
25. Mancinelli, R.; Botti, A.; Bruni, F.; Ricci, M. A.; Soper, A. K., Hydration of Sodium, Potassium, and Chloride Ions in Solution and the Concept of Structure Maker/Breaker. *The Journal of Physical Chemistry B* **2007**, *111* (48), 13570-13577.
26. Marcus, Y., Effect of ions on the structure of water: structure making and breaking. *Chemical reviews* **2009**, *109* (3), 1346-1370.
27. Kabisch, G., Intermolecular coupling of bending vibrations in liquid water. *Journal of molecular structure* **1981**, *77* (3-4), 219-226.
28. Arab, M.; Bougeard, D.; Smirnov, K. S., Molecular dynamics study of the structure and dynamics of Zn²⁺ ion in water. *Chemical Physics Letters* **2003**, *379* (3–4), 268-276.
29. Mohammed, A. M.; Loeffler, H. H.; Inada, Y.; Tanada, K.-i.; Funahashi, S., Quantum mechanical/molecular mechanical molecular dynamic simulation of zinc(II) ion in water. *Journal of Molecular Liquids* **2005**, *119* (1–3), 55-62.
30. Mhin, B. J.; Lee, S.; Cho, S. J.; Lee, K.; Kim, K. S., Zn(H₂O)₂₊₆ is very stable among aqua-Zn(II) ions. *Chemical Physics Letters* **1992**, *197* (1), 77-80.

31. Beret, E. C.; Galbis, E.; Pappalardo, R. R.; Sanchez Marcos, E., Opposite effects of successive hydration shells on the aqua ion structure of metal cations. *Molecular Simulation* **2009**, *35* (12-13), 1007-1014.
32. Cauët, E.; Bogatko, S.; Weare, J. H.; Fulton, J. L.; Schenter, G. K.; Bylaska, E. J., Structure and dynamics of the hydration shells of the Zn²⁺ ion from ab initio molecular dynamics and combined ab initio and classical molecular dynamics simulations. *The Journal of Chemical Physics* **2010**, *132* (19), 194502.
33. Munoz-Paez, A.; Pappalardo, R. R.; Sanchez Marcos, E., Determination of the Second Hydration Shell of Cr³⁺ and Zn²⁺ in Aqueous Solutions by Extended X-ray Absorption Fine Structure. *Journal of the American Chemical Society* **1995**, *117* (47), 11710-11720.
34. Bol, W.; Gerrits, G. J. A.; Van Panthaleon Eck, C. L., The hydration of divalent cations in aqueous solution. An X-ray investigation with isomorphous replacement. *Journal of Applied Crystallography* **1970**, *3* (6), 486-492.
35. Besemer, M.; Bloemenkamp, R.; Ariese, F.; Manen, H.-J. v., Identification of Multiple Water-Iodide Species in Concentrated NaI Solutions Based on the Raman Bending Vibration of Water. *The Journal of Physical Chemistry A* **2016**, *120* (5), 709-714.
36. Bergstroem, P. A.; Lindgren, J.; Kristiansson, O., An IR study of the hydration of perchlorate, nitrate, iodide, bromide, chloride and sulfate anions in aqueous solution. *The Journal of Physical Chemistry* **1991**, *95* (22), 8575-8580.
37. D'Angelo, P.; Barone, V.; Chillemi, G.; Sanna, N.; Meyer-Klaucke, W.; Pavel, N. V., Hydrogen and Higher Shell Contributions in Zn²⁺, Ni²⁺, and Co²⁺ Aqueous Solutions: An X-ray Absorption Fine Structure and Molecular Dynamics Study. *Journal of the American Chemical Society* **2002**, *124* (9), 1958-1967.
38. Soper, A. K.; Weckström, K., Ion solvation and water structure in potassium halide aqueous solutions. *Biophysical Chemistry* **2006**, *124* (3), 180-191.
39. Foxton, F.; Shutt, W., The activity of zinc chloride in concentrated solution. *Transactions of the Faraday Society* **1927**, *23*, 480-488.
40. Dunsmore, H. S.; Paterson, R., Re-determination of the standard electrode potential of zinc and mean molal activity coefficients for aqueous zinc chloride at 298.15 K. *Journal of the Chemical Society, Faraday Transactions 1: Physical Chemistry in Condensed Phases* **1976**, *72*, 495-503.
41. Mead, D. J.; Fuoss, R. M., Conductance and viscosity of concentrated solutions of calcium and zinc chlorides. *The Journal of Physical Chemistry* **1945**, *49* (5), 480-482.
42. Thomas, B.; Fray, D., The conductivity of aqueous zinc chloride solutions. *Journal of Applied Electrochemistry* **1982**, *12* (1), 1-5.

43. Mylius, F., Uber das Chlorzink. *Zeitschrift fur anorganische und allgemeine Chemie* **1905**, 44 (1), 209-220.
44. Hennings, E.; Schmidt, H.; Voigt, W., Crystal structures of $ZnCl_2 \cdot 2.5H_2O$, $ZnCl_2 \cdot 3H_2O$ and $ZnCl_2 \cdot 4.5H_2O$. *Acta Crystallographica Section E* **2014**, 70 (12), 515-518.
45. Wilcox, R. J.; Losey, B. P.; Folmer, J. C. W.; Martin, J. D.; Zeller, M.; Sommer, R., Crystalline and Liquid Structure of Zinc Chloride Trihydrate: A Unique Ionic Liquid. *Inorganic Chemistry* **2015**, 54 (3), 1109-1119.
46. Follner, H.; Brehler, B., Die Kristallstruktur des $ZnCl_2 \cdot 4/3H_2O$. *Acta Crystallographica Section B* **1970**, 26 (11), 1679-1682.
47. Maeda, M.; Ito, T.; Hori, M.; Johansson, G., The structure of zinc chloride complexes in aqueous solution. *Zeitschrift für Naturforschung A* **1996**, 51 (1-2), 63-70.
48. Yamaguchi, T.; Hayashi, S.; Ohtaki, H., X-ray diffraction and Raman studies of zinc(II) chloride hydrate melts, $ZnCl_2 \cdot rH_2O$ ($r = 1.8, 2.5, 3.0, 4.0, \text{ and } 6.2$). *The Journal of Physical Chemistry* **1989**, 93 (6), 2620-2625.
49. Kruh, R.; Standley, C., An X-ray diffraction study of aqueous zinc chloride solutions. *Inorganic chemistry* **1962**, 1 (4), 941-943.
50. Powell, D. H.; Barnes, A. C.; Enderby, J. E.; Neilson, G. W.; Salmon, P. S., The hydration structure around chloride ions in aqueous solution. *Faraday Discussions of the Chemical Society* **1988**, 85 (0), 137-146.
51. Irish, D. E.; McCarroll, B.; Young, T. F., Raman Study of Zinc Chloride Solutions. *The Journal of Chemical Physics* **1963**, 39 (12), 3436-3444.
52. Morris, D. F. C.; Short, E. L.; Waters, D. N., Zinc chloride and zinc bromide complexes—III: Structures of species in solution. *Journal of Inorganic and Nuclear Chemistry* **1963**, 25 (8), 975-983.
53. Parchment, O. G.; Vincent, M. A.; Hillier, I. H., Speciation in aqueous zinc chloride. An ab initio hybrid microsolvation/continuum approach. *The Journal of Physical Chemistry* **1996**, 100 (23), 9689-9693.

CHAPTER 2

Crystalline and Liquid Structure of Zinc Chloride Tri-hydrate: A unique ionic liquid

This chapter was previously published: Wilcox, R.J.; Losey, B.P.; Folmer, J.C.W.; Martin, J.D.; Zeller, M.; Sommer, R. *Inorg. Chem.* **2015**, 54, 1109-1119.

2.1 Introduction

Zinc chloride hydrate has been of considerable interest for various applications, as well as the subject of countless basic science investigations probing the nature of the solutes and solvent, particularly in concentrated solutions. More than one hundred fifty years ago it was discovered that concentrated zinc chloride hydrates are an effective solvent for cellulose.¹ Zinc chloride hydrates are instrumental for the formation and transport of hydrothermal ores.^{2,3} Zinc chloride hydrate solutions are ubiquitous for electroplating (galvanization), and are important in battery applications.⁴ Hydrolyzing zinc chloride hydrates is important for dental cement.⁵ Zinc plays numerous important roles in biology.^{6,7} Better knowledge of the extent in which both chloride ions and water molecules are associated with the zinc ion is critical both to the fundamental understanding and effective application of these systems. This, in turn, may lead to a better understanding of the role of this important micronutrient in biology.

Hydrates of zinc chloride afford one of the largest concentration ranges over which a salt-hydrate system is liquid at room temperature. At 25 °C ZnCl_2 exhibits solubility of 432 g/100 ml H_2O ($R = 1.75$; 64 mole % H_2O ; 31 m). (R has been used to describe the number of equivalents of water per equivalent of zinc.) In his 1968 review, Braunstein divided aqueous salt solutions into five classes defined by approximate ranges of water mole fraction: I. Debye-Hückel limiting (1 - >0.99); II. Extended Debye-Hückel theory (0.99 - 0.9); III. Hydrate melts (0.9-0.75); IV. Incomplete hydration sheaths (0.75-.01); and V. gas solubility (<0.01).⁸ Braunstein

noted that solutions with concentrations between about 1 and 80-mole percent water are of particular interest, where “the hydration shells of the ions must be incomplete and one must consider ion-ion, water-water and water-ion interactions.” As demonstrated by the $\text{ZnCl}_2 : \text{H}_2\text{O}$ phase diagram,^{9,10} four of the five Braunstein classes of hydrates are liquid at room temperature in this system. Additionally there are likely several hydrate phases that crystalize with discrete compositions below room temperature. Numerous measurements of the physical properties including for EMF,¹¹⁻¹⁵ conductivity,¹⁶⁻²² vapor pressure,^{13,14,16} density,¹⁸ viscosity,^{18,20,23} relaxation time for water exchange,²⁴ and glass transition temperatures^{11,20} of zinc chloride hydrates across the concentration range of type-II and type-III solutions indicate a variety of anomalies that suggest the likelihood of concentration controlled structural variation in the liquid hydrate phases. Any such structural variation is most likely accounted for by ion-association and/or the organization of the waters of solvation.

An extensive set of Raman²⁴⁻²⁷ and X-ray absorption spectroscopy,^{28,29} and X-ray and neutron diffraction²⁶ studies have probed the solution structure and ion speciation of zinc chloride hydrates. Various theoretical studies have further attempted to bring clarity as to the nature of hydrated species present.^{30,31} There is clear consensus that in the presence of excess chloride the ZnCl_4^{2-} anion is the most prevalent zinc containing species. However, there is significant variation in species proposed to account for the data measured for the pure zinc chloride hydrates. Possible tetrahedral $[\text{ZnCl}_n(\text{OH}_2)_{4-n}]^{2-n}$ ($n = 1-4$) and octahedral $[\text{ZnCl}_n(\text{OH}_2)_{6-n}]^{2-n}$ ($n = 0-4$) species have been proposed. The strong Raman peak at $\sim 280 \text{ cm}^{-1}$, observed across an extensive range of concentrations, is characteristic of the ZnCl_4^{2-} anion, though there is some debate as to whether this is actually $[\text{ZnCl}_4(\text{OH}_2)_2]^{2-}$.²⁴⁻²⁷ Similarly, the peak observed at $\sim 390 \text{ cm}^{-1}$, consistent with that observed for solutions of zinc perchlorate,³² is

assigned to $\text{Zn}(\text{OH}_2)_6^{2+}$. Attempts to appropriately fit peak shapes, however, have led to the suggestion of other mixed chloride/hydrate species.

Diffraction studies of concentrated solutions all imply that zinc is coordinated to both chloride and water ligands, albeit with some difference of perspective as to whether the total zinc coordination number is 4 or 6.^{26,33-36} A $^{35}\text{Cl}/^{37}\text{Cl}$ neutron diffraction study further indicated that the coordination number around Cl is 5.6 in dilute solutions ($<0.47\text{m}$, $R > 100$) and decreases to 4.4 in more concentrated (4 m, $R = 13$) solutions.³⁶ It is interesting to observe that in the Raman studies, authors accounted for the seemingly conflicting coordination information by proposing a variety of speciation. By contrast, diffraction studies tend to consider the data to be reflective of a single zinc environment. The latter requires that there is some degree of oligomerization in which chlorides are shared between zinc atoms.³³ In very concentrated solutions, $> 10\text{ M}$ ($R = 3$, 18.5 m), both Irish et al.²⁴ and Yamaguchi et al.²⁶ also suggest Raman spectroscopic evidence for oligomeric speciation.

Precedence for a variety of the proposed chloride/hydrate species can be found from single crystal structures of ternary systems. In combination with alkali cations, zinc chloride hydrates yield for example the tetrahedral ZnCl_4^{2-} anion in the crystalline structure of $\text{Li}_2\text{ZnCl}_4 \cdot 2\text{H}_2\text{O}$, the waters being uniquely associated with the Li^+ cations,³⁷ and the pseudo-tetrahedral $[\text{ZnCl}_3(\text{OH}_2)]^-$ ion in $\text{KZnCl}_3 \cdot 2\text{H}_2\text{O}$.³⁸ In the presence of large macromolecules such as the 18-crown-6 macrocycle, the neutral, pseudo tetrahedral species $\text{ZnCl}_2(\text{OH}_2)_2$ is observed.³⁹ A search of the Cambridge Structural Database and Inorganic Crystal Structure Database finds no examples of a zinc mono-chloride hydrate. The only single crystal structure of a binary zinc chloride hydrate, prior to this work, is of $\text{ZnCl}_2 \cdot 1.33\text{ H}_2\text{O}$ in which $2/3$ of the zinc atoms form polymeric chains, tetrahedrally coordinated by bridging chlorides and the remaining $1/3$ of the

zinc atoms are octahedrally coordinated with four independent water molecules and two chlorides, shared with the afore mentioned polymeric chains.⁴⁰

Given our interest in understanding and designing structure in materials at the crystalline/liquid (amorphous) interface, which we previously achieved in inorganic networks using templating organic cations,^{41,42} we were drawn to the zinc chloride hydrate system as one in which significant amorphous structure might be engineered without the inclusion of organic templates. Reinvestigation of the water/zinc chloride phase diagram identifies the three-equivalent hydrate ($R = 3$, 18.5 m, 10.1 M) to be a congruently melting phase. Here we report the single crystal structure of this hydrate, and demonstrate by synchrotron X-ray and variable temperature neutron diffraction, along with reverse Monte Carlo modeling, the high degree of structural correlation between the liquid and crystalline phases. Examination of the infrared (IR) water spectrum further demonstrates the hydrogen-bonding capacity of this novel ionic liquid.

2.2 Experimental Methods

2.2.1 Materials and synthesis

Zinc chloride was purchased from Aldrich. The material was dried under dynamic vacuum at 100 °C overnight, then sublimed. Purity of the starting material was confirmed to be the anhydrous δ -ZnCl₂ by powder X-ray diffraction, and DSC, m.p. 317 °C. Purified ZnCl₂ was stored and utilized in a nitrogen filled glove box. 18 M Ω water, was obtained from a Millipore Synergy ultra pure water filtration system. 99.99% D₂O was used as purchased from Aldrich.

DSC and capillary scale samples were prepared by placing a sample (~20 mg) of δ -ZnCl₂ into a high pressure stainless steel DSC pan, placed on the pan of a home built Environmentally Controlled Microbalance (the microbalance head was purchased from CI Electronics and is controlled by LabWeigh Software). A stream of nitrogen was passed through a water bubbler,

and the saturated water vapor passed over the sample until the desired stoichiometric amount of water had been sorbed. The hydration reaction was then stopped. Using a syringe with a 0.7 mm ID fused silica capillary affixed to the end, a 1-2 mm aliquot was drawn into the middle of the capillary, which was then flame sealed on both ends of the zinc chloride hydrate sample. The DSC pan was then sealed using a gold seal. This preparation technique assured equivalent composition for the structural and calorimetric measurements.

Bulk samples of $\text{ZnCl}_2 \cdot 3\text{H}_2\text{O}$ were prepared by adding for example 1.00 g of 18 M Ω H_2O (55.5 mmol) to 2.52 g anhydrous ZnCl_2 (18.5 mmol). The samples were prepared and stored in Teflon capped Pyrex vials. Solutions were mixed by agitation, and equilibrated for a minimum of 2 days before any physical measurements were conducted.

2.2.2 Single crystal structure

$[\text{Zn}(\text{OH}_2)_6][\text{ZnCl}_4]$: A 0.7 mm ID capillary containing a 1 mm aliquot of the liquid $\text{ZnCl}_2 \cdot 3\text{H}_2\text{O}$ was affixed to a goniometer head on a Bruker AXS SMART APEX CCD diffractometer equipped with a Kryo-flex cryostat. As a representative example, a crystal was grown from the melt by rapidly cooling the capillary to a -50 °C isotherm in the cryostat's cold stream. The sample was held at the crystallization isotherm for one hour to afford crystallization. The sample was then further cooled to 208 K for data collection. Single, or near single crystal(s) were obtained and lattice constants were measured. The best crystal was selected based on the diffraction pattern using the program Cell Now. The selected domain accounted for the most intense reflections, for all high angle reflections, and for about one half of all harvested reflections. Other domains were ignored during the integration and all reflections were used, regardless of overlap with reflections from other domains. Reflections were collected from an entire Ewald sphere with 5738 unique reflections measured for $2.88^\circ < 2\theta < 56.56^\circ$. The

final unit cell determination and structural refinement was made using a symmetry constrained fit of 2868 reflections. The data were corrected for absorption using SADABS. The structure was solved by direct methods and refined by full matrix least squares against F^2 with all reflections using SHELXL-97 (Sheldrik 2008, Bruker 2000-2003).

[Zn(OD₂)₆][ZnCl₄]: A 0.5 mm ID capillary containing a 1 mm aliquot of the liquid ZnCl₂·3H₂O was affixed to a goniometer head and placed directly into the cold stream at 253 K on a Bruker-Nonius Kappa Axis X8 Apex 2 diffractometer with an Oxford Cryosystems 700 cryostat. The sample was further cooled to 233 K at a rate of 360 °/h. A near single crystal was observed to have grown after 10 min at the 233 K isotherm. Unit cell determination and indexing were performed on the dominant domain which could be treated as a single crystal. Reflections were collected from an entire Ewald sphere with 5799 unique reflections measured for $5.78^\circ < 2\theta < 73.04^\circ$. The final unit cell determination and structural refinement was made using all unique reflections. The data were corrected for absorption using SADABS. The structure was solved by direct methods and refined by full matrix least squares against F^2 all reflections using SHELXL-2014. (Sheldrik 2014).

2.2.3 Synchrotron XRD of liquid

A 0.7 mm ID capillary containing a 1-2 mm aliquot of ZnCl₃·3H₂O molten was affixed to a goniometer head on the diffractometer on line 11-ID-B at the Advanced Photon Light Source, Argonne National Laboratory. The sample was measured at room temperature, ~295 K. A 90 KeV ($\lambda = 0.13702$ nm) X-ray beam was utilized to collect an average of 100 scans at 10 s per scan using a GE amorphous silicon detector. Data for background subtraction was obtained using the same sample capillary that was shifted such that no sample, only the fused silica capillary was in the beam. The raw 2-dimensional data was radially integrated using Fit2D.⁴³

The diffraction data was subsequently transformed into a structure factor $S(Q)$, subtracting the background and correcting the data for sample and instrument effects such as Compton scattering, Laue diffuse scattering, self-absorption, X-ray polarization and the scattering based on the elements present. Transformation of the data to obtain the $S(Q)$, and obtaining its inverse Fourier Transform pair distribution function $G(R)$ was performed using the PDFgetX2 program.⁴⁴

2.2.4 Neutron diffraction

1 ml samples were sealed into 5mm OD quartz NMR tubes (WILMAD). The samples as well as an empty NMR tube were mounted on the linear sample changer installed at the NOMAD diffractometer, Spallation Neutron Source, Oak Ridge National Lab.⁴⁵ The linear sample changer is equipped with a Cobra Plus Cryosystem from Oxford modified for use with neutron scattering to operate with temperature controlled Ar gas. Ar gas has a very small neutron scattering cross-section and hence a considerably reduced background contribution compared to the more commonly used N_2 . The neutron event data were binned as a function of Q using a calibration derived from a measurement of diamond powder as described in reference 45 and normalized to the integrated proton charge accumulated on the neutron target. Measurements obtained from a 5.8 mm diameter vanadium rod were used for the normalization of the sample data to a differential cross section. The incoherent contribution to the scattering cross section was approximated by a pseudo-Voigt function. Data was collected to $Q_{\max} = 50 \text{ \AA}^{-1}$. Based on the total scattering structure factor $S(Q)$, and the reduced atomic pair distribution function $G(r)$ was calculated using data up to $Q = 31 \text{ \AA}^{-1}$. Data were collected from 100 to 333 K for specific isotherms (sum of three 20 min scans) or with a ramped temperature profile 1 or 5 °/min.

Transformation of the data to obtain the $S(Q)$, and obtaining its inverse Fourier Transform pair distribution function $G(R)$ was performed using the NOMAD-SNS analysis suite of programs.

GSAS Structural Determination: Structure refinement for one sample was performed using GSAS and EXPGUI software.^{46,47} The sample was obtained by cooling 0.5 mL of a $R = 3$ hydrate melt to 225 K at a rate of 0.5 °C/min. The structure was refined against the neutron time-of-flight (TOF) data from one of six detector banks on the NOMAD instrument. The background of the TOF data, lattice parameters, atomic coordinates, occupancies and atomic displacement parameters were refined.

2.2.5 ATR-IR

Infrared spectra were collected using a Digilab FTS-3000 Fourier transformed infrared (FT-IR) spectrometer using a mounted crystalline germanium, attenuated total internal reflection (ATR) sampling attachment (Pike Technologies inc., MIRacle™ Single Reflection ATR) with a normal spectral response of 650 to 5500 cm^{-1} . A droplet of the molten hydrate (or 18 MΩ H_2O) was pipetted onto the ATR crystal and the crystal element capped. The infrared light was focused onto the photodiode of a liquid nitrogen-cooled, narrow band mercury-cadmium-telluride (MCT) detector with a normal spectral response of 650 to 7000 cm^{-1} . There is nominally one reflection with a spot size of approximately 100 microns. The spectrometer was purged with dry nitrogen, which reduces atmospheric water or CO_2 contamination in the spectral beam path. Spectra were recorded at room temperature, approximately $23^\circ \pm 0.5^\circ \text{C}$ with a resolution of 1 cm^{-1} . The spectra were converted into absorbance units by taking the negative of the log ratio of a sample spectrum to that of an empty crystal.

2.2.6 Raman

Approximately 0.5 ml samples of the liquid zinc chloride hydrate were placed into a septum capped 5 mm NMR tube and spun with an air piston spinning sample holder. Raman spectra were collected using a Spex 1877E Triplemate Monochromator fitted with a liquid nitrogen cooled CCD detector. The primary light source for excitation is a frequency doubled Coherent Mira 900 Ti:Sapphire laser system, which consists of a Coherent Verdi (10W) pump laser, a Coherent Mira 900 Ti:Sapphire laser used to generate 532 nm light, and an Inrad 5-050 Ultrafast Harmonic Generation system to generate 406 nm light. The output light of the Ti:Sapphire laser system was used as the excitation source for all the Raman experiments, with a typical energy of 60 mW at the sample. All spectra were recorded at room temperature, approximately $23^{\circ} \pm 0.5^{\circ}$ C. The sample Raman spectra's were calibrated using the known spectral bands of, carbon tetrachloride, indene, toluene and cyclohexane, by plotting the observed peak locations against their known position. The plot was then fitted to a line, the slope of which was used to correct the X-axis of the sample spectra.

2.2.7 Computational methods

Molecular Dynamics (MD): Molecular dynamics was performed in order to obtain the starting configuration required for the reverse Monte Carlo modeling.⁴⁸ The MD simulations were performed using the CPMD package.⁴⁹ The plane wave/pseudopotential method was employed. The basis set energy cut-off was set to 60 Ry. The Troullier-Martins pseudopotential⁵⁰ with the PBE functional⁵¹ was employed for electronic structure calculations. The starting configuration for the MD simulation originated from the crystal structure, **Id**. Initially, the lattice parameters of the crystal structure were expanded to 6.7075 Å, 6.7400 Å, 14.811 Å, 90.656° , 98.936° and 95.498° in order to match the experimentally measured density

of 1.98 g/mL for the liquid. The cell was then extended to a 2 x 2 x 1 supercell containing 192 atoms. Car-Parrinello molecular dynamics⁵² was performed on this supercell. The total simulation time was 1.56 ps using 0.12 fs timesteps. The Nosé-Hoover thermostat^{53,54} was employed with a coupling frequency of 3000 cm⁻¹ and a constant temperature of 298K. The nuclear configuration at the last timestep (i.e. 1.56 ps) was taken as the starting configuration for RMC.

Reverse Monte Carlo (RMC): RMC modeling was performed using RMCProfile⁵⁵ in order to obtain a model of the liquid system. Distance window constraints, acting as a hard sphere potential, were set equivalent to the width of the intramolecular ion pair correlations to allow for additional variation in the liquid. Refinement of the structure was performed simultaneously for both the $S(Q)$ and $g(r)$ data obtained at ~298 K from NOMAD for a R = 3 zinc chloride hydrate sample. Each simulation box contained 5184 atoms and the calculations were run for between 5 and 50 hours.

2.3 Results

2.3.1 (H/D)₂O:ZnCl₂ phase diagram

The most complete previously reported water:ZnCl₂ phase diagram is that of Mylius and Dietz 1905, i.e. prior to the discovery of X-ray diffraction. It gives indication of several potentially crystalline zinc chloride hydrate phases, though their crystalline structures are unconfirmed. Using doubly sublimed anhydrous ZnCl₂ and 18 MΩ H₂O or as purchased 99.99% D₂O, we initiated a careful re-examination of this phase diagram by differential scanning calorimetry (DSC), gravimetric analysis, synchrotron X-ray and neutron diffraction, and Raman and IR spectroscopy. Shown in Figure 2.1 is the portion of the phase diagram surrounding the R = 3 (75 mole % (H/D)₂O) composition. These data demonstrate the existence of a congruently

melting phase at the $R = 3$ composition, with no significant evidence of any solid solution formation. The H_2O compound exhibits a melting point of 6°C whereas the melting point for the D_2O compound is -1°C . It is interesting to note that this water:zinc chloride system exhibits an inverse isotope effect compared to that of water for which H_2O melts at 0°C and D_2O melts at 3.8°C .

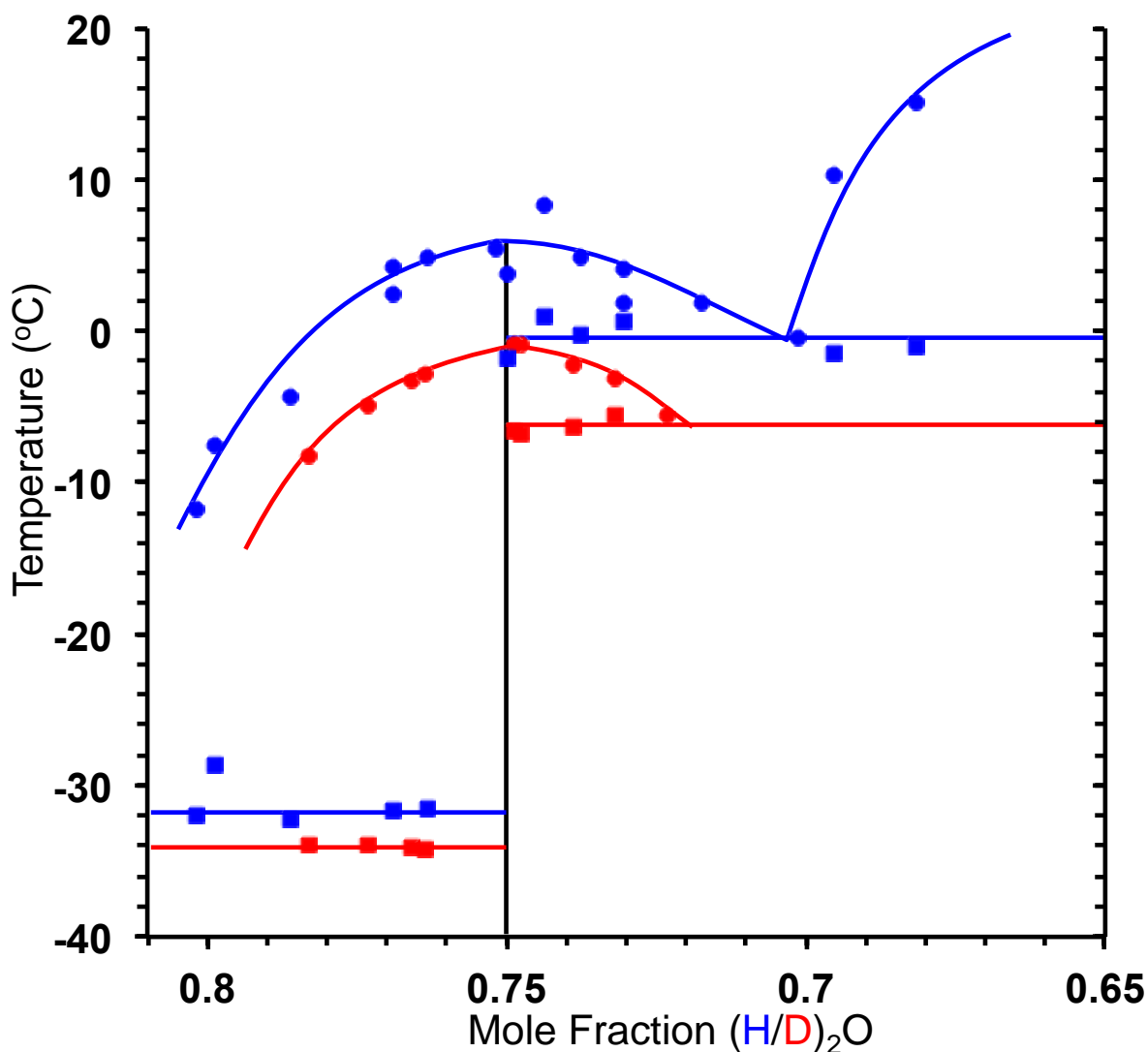


Figure 2.1 Water: zinc chloride phase diagram in the vicinity of the $R = 3$ composition. Data for H_2O are plotted in blue and data for D_2O are plotted in red.

2.3.2 Structure of $[\text{Zn}(\text{O}(\text{H}/\text{D})_2)_6][\text{ZnCl}_4]$, I_H and I_D

In other work in our laboratory we have determined that for congruently melting materials it is often possible to access conditions in which crystal nucleation is slow but growth is fast, conditions necessary for single crystal growth, by rapidly quenching a molten sample to an isotherm 5-50 ° below the melting point.⁵⁶ Single crystal growth is further facilitated by limiting the total volume of the sample being crystallized, such as within a capillary. Applying this crystallization technique to the R = 3 zinc chloride molten salt hydrate resulted in successful single crystal growth upon quenching to 253 K or 223 K isotherms. Data for three separate in situ grown single crystals of the H₂O compound (**I_H**) were collected after cooling the crystal to 254 K, 208 K and 100 K, and for single crystals of the D₂O compound (**I_D**) at 233 K. A summary of the crystallographic data is given in Table 2.1. Full details of the structure solutions are available in the supporting information.

Table 2.1 Single Crystal Data and Refinement Parameters for $[\text{Zn}(\text{O}(\text{H}/\text{D})_2)_6][\text{ZnCl}_4]$.

Empirical Formula	$\text{Zn}_2\text{Cl}_4\text{O}_6\text{H}_{12}$			$\text{Zn}_2\text{Cl}_4\text{O}_6\text{D}_{12}$
Formula weight	380.68			392.71
Crystal color	Colorless			
Crystal system	Triclinic			
Space Group	$P\bar{1}$			
Temperature K	100	208	254	233
<i>a</i> , Å	6.413(3)	6.4421(15)	6.477(3)	6.4728(9)
<i>b</i> , Å	6.506(3)	6.5034(15)	6.511(3)	6.5054(8)
<i>c</i> , Å	14.211(6)	14.281(3)	14.291(7)	14.2949(18)
α , deg	90.946(3)	90.626(3)	90.466(8)	90.656(3)
β , deg	99.278(7)	99.082(3)	98.900(8)	98.936(3)
γ , deg	95.741(7)	95.490(3)	95.575(8)	95.498(3)
V	581.9(4)	587.9(2)	592.4(5)	591.77(13)
Z	2	2	2	2
R ($F^2 > 2\sigma F^2$)	0.085	0.046	0.079	0.0223
R_w	0.190	0.128	0.184	0.0536
GOF	1.064	1.110	1.071	1.034

Of the three **I_H** single crystals examined, the one for which data was collected at 208 K was of the highest quality, and thus is the one from which distance information is reported throughout this manuscript. Other than thermal expansion for which the unit-cell volume increases by about $0.066 \text{ \AA}^3 \cdot \text{K}^{-1}$, Figure 2.2, the crystal structure is equivalent for each of the temperatures examined.

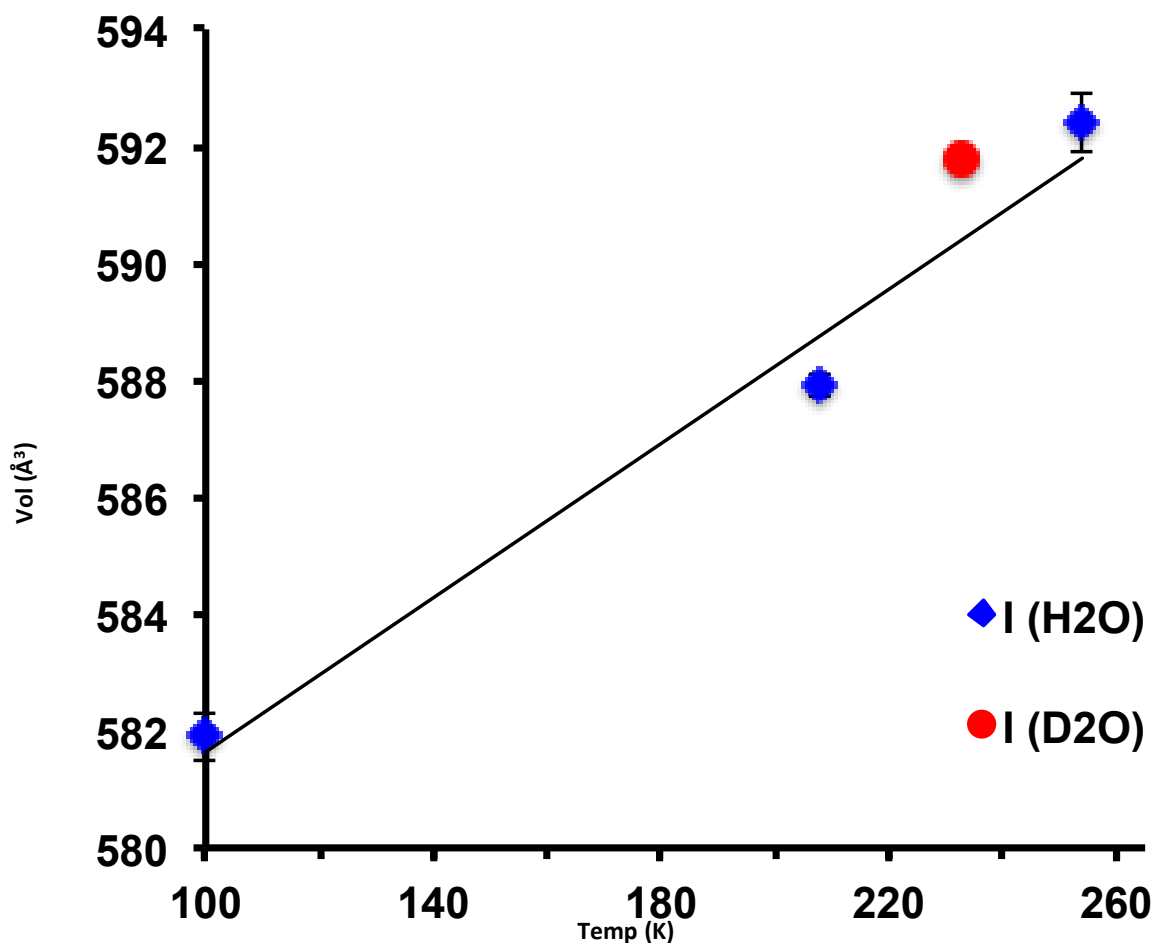


Figure 2.2 Temperature dependence of the volume of **I_H** and **I_D**.

The heavy atom arrangement in the **I_D** single crystal structure is equivalent to the **I_H** structures, but with some variation in the H/D positions. In the structure solutions, all heavy atoms were clearly located in the difference maps. Hydrogen atoms were tentatively assigned

from difference density Fourier maps. For **I_H** the O-H distances were then constrained to 0.84(2)Å, H--H distances within each water molecule were constrained to 1.35(2)Å and $U_{\text{iso}}(\text{H})$ was set to 1.5 times $U_{\text{eq}}(\text{O})$ of the adjacent oxygen atom. For **I_D** the O-D distances were then constrained to 0.95(2)Å, based on the pair distribution function (PDF) analysis of neutron diffraction data, and 1.5 times $U_{\text{iso}}(\text{D})$ was set to $U_{\text{eq}}(\text{O})$ of the adjacent oxygen atom.

Powder neutron diffraction data were collected on multiple samples of **I_D**, crystallized using various cooling profiles; quench to slow cooling. Slow cooling (0.5 K/min) to 225 K yielded the most polycrystalline sample. The significant variation in the peak intensities in the diffraction patterns, even for the same sample crystallized under different cooling regimes, is likely a result of incomplete orientational randomization due to a small number of crystallites. A reasonable GSAS refinement was obtained from the most polycrystalline of these samples, Figure 2.3. The heavy atom structure in this refinement is equivalent to that obtained from the single crystal X-ray structures, but accurate D positions were not obtained.

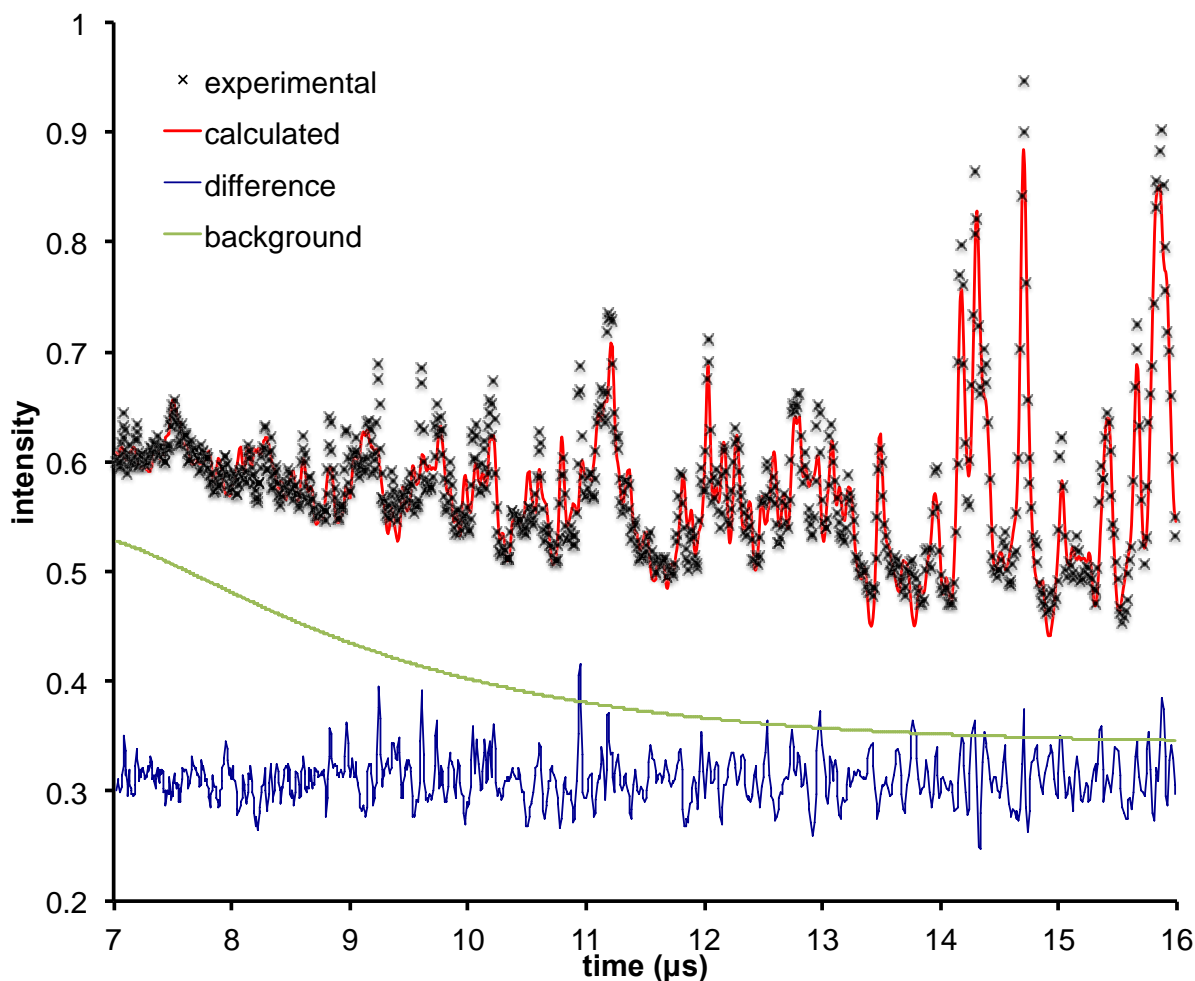


Figure 2.3 GSAS refinement using time of flight data collected on the NOMAD-SNS on an in-situ grown sample of $\mathbf{I_D}$. While this is a polycrystalline sample, it is not a powdered sample, thus preferred orientation of the limited number of crystallites results in an intensity profile that limits the structural refinement.

An ORTEP drawing of the $R=3 \mathbf{I_H}$ crystal structure is given in Figure 2.4. The crystal structure consists of a cesium chloride type packing of hexaaquozinc cations and tetrachlorozincate anions; a structure isomorphous to the previously reported $[\text{Mg}(\text{OH}_2)_6][\text{ZnCl}_4]$.⁵⁷ A summary of intra- and inter-molecular distances for the molecular ions is given in Tables 2.2 and 2.3. Two crystallographically distinct hexaaquozinc cations are observed, each located on centers of inversion. The orientation of the water molecules appears to be most strongly determined by their arrangement about the central zinc atom of the hydrated

cation. Only weak hydrogen bonding is observed between neighboring hexaaquozinc cations, with the shortest O--O contact being 3.14 Å (see Table 2.3). Because the chloride coordination environment has been of interest to the study of molten salt hydrates,³⁶ all Cl--OH₂ contacts were analyzed and summarized in Table 2.3. Each chloride has four to six water molecule neighbors with a Cl--O distance of less than 4.0 Å, filling a coordination hemisphere opposite the Zn-Cl bond. However, there is no apparent strong geometric preference to the water-Cl interactions. Only limited weak hydrogen bonding to the tetrachlorozincate anion can be implied with only one contact below 3.2 Å but several contacts between 3.2 and 3.3 Å ($\Sigma_{\text{Cl-O vdw}} = 3.3 \text{ Å}$).

Table 2.2 Selected Bond Distances observed for [Zn(OH₂)₆][ZnCl₄] at 208 K.

	[Zn(OH ₂) ₆][ZnCl ₄]
Zn-Cl	2.24-2.29 Å
Zn-O	2.04-2.10 Å
Cl-Cl _{intra}	3.61-3.81 Å
Cl-Cl _{inter}	3.44-4.11 Å (4.70 Å-5.80 Å)
O-O _{intra} <i>cis</i>	2.89-3.09 Å
<i>trans</i>	4.07-4.20 Å
O-O _{inter}	3.09-3.55 Å
Zn _{Cl} -Zn _O	5.01-7.19 Å

Table 2.3 Nearest intermolecular ion Cl--O and O--O contacts in Å observed for [Zn(OH₂)₆][ZnCl₄] at 208 K.

	Cl1	Cl2	Cl3	Cl4	
O1	3.17, 3.32	3.27, 3.73			O1--O1 3.20
O2	3.55, 4.08	3.24, 3.68	3.26		O2--O4 3.47
O3	3.23, 3.37, 4.04	3.71	3.35		O3--O3 3.19
O4		3.36	3.43, 3.96	3.30	O4--O2 3.47
O5		3.23		3.23, 3.69, 3.80	O5--O5 3.61
O6			3.25	3.31, 3.69, 4.04	O6--O6 3.14

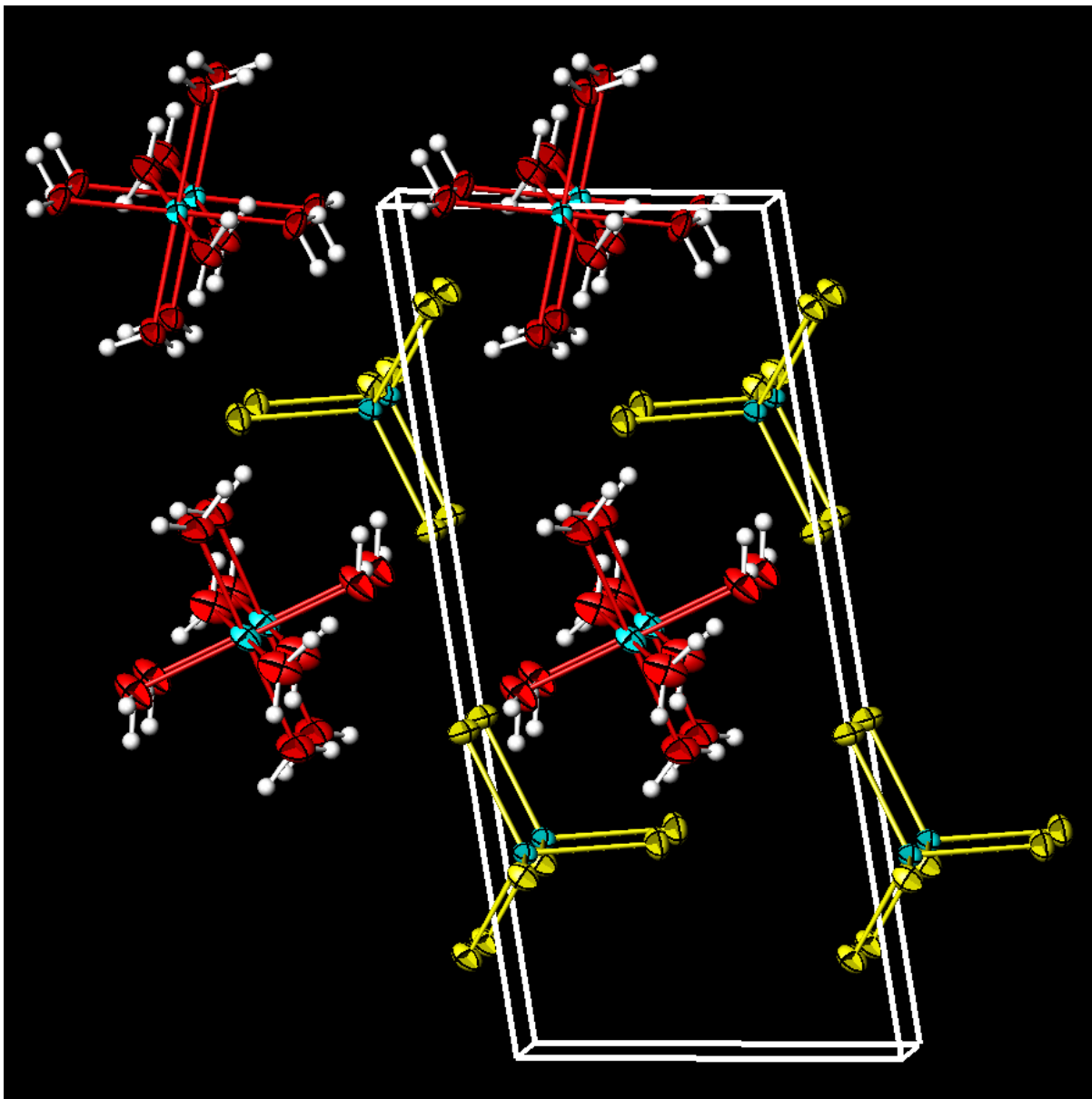


Figure 2.4 ORTEP drawing of R = 3, $[\text{Zn}(\text{OH}_2)_6][\text{ZnCl}_4]$ showing the crystallographic labeling scheme.

2.3.3 Diffraction of the molten hydrate

To understand the relationship between the crystalline and molten hydrate phases, room temperature synchrotron and variable temperature neutron diffraction data were obtained for the R = 3 hydrate. Structure factor plots of X-ray synchrotron, R = 3 melt, as well as R = 1.7, water and molten ZnCl_2 (320 °C), and neutron R=3 melt (298 K) and crystal (225 K), as well as D_2O

(298 K) and glassy ZnCl_2 (298K) scattering are shown in Figure 2.5. Grossly, the structure factor plots of the $R=3$ and $R = 1.7$ hydrates are very similar to that of molten anhydrous ZnCl_2 . The most notable difference is observed for the lowest Q peak(s). In the X-ray data, this peak shifts from 1.07 \AA^{-1} for anhydrous molten ZnCl_2 to 1.28 \AA^{-1} and 1.23 \AA^{-1} for the $R = 1.7$ and $R = 3$ hydrates, respectively. In the neutron data, this peak shifts from 1.02 \AA^{-1} for the room temperature glassy ZnCl_2 to 0.81 \AA^{-1} for the $R = 3$ hydrate. The higher- Q peaks at $\sim 2.1 \text{ \AA}^{-1}$ and $\sim 3.6 \text{ \AA}^{-1}$ are remarkably similar across all of the zinc chloride based materials, but clearly contrast those of water. Comparison of the structure factor obtained for D_2O with literature reports suggests that the shoulder on the high Q side of the peak at 2.0 \AA^{-1} is indicative of some H_2O contamination in the D_2O .⁵⁸

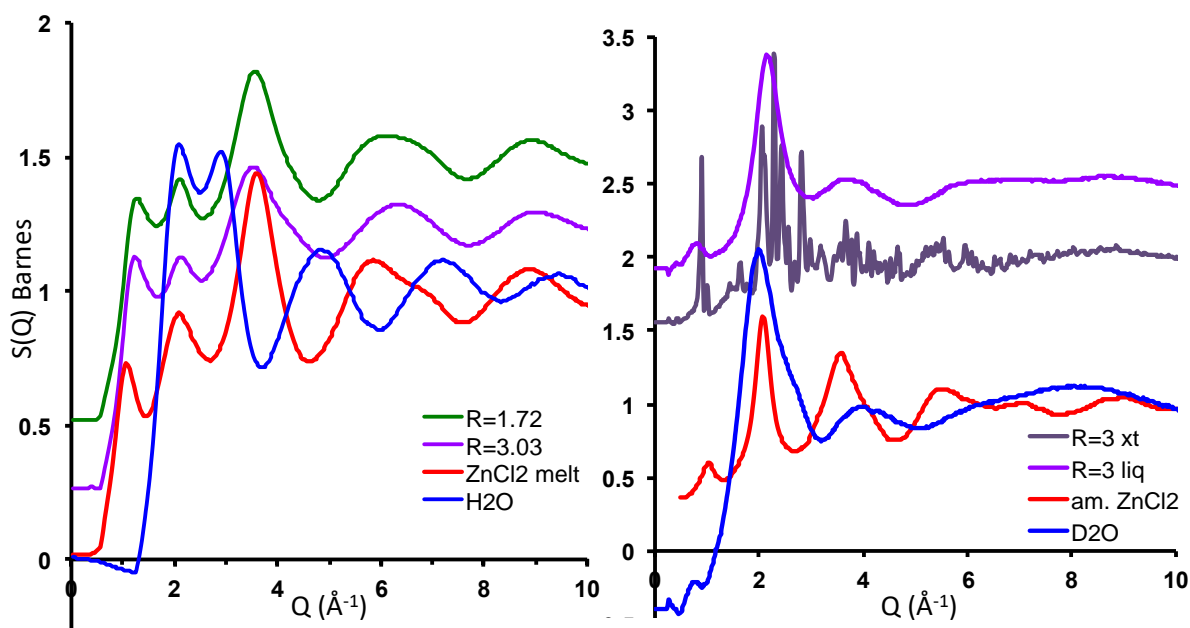


Figure 2.5 Structure factor plots of (a) the X-ray scattering of the room temperature molten hydrates $R = 3$ (purple), $R = 1.7$ (green), water (blue), and molten ZnCl_2 at $320 \text{ }^\circ\text{C}$ (red), X-ray synchrotron; and (b) the neutron scattering of the room temperature $R = 3$ molten hydrate (purple), 233 $R = 3$ crystalline (dark purple), D_2O (blue), and amorphous ZnCl_2 (red), neutron.

To verify that there are no intermediate phases between **I** and the melt, variable temperature neutron diffraction data were obtained in 1 K intervals between 255 and 280 K. As

visible in Figure 2.6, melting is complete over a 1-2 K interval, with no evidence of any intermediate phases. This supports the DSC data in the phase diagram in Figure 2.1 that implied the $R = 3$ material is congruently melting.

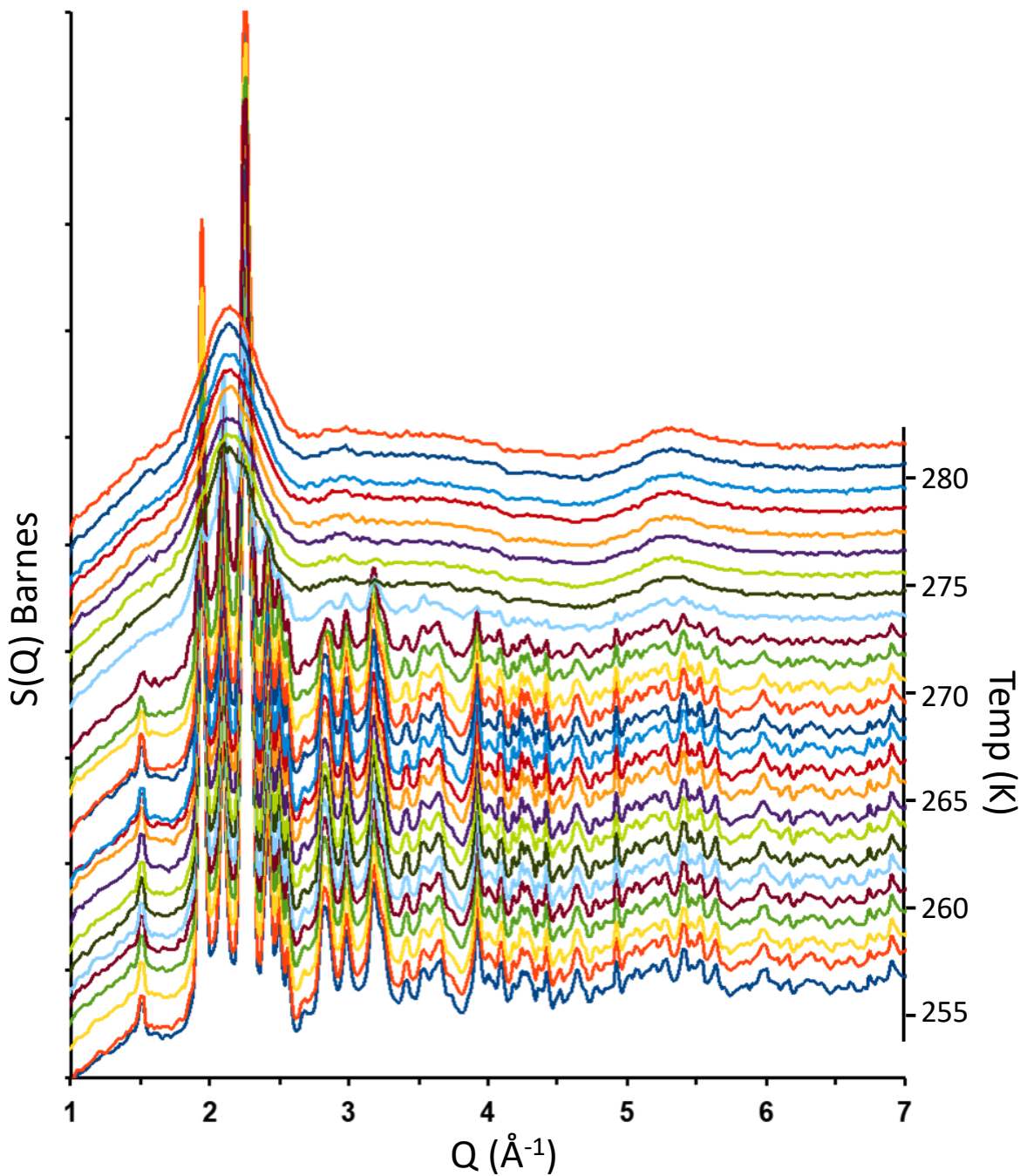


Figure 2.6 Structure factor plot of the variable temperature (255 to 280 K) diffraction of the $R = 3$ zinc chloride hydrate.

2.3.4 Raman spectroscopy of the molten salt hydrate

The Raman spectra of zinc chloride hydrates have been extensively studied.²⁴⁻²⁷ As described in previous work, we find the $R = 3$ hydrate spectrum is dominated by strong absorption at 286 cm^{-1} assigned to the symmetric stretch of the tetrahedral ZnCl_4^{2-} anion, Figure 2.7. The much weaker absorption at 390 cm^{-1} is consistent with the symmetric stretch of the octahedral $\text{Zn}(\text{OH}_2)_6^{2+}$ cation. Though not discussed in previous studies, and presumably being treated as background, we observe that these peaks are superimposed on a strong luminescence. This luminescence dramatically increases for systems more concentrated than the eutectic composition at $R \sim 2.4$, and decreases to negligible as R increases beyond 3, as will be reported in greater detail in a subsequent manuscript describing the full phase diagram.

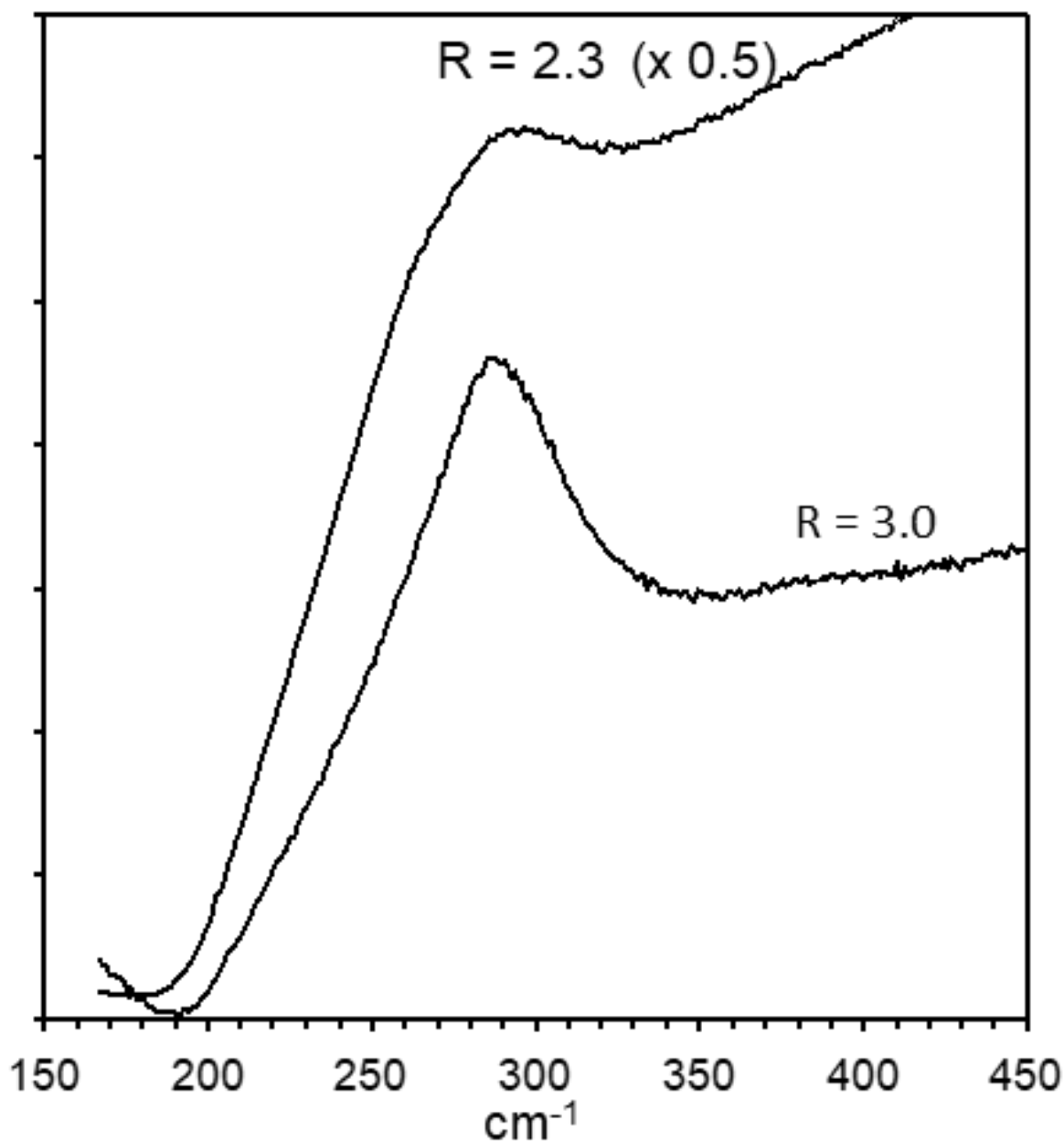


Figure 2.7 Raman spectra of the $R = 3$ and $R = 2.3$ zinc chloride hydrates. Because of the strong luminescence of the lower hydrates, the $R = 2.3$ spectrum is plotted at 50% the scale as the $R = 3$ spectrum.

2.3.5 ATR-IR spectroscopy of the water of hydration

The infrared spectrum of $18\text{ M}\Omega\text{ H}_2\text{O}$, as well as that of the $R = 3$ and $R = 2$ molten hydrates is given in Figure 2.8. In the molten hydrates, the ν_{HOH} bend sharpens, increases in

intensity and red shifts from 1638 cm^{-1} in bulk H_2O to 1617 cm^{-1} and 1614 cm^{-1} for the $R = 3$ and $R = 2$ solutions, respectively. These spectra are not normalized with respect to the mole fraction of water. The maximum of the ν_{OH} stretching blue shifts from 3362 cm^{-1} in bulk H_2O to 3414 cm^{-1} and 3410 cm^{-1} in the $R = 3$ and $R = 2$ solutions, respectively. The shoulder to the low energy side of this peak (identified by the minimum in the first derivative of the spectrum), assigned as an overtone of the bending vibration and a result of network hydrogen bonding,⁵⁹ is significantly reduced in intensity and red shifted from 3285 cm^{-1} in bulk H_2O to 3230 cm^{-1} and 3225 cm^{-1} for the $R = 3$ and $R = 2$ solutions, respectively. The much weaker broad peak at $\sim 2120\text{ cm}^{-1}$ in bulk H_2O , a combination of liberation, $\nu_{\text{lib}} (<650\text{ cm}^{-1})$, and the ν_{HOH} bending modes, a consequence of a collective of many water molecules, is split into two broad peaks at 2290 cm^{-1} and 2000 cm^{-1} for $R = 3$ and 2280 cm^{-1} and 1990 cm^{-1} for $R = 2$ solutions. A dilution series finds that the 2120 cm^{-1} peak of bulk water is red shifted while the higher energy peak grows in with increasing zinc chloride concentration. This higher energy peak begins as a shoulder to the main peak at high dilution, achieving approximate parity in the $R = 3$ composition, and becoming the more intense of the two in the $R = 2$ spectrum.

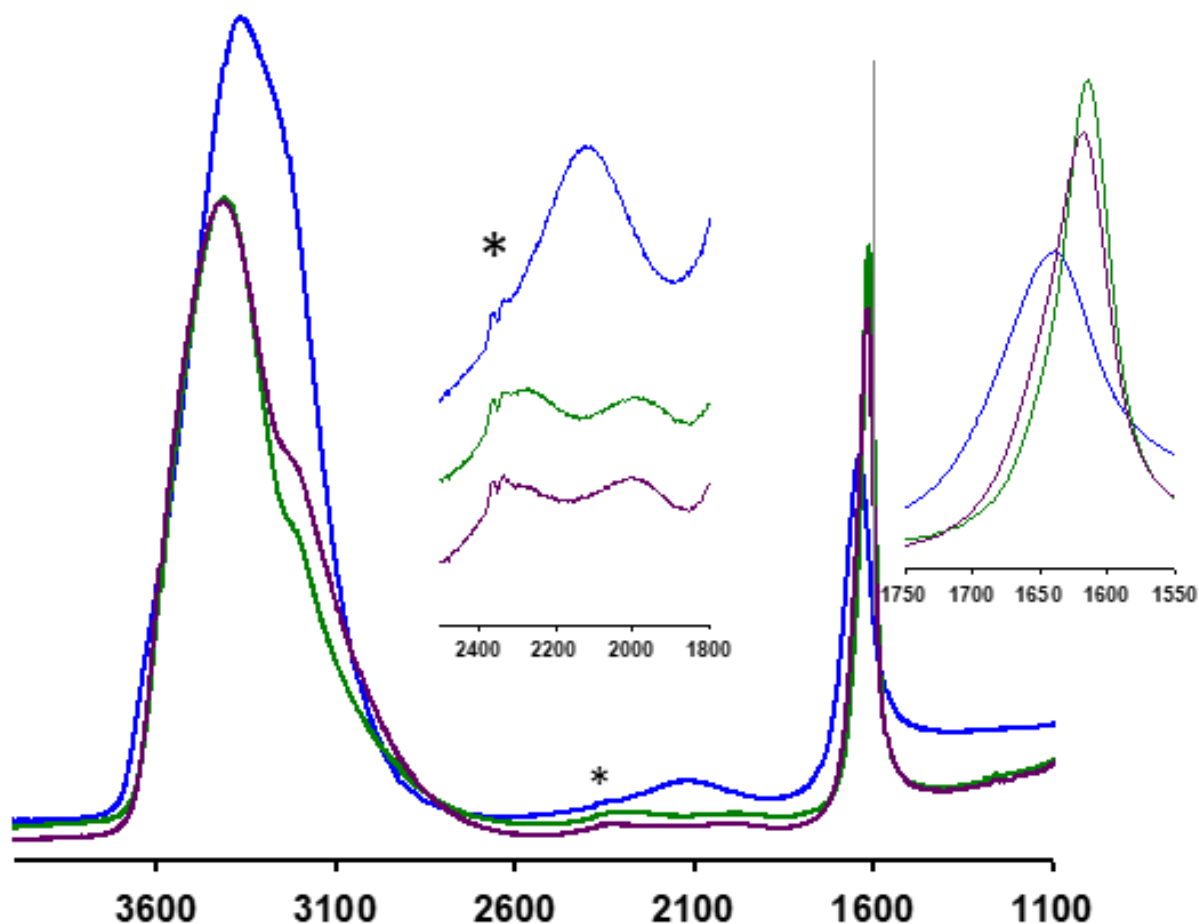


Figure 2.8 ATR-IR spectra of the R = 3 (purple) and R = 2 zinc chloride hydrates (green), compared with that of 18 MΩ H₂O (blue). Insets emphasize the splitting of the band at ~ 2100 cm⁻¹ band, and the shift of the H-O-H bend, respectively. * indicates a trace of CO₂ in the spectrometer's beam path.

2.4 Discussion

2.4.1 Crystalline structure of *I*

One of the most significant features of the crystalline structure of **I** is the ligand partitioning such that there are two distinct zinc coordination environments; one coordinated exclusively by water and the other exclusively by chloride. That such ligand sphere differentiation is observed might have been predicted based on the crystalline structure of the R = 1.33 hydrate in which the waters of hydration are restricted to only one third of the zinc cations; the remaining two thirds of the zinc atoms being coordinated exclusively to chloride

forming $[\text{Zn}_2\text{Cl}_6]^{2-}$ polymeric chains.⁴⁰ In fact we are finding that even under dilute conditions, in the presence of chloride there is a strong preference for aqueous Zn^{2+} to form the ZnCl_4^{2-} anion. The strong chlorophilicity of zinc must be a result of relatively strong covalency of the Zn-Cl bonding, which can be anticipated given that Si^{4+} and Zn^{2+} exhibit similar electronegativities; i.e. ZnCl_4^{2-} is an analog of SiCl_4 . Further evidence of this is seen in the structure of $[\text{Mg}(\text{OH}_2)_6][\text{ZnCl}_4]$ in which the water is exclusively coordinated to the more oxophilic magnesium.⁵⁷

As described in the results section (Table 2.3), the relatively long inter molecular ion O--O and O--Cl distances indicate that only weak hydrogen bonding exists within the crystalline network. This contrasts with the strong hydrogen bonding observed in bulk water. Interestingly, while stronger O--D bonding in D_2O compared to the O--H hydrogen bonding in H_2O results in its melting point being 3.8 ° higher, **I_D** exhibits a 7 ° lower melting point than **I_H**. Together, the intermolecular ion distances and the inverse isotope effect observed for the melting point demonstrate that hydrogen bonding does not provide the major organizing influence on the structure of **I**.

Instead, multiple levels of crystal packing principles are required to understand the structural organization of the respective molecular ions in **I**. It is observed that the $[\text{Zn}(\text{OH}_2)_6]^{2+}$ cations and $[\text{ZnCl}_4]^{2-}$ anions are of similar size with respect to a spherical approximation of ionic radii ($r \sim 3.5\text{-}3.8 \text{ \AA}$ and $4.0\text{-}4.2 \text{ \AA}$, respectively). The resulting radius ratio, from a simple perspective of packing of ionic spheres is consistent with the observed CsCl-type packing of the molecular ions. The triclinic cell of crystalline **I** is essentially a stacked set of two CsCl-type cubes, stretched along **c** due to the shape and orientation of the $[\text{ZnCl}_4]^{2-}$ anions (Figure 2.4). At

a finer level of structural analysis it is observed that the chlorides of the $[\text{ZnCl}_4]^{2-}$ are oriented such that they adopt an approximately cubic close packed positions, Figure 2.9.

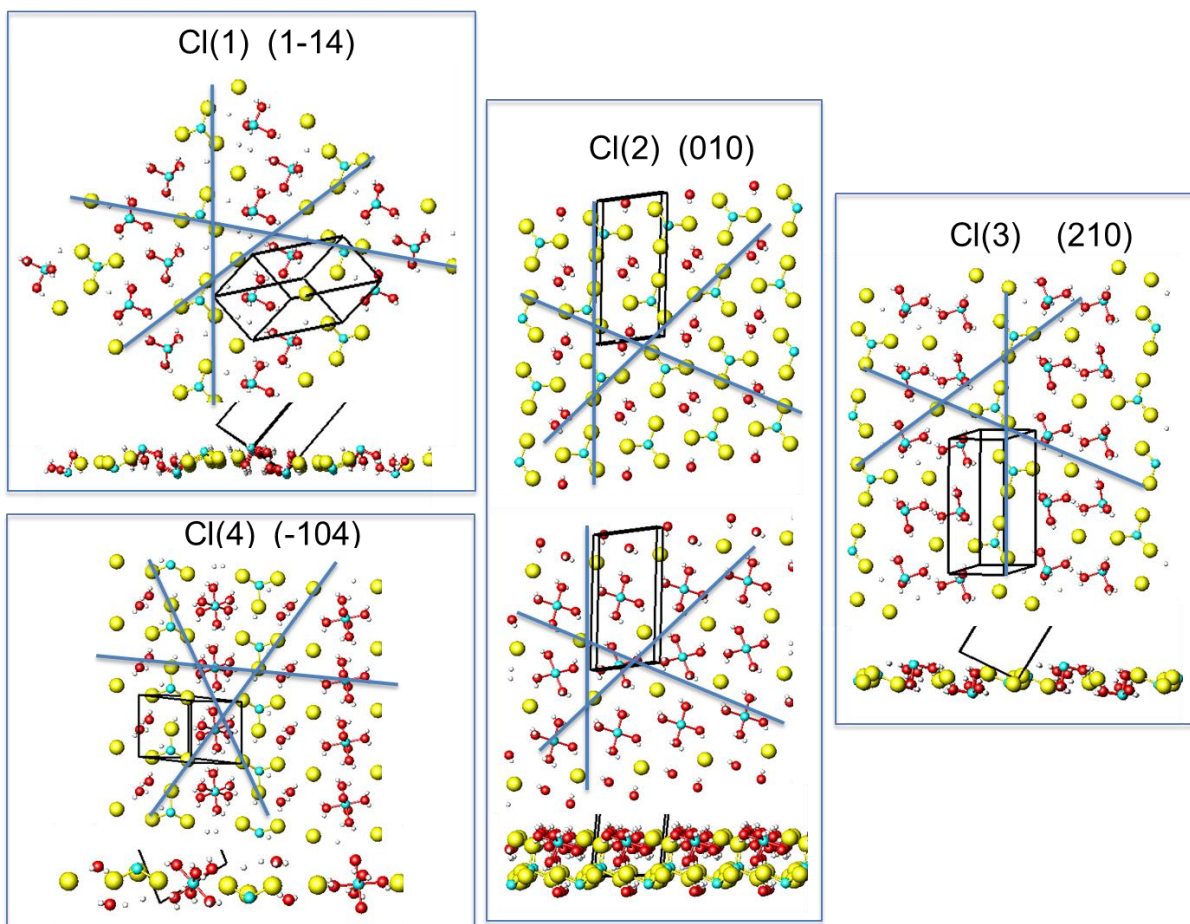


Figure 2.9 Slices of the four pseudo-close packed ligand planes, viewed parallel and perpendicular to each of the four Zn-Cl bond vectors. Light blue lines provide visual guides to the ligand close packing.

The water ligands are too small, and the $[\text{Zn}(\text{OH}_2)_6]^{2+}$ cations are too large to perfectly fill the holes the pseudo-*ccp* layers. As a result some combination of single water ligands, pairs of water ligands, or the entire $[\text{Zn}(\text{OH}_2)_6]^{2+}$ ions fill close-packed positions. It is also observed that the octahedral $[\text{Zn}(\text{OH}_2)_6]^{2+}$ cations are oriented such that if pairs of inter-molecular water-water contacts are treated as a single bridging unit, then this material adopts ABX_3 -type network

in which the $[\text{ZnCl}_4]^{2-}$ fill the A-type void in the center of a $[\text{Zn}\{(\text{OH}_2)\}_{6/2}]^{2+}$ BX_3 -type network, resulting in an anti-perovskite structure type.

Notably, the adopted crystalline structure is intermediate between the ideal model limits of these more isotropic CsCl-type and ligand-close packed-type structures. Shifting the observed triclinic lattice constants of $\mathbf{a} = 6.44 \text{ \AA}$, $\mathbf{b} = 6.50 \text{ \AA}$, $\mathbf{c} = 14.28 \text{ \AA}$, $\alpha = 91^\circ$, $\beta = 99^\circ$ and $\gamma = 96^\circ$ to lattice constants with $\mathbf{a} = \mathbf{b} = 0.5 \mathbf{c}$ and $\alpha = \beta = \gamma = 90^\circ$ affords the ideal CsCl-type organization. By contrast, shifting the lattice constants to $\mathbf{a} = \mathbf{b}$ and $\mathbf{c} = 4\mathbf{a} \sin(70.53^\circ/2)$, $\alpha = \beta = 90^\circ$ and $\gamma = 109.47^\circ$ creates the ideal lattice for ligand cubic-close packing (LCCP), which also affords the anti-perovskite-type lattice. This LCCP lattice also corresponds to a cube with $\mathbf{a}' = 2\mathbf{a} \sin(109.47^\circ/2)$, although the arrangement of the molecular ions in this cell do not exhibit cubic symmetry.

2.4.2 Structure of the molten salt hydrate

As reviewed in the Introduction, the structure of molten zinc chloride hydrates has been a matter of significant interest for applied and fundamental scientific reasons.^{24-29, 33-36} Many previous reports suggest the prevalence of hexaquo zinc and/or tetrachlorozincate species in molten hydrates. But to our knowledge, no reports have addressed exactly how these two molecular ions coexist in the liquids. Furthermore, a majority of analysis techniques provide only a picture of the averaged structure and thus apparent evidence of zinc coordination to both chloride and water. This resulted in the presumed existence and search for a variety of zinc chloride hydrate species, $[\text{ZnCl}_n(\text{OH}_2)_{4-n}]^{2-n}$ ($n = 1-4$) and/or $[\text{ZnCl}_n(\text{OH}_2)_{6-n}]^{2-n}$ ($n = 0-4$). When considered from a condensed phase perspective, stoichiometry limits structural possibilities such that models with bridging chlorides to form oligomers have been proposed for concentrated zinc chloride hydrate solutions ($R < 4$).^{24, 26, 33} The structural paradoxes of molten zinc chloride

hydrates begin to be resolved with structural information from the crystal structure **I** for which it is demonstrated that (a) two non-equivalent zinc coordination environments can co-exist, (b) $[\text{Zn}(\text{OH}_2)_6]^{2+}$ cations and $[\text{ZnCl}_4]^{2-}$ anions are the only species present, (c) zinc is coordinated to both chloride and water, just not in the same molecular-ion species, and (d) the low-water content condensed phase is realized with a salt-like packing of distinct molecular ions rather than forming oligomeric zinc-chloride bridged species; albeit oligomers are observed for the $R = 1.33$ structure.⁴⁰ It is important, then, to consider the extent to which the structure observed in the crystalline state is preserved into the liquid state.

The Raman spectrum of the $R = 3$ melt (Figure 2.7), like that reported in the literature,²⁴⁻²⁷ implies that in the room temperature melt, both $[\text{Zn}(\text{OH}_2)_6]^{2+}$ and $[\text{ZnCl}_4]^{2-}$ are present. Stoichiometry requires that the existence of any additional “water of solution” would also require additional zinc chloride species. But the exclusive co-existence of $[\text{Zn}(\text{OH}_2)_6]^{2+}$ and $[\text{ZnCl}_4]^{2-}$ in the $R = 3$ hydrate melt requires a salt-type packing of the ions.

PDF analysis of the synchrotron X-ray and neutron diffraction of this molten salt hydrate along with comparison to the PDFs of crystalline **I**, bulk water and amorphous anhydrous ZnCl_2 , shown in Figure 2.10, provide additional insight into the liquid structure.

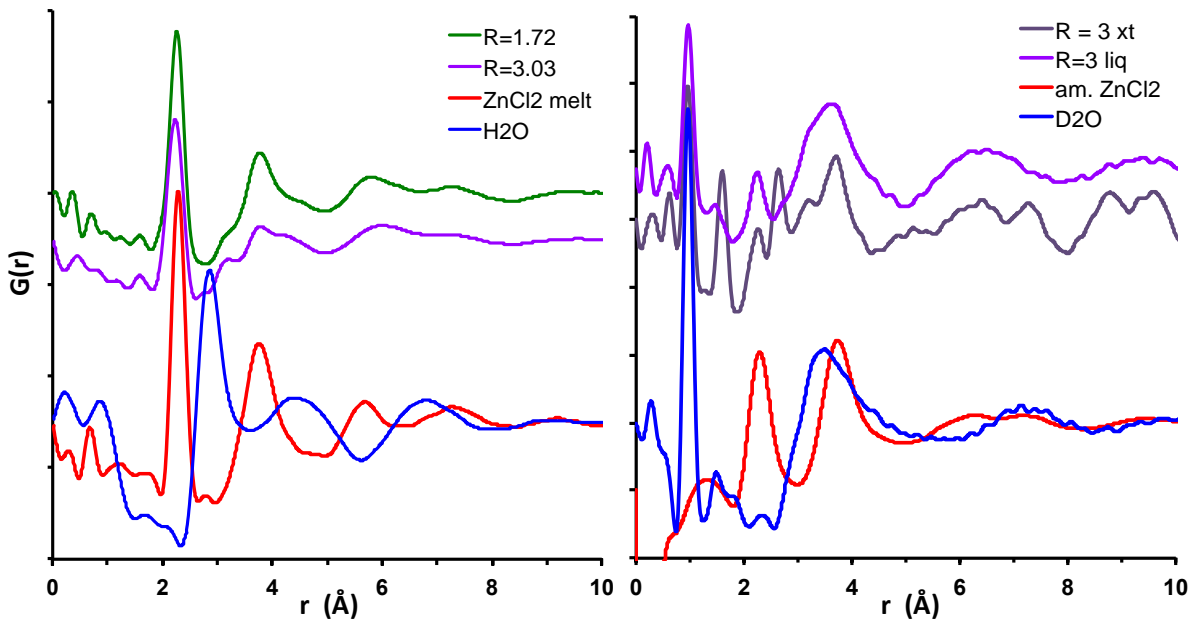


Figure 2.10 Pair distribution function plots of (a) the X-ray scattering of the room temperature molten hydrates $R = 3.03$ (purple), $R = 1.72$ (green), $18 \text{ M}\Omega \text{ H}_2\text{O}$ (blue), and molten anhydrous ZnCl_2 at $320 \text{ }^\circ\text{C}$ (red); and (b) the neutron scattering of the room temperature $R = 3$ molten hydrate (purple), $233 R = 3$ crystals (dark purple), D_2O (blue), and amorphous ZnCl_2 (red). Yellow arrows denote pair correlations previously assigned to zinc chloride oligomers, but are instead include O-O pair correlations.

Historically the PDF data has been interpreted as providing evidence of both water and chloride coordination to zinc,^{26, 33-36} thus contradicting the interpretations of the Raman spectra because of the presumption of only a single coordination environment for zinc. But with the crystalline structure of **I**, explicit definition of individual pair correlations is possible, which can further be compared with the PDFs of the liquid. The partial PDFs calculated from the crystalline structure are given in Figure 2.11.

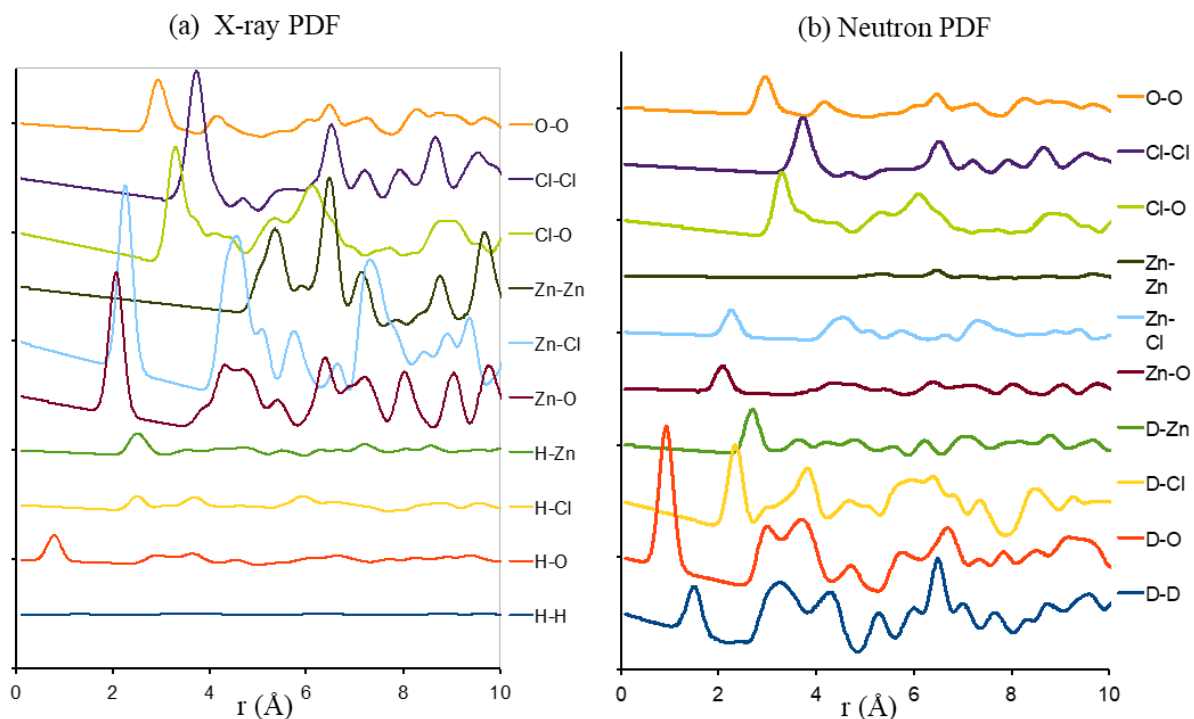


Figure 2.11 Calculated partial pair correlations from the crystal structure of **I** for (a) X-ray and (b) neutron scattering.

The smallest r peaks in the neutron PDF are the O-D and D-D pair correlations of the water molecules, which are not seen in the X-ray PDF. Notably, the feature at 1.8 Å in the neutron D₂O PDF, characteristic of the intermolecular hydrogen bond distance of bulk water, is not observed in the $R = 3$ X-ray PDF. The smallest r peak that is common to both X-ray and neutron PDFs is at 2.24 Å, which is a combination of the shorter Zn-OH₂ and slightly longer Zn-Cl pair correlations, resulting in a distance slightly shorter than that observed for molten or glassy anhydrous ZnCl₂. It is important to recognize that the PDF analysis does not discriminate between a case in which water and chloride are coordinated to the same zinc, from one in which half the zincs are coordinated to water and the other half to chloride, and thus a weighted average distance is observed.

In both X-ray and neutron PDFs, there is a decrease in the number of pair correlations at 3.8 Å, assigned to Cl-Cl and Zn-Zn, with increasing amounts of hydration, i.e. $ZnCl_2 > (R = 1.72) > (R = 3)$. The peaks at 3.2 and 4.3 Å in the X-ray PDF, which emerge in the molten hydrate, have historically been proposed as evidence of zinc chloride oligomers.²⁶ However, in light of pair correlations calculated from the single crystal structure of **I**, we suggest these are more likely intra- and inter-molecular-ion O-O, Cl-O, Zn-Cl and Zn-O contacts. These peaks are somewhat masked in the neutron PDF by overlapping D-Cl, D-O, D-D and D-Zn correlations. The two broad peaks in the X-ray PDF between 5 and 8 Å, which are further broadened by the D-X pair correlations in the neutron PDF, are consistent with the pseudo body-centered molecular cation-anion interactions, and the pseudo cubic molecular cation-cation and anion-anion correlations.

The Raman and PDF analysis, which emphasize local structure, give strong confirmation that the $[Zn(OH_2)_6]^{2+}$ and $[ZnCl_4]^{2-}$ ions persist into the liquid state. And while the PDFs give indication of inter-molecular ion interactions, it is also important to consider the reciprocal space structure factor for evidence of any longer range ordering of these ions. In 1935 Prins, studying solutions of thorium and uranium nitrates by X-ray diffraction, described the regular arrangement of ions in the liquid as giving rise to scattering consistent with a “superarrangement” analogous to a superlattice observed for some alloys.⁶⁰ Others too have observed that the low angle diffraction peak(s) in the X-ray and neutron scattering of solutions is indicative of a “quasi-close packing of solute ions”.^{29, 61-62} Examination of the neutron structure factor plots for the crystalline and liquid samples of **Ib**, in Figure 2.5b, demonstrates a high correlation between them, albeit with an expected lattice expansion, consistent with a lowering

of the density from 2.13 g/cm³ for crystalline **I_H** and 2.20 g/cm³ for crystalline **I_D** to 1.93 g/cm³ and 1.98 g/cm³, respectively, for their room temperature liquids; an 11% volume expansion.

Of particular note are the low-Q diffraction peak(s), whose origin has been the subject of considerable investigation, albeit with no clear interpretation, in anhydrous ZnCl₂ as well as other materials.⁶³ Unlike anhydrous ZnCl₂ where this low-Q peak is equivalent in both the neutron and X-ray scattering, the R = 3 hydrate exhibits two distinct low-Q peaks at 0.81 Å⁻¹ and 1.23 Å⁻¹ for the neutron and X-ray scattering, respectively. Similarly distinct diffraction patterns are observed for neutron and X-ray patterns calculated for the crystalline **I_D** and **I_H**.

Shown in Figure 2.12 are the calculated crystalline neutron and X-ray patterns for the hypothetical structure of **I**, expanded such that the density matches the experimental liquid density, and idealized to both the CsCl- (**a** = 6.89 Å) and LCCP-type (**a** = 6.71 Å and **c** = 15.49 Å, or **a'** = 10.89 Å) lattices. These idealized and more isotropic structures simplify the diffraction patterns from that of the lower symmetry triclinic crystal, and likely provide a better model of the liquid. Notably in both cases, the low-Q features of the neutron patterns are the peaks corresponding to the edges of the pseudo cubic CsCl-type box, (001) and (002); spacing between respective cation and anion planes. By contrast the low-Q X-ray scattering emphasizes the peaks corresponding to the face centered layers, (101), (110) and (012), which each contain a mixture of anions and cations. The planes corresponding to ligand-ligand interactions, i.e. the height of the tetrahedron or octahedron, result in the diffraction peaks with scattering around 2 ± 0.5 Å⁻¹.

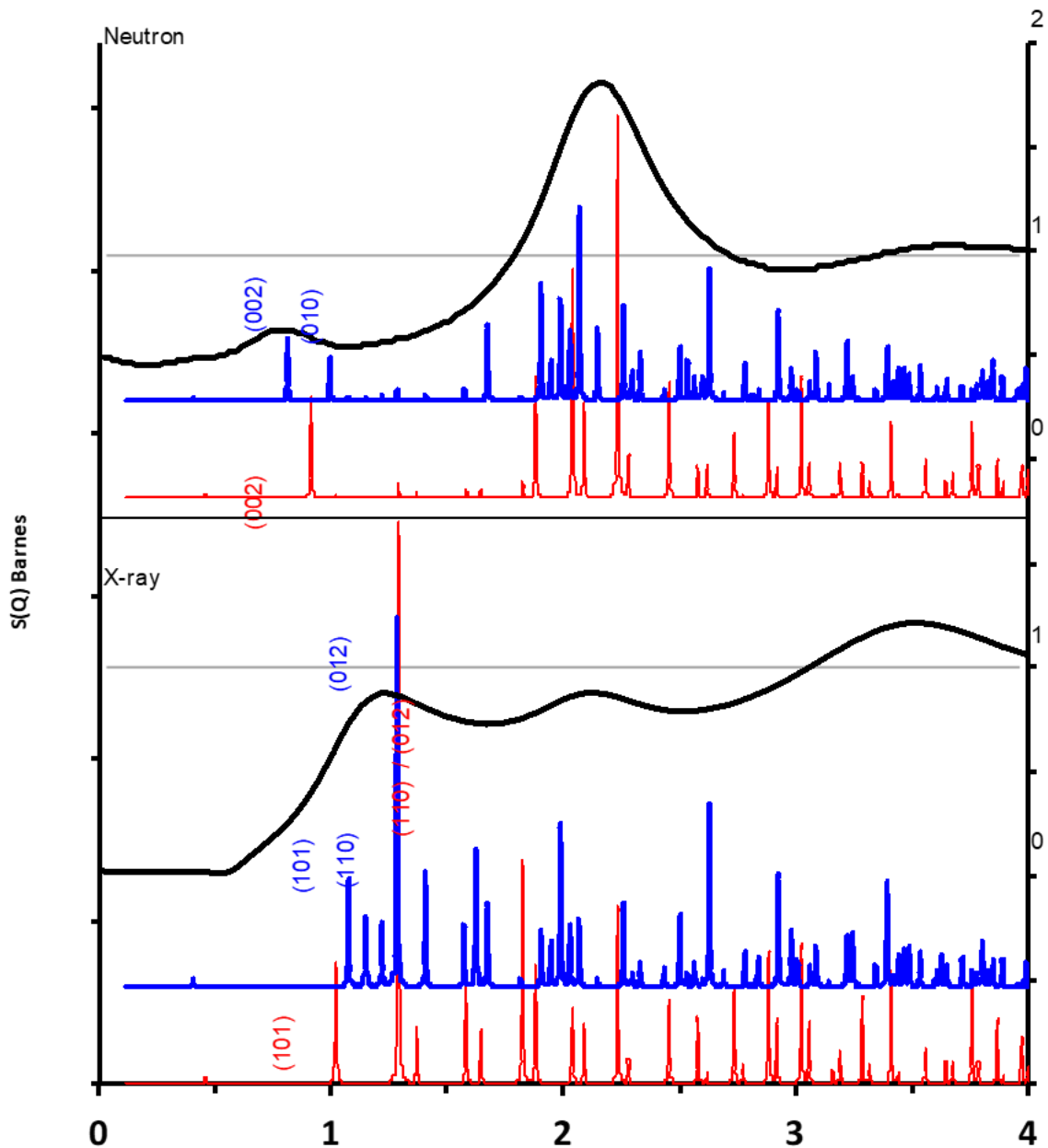


Figure 2.12 Low Q portion of the experimental neutron and X-ray structure factor plots for the $R = 3$ room temperature liquid (black) compared with the respective calculated crystalline powder patterns for I_D neutron and I_H X-ray scattering for the CsCl-type (red) and LCCP-type (blue) lattices expanded to match the experimental liquid density.

The difference between the X-ray and neutron patterns is a result of the scattering power of the respective elements under the different types of radiation. In X-ray scattering, the scattering power scales with the number of electrons, thus ZnO_6H_{12} exhibits 92% the scattering

of ZnCl_4 . By contrast, the neutron scattering length cross sections ($\text{D} = 6.7 \text{ fm}$, $\text{O} = 5.8 \text{ fm}$, $\text{Cl} = 9.6 \text{ fm}$ and $\text{Zn} = 5.6 \text{ fm}$) result in $\text{ZnO}_6\text{D}_{12}$ exhibiting 275% the scattering of ZnCl_4 . As a result, cation/cation planes and any planes with water-water interactions, will dominate neutron scattering, whereas X-ray scattering gives stronger weight to planes with anion/cation or Cl-Cl interactions.

Specifically evaluation of the low-Q peaks from the calculated crystal structures allows evaluation of the CsCl- vs. LCCP-type structures as models of the liquid structure. While the observed neutron low-Q peak of the $R = 3$ hydrate occurs at 0.81 \AA^{-1} the lowest peak with significant intensity in the CsCl-type structure occurs at 0.91 \AA^{-1} . By contrast the LCCP model indicates two peaks at 0.81 and 0.99 \AA^{-1} , with the former being the most intense. The low-Q peak of the liquid X-ray pattern, at 1.23 \AA^{-1} , is likely related to the dominant (012) peak at 1.28 \AA^{-1} for both structure types. But its broadening to low Q with the {110} peaks in the LCCP model suggest this model is more consistent with the observed liquid scattering than is the CsCl model in which the {110} and {012} peaks are equivalent. Based on the above, we propose that the distinct behavior of the low-Q liquid diffraction peaks with respect to neutron and X-ray scattering originate from lattice-type diffraction and systematic extinction conditions. And as such, the liquid most likely exhibits a disordered version of the LCCP structure that is dominated by ligand packing.

2.4.3 Reverse Monte Carlo modeling (RMC)

To gain further insight into this proposed ionic liquid structural model of the $R = 3$ hydrate, we performed a set of RMC calculations to fit the neutron scattering data. Structure factor, $S(Q)$, and PDF, $G(r)$, plots of these calculations are given in Figure 2.13. A simulation box was constructed by taking the pseudo cubic set of four \mathbf{I}_D unit cells ($2\mathbf{a} \times 2\mathbf{b} \times \mathbf{c}$) and

expanding them isotropically so as to match the experimental density. A molecular dynamics (MD) simulation was run on this expanded triclinic box to reassemble the molecular ions to reasonable metric parameters, and to introduce disorder into the system. To also consider the CsCl- and LCCP-type structures, this MD box was idealized into a cubic modeling box ($a = 13.8$ Å) and a monoclinic box ($a = b = 6.71$ Å, $c = 15.49$ Å, $\gamma = 109.47^\circ$), respectively. Reverse Monte Carlo modeling of $3 \times 3 \times 3$ supercells of these boxes (equivalent to 108 \mathbf{Ib} unit cells), was performed with intra-molecular ion bond distances constrained to those of the above characterized $[\text{Zn}(\text{OD}_2)_6]^{2+}$ and $[\text{ZnCl}_4]^{2-}$ ions.

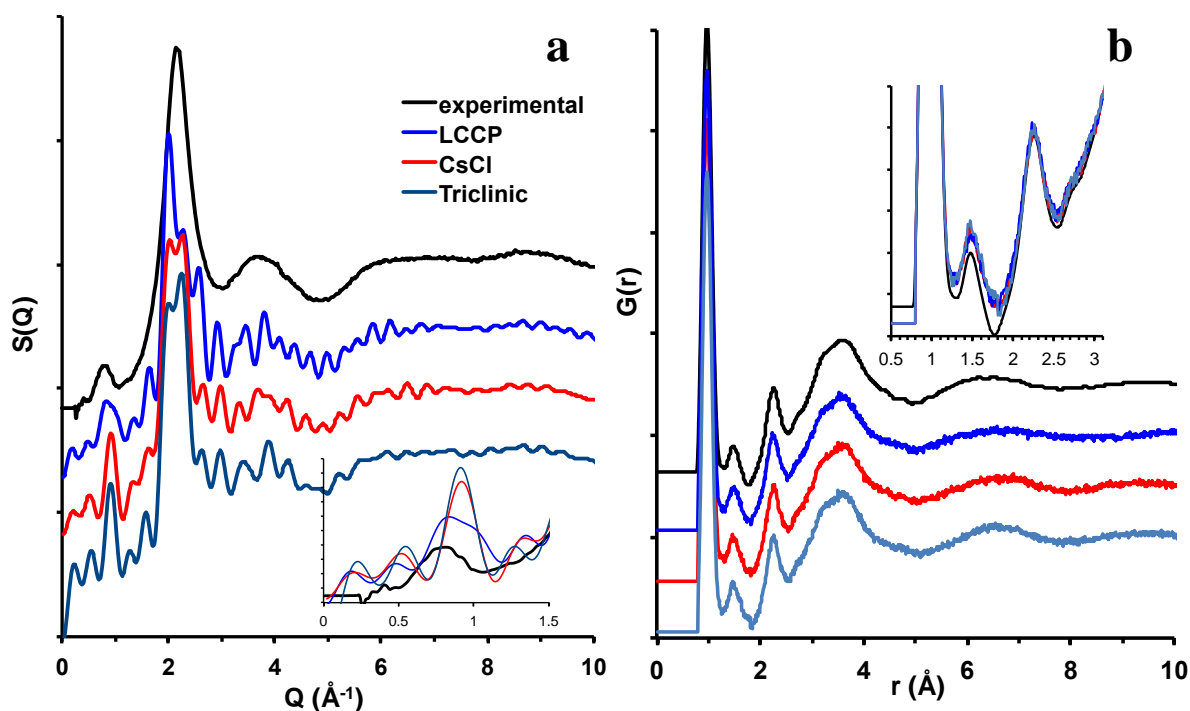


Figure 2.13 (a) Structure factor and (b) PDF plots comparing the experimental neutron scattering data for the $R = 3$ hydrate (black) with the RMC modeling of 5184-atom boxes based on the expanded triclinic (aqua), CsCl (red) and ligand cubic close packed (LCCP) model structures. Inset in (a) is an expanded view of the low- Q peak. Inset in (b) is a $2 \times$ expanded view of the low r PDF.

The PDF of each of these simulations provides a remarkably good fit to the experimental PDF, with the only substantive difference between the calculated and experimental PDFs being

observed for the intra-water D-D pair correlation at 1.47 Å, as seen in the inset of Figure 2.13. The MD and the RMC components of the simulation both introduce disorder into the system, but the overall crystal-type packing is clearly apparent as observed in the LCCP simulation shown in Figure 2.14. While these simulated PDFs effectively replicate the local structure of the liquid, they do not provide sufficient detail to distinguish between the three simulation models.

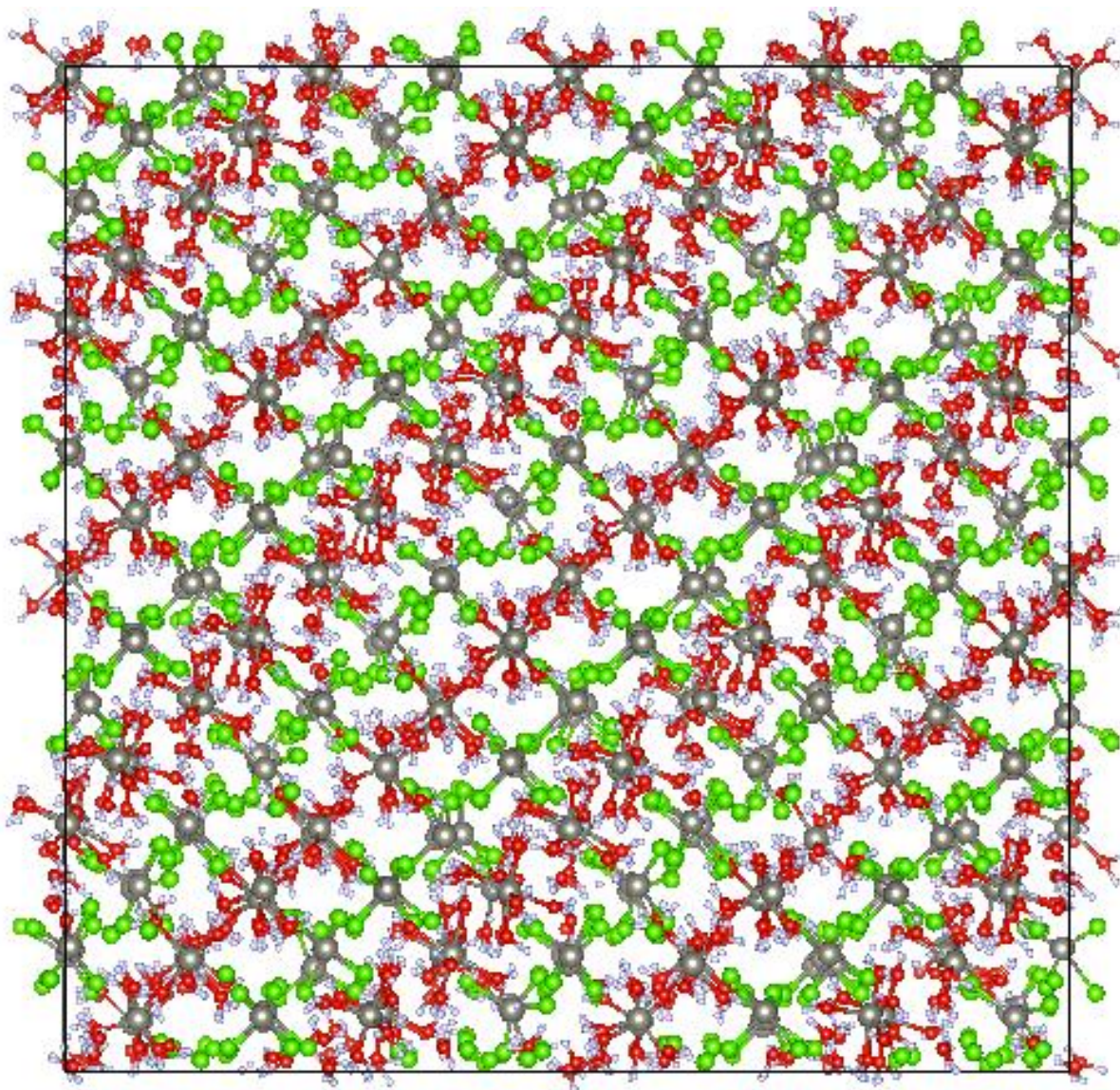


Figure 2.14 Ball and stick drawing of the RMC simulation box resultant from the LCCP model.

Somewhat greater structural insight is gained from the structure factor plots, Figure 2.13a. The structure factor plots from each of the models, demonstrate that the diffraction patterns, while significantly broadened from those of the crystalline models, exhibit much more long range order than is observed in the liquid. Nevertheless, the overall form of the simulation $S(Q)$ functions is consistent with the observed liquid scattering. Most significantly, however, the calculated position of the low Q peak, see inset of Figure 2.13a, is 0.91 \AA^{-1} for the triclinic simulation, 0.92 \AA^{-1} for the CsCl simulation and 0.83 \AA^{-1} for the LCCP simulation. The LCCP model also exhibits a broadened and less intense peak than was observed for either the triclinic or CsCl models. This peak, along with the peak at 2 \AA^{-1} , is extremely sensitive to the position of the water ligands, and also the position of the D atoms relative to the Zn-O. Thus we propose that a more extensive disordering of the orientation of the water ligands of the $[\text{Zn}(\text{OD}_2)_6]^{2+}$ is key to achieving a better model of the liquid structure. We suspect that the disordering of the water orientations is not completely random. Rather, as we demonstrated for the plastic crystalline CBr_4 ,⁶⁴ which like **I** must orient tetrahedra into an average cubic structure, there are likely a restricted set of possible orientations for the water ligands, defined by the overall LCCP-type packing.

2.4.4 Understanding the water of hydration

Examination of the infrared spectrum (Figure 2.8) of the water of hydration provides important insight into physical characteristics of this liquid that can be exploited for unique solvating properties. Unlike bulk water, the $R = 3$ hydrate exhibits only weak water-water and water-Cl hydrogen bonding. However, whereas strong hydrogen bonding in bulk water causes the ν_{OH} stretches (3363 cm^{-1}) to be significantly red shifted from the resolved molecular symmetric and asymmetric stretches in the gas phase (3756 cm^{-1} and 3652 cm^{-1}), the $R = 3$

hydrate still exhibits a major red-shift in the ν_{OH} to 3414 cm^{-1} ; approximately 85% of the O-H bond weakening observed for the difference between gas phase and bulk liquid water at room temperature. This is comparable (within 5%) to the OH stretch of bulk water at $91.1 \text{ }^\circ\text{C}$.⁶⁵ However, in the $R = 3$ hydrate, the weakening of the O-H interactions is a result of O-H bond activation by coordination to the Lewis acidic Zn^{2+} . In a complementary fashion, the hydrogen bonded network in bulk water strengthens the ν_{HOH} bend from the gas phase value of 1595 cm^{-1} to 1638 cm^{-1} whereas the more isolated coordinated water in the $R = 3$ hydrate exhibits an intermediate ν_{HOH} of 1617 cm^{-1} ; this amounts to 51% of the difference between molecular bend in the gas phase and the network-restricted bend in the room temperature bulk liquid. In addition, this red shifted $R = 3$ ν_{HOH} peak is significantly sharpened while its corresponding overtone observed at 3230 cm^{-1} is both red shifted and diminished in intensity compared to that of bulk water, consistent with the oscillator becoming less strongly anharmonic as intermolecular hydrogen bonding is diminished. This contrasts to the behavior of the ν_{HOH} and its overtone in bulk water at $91 \text{ }^\circ\text{C}$ for which there is very little change to either.⁶⁵ The region assigned as the intramolecular bend overtone has also recently been suggested to be a result of intermolecular coupling.⁵⁹ Any intermolecular coupling in the liquid network would also be expected to diminish for the more isolated water molecules of the concentrated hydrate melt.

The much broader and weaker liberation + bend combination band, $\nu_{\text{lib+HOH}}$, exhibits a more dramatic change from that of bulk water (see inset of Figure 2.8). This band is not observed in the gas phase spectrum as it results from intermolecular bulk interactions. Upon dilution, this band at 2120 cm^{-1} in bulk water begins to shift to lower energy becoming the band at 2000 cm^{-1} in the $R = 3$ liquid. The weakened ν_{HOH} cannot independently account for this substantial red shift, suggesting the ν_{lib} is also substantially weakened with the loss of

intermolecular hydrogen bonding. By comparison, heating water from 31.0 to 91.1 °C only red-shifted this peak by 45 cm⁻¹,⁶⁵ indicating the water-water network interaction is much more disrupted in the R = 3 hydrate than in water near its boiling point. Furthermore, a second combination band to higher energy becomes visible with the addition of about 10 mole % ZnCl₂ (R = 9), and is clearly resolved at 2290 cm⁻¹ in the R = 3 liquid. At the R = 3 composition these two bands are approximately equal in intensity, with the new high-energy band surpassing the original lower energy band in the R = 2 hydrate melt. We propose that this higher energy band is a result of the restricted libration of water molecules tightly bound to zinc in the [Zn(OH₂)₆]²⁺ cation in combination with the ν_{HOH} .

Together, these IR data suggest that the water molecules in the R = 3 hydrate are substantially activated, and as such they could be very strong hydrogen bond donors. Such hydrogen bonding is not realized in the neat liquid because the [ZnCl₄]²⁻ anion and the oxygen atoms of the water coordinated to zinc are poor hydrogen bond acceptors. As a result, the untapped hydrogen bond donating capacity can likely be exploited toward hydrogen bond accepting solutes.

2.5 Conclusion

This collection of thermodynamic, diffraction and spectroscopic data clearly demonstrates the existence of the congruently melting zinc chloride trihydrate (R=3) as a line phase. Solution of its single crystal structure demonstrates that [Zn(OH₂)₆][ZnCl₄] is rightly classified as a “zinc zincate” in which the two types of ligands, water and chloride ion, are associated with two different zinc atoms in strict segregation. Comparative analysis of the crystalline and liquid diffraction data, and the vibrational spectra of the liquid, all indicate that the pseudo-ligand cubic close packed structure with a CsCl-type arrangement of the molecular

ions of the $R = 3$ solid persists in its melt. As such this hydrate melt is best described as a room temperature ionic liquid.

Vibrational spectroscopy demonstrates that by sequestering the water molecules on the zinc ions, the O-H bonds are significantly activated such that they should be well suited to be hydrogen bond donors. However, neither the zinc bound oxygen atoms, nor the tetrachlorozincate anion is an effective hydrogen bond acceptor. The absence of significant inter-molecular hydrogen bonding and the low charge density of the respective molecular ions are responsible for the observed low melting temperature of this “salt,” as well as the melting point H/D inverse isotope effect.

Together these features make the $R = 3$ hydrate a unique ionic liquid solvent. Notably neither ion of this molten hydrate exhibits a molecular dipole. As such the packing of molecular ion monopoles in the liquid effectively makes this material a non-polar solvent; albeit one that contains strong hydrogen bond donors. We suggest the historically documented solubility of cellulose in the $R = 3$ zinc chloride hydrate provides an example of the unique solvating characteristics of this novel ionic liquid. The strong hydrogen bond donation apparently disrupts the highly hydrogen-bond cross-linked network, while the non-polar (monopolar) ionic liquid matrix stabilizes the isolated biopolymer molecules. Not only does this newly articulated structural description of the $R = 3$ zinc chloride hydrate ionic liquid provide explanation to its physical properties, the impact of the network deconstruction on the IR spectrum of water provides useful contribution to the ongoing effort to understand the structure of water, and the contrast between the neutron and X-ray scattering provides unprecedented insight into the origin of the low-Q diffraction peaks in liquids.

2.6 References

1. Taylor, T. 1859.
2. Barnes, H.; Rose, A., Origins of hydrothermal ores. *Science* **1998**, 279 (5359), 2064-2065.
3. Crerar, D.; Wood, S.; Brantley, S.; Bocarsly, A., Chemical controls on solubility of ore-forming minerals in hydrothermal solutions. *The Canadian Mineralogist* **1985**, 23 (3), 333-352.
4. Beck, F.; Rüetschi, P., Rechargeable batteries with aqueous electrolytes. *Electrochimica Acta* **2000**, 45 (15), 2467-2482.
5. Nicholson, J.; Parker, L., The chemistry of cements formed between zinc oxide and aqueous zinc chloride. *Journal of materials science* **1998**, 33 (9), 2251-2254.
6. Christianson, D. W., Structural biology of zinc. *Advances in protein chemistry* **1991**, 42, 281-355.
7. Prasad, A. S., Zinc: the biology and therapeutics of an ion. *Annals of internal medicine* **1996**, 125 (2), 142-143.
8. Braunstein, J., Some aspects of solution chemistry in liquid mixtures of inorganic salts with water. *Inorganica Chimica Acta Reviews* **1968**, 2, 19-30.
9. Mylius, F., Uber das Chlorzink. *Zeitschrift fur anorganische und allgemeine Chemie* **1905**, 44 (1), 209-220.
10. Angell, C.; Sare, E., Glass-Forming Composition Regions and Glass Transition Temperatures for Aqueous Electrolyte Solutions. *The Journal of Chemical Physics* **1970**, 52 (3), 1058-1068.
11. Harris, A.; Parton, H., The transport numbers of zinc chloride from emf measurements. *Transactions of the Faraday Society* **1940**, 36, 1139-1141.
12. Foxton, F.; Shutt, W., The activity of zinc chloride in concentrated solution. *Transactions of the Faraday Society* **1927**, 23, 480-488.
13. Robinson, R.; Stokes, R.; Wilson, J. M., A thermodynamic study of bivalent metal halides in aqueous solution. *Transactions of the Faraday Society* **1940**, 36, 733-748.
14. Dunsmore, H. S.; Paterson, R., Re-determination of the standard electrode potential of zinc and mean molal activity coefficients for aqueous zinc chloride at 298.15 K. *Journal of the Chemical Society, Faraday Transactions 1: Physical Chemistry in Condensed Phases* **1976**, 72, 495-503.

15. Goldberg, R. N., Evaluated activity and osmotic coefficients for aqueous solutions: Bi-univalent compounds of zinc, cadmium, and ethylene bis (trimethylammonium) chloride and iodide. *Journal of Physical and Chemical Reference Data* **1981**, 10 (1), 1-56.
16. Hittorf, W., Das Verhalten der Diaphragmen bei der Elektrolyse von Salzlösungen. *Zeitschrift für Physikalische Chemie* **1903**, 43 (1), 239-249.
17. Rabinowitsch, A., Über die anomale Dissoziation in wässrigen Lösungen. *Zeitschrift für Physikalische Chemie* **1921**, 99 (1), 338-360.
18. Mead, D. J.; Fuoss, R. M., Conductance and viscosity of concentrated solutions of calcium and zinc chlorides. *The Journal of Physical Chemistry* **1945**, 49 (5), 480-482.
19. Easteal, A.; Sare, E.; Moynihan, C.; Angell, C., Glass-transition temperature, electrical conductance, viscosity, molar volume, refractive index, and proton magnetic resonance study of chlorozinc complexation in the system $ZnCl_2 + LiCl + H_2O$. *Journal of solution chemistry* **1974**, 3 (11), 807-821.
20. Agnew, A.; Paterson, R., Transport in aqueous solutions of group IIB metal salts at 298.15 K. Part 6.—Irreversible thermodynamic parameters for zinc chloride and verification of Onsager's reciprocal relationships. *Journal of the Chemical Society, Faraday Transactions 1: Physical Chemistry in Condensed Phases* **1978**, 74, 2896-2906.
21. Miller, D. G.; Rard, J. A., Generalized isothermal transport coefficients of $ZnCl_2-H_2O$ at 25° C. *Journal of Molecular Liquids* **1992**, 52, 145-179.
22. Thomas, B.; Fray, D., The conductivity of aqueous zinc chloride solutions. *Journal of Applied Electrochemistry* **1982**, 12 (1), 1-5.
23. Nakamura, Y.; Shimokawa, S.; Futamata, K.; Shimoji, M., NMR relaxation study of water molecules in concentrated zinc chloride solutions. *The Journal of Chemical Physics* **1982**, 77 (6), 3258-3262.
24. Irish, D. E.; McCarroll, B.; Young, T. F., Raman Study of Zinc Chloride Solutions. *The Journal of Chemical Physics* **1963**, 39 (12), 3436-3444.
25. Morris, D. F. C.; Short, E. L.; Waters, D. N., Zinc chloride and zinc bromide complexes—III: Structures of species in solution. *Journal of Inorganic and Nuclear Chemistry* **1963**, 25 (8), 975-983.
26. Yamaguchi, T.; Hayashi, S.; Ohtaki, H., X-ray diffraction and Raman studies of zinc(II) chloride hydrate melts, $ZnCl_2 \cdot rH_2O$ ($r = 1.8, 2.5, 3.0, 4.0, \text{ and } 6.2$). *The Journal of Physical Chemistry* **1989**, 93 (6), 2620-2625.
27. Kanno, H.; Hiraishi, J., Raman spectroscopic study of glassy aqueous zinc halide solutions. *Journal of Raman Spectroscopy* **1980**, 9 (2), 85-89.

28. Mayanovic, R. A.; Anderson, A. J.; Bassett, W. A.; Chou, I., XAFS measurements on zinc chloride aqueous solutions from ambient to supercritical conditions using the diamond anvil cell. *Journal of synchrotron radiation* **1999**, *6* (3), 195-197.
29. Matsubara, E.; Waseda, Y., An anomalous X-ray scattering study of an aqueous solution of ZnCl₂. *Journal of Physics: Condensed Matter* **1989**, *1* (44), 8575.
30. Parchment, O. G.; Vincent, M. A.; Hillier, I. H., Speciation in aqueous zinc chloride. An ab initio hybrid microsolvation/continuum approach. *The Journal of Physical Chemistry* **1996**, *100* (23), 9689-9693.
31. Tossell, J. A., Calculations of the structures, stabilities, and Raman and zinc NMR spectra of zinc aqua chloride ZnCl_n(OH)_{2-n} species in aqueous solution. *The Journal of Physical Chemistry* **1991**, *95* (1), 366-371.
32. Rudolph, W. W.; Pye, C. C., Zinc (II) hydration in aqueous solution. A Raman spectroscopic investigation and an ab-initio molecular orbital study. *Physical Chemistry Chemical Physics* **1999**, *1* (19), 4583-4593.
33. Kruh, R.; Standley, C., An X-ray diffraction study of aqueous zinc chloride solutions. *Inorganic chemistry* **1962**, *1* (4), 941-943.
34. Wertz, D.; Bell, J., Solute species and equilibria in concentrated zinc chloride/hydrochloric acid solutions. *Journal of Inorganic and Nuclear Chemistry* **1973**, *35* (3), 861-868.
35. Paschina, G.; Piccaluga, G.; Pinna, G.; Magini, M., Chloro-complexes formation in a ZnCl₂-CdCl₂ aqueous solution: An x-ray diffraction study. *The Journal of Chemical Physics* **1983**, *78* (9), 5745-5749.
36. Powell, D. H.; Barnes, A. C.; Enderby, J. E.; Neilson, G. W.; Salmon, P. S., The hydration structure around chloride ions in aqueous solution. *Faraday Discussions of the Chemical Society* **1988**, *85* (0), 137-146.
37. Brehler, B.; Jacobi, H., Die Kristallstruktur des Li₂ZnCl₄·2H₂O. *Naturwissenschaften* **1964**, *51* (1), 11-11.
38. Brehler, B.; Süssle, P., Zur Kristallstruktur des KZnCl₃·2H₂O. *Naturwissenschaften* **1963**, *50* (15), 517-517.
39. Liu, X.; Guo, G.-C.; Sun, Y.-Y., Diaquachlorozinc (II)-18-crown-6-water (1/1/1). *Acta Crystallographica Section E: Structure Reports Online* **2007**, *63* (1), m275-m277.
40. Follner, H.; Brehler, B., Die Kristallstruktur des ZnCl₂·4/3H₂O. *Acta Crystallographica Section B* **1970**, *26* (11), 1679-1682.

41. Martin, J. D.; Goettler, S. J.; Fossé, N.; Iton, L., Designing intermediate-range order in amorphous materials. *Nature* **2002**, *419* (6905), 381-384.
42. Martin, J. D.; Keary, C. L.; Thornton, T. A.; Novotnak, M. P.; Knutson, J. W.; Folmer, J. C., Metallotropic liquid crystals formed by surfactant templating of molten metal halides. *Nature materials* **2006**, *5* (4), 271-275.
43. Hammersley, A., FIT2D: an introduction and overview. *European Synchrotron Radiation Facility Internal Report ESRF97HA02T* **1997**.
44. Qiu, X.; Thompson, J. W.; Billinge, S. J. L., PDFgetX2: a GUI-driven program to obtain the pair distribution function from X-ray powder diffraction data. *Journal of Applied Crystallography* **2004**, *37* (4), 678.
45. Neuefeind, J.; Feygenson, M.; Carruth, J.; Hoffmann, R.; Chipley, K. K., The Nanoscale Ordered MAterials Diffractometer NOMAD at the Spallation Neutron Source SNS. *Nuclear Instruments and Methods in Physics Research Section B: Beam Interactions with Materials and Atoms* **2012**, *287*, 68-75.
46. Larsen, A.; Von Dreele, R., GSAS. Report LAUR 86-748. Los Alamos National Laboratory, New Mexico, USA. 2000.
47. Toby, B. H., EXPGUI, a graphical user interface for GSAS. *Journal of applied crystallography* **2001**, *34* (2), 210-213.
48. McGreevy, R.; Pusztai, L., Reverse Monte Carlo simulation: a new technique for the determination of disordered structures. *Molecular Simulation* **1988**, *1* (6), 359-367.
49. Hutter, J.; Alavi, A.; Deutsch, T.; Bernasconi, M.; Goedecker, S.; Marx, D.; Tuckerman, M.; Parrinello, M., CPMD: Car-Parinello Molecular Dynamics, version 3.17. 1.; IBM Corp 1990– 2008 and MPI für Festkörperforschung Stuttgart 1997– 2001.
50. Troullier, N.; Martins, J. L., Efficient pseudopotentials for plane-wave calculations. *Physical review B* **1991**, *43* (3), 1993.
51. Perdew, J. P.; Burke, K.; Ernzerhof, M., Generalized gradient approximation made simple. *Physical review letters* **1996**, *77* (18), 3865.
52. Car, R.; Parrinello, M., Unified approach for molecular dynamics and density-functional theory. *Physical review letters* **1985**, *55* (22), 2471.
53. Nosé, S., A unified formulation of the constant temperature molecular dynamics methods. *The Journal of Chemical Physics* **1984**, *81* (1), 511-519.
54. Hoover, W. G., Canonical dynamics: equilibrium phase-space distributions. *Physical review A* **1985**, *31* (3), 1695.

55. Tucker, M. G.; Keen, D. A.; Dove, M. T.; Goodwin, A. L.; Hui, Q., RMCProfile: reverse Monte Carlo for polycrystalline materials. *Journal of Physics: Condensed Matter* **2007**, *19* (33), 335218.
56. Josey, A. A. The Structure and Mechanism of Melt Crystallization of CZX-1, a Templated ZnCl₂ Network Material. North Carolina State University, Raleigh, 2009.
57. Duhlev, R.; Macicek, J., Structure of magnesium zinc tetrachloride hexahydrate MgZnCl₄·6H₂O. *Acta Crystallographica Section C: Crystal Structure Communications* **1991**, *47* (8), 1573-1575.
58. Soper, A. K., Joint structure refinement of x-ray and neutron diffraction data on disordered materials: application to liquid water. *Journal of Physics: Condensed Matter* **2007**, *19* (33), 335206.
59. Shi, L.; Gruenbaum, S.; Skinner, J., Interpretation of IR and Raman line shapes for H₂O and D₂O ice Ih. *The Journal of Physical Chemistry B* **2012**, *116* (47), 13821-13830.
60. Prins, J. A., Molecular Arrangement and X-Ray Diffraction in Ionic Solutions. *The Journal of Chemical Physics* **1935**, *3* (2), 72-80.
61. Marques, M. A.; Cabaço, M.; de Barros Marques, M.; Gaspar, A., Intermediate-range order in aqueous solutions of salts constituted of divalent ions combined with monovalent counter-ions. *Journal of Physics: Condensed Matter* **2002**, *14* (32), 7427.
62. Angell, C. A.; Byrne, N.; Belieres, J.-P., Parallel developments in aprotic and protic ionic liquids: Physical chemistry and applications. *Accounts of chemical research* **2007**, *40* (11), 1228-1236.
63. Wright, A., Diffraction studies of glass structure: The first 70 years. *Glass physics and chemistry* **1998**, *24* (3), 148-179.
64. Folmer, J. C.; Withers, R. L.; Welberry, T.; Martin, J. D., Coupled orientational and displacive degrees of freedom in the high-temperature plastic phase of the carbon tetrabromide α -CBr₄. *Physical review B* **2008**, *77* (14), 144205.
65. Larouche, P.; Max, J.-J.; Chapados, C., Isotope effects in liquid water by infrared spectroscopy. II. Factor analysis of the temperature effect on H₂O and D₂O. *The Journal of Chemical Physics* **2008**, *129* (6), 064503.

CHAPTER 3

Liquid Structure of $\text{ZnCl}_2 \cdot n\text{H}_2\text{O}$ from $n = 3$ to $n = 250$

3.1 Introduction

Zinc chloride solutions have been of significant interest both for applied and fundamental research. Beginning in 1859, the industrial importance of zinc chloride was recognized when it was discovered to be an effective solvent for the dissolution of cellulose.¹ Modern industrial applications of zinc chloride solutions include electroplating² and battery technology³⁻⁴ as well as use in phase change materials⁵ and solar energy conversion through their utilization in the production of doped solar cells.⁶ In addition, zinc chloride has also been found to play significant roles in nature. For example, zinc chloride hydrates are important geologically in the formation and transport of hydrothermal ores.^{7,8} Furthermore, both Zn^{2+} and Cl^- are important biological ions^{9,10-11} and their interaction has been observed to be related to zinc toxicity.¹² A deeper understanding of zinc chloride solutions could result in better knowledge of the manner in which these ions interact in vivo. This, in turn, may result in a better understanding of the role of these important micronutrients in biological systems.

The high solubility of zinc chloride, 432 g/100 ml H_2O ($R = 1.75$; 64 mole % H_2O ; 31 m) at 25 °C, allows for an incredibly broad range of concentrations over which to examine the solution structure. These compositions not only include the dilute regions labeled as the Debye-Hückel limiting (100 – > 99 % water) and Extended Debye-Hückel (99 – 90 % water) regions by Braunstein but also the region of Hydrate melts (90 – 75 % water) and Incomplete hydration sheaths (75 – 1 % water).¹³ Measurements of the physical properties such as EMF,¹⁴⁻¹⁸ conductivity,¹⁹⁻²⁵ vapor pressure,^{16,17,19} density,²¹ viscosity,^{21,23,26} relaxation time for water exchange,²⁷ and glass transition temperatures^{14,23} of zinc chloride solutions have indicated

anomalous behavior in the Extended Debye-Hückel and Hydrate Melt regions of the ZnCl_2 : R H_2O system. Additionally, the thermal properties of zinc chloride solutions have been investigated numerous times over the past decades. This includes multiple reports of the $\text{ZnCl}_2/\text{H}_2\text{O}$ binary phase diagram which have indicated the existence of discrete hydrate phases occurring at compositions of $R = 1.5, 2.0, 2.5, 3.0$ and 4.0 as well as the indication of a deep eutectic at $R = 6$ for which a solidus line is not observed.²⁸⁻³⁰ Of the hydrate phases reported, crystal structures of the $R = 1.3, 2.5, 3.0$ and 4.5 hydrate compositions have been determined,³¹⁻³³ though as discussed below, the 2.5 and 4.5 equivalent hydrate compositions may be a result of a small hydroxyl impurity. Furthermore, while the glass forming capabilities of pure zinc chloride have been extensively investigated³⁴⁻³⁷, those of the aqueous zinc chloride system are less well understood. Aqueous ZnCl_2 is reported to have more anomalous behavior across a wider concentration range than other aqueous salt systems.²² Moreover, investigations of glass transitions in aqueous zinc chloride solutions have found that glass formation occurs in the compositional region from $2 < R < 17$ ²⁹ and that the $8 < R < 13$ region is most prone to glass formation for which it is suggested that this is due to the formation of polymeric chains in the solution.³⁸ The proposal of polymeric chains in the concentrated solutions has also been suggested based on Raman spectroscopic measurements of aqueous zinc chloride solutions.²⁷

Crystallography has provided confirmation of the $\text{Zn}(\text{H}_2\text{O})_6^{2+}$ and ZnCl_4^{2-} species existing independently in the hexaaquozinc triflate³⁹ and magnesium zinc tetrachloride hexahydrate⁴⁰, respectively, while they have also been found to exist together in zinc chloride trihydrate.³³ The traditional view of ionic solutions is that ions, other than commonly accepted stable complex ions such as SO_4^{2-} and NO_3^- , completely dissociate and are hydrated individually.⁴¹⁻⁴² However, highly concentrated solutions cannot be explained by the classical

hydration of ions given the deficiency of sufficient water molecules required to fully hydrate all ions present. As discussed in Chapter 2 and reference 33, the formation of complex ions for the $R = 3$ composition that do not pack efficiently or exhibit strong intermolecular forces between them makes this ionic compound liquid at room temperature. Such complex ion formation is typically thought to only be observed in highly concentrated solutions regarded as hydrate melts, since the stability of these compounds is expected to decrease upon dilution as the stoichiometric ratio of water becomes such that each atomic ion can be fully hydrated. However, it has been found that in many cases ions interact strongly in solution and play a significant role in the overall properties of the solution.^{43,44,45} Additionally, there are documented cases of complex ions, such as of iron(II), cobalt(II), and nickel(II) bromides with mixed water/halide coordination persisting to high dilution in the liquid state, thus contradicting the assumption that dilute aqueous solutions must consist of individually hydrated atomic ions.^{46,47} For zinc chloride solutions, mixed water/chloride species as well as $[\text{ZnCl}_n]^{(2-n)}$ have been proposed based on X-ray diffraction and Raman spectroscopy measurements.^{27, 48-49} In addition to the experimental evidence of complex ions in aqueous zinc chloride solutions, ab initio computational methods have also shown evidence for the stability of multiple mixed coordination species as well as ZnCl_4^{2-} .⁵⁰ While there are reports, based on neutron diffraction measurements, of chloride ions being hydrated in aqueous zinc chloride solutions at concentrations as high as 4 m ($R = 14$)^{41, 51}, others have proposed that the ZnCl_4^{2-} anion exists across a wide concentration range based on the strong Raman peak at $\sim 280 \text{ cm}^{-1}$, however, there is some debate as to whether this is actually $[\text{ZnCl}_4(\text{OH}_2)_2]^{2-}$.^{27, 30, 48, 52} Additionally, interpretation of EXAFS data has also led to questions about the true identity of complexes formed in aqueous zinc chloride solutions.⁵³

In addition to the interactions of Zn^{2+} with Cl^- there have also been many studies aimed at understanding the interaction of zinc ions with water. Both computational and experimental work has shown that Zn^{2+} is coordinated by six waters in aqueous solutions,⁵⁴⁻⁵⁶ including at the highly concentrated $R = 3$ composition as discussed in Chapter 2 and reference 33 in which this coordination was observed both in the crystal structure and in the melt. The $\text{Zn}(\text{H}_2\text{O})_6^{2+}$ species has been confirmed in more dilute solutions of zinc perchlorate via Raman spectroscopy in which the Zn-O symmetric stretching mode is observed at $\sim 390 \text{ cm}^{-1}$.⁵⁷ While the direct coordination of waters to the metal may not change upon dilution, there is still a question as to the interaction of additional waters in the system. The existence of a second hydration shell around cations has been proposed based on EXAFS data for multiple species such as Zn^{2+} , Ni^{2+} and Co^{2+} , although experimental observation of a second hydration shell is difficult due to multiple scattering events and thermal disorder which cancels out scattering from the second shell.^{55,58} While experimental observations are limited, the preference of a second hydration shell around the zinc ion in an aqueous environment is suggested by ab initio MD⁵⁹⁻⁶⁰ and DFT⁶¹ calculations. Ab initio MD simulations of hydrated Zn^{2+} suggest the first shell is highly polarized while the second shell is only slightly more polarized than bulk water. However, past the second shell the tetrahedral network of pure water is the observed arrangement.⁶⁰

While computational studies can be useful for understanding liquids and solutions, these studies often fall far short of representing a real system. The goal of many previous diffraction and MD studies of aqueous solutions are focused on the determination of the hydration shell(s) of individual ions, such as an isolated Zn^{2+} , without considering issues of charge balancing in the presence of counter ions or the application of liquid lattice theories that may result in the appearance of intermediate range ordering in the system.^{62,60} There has been a great deal of

interest since the early twentieth century regarding the use of crystalline-type packing ideas to understand intermediate range order in simple liquids.^{63,64} Crystal-type packing to describe the structure of aqueous solutions is likely manifest by low-Q peaks in the structure factor data obtained from diffraction measurements, particularly in the region $Q < 1.0 \text{ \AA}^{-1}$.^{65,66} Previous studies suggested the low-Q peak is characteristic of aqueous solutions of II-I electrolytes.⁶⁷ A low-Q peak is observed in aqueous ZnCl_2 solutions at concentrations greater than 1.0 m ($R < 55.5$) via neutron diffraction.⁶⁸ Furthermore, molecular dynamics simulations of solution structure report low-Q peaks as resulting from a quasi-close packing of cations in solution.⁶⁹ Low-Q peaks in X-ray diffraction measurements of aqueous CaCl_2 solutions of $R < 26$ also suggest the existence of lattice-like ordering in the system based.⁷⁰

As surveyed above, the literature demonstrates both significant interest in, but no clear conclusion to the question of structural organization in the complex zinc chloride hydrates. The Martin group's discovery of the structure of the congruently melting phase at the $R = 3$ composition for which the CsCl-type structure of crystalline $[\text{Zn}(\text{H}_2\text{O})_6][\text{ZnCl}_4]$ persists into the liquid state as an ionic liquid provide great insight into the nature of the aqueous zinc chloride system, specifically by confirming the segregation of zinc into two different environments.³³ The persistence of these molecular ions, and the corresponding structural organization of more dilute solutions remains unresolved. In this chapter, I exploit diverse measurement techniques, consistent with those used to determine the liquid structure of the $R = 3$ zinc chloride hydrate discussed in Chapter 2, to investigate the structure of more dilute solution. The methods include a full reexamination of the $\text{ZnCl}_2:\text{H}_2\text{O}$ phase diagram using DSC and variable temperature neutron diffraction. Liquid phase X-ray and neutron diffraction measurements are utilized to determine the changes in the local and intermediate range order as a function of concentration.

Raman spectroscopy was also utilized to identify the existence and identity of complex ions present in the system upon dilution.

3.2 Experimental Methods

3.2.1 Materials and synthesis

Zinc chloride (Aldrich) was dried under dynamic vacuum at 100 °C for ~12 hours prior to sublimation. The ZnCl₂ was then sublimed for 8 – 12 hours at 400 °C. Powder XRD and DSC analysis confirmed the sublimed material to be anhydrous δ -ZnCl₂ (m.p. 317 °C). The purified zinc chloride was stored and utilized in a nitrogen filled glove box. 18 M Ω water, obtained from a Millipore Synergy ultra-pure water filtration system, and as purchased 99.99% D₂O (Aldrich) were utilized to make all solutions.

DSC and capillary scale samples were prepared by placing a sample (~20 mg) of δ -ZnCl₂ into a high pressure stainless steel DSC pan, which was then placed on the pan of a home built Environmentally Controlled Microbalance (the microbalance head was purchased from CI Electronics and is controlled by LabWeigh Software). A stream of nitrogen was passed through a water bubbler, and the saturated water vapor passed over the sample until the desired stoichiometric amount of water was sorbed, at which point the hydration reaction was stopped. Using a syringe with a 0.7 mm ID fused silica capillary affixed to the end, a 1-2 mm aliquot was drawn into the middle of a capillary, which was then flame sealed on both ends of the zinc chloride hydrate sample. The DSC pan was then sealed using a gold seal. This preparation technique assured equivalent composition for structural and calorimetric measurements. ZnCl₂:D₂O samples were prepared for DSC analysis by adding appropriate amounts of D₂O to the sublimed zinc chloride in a nitrogen filled glove box. The sample was then placed into a stainless-steel DSC pan and sealed with a gold seal in the glove box.

Bulk samples of $\text{ZnCl}_2 \cdot n\text{H}_2\text{O}$ were prepared by adding for example for a $R = 3$ solution, 1.00 g of 18 MΩ H_2O (55.5 mmol) to 2.52 g anhydrous ZnCl_2 (18.5 mmol) which were then mixed by agitation until fully dissolved. Alternatively, water rich compositions were prepared by dilution of concentrated samples to obtain the desired composition. All samples were prepared and stored in Teflon capped Pyrex vials.

3.2.2 Synchrotron XRD of liquid

Samples were prepared via the method outlined above for aqueous zinc chloride samples of $R = 3$ (75% water) to $R = 100$ (99% water). A 0.7 mm ID capillary containing a 1-2 mm aliquot of liquid $\text{ZnCl}_2 \cdot n\text{H}_2\text{O}$ was affixed to a goniometer head on the diffractometer on line 11-ID-B at the Advanced Photon Light Source, Argonne National Laboratory. Diffraction data were measured at room temperature, ~ 295 K. A 90 KeV ($\lambda = 0.13702$ nm) X-ray beam was utilized to collect an average of 100 scans at 10 s per scan using a GE amorphous silicon detector. Data for background subtraction was obtained using the same sample capillary that was shifted such that no sample, only the fused silica capillary was in the beam. Raw 2-dimensional data was radially integrated using Fit2D.⁷¹ The diffraction data was subsequently transformed into a structure factor $S(Q)$, subtracting the background and correcting the data for sample and instrument effects such as Compton scattering, Laue diffuse scattering, self-absorption, X-ray polarization and scattering based on the elements present. Transformation of the data to obtain the $S(Q)$, and its inverse Fourier Transform pair distribution function $G(R)$ was performed using PDFgetX2.⁷²

3.2.3 Neutron diffraction

Samples were prepared as stated above for aqueous zinc chloride samples of $R = 3$ to $R = 250$ (99.6% water). 1 mL samples were sealed into 5mm OD fused silica NMR tubes

(WILMAD). The samples as well as an empty NMR tube were mounted on the linear sample changer installed on the NOMAD diffractometer, Spallation Neutron Source, Oak Ridge National Lab.⁷³ The linear sample changer is equipped with a Cobra Plus Cryosystem from Oxford modified for use with neutron scattering to operate with temperature controlled Ar gas. Ar gas has a very small neutron scattering cross-section and hence a reduced background. Neutron event data were binned as a function of Q using a calibration derived from a measurement of diamond powder as described in reference 73 and normalized to the integrated proton charge accumulated on the neutron target. Measurements obtained from a 5.8 mm diameter vanadium rod were used for the normalization of the sample data to a differential cross section. The incoherent contribution to the scattering cross section was approximated by a pseudo-Voigt function. Data was collected to $Q_{\max} = 50 \text{ \AA}^{-1}$. Based on the total scattering structure factor $S(Q)$, and the reduced atomic pair distribution function $G(r)$ was calculated using data up to $Q = 31 \text{ \AA}^{-1}$. Data were collected for specific isotherms between 100 to 333 K (sum of three 20 min scans) or with a ramped temperature profile 1 or 5 °/min. Transformation of the data to obtain the $S(Q)$, and its inverse Fourier Transform pair distribution function $G(R)$ was performed using the NOMAD-SNS analysis suite of programs.

3.2.4 Raman

A dilution series was prepared by diluting an initially prepared sample of the $R = 3$ solution with subsequent aliquots of water required to achieve the next most dilute solution. Upon water addition, each sample was agitated for approximately 30 seconds and allowed to stand for at least 2 minutes before the Raman spectrum was obtained. Approximately 1.0 mL samples of liquid zinc chloride hydrates, ranging in concentration from $R = 3$ to $R = 250$ as well as a pure water sample, were placed into a 1 cm³ quartz cuvette. Raman spectra were collected

in the frequency range of 40 to 2250 cm^{-1} using a water cooled Coherent Ar/Kr laser running at 30 A. Measurements were taken at room temperature using a 488-nm excitation wavelength. A PIXIS charge coupled device (CCD) detector was used to collect the scattered light. For each set of measurements, the vertical and horizontal alignment of the laser was fine-tuned, and the instrument mirrors were adjusted to obtain the highest signal-to-noise ratio. A calibration curve was constructed using the spectral bands of toluene as a reference by plotting the observed peak locations against their known position. The plot was then fitted to a line, the slope of which was used to correct the frequency of the sample spectra.

3.2.5 Computational methods

Reverse Monte Carlo (RMC) modelling was performed using RMCProfile program.⁷⁴ Simulations were performed for both the $R = 9$ and $R = 21$ compositions. The starting configurations for these simulations were obtained by adding 12 and 24 waters into second and third hydration shells, respectively, around each hydrated zinc ion. Models were constructed with molecular ions arranged in both CsCl- and NaCl-type structures, albeit with a P1 space group. The unit cell was then expanded to a 4x4x4 supercell. To introduce disorder into the system the ions were randomized utilizing a Visual Basic macro that randomly in three-dimensions translated the molecular center of each ion by as much as 1.0 Å. Following the random translation each complex was independently rotated in both the XY and XZ plan by a random angle from 0 to 360°. During the simulation the intramolecular ion distances of the $\text{Zn}(\text{H}_2\text{O})_6^{2+}$, ZnCl_4^{2-} and H_2O were tightly constrained (allowed to vary by less than 1.0 Å) about the experimentally determined values observed in the X-ray and neutron diffraction pair distribution functions (PDFs). These included the intramolecular Zn-O, Zn-Cl, Cl-Cl, equatorial O-O, O-H and H-H pair correlations. The remaining pair correlations, which include the inter-

ion distances such as the Cl-O and Zn-Zn along with those of the second hydration shell (i.e. Zn-O_{II} and O_I-O_{II}) were allowed to vary up to 2.0 Å.

3.3 Results

3.3.1 ZnCl₂:H₂O phase diagram

The water:ZnCl₂ phase diagram provides the fundamental basis for understanding the temperature/composition dependent structure of the aqueous zinc chloride system. The phase diagram originally constructed by Mylius and Dietz in 1905,²⁸ reprinted here as Figure 3.1, gives indication of multiple crystalline hydrate phases, ZnCl₂·R H₂O, R = 4, 3, 2.5, 2 and 1.5. Subsequently, Hennings, et. al. published crystal structures of R = 2.5 and R = 4.5 hydrates,³² although it must be noted that neither phase was reported to be grown from its stoichiometric composition. Notably, the crystallographically characterized R = 1.33 hydrate phase³¹ does not appear on the original phase diagram. In our initial investigation of the water:ZnCl₂ phase diagram in the immediate vicinity of the congruently melting R = 3 hydrate, Chapter 2 and reference 33, a more standard eutectic-type behavior is observed with both H₂O and D₂O, for which there is no evidence of a crystalline phase at compositions R = 4.5 (82% water) or R = 2.5 (71% water). It is our hypothesis that the apparent conflict between the Mylius and Dietz phase diagram, Hennings crystalline hydrates, and our investigation of the water:ZnCl₂ phase diagram is a result of impurities, likely hydroxyl impurities, in the zinc chloride source.

atmosphere, equilibrated for 2-12 h with periodic agitation, then sealed within high pressure stainless steel pans. The sample was then placed into the DSC at 40 °C, and cycled through cooling and heating profiles from -50 °C or -80 °C to 25 °C or 50 °C at either 0.5, 1.0 or 5 °C/min, with the temperature held isothermally for five minutes at each low and high temperature cycle limit. Exemplar DSC data are presented in Figures 3.2 - 3.4. At the congruently melting $R = 3$ composition (75% water) a single reasonably sharp melting event is observed at a temperature of 3 °C for the H₂O solution and -1 °C for the D₂O solution, Figure 3.2. Through four cool-heat cycles, no change is observed in the melting endotherm. However, the crystallization onset temperature, and thus also the rate of crystallization, is observed to shift slightly from run to run (-26 to -27 °C for H₂O solutions, and -23 to -35 °C for D₂O solutions which were very slightly off composition at $R = 2.98$). The water:ZnCl₂ system exhibits an inverse isotope effect compared to that of pure water for which H₂O melts at 0 °C and D₂O melts at 3.8 °C.

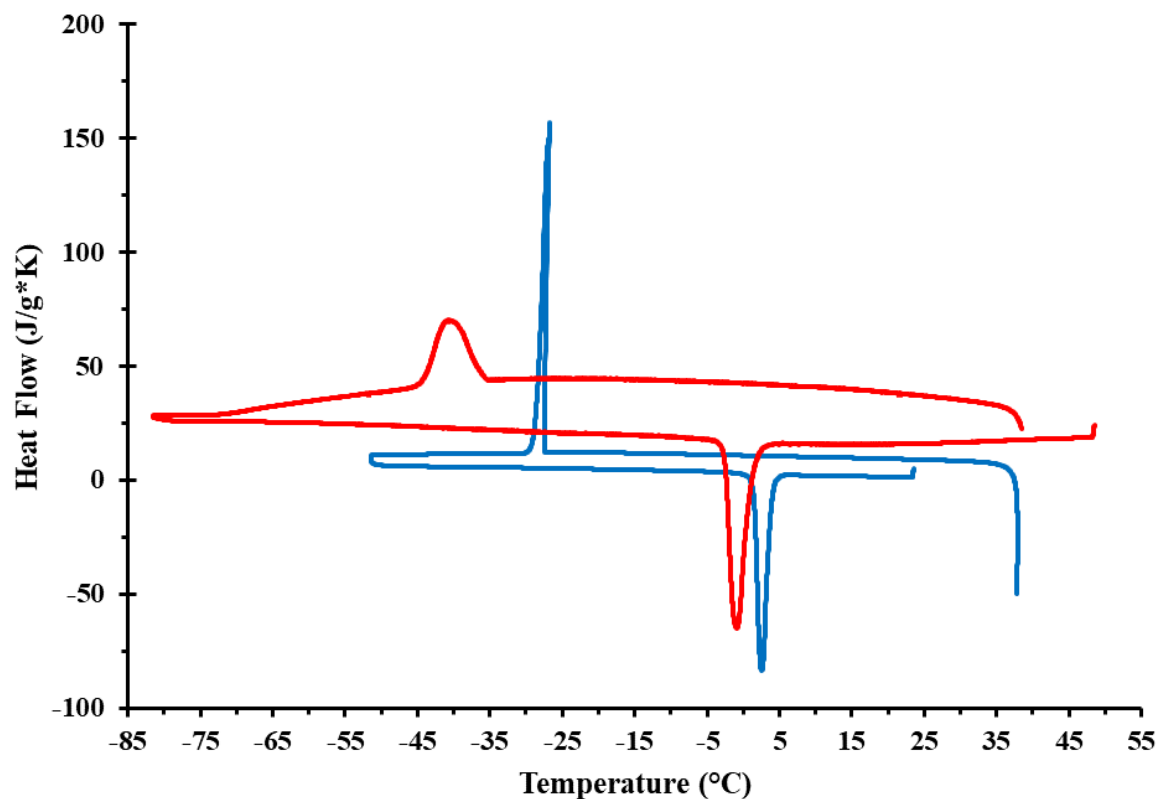


Figure 3.2 DSC plots of the $R = 3$ (75% water) ZnCl_2 hydrate for H_2O (blue) cycled from -50 to 25 $^\circ\text{C}$ at a rate of 0.5 $^\circ\text{C}/\text{min}$ and D_2O (red) cycled from -80 to 50 $^\circ\text{C}$ at a rate of 1.0 $^\circ\text{C}/\text{min}$.

Compositions shifted away from the congruently melting $R = 3$ stoichiometric hydrate exhibit a more complex cooling-heating profile, as demonstrated in Figures 3.3 and 3.4 for the D_2O solutions across the 2.5 (71%) $< R < 3$ (75%) and 3 (75%) $< R < 4$ (80%) composition ranges, respectively. Similar behavior is observed for the H_2O solutions. The data is only shown for the D_2O solutions which were measured at slower cool-heat rates thus affording greater resolution of the transitions. Two endothermic events are observed upon heating corresponding to the eutectic and liquidus transitions. The relative intensity of the eutectic and liquidus peaks vary as a function of composition; the former becoming more intense as the eutectic is approached and the latter as the composition of the congruently melting phase is approached. For each composition investigated, the melting endotherms, including the eutectic and liquidus

features, are equivalent through multiple cool-heat cycles as demonstrated by the endotherm insets for each of the figures. The eutectic temperatures, T_{eutectic} , are essentially invariant between pairs of crystalline phases, $-6\text{ }^{\circ}\text{C}$ (D_2O) for $3 > R > 1.5$, and $-32\text{ }^{\circ}\text{C}$ (H_2O) and $-34\text{ }^{\circ}\text{C}$ (D_2O) for $\infty > R > 3$. The liquidus temperatures are significantly concentration dependent, with maxima corresponding to unique hydrate phases and minima at the eutectic compositions. A very small endotherm is observed at $-33\text{ }^{\circ}\text{C}$ (H_2O) and $-37\text{ }^{\circ}\text{C}$ (D_2O) for all compositions between $4 > R > 3$. The origin of this endotherm is not yet known, but may be indicative of a crystal-crystal phase transition just prior to the eutectic melting.

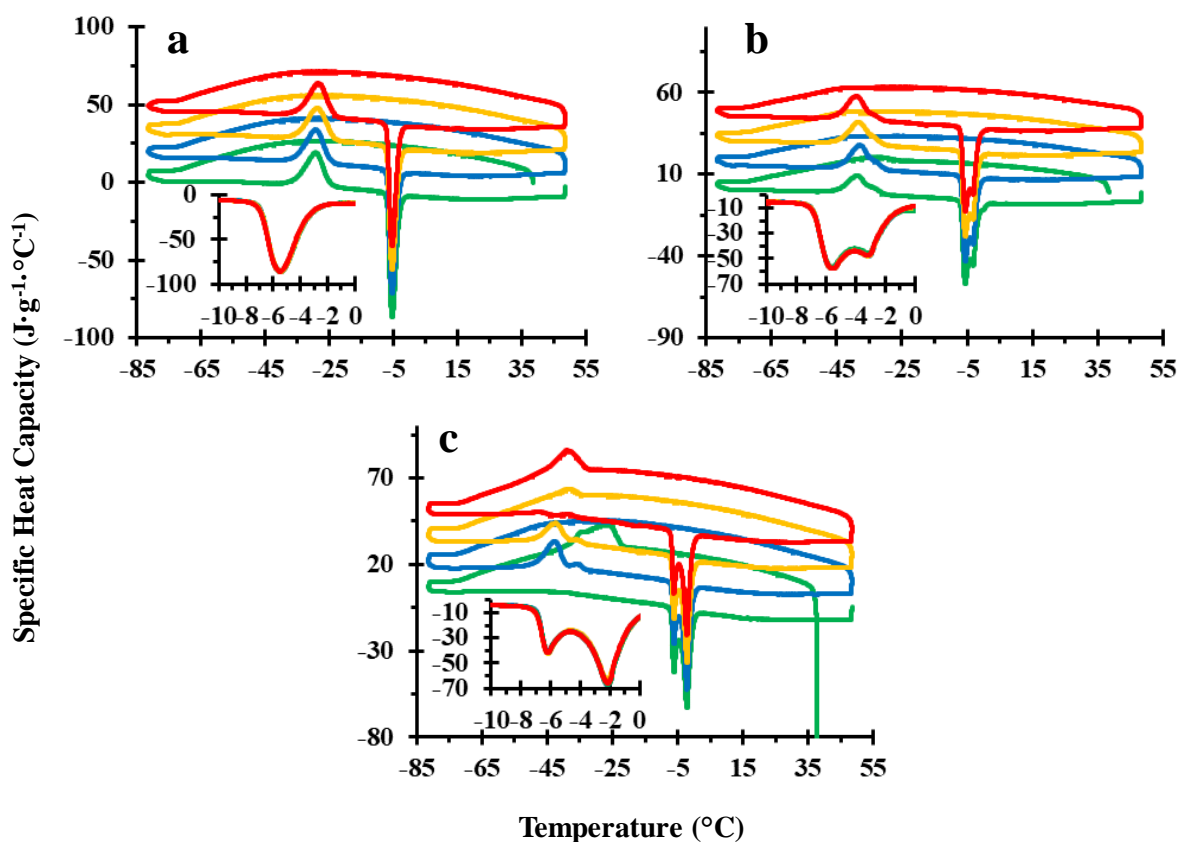


Figure 3.3 Stack plots of the DSC cycling of $\text{ZnCl}_2:\text{D}_2\text{O}$ samples of a) $R = 2.61$ (72.3% water), b) $R = 2.73$ (73.2% water), and c) $R = 2.83$ (73.9% water). All samples were cycled four times from -80 to 50 $^\circ\text{C}$ at a rate of 1.0 $^\circ\text{C}/\text{min}$ and are shown as cycle 1 (green), cycle 2 (blue), cycle 3 (orange) and cycle 4 (red). Insets for each composition show an expansion of the melting regions.

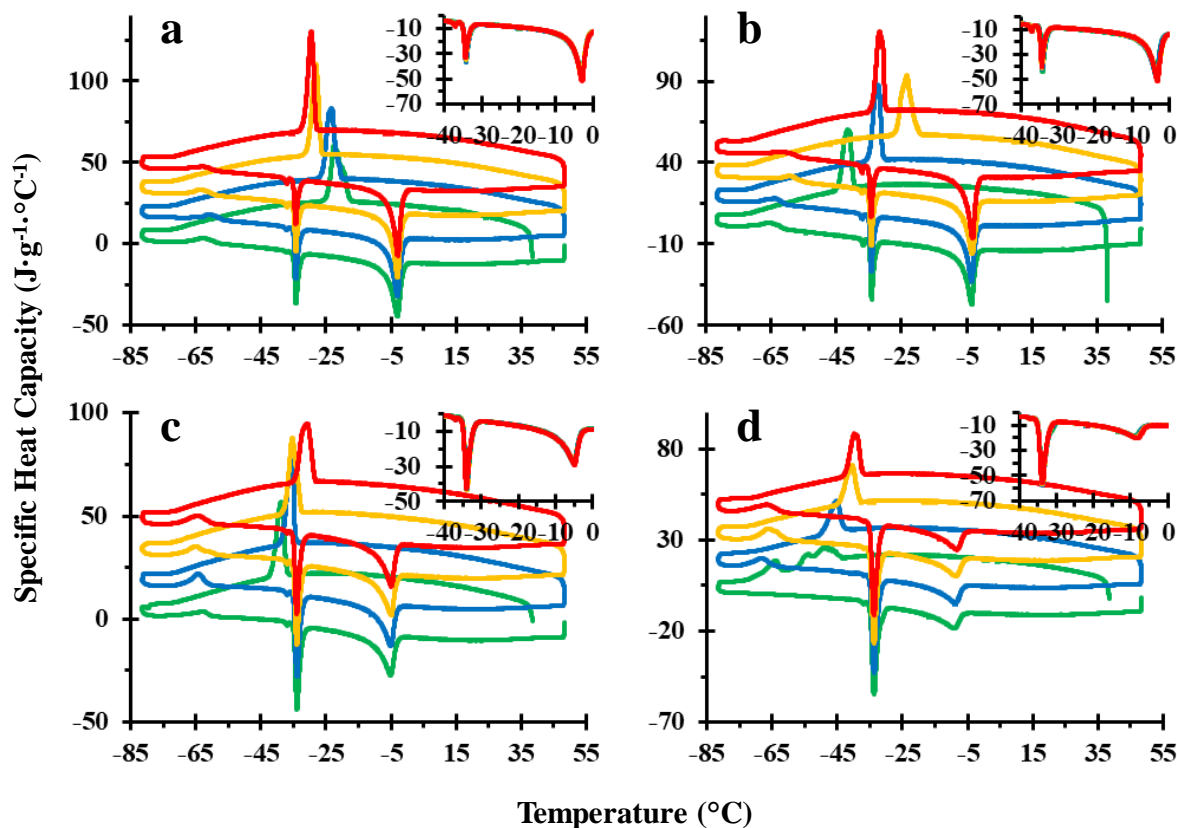


Figure 3.4 Stack plots of the DSC cycling of $\text{ZnCl}_2:\text{D}_2\text{O}$ samples of a) $R = 3.23$ (76.4 % water), b) $R = 3.27$ (76.6% water), c) $R = 3.41$ (77% water), and d) $R = 3.61$ (78% water). All samples were cycled from -80 to 50 °C at a rate of 1.0 °C/min and are shown as cycle 1 (green), cycle 2 (blue), cycle 3 (orange) and cycle 4 (red). Insets for each composition show an expansion of the melting regions.

The crystallization behavior of the off-hydrate composition samples is significantly more complex. Distinct behavior is observed for the initial vs. subsequent crystallization cycles, in direct contrast to the melting isotherms which are equivalent for each set of cool-heat cycles. Depending on concentration and cycle, exotherms resulting from liquidus and eutectic crystallization, as well as for crystallization upon cooling from the melt (hot crystallization) or heating from a glass (cold crystallization) may be observed. On the water deficient side of the congruently melting $R = 3$ hydrate, hot crystallization proceeds at a notably slower rate than is observed on the water rich side of the $R = 3$ hydrate; broader peaks correspond to slower

transitions. For the $R = 2.83$ composition, Figure 3.3c, essentially the entire sample crystallizes upon cooling for the first cool-heat cycle, albeit with a broad irregularly shaped exothermic peak. By contrast, essentially no hot crystallization is observed in the second cycle. Instead, two cold crystallization exotherms, assigned to eutectic and liquidus crystallization of the primary $R = 3$ and minor $R = 1.5$ crystalline phases are observed with an onset about $40\text{ }^{\circ}\text{C}$ below the T_{eutectic} . Some hot crystallization, 48% then 82% respectively, is again observed in the third and fourth cool-heat cycles, albeit with an onset temperature about $10\text{ }^{\circ}\text{C}$ lower than observed for the first cooling. The more water deficient $R = 2.73$ and 2.61 samples exhibit essentially only cold crystallization in each of four cool-heat cycles, with a single eutectic crystallization exotherm for the $R = 2.61$ sample.

The samples measured on the water rich side of the $R = 3$ hydrate, $3 < R < 4$, all exhibit a majority of crystal growth by hot crystallization. Interestingly, for the $R = 3.23$ sample, the onset temperature of hot crystallization decreases from $-18\text{ }^{\circ}\text{C}$ in the first cycle to $-28\text{ }^{\circ}\text{C}$ in the fourth cycle. By contrast the onset of hot crystallization in the more water rich $R = 3.27$, 3.41 and 3.61 samples is lowest for the first cycle, approximately $-40\text{ }^{\circ}\text{C}$ for all three, but increases significantly in subsequent cool-heat cycles to an average temperature of $-33\text{ }^{\circ}\text{C}$. The ratio of the hot vs. cold crystallization can be estimated by the relative size of the integrated exotherms. For the $R = 3.23$ and 3.27 solutions, the hot vs. cold crystallization ratios remain relatively constant at 86 % hot for each of four cool-heat cycles. A similar ratio is observed for the first cool-heat cycle for the $R = 3.41$ solution, but for subsequent crystallization cycles the fraction of hot crystallization is reduced to only about 79%. The first crystallization of the $R = 3.61$ solution exhibits complete hot crystallization, albeit with an irregular first crystallization exotherm, onset

temperature of $-44\text{ }^{\circ}\text{C}$ with two maxima corresponding to 82% of the heat of crystallization, followed by additional crystallization with an onset temperature of $-62\text{ }^{\circ}\text{C}$.

The latter crystallization exotherm occurs in the same vicinity of the cold crystallization exotherms observed for crystallization cycles 2-4. The integrated area under the curves for runs 2-4, however, suggests that only 75 % of the material crystallizes by hot crystallization. The cycle dependence of the relative hot vs. cold crystallization of these solutions suggests that the initial solutions are most homogeneous, with solutions of subsequent crystallization cycles exhibiting a “memory” of their phase segregated crystalline precursors.

The composition dependent eutectic and liquidus melting temperatures for all compositions investigated are plotted to construct the phase diagram of Figure 3.5. This phase diagram, constructed from pure, doubly sublimed ZnCl_2 is notably simpler than that originally reported by Mylius and Dietz, Figure 3.1. We find evidence for only one congruently melting hydrate phase at $R = 3$, along with two incongruently melting crystalline phases at $R = 1.5$ and 1.3 (H_2O) with peritectic temperatures of $23\text{ }^{\circ}\text{C}$ and $26\text{ }^{\circ}\text{C}$, respectively. The $R = 1.3$ hydrate was previously crystallographically characterized.³¹ The $R = 1.5$ hydrate has not yet been crystallographically characterized, but, R. Wilcox also observed it by gravimetric analysis to be the first solid phase that forms upon dehydration of the $R = 3$ liquid. Between $1.5 < R < 3$, there is no evidence of thermal transitions, nor, have we observed any evidence for solid phases with melting points higher than that observed for the $R = 3$ hydrate, implied by the Mylius and Dietz phase diagram and Henning’s reported crystalline $R = 2.5$ hydrate. Instead, a eutectic is observed at $R = 2.4$ and $T_{\text{eutectic}} = -1\text{ }^{\circ}\text{C}$ for H_2O solutions, which is apparently shifted toward $R = 2.6$ and $T_{\text{eutectic}} = -6\text{ }^{\circ}\text{C}$ for D_2O . Similarly, there is no evidence for any additional crystalline phases between the $R = 3$ hydrate and pure water ice. Notably, no crystallization has been

observed for compositions between $4 < R < 10$. Attempts to grow crystalline phases at these compositions have included slow temperature ramps from room temperature to 100 K, and low temperature isothermal experiments of up to one week. Crystallization is again observed for compositions with greater than 10 equivalents of water. On both sides of this “amorphous chasm” a eutectic temperature of $-30\text{ }^{\circ}\text{C}$ (H_2O) and $-34\text{ }^{\circ}\text{C}$ (D_2O) is observed, allowing us to estimate a eutectic composition to be approximately $R = 5$ (83% water).

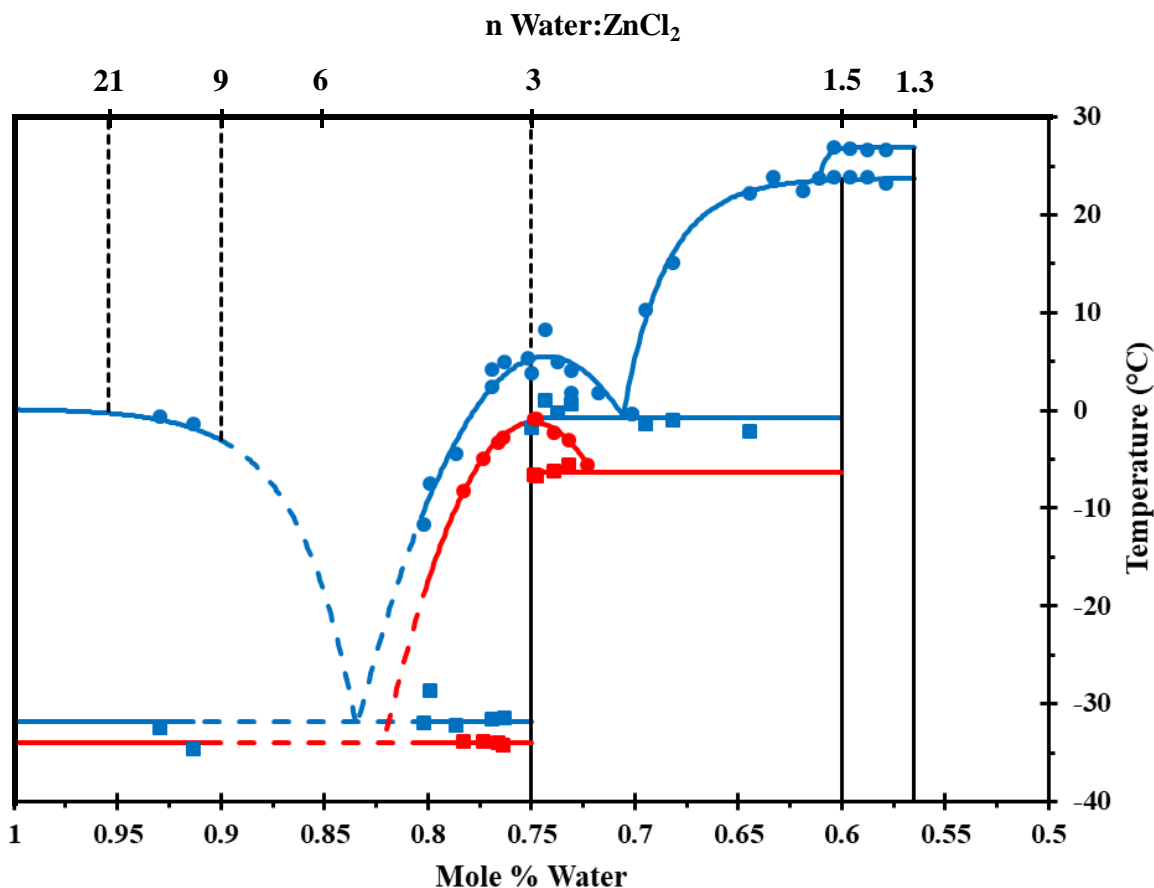


Figure 3.5 Water:ZnCl₂ phase diagram for both H₂O (blue) and D₂O (red) in the compositional region between $R = 1.3$ (57% water) and pure water. Squares represent eutectic points and circles represent melting points (liquidous curve).

A series of variable temperature neutron and X-ray diffraction measurements were conducted for phase identification at various compositions in order to further understand the

contrasting results between our and Mylius and Dietz phase diagram. Shown in Figure 3.6 are low temperature neutron diffraction patterns for the compositions of $R = 3, 4, 9, 21$, and pure D_2O . Neutron diffraction samples were sealed into 5-mm quartz NMR tubes and quenched to isotherms ranging from 103 to 233 K. The samples were held at these temperatures for time periods between 5 to 60 minutes prior to measuring their diffraction patterns. Crystallization of the $R = 3$ hydrate was observed for the stoichiometric composition. And the crystal structure of D_2O ice was observed in both the pure water and $R = 21$ samples. No other crystallization was observed in the quenched-sample neutron diffraction measurements. In addition, neutron diffraction data was collected for the $R = 9$ sample while being heated from 118 K to 273 K at a rate of $1\text{ }^\circ\text{C}/\text{min}$. Again no crystallization was observed. Related *in situ* crystal growth/ X-ray diffraction experiments were conducted, by R. Wilcox,⁷⁵ by sealing samples of the zinc chloride hydrate (H_2O) solutions into 0.5 mm fused silica capillaries, that were then cooled to various isotherms down to 100 K. The crystalline product observed to grow from solutions with $R > 10$ could be indexed to the unit cell of water ice, indicating that no thermodynamically stable crystalline hydrate composition exists between water ice and the “amorphous chasm” from $4 < R < 10$. All crystals grown from solutions between $2.5 < R < 4$ could be indexed to the unit cell of the $R = 3$ hydrate phase. No other crystalline products were observed.

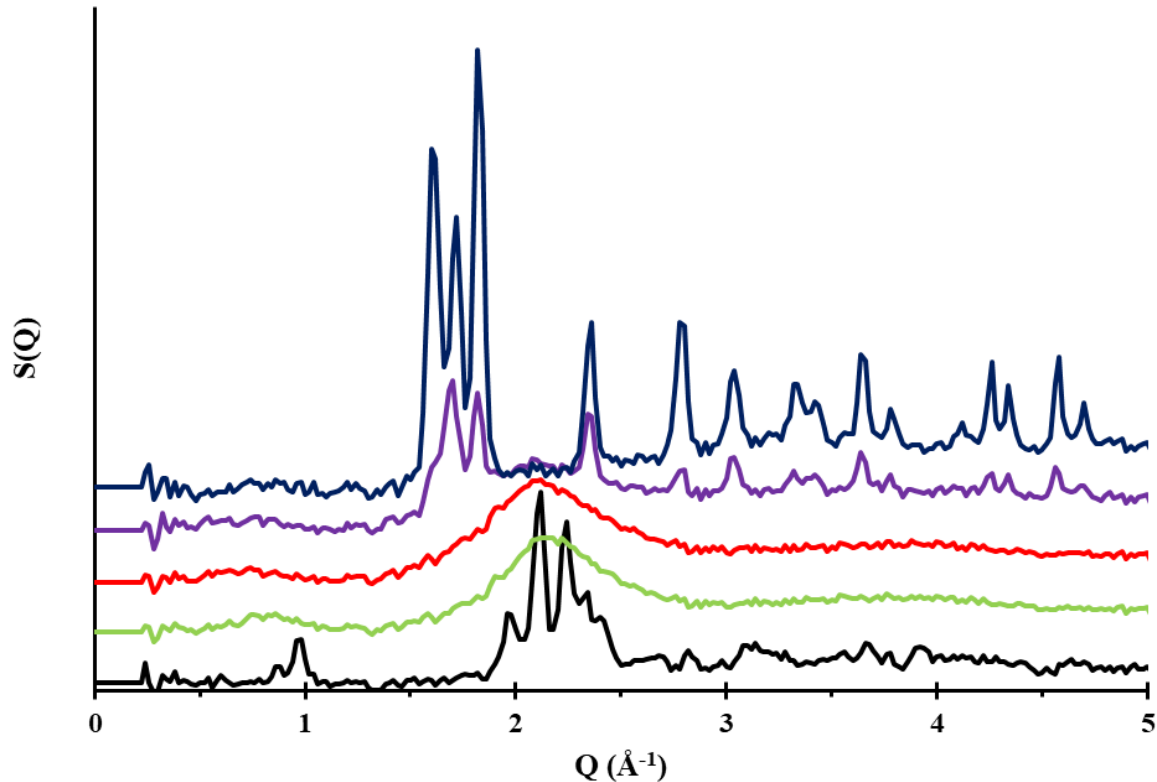


Figure 3.6 Neutron diffraction structure factors of $\text{ZnCl}_2\cdot\text{D}_2\text{O}$ solutions of $R = 3$ (black) at 223 K, $R = 4$ (light green) at 213 K, $R = 9$ (red) at 213 K, $R = 21$ (purple) at 213 K and pure D_2O (dark blue) at 193 K.

3.3.2 Liquid phase diffraction of ZnCl_2 dilution series

To investigate the effects of dilution on both intra- and intermolecular structural features observed at the $R = 3$ composition, as reported in Chapter 2 and reference 33, room temperature neutron and X-ray diffraction measurements were performed on a series of aqueous zinc chloride solutions. Synchrotron X-ray diffraction measurements were obtained at room temperature for solutions with concentrations 1.72 (63% water) $\leq R \leq 100$ (99% water) and $18 \text{ M}\Omega \text{ H}_2\text{O}$, as well as for molten ZnCl_2 at $320 \text{ }^\circ\text{C}$. Neutron diffraction measurements were obtained at room temperature for samples with concentrations 3 (75% water) $\leq R \leq 250$ (99.6% water), as

purchased D₂O (Aldrich 99.999%), and glassy ZnCl₂ (298 K). Representative structure factor data from these experiments is shown in Figures 3.7 and 3.8.

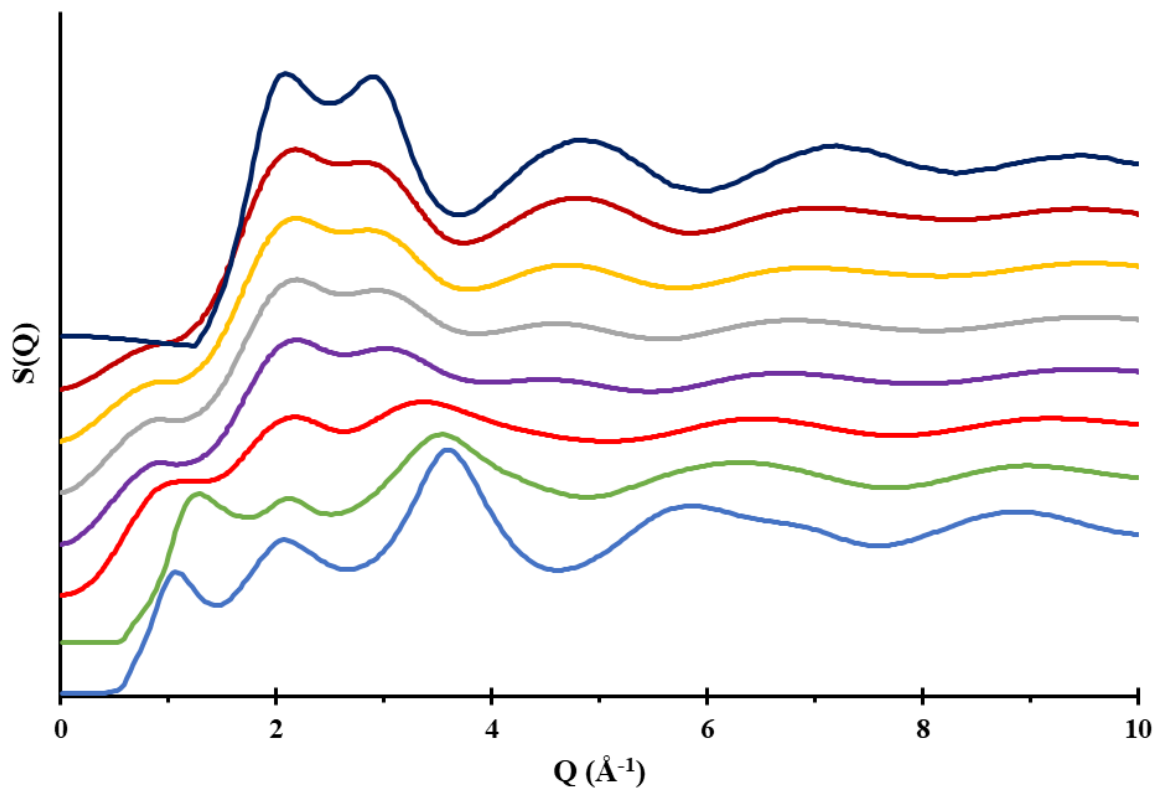


Figure 3.7 Structure factor plots of select X-ray diffraction patterns for molten anhydrous ZnCl₂ at 320 °C (blue), R = 2.9 (green), R = 9 (red), R = 21 (purple), R = 30 (gray), R = 50 (orange), R = 100 (dark red), pure H₂O (dark blue).

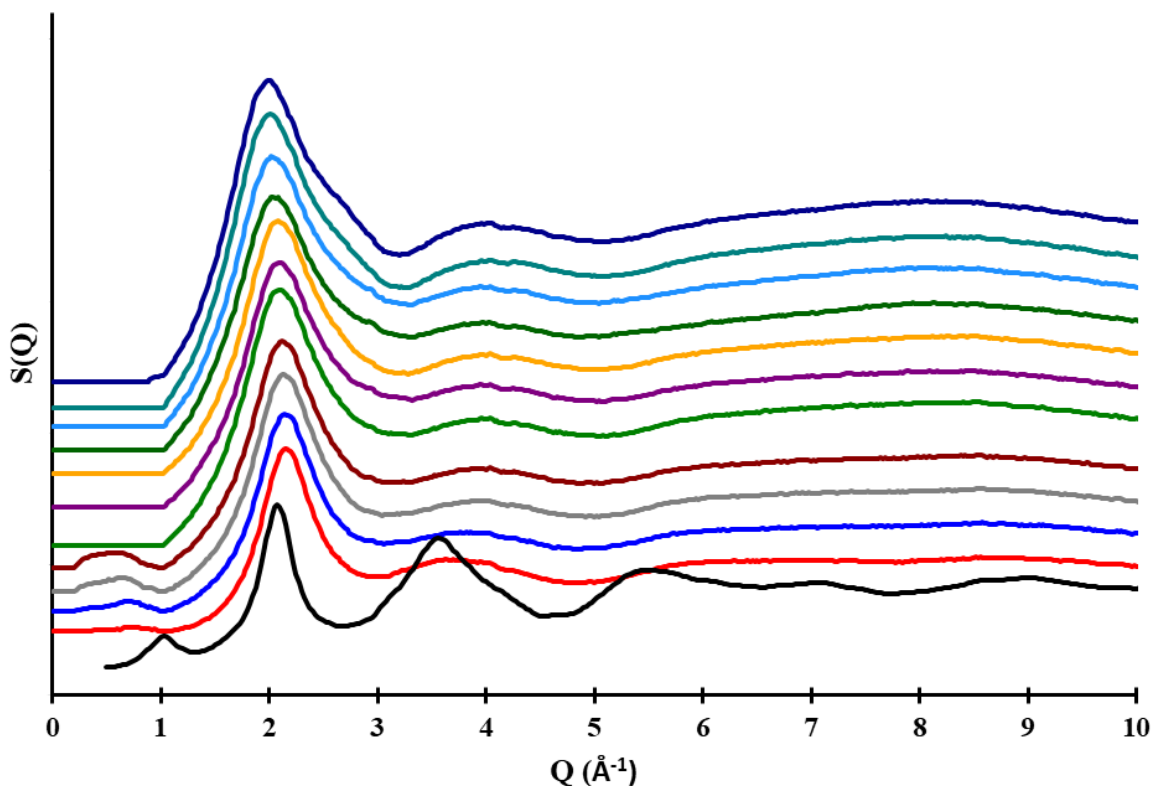


Figure 3.8 Structure factor plots of data collection of the neutron diffraction patterns for glassy ZnCl_2 (black) as well as room temperature ZnCl_2 aqueous solutions of $R = 3$ (red), $R = 5$ (blue), $R = 7$ (gray), $R = 9$ (dark red), $R = 13$ (green), $R = 18$ (purple), $R = 21$ (orange), $R = 45$ (dark green), $R = 93$ (light blue), $R = 175$ (teal) and pure D_2O (dark blue).

In the X-ray structure factor plot of molten ZnCl_2 , three reasonably sharp peaks are observed at 1.07 , 2.09 , and 3.59 \AA^{-1} , with broader features observed at higher values of Q . A set of peaks analogous to these three low- Q peaks is observed in the structure factor plot of all of the zinc chloride hydrate solutions examined, with the latter two being reminiscent of the two primary diffraction peaks of pure water. However, the respective position of these peaks exhibits a clear composition dependence as highlighted in Figure 3.9. The lowest reciprocal space peak, often ascribed to intermediate range order in liquids, shifts from 1.07 \AA^{-1} for molten ZnCl_2 to 1.2 \AA^{-1} for the concentrated hydrates $R < 3.25$ hydrate and then shifts back to lower Q upon subsequent dilution to 0.93 \AA^{-1} at $R = 100$. Notably, the shift in this low- Q reciprocal scattering

vector does not exhibit a monotonic correlation between Q and concentration. Rather a stepwise pattern is observed. As demonstrated in Figure 3.8a, the reciprocal scattering vector is relatively invariant across the composition range 1.72 (0.63% water) $< R < 3.24$ (76% water). Upon further dilution between 3.67 (77% water) $< R < 9$ (90% water), the reciprocal scattering vector exhibits a linear decrease in Q is observed (a slope of -0.69 (0.03)), along with notable peak broadening. Beyond $R = 9$ (90% water) to $R = 21$ (95% water), this low- Q peak sharpens slightly, but a dramatically steeper concentration dependence on the reciprocal scattering vector is observed (a slope of -5.3 (1.1)). Past the $R = 21$ composition no additional statistically significant change in the low- Q peak position is observed.

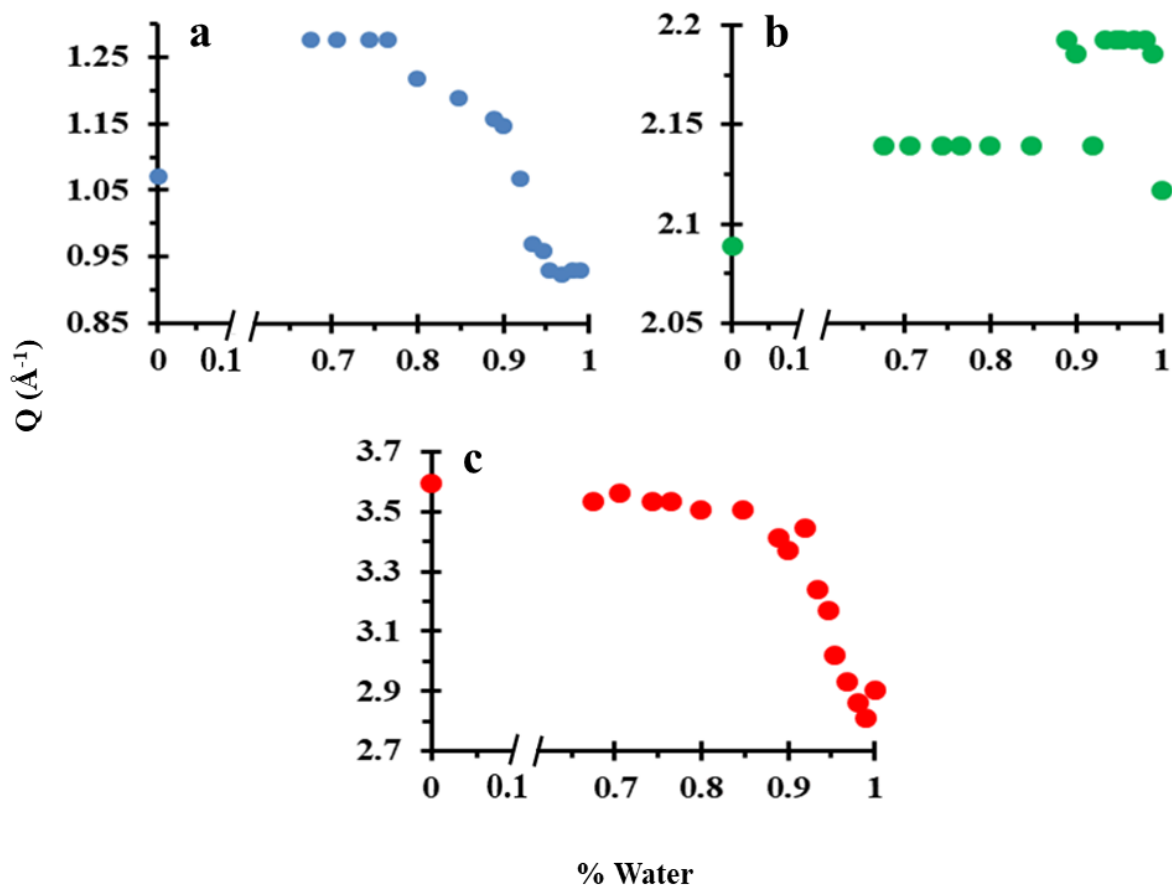


Figure 3.9 a) Position of the low-Q X-ray diffraction peak as a function of zinc chloride concentration from $R = 2.07$ (67% water) to $R = 100$ (99% water), b) the 2.09 \AA^{-1} peak and c) Shift in the 3.59 \AA^{-1} peak from molten zinc chloride to pure water as a function of mole percent H_2O .

The second peak, observed at 2.09 \AA^{-1} in the molten ZnCl_2 X-ray scattering data, is generally assigned to the pseudo-close packing of chlorides creating the tetrahedral network. As shown in Figure 3.8b, this reciprocal scattering vector is statistically unchanged for all of the zinc chloride hydrate solutions examined. It is further analogous to the first diffraction peak in pure water, $Q = 2.09 \text{ \AA}^{-1}$, that corresponds to its tetrahedral network.

The third peak, observed at 3.59 \AA^{-1} in molten ZnCl_2 , and 3.57 in the $R = 3$ hydrate, also exhibits a significant concentration dependence, as shown in Figure 3.8c. A relatively small concentration dependence in Q is observed for the highly concentrated solutions, $R < 6$, (a slope

of -0.09 (0.03)). Upon further dilution, $R > 8$ (89% water) a dramatically increased, and approximately linear concentration dependence up to the structure factor of pure water, is observed (a slope of -6.1 (0.8)). Additionally, both the 2.09 and 3.59 \AA^{-1} peaks are observed to broaden and diminish in intensity upon dilution, however, the 3.59 \AA^{-1} peak does diminish at a faster rate than the 2.09 \AA^{-1} . Furthermore, from examination of Figure 3.7 it can be seen that both of these peaks are dramatically sharper in pure water when compared to the dilute zinc chloride samples ($R > 21$).

The higher reciprocal space scattering vectors, $Q > 4 \text{\AA}^{-1}$, are significantly broader than the low- Q features. However, these too exhibit an interesting progression between the structure factors of pure molten ZnCl_2 and pure water. Notably, a broad scattering feature, analogous to pure water's peak at $Q = 4.8 \text{\AA}^{-1}$, is observed to gradually emerge in the structure factors of hydrate solutions between $R = 11.6$ and $R = 14$, with $Q = 4.7 \text{\AA}^{-1}$. Upon further dilution, this peak sharpens but does not significantly shift position. By contrast, the broad features at $Q = 6.3 \text{\AA}^{-1}$ and 9.0\AA^{-1} observed in the concentrated hydrates, analogous to broad features in pure ZnCl_2 , are observed to shift to higher Q upon dilution, 7.1\AA^{-1} and 9.6\AA^{-1} , respectively at $R = 100$, analogous to broad peaks in the structure factor of pure water at 7.2\AA^{-1} and 9.5\AA^{-1} .

As described in the previous report of the liquid structure of the $R = 3$ hydrate, the intensity profile of the structure factors are significantly different for X-ray and neutron scattering; the former being dominated by heavy atoms and the later dominated by scattering from the D atoms. As such, for the $R = 3$ hydrate, which exhibits a pseudo cubic CsCl-type packing of the $[\text{Zn}(\text{OH}_2)_6][\text{ZnCl}_4]$ ionic liquid, the low- Q peak in the X-ray structure factor is dominated by (110) type lattice features, whereas the the (200) type lattice features define the lowest Q peak in the neutron structure factor. Neutron scattering data, shown in Figure 3.10,

displays a low-Q diffraction peak in the region from 0.5 to 1.1 \AA^{-1} in the concentration range of $R = 3$ to $R = 9$ as well as molten ZnCl_2 . Figure 3.11 shows the shift in the low-Q neutron diffraction peak for the higher concentrations in which it is observed. The most dramatic change in the low-Q peak occurs between amorphous zinc chloride, with a value of 1.02 \AA^{-1} , and the $R = 3$ composition which has a Q-value of 0.78 \AA^{-1} . The compositional range in which the low-Q peak is observed for the neutron scattering measurements displays a linear trend with a slope of -1.3 (0.1).

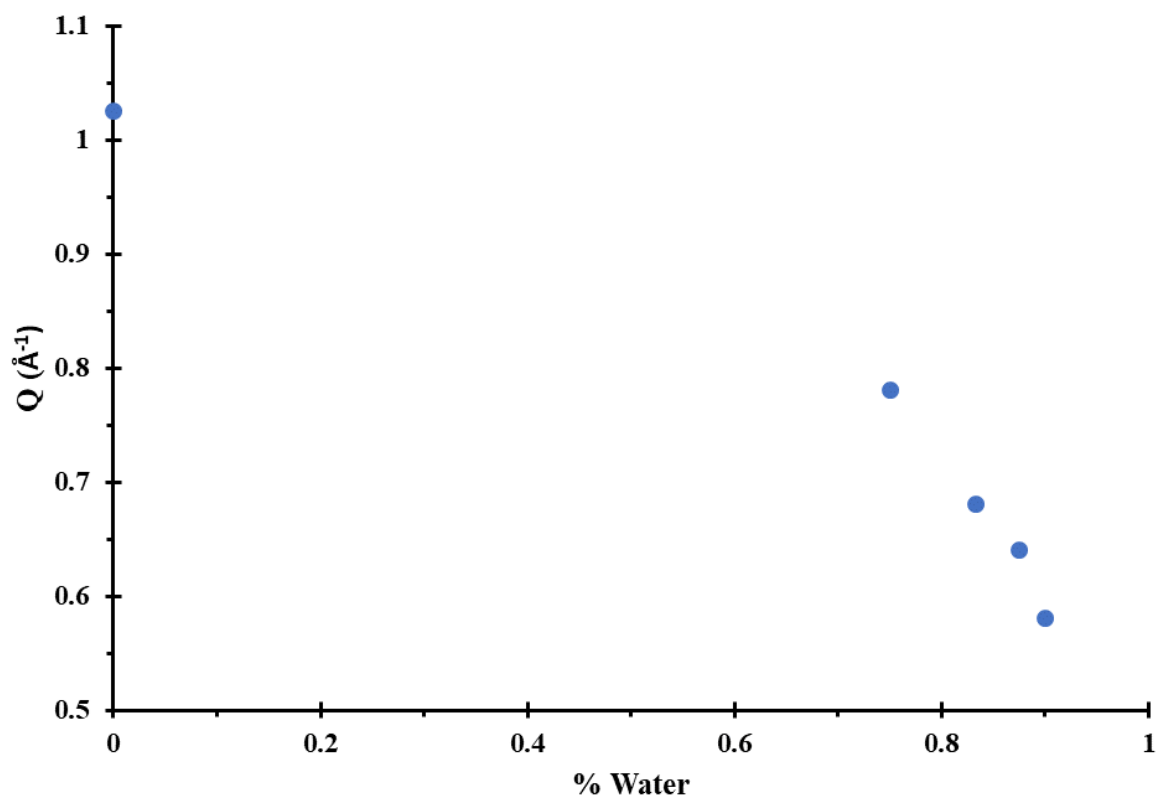


Figure 3.10 Position of the low-Q neutron diffraction peak as a function of percent water.

The neutron diffraction peak at 2.07 \AA^{-1} in the pattern for amorphous ZnCl_2 , shown in Figure 3.10, is observed to shift to a larger Q-value of $\sim 2.15 \text{\AA}^{-1}$ at a composition of $R = 3$. Upon dilution of the $R = 3$ hydrate, a shift to lower Q is observed. The reciprocal scattering

vector of this peak as a function of concentration is shown in Figure 3.12 in which a shift from 2.15 to 1.95 \AA^{-1} is observed when going from R = 3 to pure D₂O. Beginning at R = 3 the change in Q is very gradual with a slope of -0.44 (0.07). However, at the composition of R = 21 a dramatic change in the slope to a value of -2.7 (0.2) is observed.

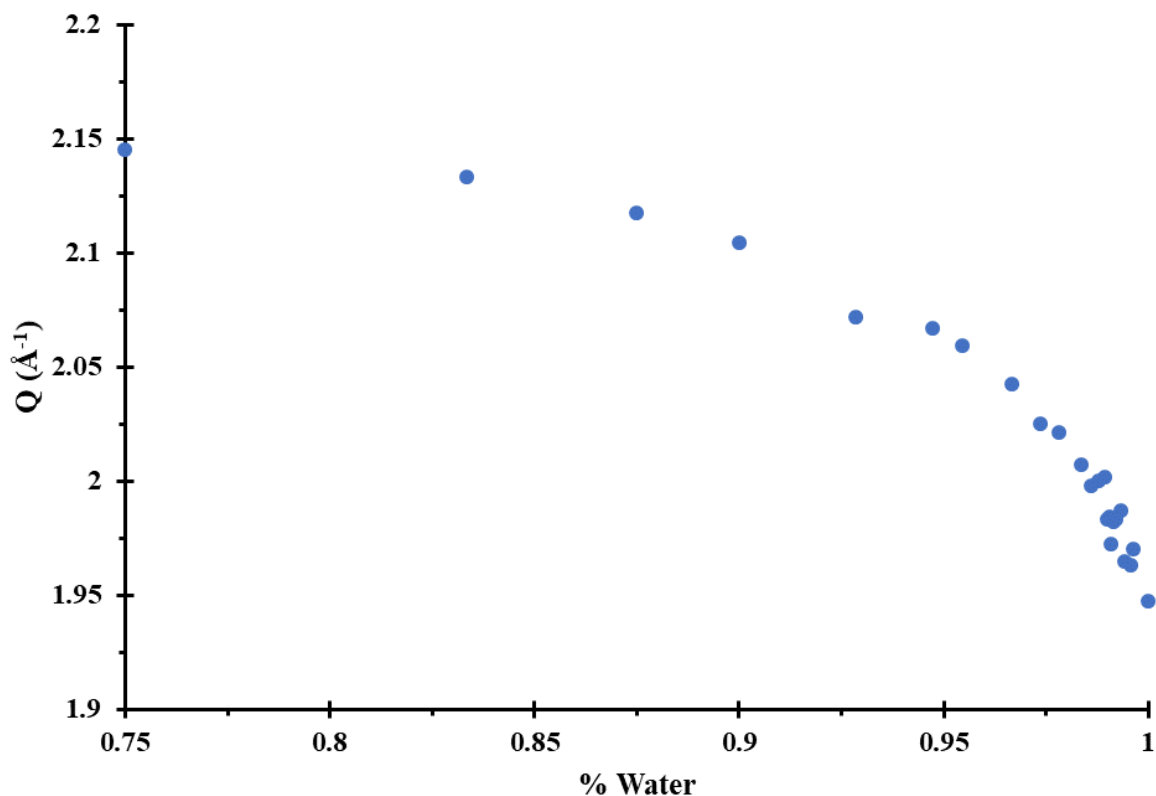


Figure 3.11 Shift in the neutron diffraction principal peak as a function of zinc chloride concentration.

3.3.3 Raman spectroscopy of the dilution series

Raman spectroscopy of aqueous zinc chloride solutions was obtained to investigate changes in the speciation of the molecular ions upon dilution. As reported in Chapter 2 and reference 33, symmetric stretching modes of the ZnCl_4^{2-} and $\text{Zn}(\text{H}_2\text{O})_6^{2+}$ complexes are observed for the R = 3 hydrate at 286 and 390 cm^{-1} , respectively. Other literature reports concur that the ZnCl_4^{2-} molecular anion exists in concentrated solutions, $6 < R < 26$, as well as in the presence of excess chloride.^{76,77} Some reports suggested the existence of polymeric aggregates in highly

concentrated solutions, $R < 6$,³⁰ although solution of the crystal structure of $[\text{Zn}(\text{OH}_2)_6][\text{ZnCl}_4]$ and subsequent demonstration that ionic liquid structure persists into the melt provides evidence that polymeric structures do not exist in $R \geq 3$ solutions.³³ In more dilute solutions, $R > 8$, the measured spectra were interpreted to be the result of complex, mixed-ligand species including the tetrahedral $[\text{ZnCl}_n(\text{OH}_2)_{4-n}]^{2-n}$ ($n = 1-4$) and octahedral $[\text{ZnCl}_n(\text{OH}_2)_{6-n}]^{2-n}$ ($n = 0-4$).^{27,48} Raman studies of the hydration of Zn^{2+} in the presence of non-coordinating nitrate and perchlorate anions identify the complex cation $\text{Zn}(\text{H}_2\text{O})_6^{2+}$ at $\sim 390 \text{ cm}^{-1}$.^{78,57} In light of our recent discovery of the ionic liquid nature of the $R = 3$ zinc chloride hydrate, which demonstrates the segregation of zinc into two distinct molecular ions, $\text{Zn}(\text{H}_2\text{O})_6^{2+}$ and ZnCl_4^{2-} , an in depth set of Raman measurements was obtained to investigate their persistence upon dilution.

Raman spectra were collected for three separate preparations of dilution series of aqueous zinc chloride solutions, two (D1 and D2) in the concentration range 3 (75% water) $\leq R \leq 250$ (99.6% water) and one (D3) across the concentration range $3 \leq R \leq 100$ (99.0% water). To ensure there is no aging effect on the hydrate solutions, a set of solutions with $R = 3, 9, 21,$ and 100 were prepared 2, 24, 48 hours and immediately prior to Raman measurements. Samples of equivalent composition were observed to be identical within experimental error, irrespective of their time after mixing.

Representative Raman spectra from dilution series D1, $3 \leq R \leq 250$, plus that of pure water are shown in Figure 3.12. The major features of the spectra consist of a strong absorption at approximately 290 cm^{-1} , and weaker peaks at about 390 and 1640 cm^{-1} . The former two diminish in intensity with increasing dilution. Superimposed on the Raman absorption spectra is a strong, broad luminescence, increasingly dominant at higher wave number, and significant Rayleigh scattering that is most significant between 200 cm^{-1} and the low wavenumber

instrumental limit. The luminescence and Rayleigh scattering also substantially diminish with increasing sample dilution. Lower intensity broad features at around 1100 cm^{-1} , 800 cm^{-1} and below 500 cm^{-1} , characteristic absorptions of the water network, become more apparent at compositions $21 \leq R$.

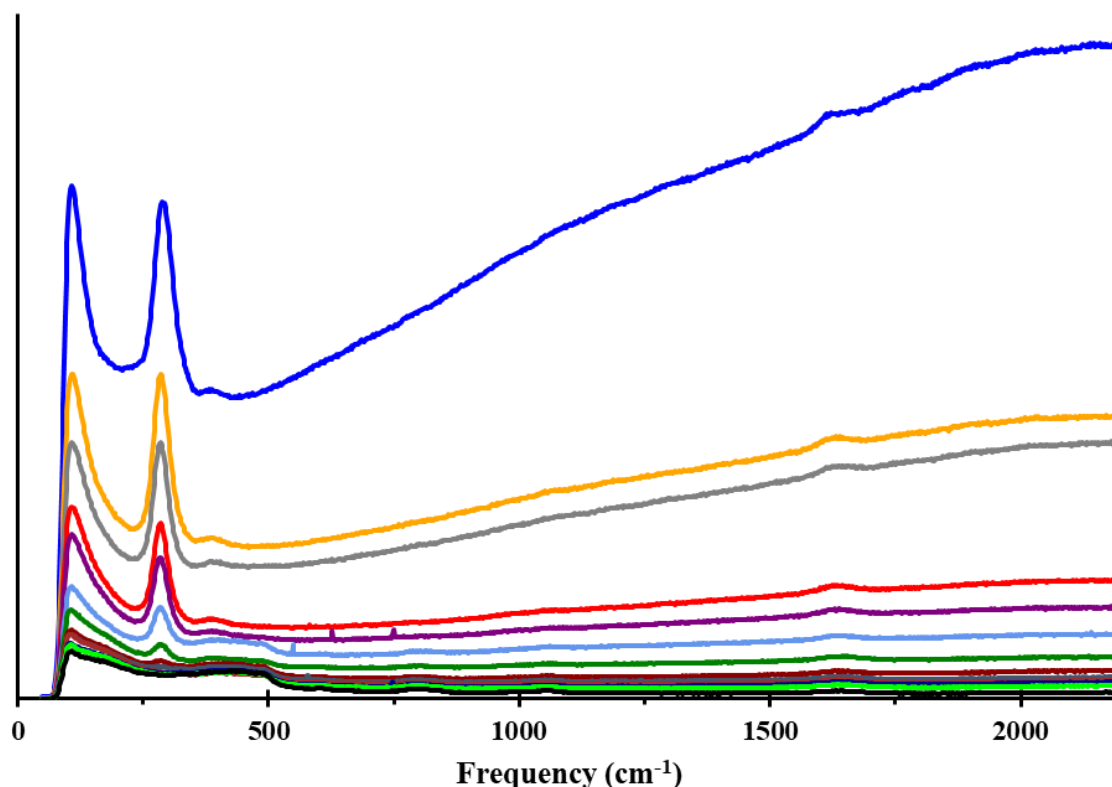


Figure 3.12 Raman spectra of the zinc chloride hydrates for dilution series D1 R = 3 (blue), R = 6 (orange), R = 9 (gray), R = 12 (red), R = 15 (purple), R = 21 (light blue), R = 40 (green), R = 60 (dark red), R = 80 (blue-gray), R = 100 (brown), R = 175 (dark blue), R = 250 (light green), and pure H₂O (black).

To extract greater detail on complex ion speciation from these Raman spectra, singular value decomposition (SVD) was applied to each of the three dilution series. Methods for SVD analysis have been previously described.^{79,80} The Raman spectra were aggregated into an $\mathbf{m} \times \mathbf{n}$ data matrix \mathbf{A} , where \mathbf{m} is the number of frequency values in each spectrum and \mathbf{n} is the number of

spectra collected (i.e., concentrations). These concentration-dependent data were deconvoluted into two sets of orthonormal basis functions according to Equation 3.1

$$\mathbf{A} = \mathbf{U}\mathbf{\Sigma}\mathbf{V}^T \quad (3.1)$$

where the left singular matrix \mathbf{U} corresponds to the concentration-independent basis vectors (i.e., components of the total data), the right singular matrix \mathbf{V}^T corresponds to their concentration dependence and $\mathbf{\Sigma}$ is composed of singular values (i.e., weighting factors) that describe the contribution of the corresponding singular vectors and are sorted in decreasing magnitude. The first two components, \mathbf{u}_1 and \mathbf{u}_2 , respectively represent 85% and 10% of the original \mathbf{A} matrix. The third component represents 1.5-3.5% of the data, depending on the dilution series, and may correlate with concentration dependent shifts in the spectra, while the remaining 2-3% of the data is spread across 20 and 15 additional basis for vectors (D1 and D2) and (D3), respectively, that have no apparent physical interpretation (i.e. noise). Given that all columns of the \mathbf{U} and \mathbf{V} matrices are orthogonal, modified basis vectors can be obtained by taking a linear combination of the original basis vectors, for example rotation by the matrix shown in Equation 3.2

$$\begin{bmatrix} \mathbf{u}_1' \\ \mathbf{u}_2' \end{bmatrix} = \begin{bmatrix} \cos \theta & -\sin \theta \\ \sin \theta & \cos \theta \end{bmatrix} \begin{bmatrix} \mathbf{u}_1 \\ \mathbf{u}_2 \end{bmatrix} \quad (3.2)$$

where θ is the angle over which the original basis vectors are rotated. Rotation was performed to optimize separation of spectral features corresponding the concentrated and dilute aqueous zinc chloride solutions in the primary basis vectors \mathbf{u}_1 and \mathbf{u}_2 . Datasets from dilution series D1, D2 and D3, evaluated independently, require rotations of $\theta = 7.1^\circ$, 10.7° and 17.9° , respectively. The first two modified basis vectors of the \mathbf{U} matrix, \mathbf{u}_1' and \mathbf{u}_2' , are shown in Figures 3.13a and 3.13b for each of the three data series. To maintain consistency between the \mathbf{U} and \mathbf{V} matrices, the basis vectors \mathbf{v}_1 and \mathbf{v}_2 were also rotated by angle θ , resulting in the modified basis vectors

\mathbf{v}_1' and \mathbf{v}_2' . The latter correspond to the respective loadings of components \mathbf{u}_1' and \mathbf{u}_2' , respectively, and are shown in Figures 3.13c and 3.13d.

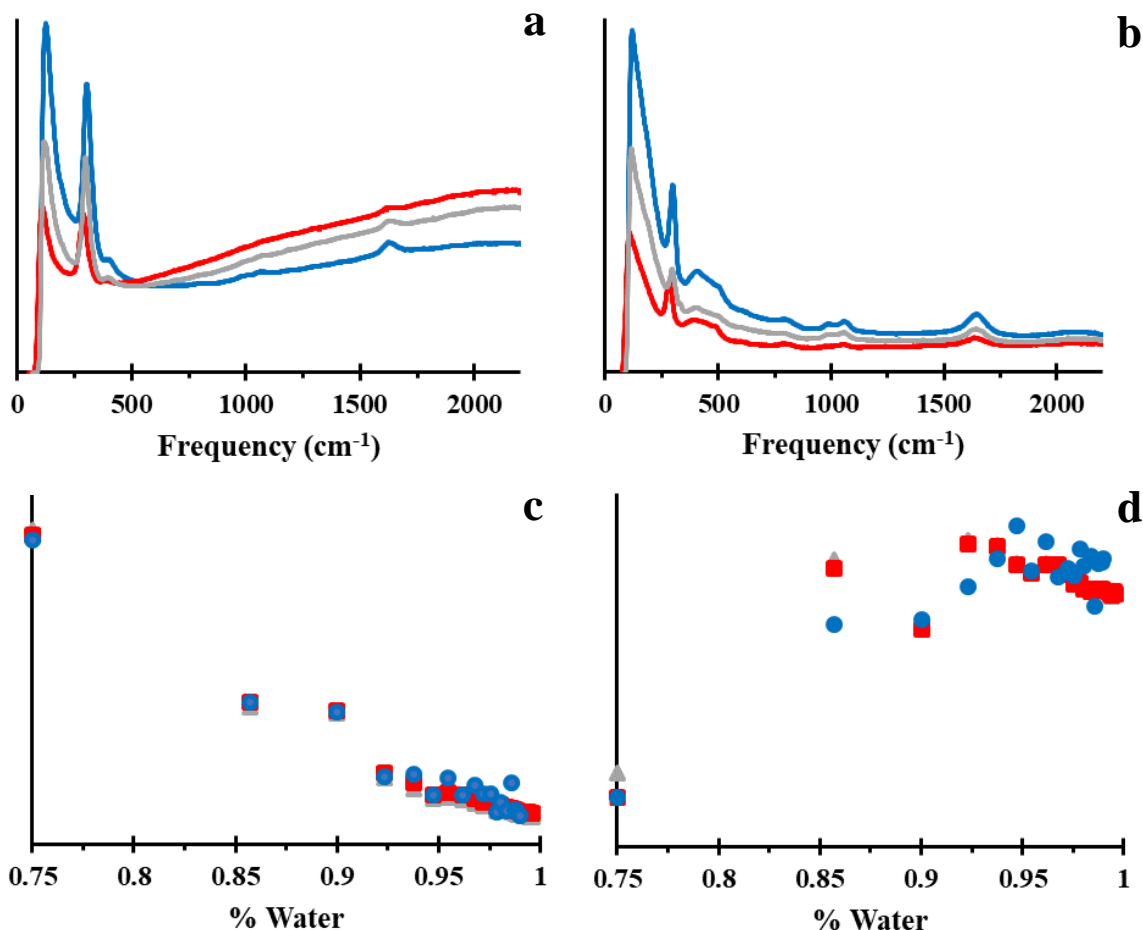


Figure 3.13 Rotated SVD basis vectors of (a) \mathbf{u}_1' , (b) \mathbf{u}_2' , (c) \mathbf{v}_1' , and (d) \mathbf{v}_2' . Dilution series are represented as D1 (red), D2 (gray) and D3 (blue).

The $R = 3$ spectrum, observed in Figure 3.12, is dominated by the a_1 and a_{1g} symmetric stretching modes of ZnCl_4^{2-} and $\text{Zn}(\text{H}_2\text{O})_6^{2+}$, respectively, occurring at 298 (5) and 377 (5) cm^{-1} . A strong background luminescence is also observed. Grossly, the \mathbf{u}_1' basis vector is very similar to the $R = 3$ spectrum, exhibiting primary peaks at 296 (5) and 391 (3) cm^{-1} , consistent with the symmetric stretches of the ZnCl_4^{2-} and $\text{Zn}(\text{OH}_2)_6^{2+}$, respectively. However, the much weaker Raman active modes of $e + 2t_2$ and $e_g + t_{2g}$ for tetrahedral ZnCl_4^{2-} and octahedral $\text{Zn}(\text{H}_2\text{O})_6^{2+}$,

respectively, are not apparent in the raw data or SVD analysis, largely overshadowed by the strong Rayleigh wing.^{52, 81} Their absence is consistent with other literature reports.⁵² Upon dilution the luminescence background decreases and the vibrational features of water, which include the bending mode at 1637 (1) cm^{-1} as well as libration modes at 437 (8), 794 (4), and 1058 (2) cm^{-1} , become more prominent, reflected as the primary features of the \mathbf{u}_2' basis vector. However, the \mathbf{u}_2' basis vector also includes a significant peak at 293 (5) cm^{-1} and smaller peak at 400 (5) cm^{-1} characteristic of the symmetric stretch for the ZnCl_4^{2-} and $\text{Zn}(\text{OH}_2)_6^{2+}$ complex ions, which are not observed in pure water, and are more dominant in the basis vector than is observed in the raw spectra of dilute solutions. The presence of these peaks in the \mathbf{u}_2' basis vector, at a slightly lower energy than the primary ZnCl_2^- peak and higher energy than the primary $\text{Zn}(\text{OH}_2)_6^{2+}$ peak in the \mathbf{u}_1' basis vector, is reflective of the energy shift of these absorptions due to the changing chemical environment upon dilution.

To evaluate the co-persistence of the ZnCl_4^{2-} and $\text{Zn}(\text{H}_2\text{O})_6^{2+}$ ions, as opposed to their possible dissociation into $\text{Zn}^{2+}_{\text{aq}}$ and Cl^-_{aq} ions, the relative intensities of the respective a_1 and a_{1g} modes are plotted as a function of concentration in Figure 3.14. The intensity of both peaks diminish commensurately as more water is added to the system. This is consistent with the fact that the primary absorption for these two ions is contained in the same component, \mathbf{u}_1' . Notably, while basis vector \mathbf{v}_1' diminishes and basis vector \mathbf{v}_2' generally increases with increasing dilution, the contribution of these two ions, and their respective energy shifts transform commensurately.

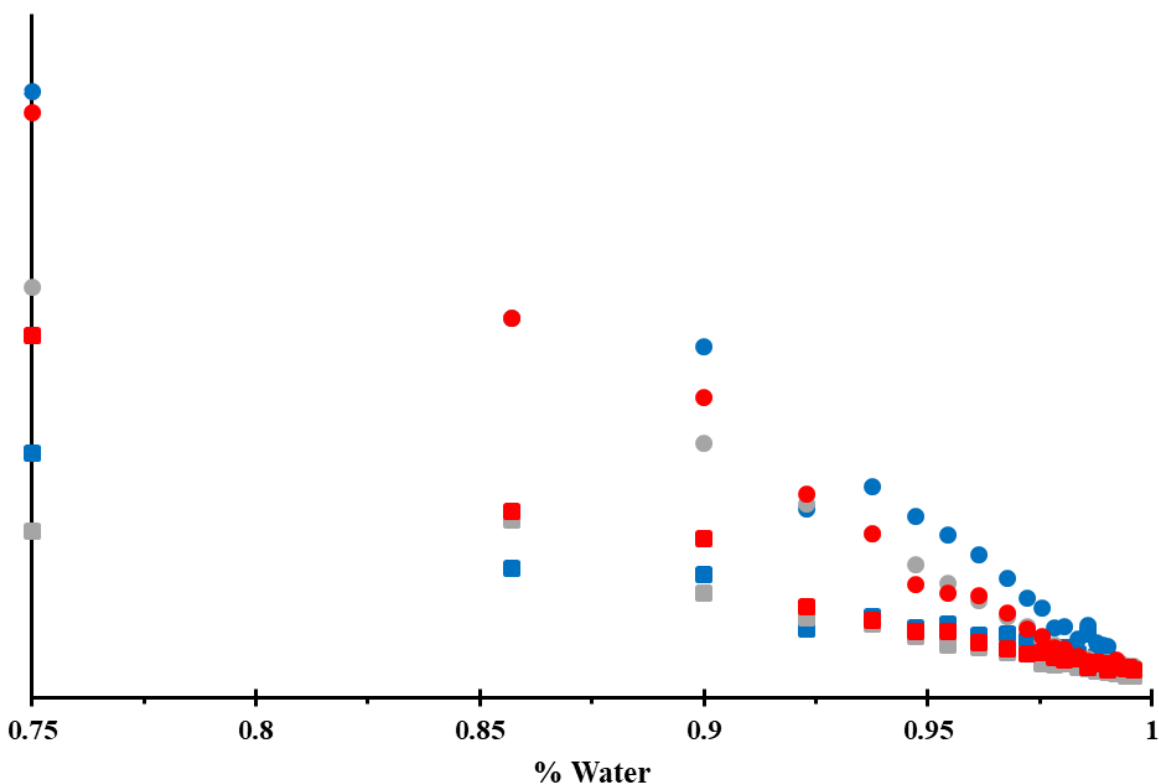


Figure 3.14 Peak intensities of the Raman peaks at 283 cm^{-1} (circles) and 400 cm^{-1} (squares) for aqueous zinc chloride as a function of percent water for the dilution series D1 (red), D2 (gray) and D3 (blue).

As reflected by the presence of absorption peaks for the ZnCl_4^{2-} and $\text{Zn}(\text{H}_2\text{O})_6^{2+}$ ions in both \mathbf{u}_1' and \mathbf{u}_2' basis vectors, there is a concentration dependence of energy of these absorptions. The shift to slightly higher energy of the weaker and broad $\text{Zn}(\text{H}_2\text{O})_6^{2+}$ symmetric stretch upon dilution cannot be cleanly resolved. However, there is a clearly discernable red-shift of the ZnCl_4^{2-} a_1 mode upon dilution. The peak frequency of the ZnCl_4^{2-} totally symmetric stretching mode as a function of concentration obtained through Gaussian fitting of the experimental data in the region from 200 to 300 cm^{-1} is plotted in Figure 3.15. While it is observed that the peak continually shifts to lower energy upon dilution, the largest shift of 4.3 (0.6) cm^{-1} occurs between the $R = 3$ and $R = 6$ compositions. Evidence of this energy shift also

appears in the \mathbf{u}_2' basis vector as the sharp peak occurring at 293 (4.6) cm^{-1} which matches closely with the experimental value of 294 (4.4) cm^{-1} found in the $R = 6$ composition.

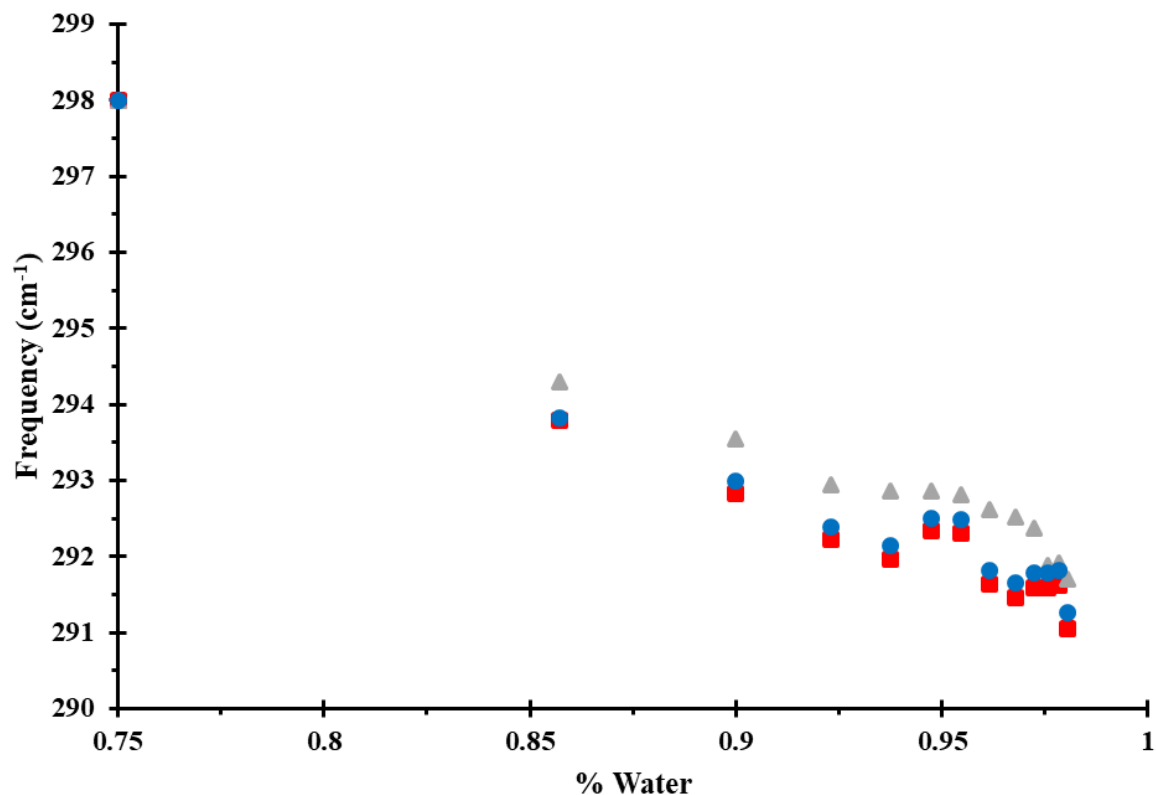


Figure 3.15 Frequency of the ZnCl_4^{2-} totally symmetric stretching mode as a function of concentration for dilution series D1 (red), D2 (gray) and D3 (blue).

3.4 Discussion

3.4.1 DSC and phase change behavior

The DSC and crystallization diffraction data reported here clarify the phase characteristics of the zinc chloride: water system. Using the carefully purified ZnCl_2 as the starting material, the actual phase behavior is demonstrated to be less complex than implied by the original Mylius and Dietz phase diagram²⁸, or by the reports of $R = 2.5$ and 4.5 crystallin hydrates.³² The existence of a crystalline phase at a eutectic composition, which would be the case for an $R = 2.5$ hydrate, is not thermodynamically possible. Similarly, there is no evidence

for peritectic, let alone eutectic behavior consistent with an $R = 4.5$ crystalline hydrate. Thus, we must conclude those crystalline hydrate structures, as well as the greater complexity of the first reported phase diagram are the result of additional impurities, likely hydroxyls, in the ZnCl_2 starting materials. While the zinc chloride: water phase diagram is less complex with respect to crystalline hydrates than initially reported, this investigation of the phase transitions, as well as diffraction studies of the liquid structure suggest that the liquid hydrate structure in this system is significantly more complex than traditional models for salt solutions.

Crystallization of a pure phase material occurs when the lattice energy gained from the phase change outweighs the decrease in entropy due to the organization of the system, yielding an overall negative Gibbs free energy associated with the process.⁸²⁻⁸³ This occurs in the $R = 3$ hydrate because of the approximate “spherical” shape and compatible radius ratios of the $\text{Zn}(\text{H}_2\text{O})_6^{2+}$ and ZnCl_4^{2-} ions, which allows them to pack into a pseudo-cubic arrangement, as reported in Chapter 2 and reference 33. The congruently melting behavior of the $R = 3$ phase is observed in the DSC data, shown in Figure 3.2, as a single, sharp melting peak.

However, at compositions off that of the congruently melting crystalline phase, for example an $R = 3.5$ composition, the trihydrate will be observed to crystallize out of solution beginning when the temperature drops below the liquidus line and continuing until the eutectic temperature is reached. In a binary system, such as the $\text{ZnCl}_2:\text{H}_2\text{O}$ system, this process requires phase segregation into the pure phase which crystallizes, and a solution of variable composition depending on the extent of crystallization. For this to occur, not only must the lattice energy of the $R = 3$ hydrate overcome the entropy associated with crystallization, as in a pure phase, but must also overcome a term associated with the intermolecular interactions between itself and the excess water. The process of overcoming this association is what we denote here as “solvent

exclusion". Presumably, the degree to which solvent exclusion can occur in aqueous solutions is heavily influenced by the magnitude of interaction between "free" water molecules compared with the interaction between "free" water and water that is coordinated to the dissolved ions as part of its hydration shells. The process of solvent exclusion can be expected to slow the process of crystallization, as observed in the DSC measurements in Figures 3.3 and 3.4. There, the extent of crystallization of the off stoichiometry compositions, $3 < R < 4$ and $1.5 < R < 3$, is significantly reduced during cooling, with substantial glass formation observed instead. Complete crystallization, however, is observed upon heating the glass, also known as "cold crystallization". These data indicate that the crystallization process, including crystallization of the pure $R = 3$ phase and solvent exclusion, results in a crystallization rate that is slower than the instrumental cooling rate, in contrast to that observed for crystallization of the pure phase, shown in Figure 3.2.

Furthermore, as shown in Figures 3.3 and 3.4, there must be a substantial concentration dependence to the nucleation probability of the $R = 3$ crystalline hydrate. In the $R < 3$ compositions, nucleation is only observed on cooling for the $R = 2.8$ composition; the closest to stoichiometric composition. For that sample, Figure 3.3c, nucleation is observed upon cooling for the first cycle, likely due to heterogeneities in the sample, but no nucleation is observed on cooling for the second heat-cool cycle. The third and fourth cycles then exhibit increasing extents of nucleation upon cooling, suggestive of a sample memory effect by which after each crystallization/melt cycle, the melt solution was not fully homogenized such that the solvent exclusion barrier to crystallization is minimized in the later cycles. A similar effect is observed in the $R > 3$ compositions shown in Figure 3.4b-c for which nucleation is observed at higher temperatures, i.e. sooner in the cooling cycles, for subsequent cycles. The facilitated nucleation

in subsequent cycles again may be indicative of the formation of domains of a crystal-like structural memory in the melt that facilitates nucleation, which become more significant with each cycle. Interestingly, Figure 3.4a, the composition closest to the pure phase composition, exhibits the inverse trend with respect to crystal nucleation, possibly a result of annealing out heterogeneous nucleation sites with each subsequent cycle.

Together, the concentration dependence of the crystallization and nucleation rates, as well as the distinct crystallization behavior as a function of crystallization cycle suggest that the liquid/melt itself is more highly structured than conventional perceptions of salt solutions. Specifically, these data suggest that structural ordering in the melt can facilitate crystallization, while strong solute-solvent interactions hinder the phase segregation necessary for crystallization.

The impact of solution structure on crystallization, or inhibition thereof becomes even more clear for compositions in the region of $4 < R < 10$, where no hot- or cold-crystallization is observed, even when cycled to $-80\text{ }^{\circ}\text{C}$, as confirmed by DSC and low temperature neutron diffraction (Figures 3.5 and 3.6), as well as by variable temperature X-ray diffraction measurements. This behavior, while curious, is not completely unprecedented, for example, it has been reported that fructose cannot be crystallized from its aqueous solutions⁸⁴ and that, for a binary water-sucrose system, no eutectic mixtures can be crystallized within the time scale of DSC experiments.⁸⁵ Additionally, it has been shown that for aqueous salt solutions, compositions near the eutectic region are particularly prone to supercooling, and crystallization is found to be difficult.^{29, 86-87} Frequently, for divalent metal chloride salts glass formation is most readily observed in the region of $R \sim 17-20$ waters.²⁹ It is suggested that such glass formation in aqueous salt solutions is a result of the glass being the thermodynamically stable

state near the eutectic temperature.^{84, 86} In aqueous zinc chloride, Mylius and Dietz claimed to have observed an 83.5 mole % solution to become highly viscous at 0 °C and form a glass at -70 °C; additionally, crystallization was never achieved for this composition.²⁸ Investigations of glass transitions in aqueous zinc chloride solutions have found that glass formation occurs in the compositional region from $2 < R < 17$ ²⁹ and that the $8 < R < 13$ region is most prone to glass formation.³⁸

To explain the anomalous behavior of aqueous ZnCl_2 which exhibits glass formation over the largest compositional region of salt hydrates, it has been suggested that structural organization into polymeric units with bridging Cl^- and/or water ligation is responsible for preventing crystallization.³⁸ However, our demonstration of the existence of the pure crystalline phase at $R = 3$, consisting of $[\text{Zn}(\text{H}_2\text{O})_6][\text{ZnCl}_4]$, and the persistence of this structure above the melt as an ionic liquid, contradicts the polymeric interpretation.³³ Furthermore, as demonstrated by the Raman spectroscopy, Figure 3.12, and SVD analysis, Figures 3.13 and 3.14, the persistence of the ZnCl_4^{2-} anion to high levels of dilution is also inconsistent with a polymeric argument. Nevertheless, the inability of ice or the $R = 3$ hydrate to phase segregate in the $4 < R < 10$ region suggests that the strength of the intermolecular interactions between water and the zinc chloride hydrate system are greater than the energy gained by crystallization of either ice or the pure $R = 3$ hydrate, depending on which side of the eutectic is being observed.

As described below in the evaluation of the liquid structure, and most clearly defined by spectroscopic methods in Chapters 4 and 5, a complete second hydration shell is formed around the zinc cation at the $R = 9$ composition, resulting in the ionic liquid structure $[\text{Zn}(\text{H}_2\text{O})_6(\text{H}_2\text{O})_{12}][\text{ZnCl}_4]$. Notably, this second-shell ionic liquid composition is close to the edge of the non-crystallizing region, which had previously reported to be indicative of the total

hydration number in aqueous solutions.²⁹ Up to twelve water molecules form the second-hydration-shell, strongly hydrogen bound to the six first-hydration-shell water molecules that are directly bound to the zinc cation. While the organization of these second-shell water molecules is not ordered sufficiently to form a unique crystalline hydrate, these intra-hydrate water-water interactions are too strong to readily phase segregate as is required to crystallize either the $R = 3$ hydrate or ice. Thus, this primary glass forming composition region, $4 < R < 10$, appears to be a result of a pseudo-eutectic between the non-crystallizing $R = 9$ ionic liquid and the $R = 3$ crystalline hydrate. Between about $4 < R < 5$, the $R = 3$ phase cannot phase segregate and crystallize, and between about $5 < R \leq 9$ pure water cannot phase segregate to crystallize ice. This is consistent with reports that the interaction between 1st and 2nd shell water for the zinc ion are stronger than those in pure water.⁸⁸ It has also been reported that trivalent cations disrupt the water structure at concentrations as low as 3 mol % salt ($R = 32$),⁸⁴ which hinders ice crystallization given that the fast crystallization of ice is related to the “ice-like” network of water in the liquid state.⁸⁹⁻⁹⁰ In the zinc chloride hydrate system, addition of water beyond the $R > 9$ begins to form a third molecular shell around Zn^{2+} cation. Apparently, interactions between these third-shell water molecules is similar enough to interactions in pure water that, upon cooling, crystalline ice can be observed for $R \geq 10$. Additionally, the observation of ice in this region confirms that there are no other pure hydrate phases between the $R = 3$ and pure water.

3.4.2 Local order of the dilution series

While examination of the zinc chloride: water system using pure $ZnCl_2$ demonstrated that the crystalline hydrate portion of the phase diagram is significantly less complex than that initially reported by Mylius and Dietz²⁸, investigation of the liquid structure, by contrast, demonstrates significantly greater complexity than previously reported. The results of both

synchrotron X-ray (Figure 3.7) and neutron (Figure 3.8) scattering of aqueous zinc chloride solutions demonstrate considerable structural variation across the dilution series $1.7 < R < 250$. As most clearly identified by the position of the lowest-Q peak in the X-ray structure factor plot, Figure 3.9a, the evolution of structure in this dilution series is distinctly non monotonic. Rather, breaks in relatively linear trends in the structural evolution are observed at $R = 3$ (75% water), $R = 9$ (90% water) and $R = 21$ (95% water). These steps in the dilution series imply the existence of special compositions, likely corresponding to specific compound formation, potentially related to the formation of azeotropes. To further investigate the composition dependent liquid structure of this molten salt hydrate system, the inverse Fourier transform of the structure factor data, which yields the pair distribution functions (PDFs) were evaluated. X-ray and neutron diffraction PDF data for selected compositions are plotted in Figures 3.16 and 3.17, respectively.

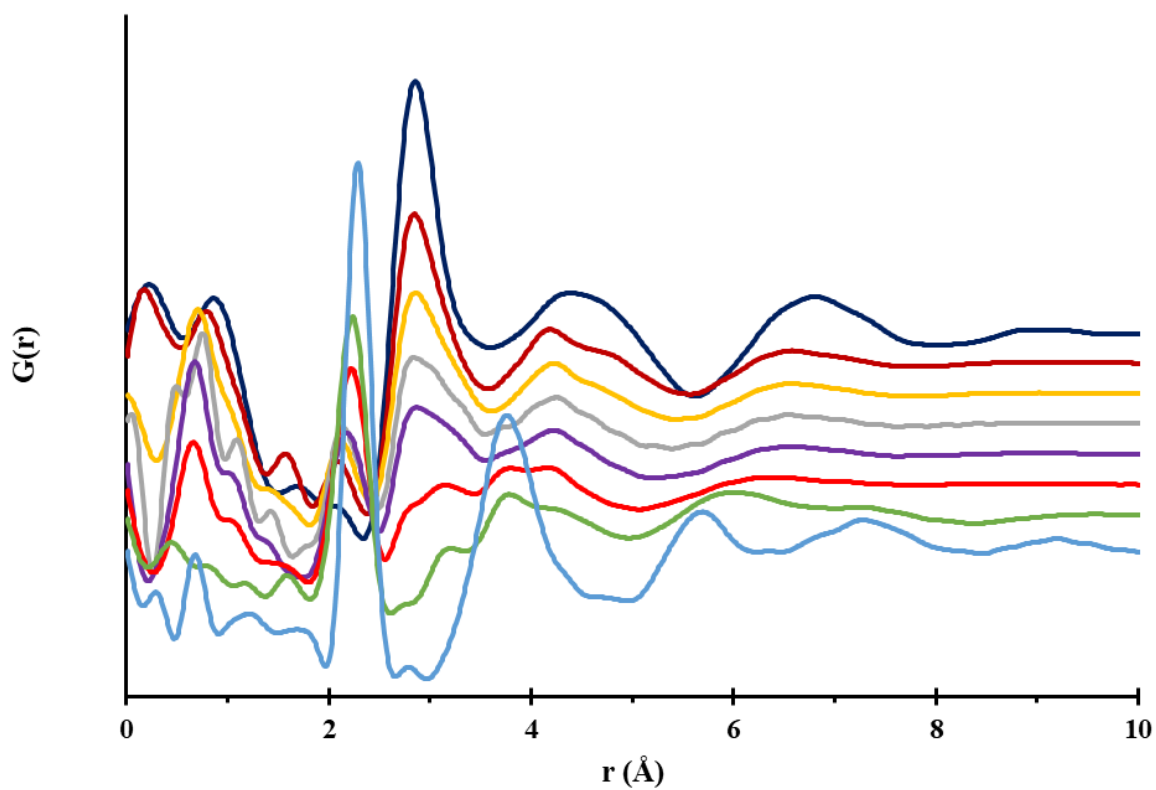


Figure 3.16 X-ray diffraction PDFs for molten anhydrous ZnCl_2 at 320°C (blue) as well as room temperature aqueous zinc chloride solutions of concentration $R = 2.9$ (green), $R = 9$ (red), $R = 21$ (purple), $R = 30$ (gray), $R = 50$ (orange), $R = 100$ (dark red) and pure H_2O (dark blue).

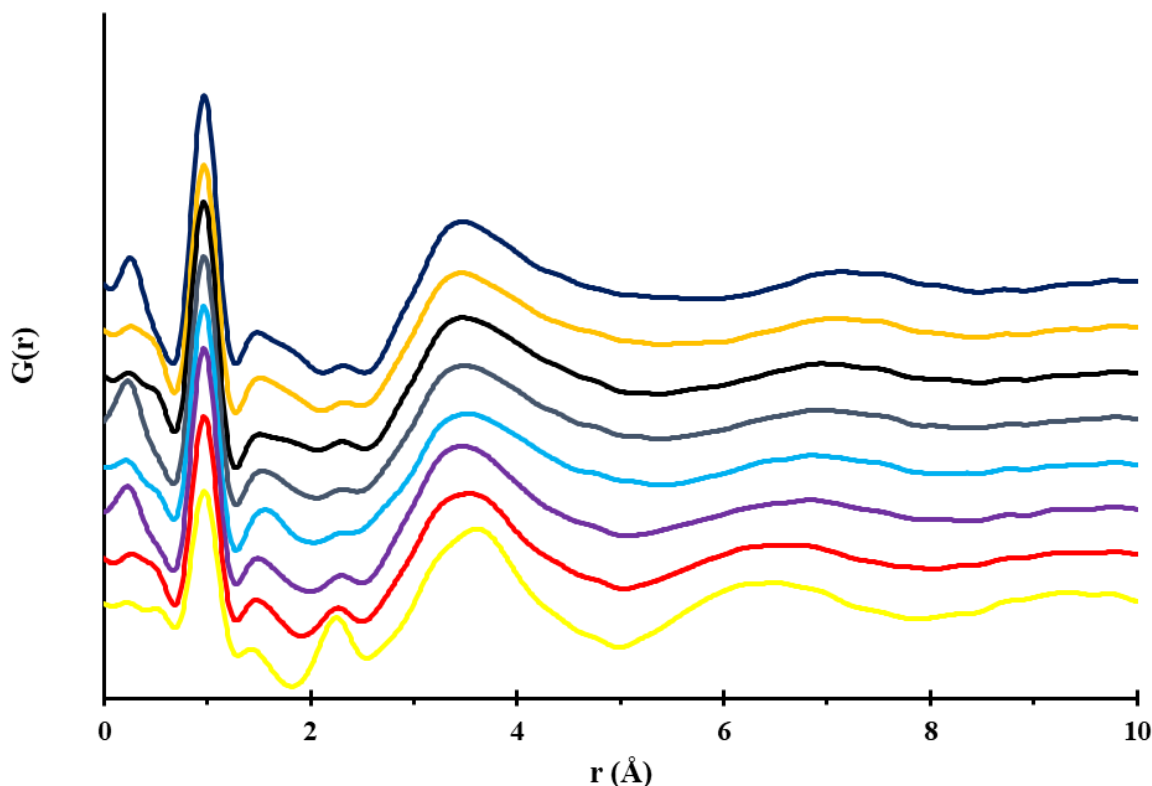


Figure 3.17 Neutron diffraction PDFs for room temperature aqueous zinc chloride solutions of composition $R = 3$ (yellow), $R = 9$ (red), $R = 21$ (purple), $R = 45$ (light blue), $R = 93$ (blue-gray), $R = 150$ (black), $R = 275$ (gold) and pure D_2O (dark blue).

The most clearly identified features of the neutron diffraction PDF include the intramolecular pair correlations of water observed at 0.95 \AA (O-D) and 1.5 \AA (D-D). A new pair correlation at 1.8 \AA , observed as a shoulder on the D-D peak, grows in intensity with increasing dilution, which corresponds to O-D hydrogen bonding. As was reported in Chapter 2 and reference 33, the crystal structure of the $R = 3$ hydrate exhibits two unique zinc environments corresponding to the $Zn(H_2O)_6^{2+}$ and $ZnCl_4^{2-}$ molecular ions, which persist into the melt. The corresponding Zn-O and Zn-Cl pair correlations for these ions appear as a single combination peak at 2.24 \AA in the PDF of both the neutron and X-ray data. This distance reasonably corresponds to the weighted average of four Zn-Cl distances of 2.3 \AA and six Zn-O distances of 2.2 \AA , albeit which is larger than the crystallographically determined distances of Zn-Cl = $2.24 -$

2.29 Å and Zn-O distances of 2.04 – 2.10 Å as might be expected. Pair correlations corresponding to intramolecular Cl-Cl distances of the ZnCl_4^{2-} ion, observed as an intense peak in the X-ray PDF of molten ZnCl_2 at 3.8 Å, which clearly persist in the PDFs of the R = 3 and R = 9 solutions. At dilutions of $R \geq 21$ the Cl-Cl pair correlation can no-longer be uniquely identified, but likely accounts for the low-r shoulder on the O-O pair correlation also seen in pure water. The equatorial O-O pair correlation at 3.2 Å of the $\text{Zn}(\text{H}_2\text{O})_6^{2+}$, previously suggested to be evidence of polymeric structures,²⁷ is readily identified in the X-ray PDFs of $R \leq 9$. Upon further dilution this peak is observed as a shoulder on the strong intermolecular water O-O pair correlation at 2.8 Å. The intramolecular Cl-Cl and O-O and intermolecular O-O pair correlations are more clearly observed in the X-ray PDF while being masked in the neutron PDF by a broad peak, 2.5 – 4.5 Å, resulting from multiple D-D, D-O and D-Cl correlations.^{33, 91}

A more detailed evaluation of certain pair correlations is warranted in order to decipher the structural origin of the steps noted above for certain diffraction signatures, most evident in Figure 3.9. The peak at 2.24 Å corresponding to both Zn-Cl and Zn-O pair correlations in the PDF of the R = 3 composition is observed to persist in both the neutron and X-ray diffraction patterns to the highest extents of dilution measured (up to R = 250). Notably, however, this peak exhibits distinct concentration dependence for X-ray vs. neutron PDFs, as shown in Figure 3.18. In the X-ray PDFs position of this peak is relatively invariant until $R > 12$ (92% water), after which the peak maximum shifts to smaller r-value. At the same time this peak significantly diminishes in intensity and adopts a more asymmetric shape, somewhat broadened in the larger-r direction. Notably, a diminished peak, possibly corresponding to a H-H pair correlation is present in the PDF of pure water. The corresponding pair correlation in the neutron PDF appears to shift to slightly larger-r upon dilution while diminishing in intensity between 3 (75% water) >

$R > 45$ (98% water). Then for $R > 45$, the intensity of this peak seems to increase slightly, while growing toward the minor peak at 2.34 Å in pure water that Soper et al. has assigned to be an intermolecular D-D correlation.⁹¹

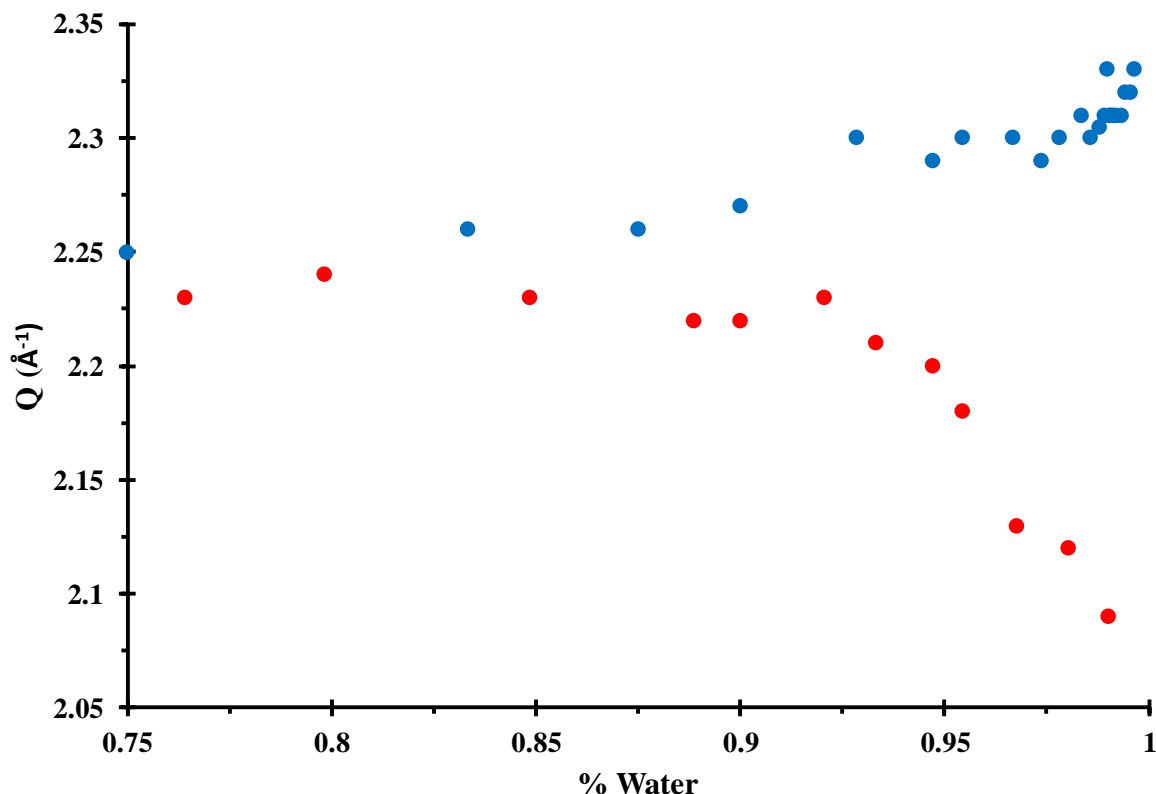


Figure 3.18 Concentration dependent shift in the combination peak corresponding to the Zn-O/Zn-Cl pair correlations of the ZnCl_4^{2-} and $\text{Zn}(\text{H}_2\text{O})_6^{2+}$ ions observed from neutron (blue) and X-ray (red) diffraction.

These data must be understood in the context of the corresponding Raman spectroscopy. Figure 3.14 demonstrates that both the $\text{Zn}(\text{H}_2\text{O})_6^{2+}$ and ZnCl_4^{2-} molecular ions concurrently diminish in intensity upon dilution. Thus, the apparent decrease in this combination pair correlation distance cannot be interpreted to be a result of dissociation of the ZnCl_4^{2-} anion with corresponding increase in abundance of the $\text{Zn}(\text{H}_2\text{O})_6^{2+}$ cation. Rather, the increasing asymmetry of this peak may be a result of the combined peak slightly separating into distinct Zn-O and Zn-Cl peaks, along with an increasing contribution of the H-H correlation. Notably, the

Raman spectral peak corresponding to the symmetric stretch of the ZnCl_4^{2-} anion shifts toward lower energy with increasing dilution (Figure 3.15), which is consistent with the slight increase in what is likely the Zn-Cl pair correlation in the neutron PDF peak.

The intra-molecular ion PDF data is consistent with the Raman data supporting the persistence of $\text{Zn}(\text{H}_2\text{O})_6^{2+}$ and ZnCl_4^{2-} upon dilution. However, the longer distance correlations indicative of inter-molecular ion contacts must be examined to decipher potential intermediate range order originating from higher hydration shells. The neutron PDF O-D pair correlation at 1.5 Å is the shortest intermolecular contact, and is clearly observed in the neutron PDF of all hydrates and pure water. Absent from the concentrated solutions, however, is a distinct pair correlation around 1.8 Å ascribed to an inter-molecular O-D pair correlation. This O-D pair correlation may begin to be observed as a shoulder to the 1.5 Å D-D peak around $R = 9$, however it is not clearly identified as a separate pair correlation until the PDF of the $R = 150$ dilution. Similarly, the O-O inter-molecular pair correlation, observed in the X-ray PDF at approximately 2.8 Å, just to lower- r than the intra-molecular cis O-O pair correlation at 3.2 Å, is first significantly observed in the $R = 9$ solution. The maximum in this pair correlation shifts from about 2.79 Å in the $R = 9$ solution to about 2.83 Å in solutions $R \geq 21$. The $R = 21$ and 30 PDFs show this peak to be significantly broadened to larger- r . It then narrows to only a single pair correlation at 2.83 Å for pure water.⁹² The appearance of, and slight lengthening of this O-O pair correlation is consistent with reported molecular dynamics simulations which suggest that, for Zn^{2+} , the first to second hydration shell O-O ($\text{O}_I\text{-O}_{II}$) distance is approximately 3% shorter than those in pure water.⁶⁰

The evolution of the X-ray PDFs between 4-5 Å further exhibits significant structural change upon dilution. Pair correlations at 4.2 Å are suggested to correspond to the Zn-O_{II}

distance, where O_{II} are a set of 12 second hydration shell water molecules.^{93,94,58,95,96,97} Pair correlations around 4.5 Å are also observed for second nearest neighbor molecules in pure water.^{91, 98} There is clear enhancement of the 4.2 Å pair correlation between $R = 3$ and $R = 9$ in the X-ray PDFs. This peak sharpens and correlations at higher- r begin to grow in with the PDF of the $R = 21$ solution, becoming a distinct correlation at about 4.8 Å in the PDFs of the $R = 50$ and 100 solutions.

A hydration shell model of the zinc chloride hydrate solutions seems to emerge from the combined structure factor, Raman and PDF data. Based on the single crystal and liquid structure reported in Chapter 2, the $R = 3$ molten hydrate is clearly identified as the ionic liquid $[Zn(H_2O)_6][ZnCl_4]$. The Raman data provides convincing evidence that the $[ZnCl_4]^{2-}$ anion persists to the highest levels of dilution. Therefore, the total number of water molecules hydrating the remaining zinc cation is twice the value of the hydrate. Thus, at the hydration of $R = 9$, the next break point observed in the structural data, the stoichiometry is consistent with the formation of complete first and second hydration shells to yield a second ionic liquid $[Zn(H_2O)_6(H_2O)_{12}][ZnCl_4]$. The stability of this second-shell ionic liquid is further consistent with the glass forming ability of the $4 < R < 10$ hydrate compositions. A subsequent next break point in the dilution series appears to fall around the $R = 21$ composition, which would be consistent with a third-hydration shell ionic liquid, $[Zn(H_2O)_6(H_2O)_{12}(H_2O)_{24}][ZnCl_4]$. The structural data reported here are not sufficient to identify additional unique solution compositions. Nevertheless, the change in the signature of the D-D pair correlation in the neutron PDF (Figure 3.18) around the $R = 45$ composition is consistent with a fourth-shell ionic liquid, $[Zn(H_2O)_6(H_2O)_{12}(H_2O)_{24}(H_2O)_{48}][ZnCl_4]$. It seems beyond coincidence that the various breaks in structural feature trends in this dilution series occur at compositions that correspond to

the likely composition of complete hydration shells. It is not certain what extent of dilution establishes the outer limit of the influence of the hydrated zinc cation on the surrounding water. However, as clearly evident from both the X-ray and neutron PDF analysis, the zinc cations significantly perturb the structure of water at least to an $R = 100$ dilution.

3.4.3 Intermediate range order in the system

While the PDF gives information regarding the local order (i.e. primarily intra-molecular ion pair correlations), it is also important to examine the reciprocal space structure factor data for evidence of any intermediate range order in the system. Experimental and computational studies have proposed that the low angle diffraction peak(s) in the X-ray and neutron scattering of aqueous solutions indicate the existence of “quasi-lattice” type ordering in solution.^{69-70, 99} As was laid out in Chapter 2 and reference 33, the $R = 3$ liquid hydrate can be described using both CsCl- and LCCP- or perovskite-type packing motifs. Likewise, the more dilute species can also be described using idealized cubic models. The persistence of the ZnCl_4^{2-} ion upon dilution, as confirmed by PDF and Raman analysis, allows for a suitable packing ratio with Zn^{2+} containing multiple hydration shells; indications of which began to be observed in the X-ray PDF with the appearance of the 4.2 \AA Zn-O_{II} pair correlation. Here, we have modelled the $R = 9$ and $R = 21$ liquid structures. These compositions were chosen because by making the approximation that each additional hydration shell around the hydrated zinc ions have double the amount of water, as well as knowledge of experimental evidence that the ZnCl_4^{2-} do not interact strongly with waters, this would mean that there should be stable compositions at $R = 9$, $[\text{Zn}(\text{H}_2\text{O})_6(\text{H}_2\text{O})_{12}][\text{ZnCl}_4]$, and $R = 21$, $[\text{Zn}(\text{H}_2\text{O})_6(\text{H}_2\text{O})_{12}(\text{H}_2\text{O})_{24}][\text{ZnCl}_4]$. These completed hydration shell species can be approximated as spherical. This allows for the application of

packing motifs as in Chapter 2 and reference 33. In this case, the radius ratio can allow for either CsCl- or NaCl-type packing.

Shown in Figure 3.19 is the calculated X-ray and neutron diffraction patterns of idealized CsCl- and NaCl-type packing motifs of the $R = 9$ composition, adjusted to the experimental density of the liquid resulting in lattice parameters of CsCl- ($a = 8.72 \text{ \AA}$) and NaCl- ($a = 13.85 \text{ \AA}$). The complete second hydration shell was added by placing 12 water molecules in the vertices of the first shell water molecules. The placement of the second shell waters was chosen so each of the second shell waters would have two hydrogen-bonded contacts to the first shell. Figure 3.20 shows the calculated X-ray and neutron diffraction patterns of idealized CsCl- and NaCl-type packing motifs of the $R = 21$ composition, adjusted to the experimental density of the liquid resulting in lattice parameters of CsCl- ($a = 11.04 \text{ \AA}$) and NaCl- ($a = 17.52 \text{ \AA}$). The complete third hydration shell was added by placing 24 water molecules in the vertices of the second shell water molecules. This placement of the third shell waters was chosen so that each of the third shell waters would have two hydrogen bonded contacts to the second shell.

The low-Q diffraction peaks for the CsCl-type structure are observed to belong to the same scattering planes in both the $R = 9$ and $R = 21$ compositions. In the X-ray diffraction, the low-Q peak corresponds to the (110) indices containing mixtures of cations and anions. For the neutron diffraction, which emphasizes deuterium scattering, the low-Q peak corresponds to the (100) scattering planes. These planes contain the $\text{Zn}(\text{H}_2\text{O})_6(\text{H}_2\text{O})_{12}^{2+}$ and $\text{Zn}(\text{H}_2\text{O})_6(\text{H}_2\text{O})_{12}(\text{H}_2\text{O})_{24}^{2+}$ ions in the $R = 9$ and $R = 21$ structures, respectively. In each case, the planes contain multiple deuterium/hydrogen atoms from waters in the first and second hydration shells. The higher Q-value peak at approximately 2.0 \AA^{-1} corresponds to the (300) for $R = 9$ and (222) for $R = 21$. In both cases, these planes are observed to correspond to the height

of the octahedra and tetrahedra, as well as having scattering contributions from first and second shell waters.

For the NaCl-type structure in both the $R = 9$ and $R = 21$, there is an intense peak at $Q < 1 \text{ \AA}^{-1}$ with very little scattering intensity at higher Q -values. At the $R = 9$ composition, the (200) scattering plane containing a mixture of cations and anions is observed at 0.9 \AA^{-1} , which matches the low- Q peak of the X-ray liquid scattering data, but is larger than that observed for the corresponding neutron diffraction. In the $R = 21$ powder pattern, the low- Q intensity comes from the (100) scattering plane and also corresponds to planes of mixed cation and anion scattering. However, with a Q -value of approximately 0.35 \AA^{-1} , this peak is much lower than the low- Q peak observed in either the X-ray or neutron diffraction experimental data.

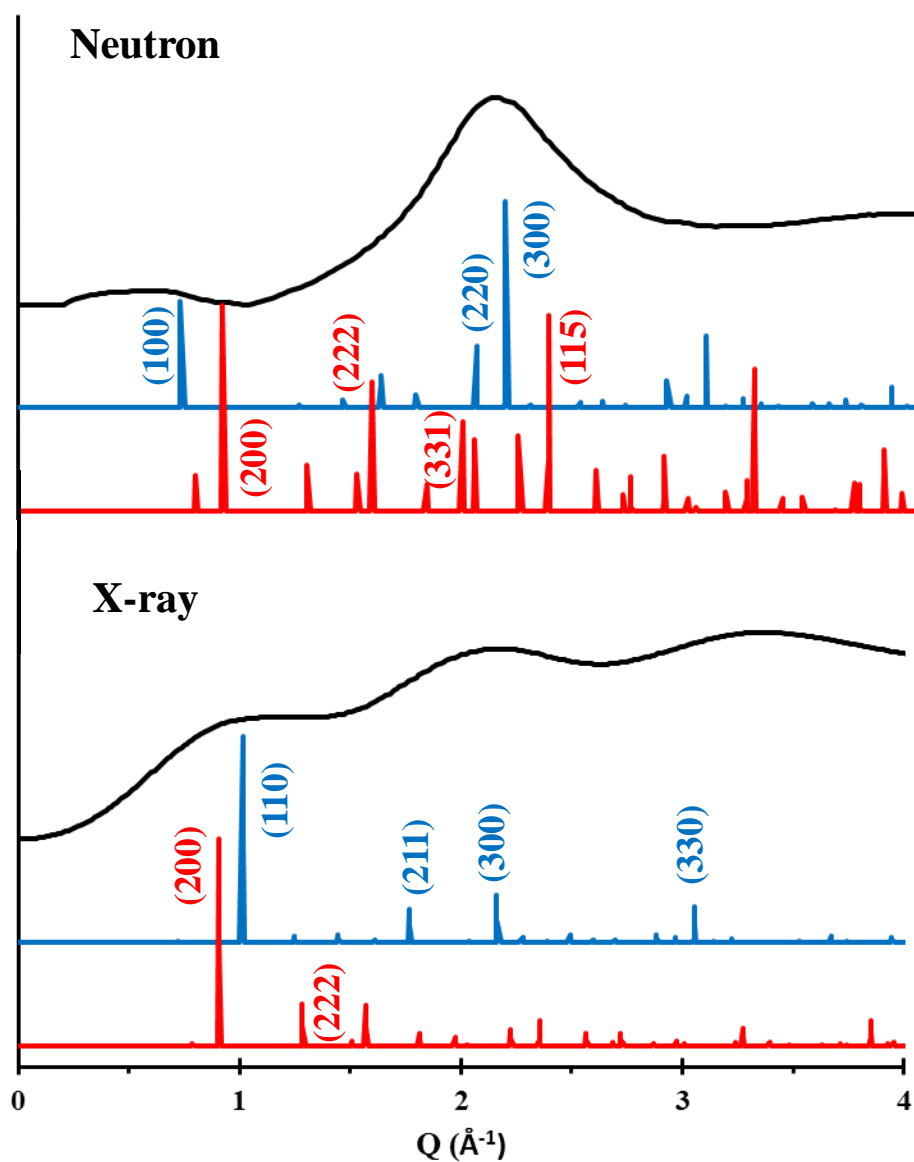


Figure 3.19 Experimental neutron and X-ray structure factor plots of the R = 9 aqueous zinc chloride (black) compared with the calculated powder diffraction patterns of the idealized CsCl- (blue) and NaCl-type (red) packing structures.

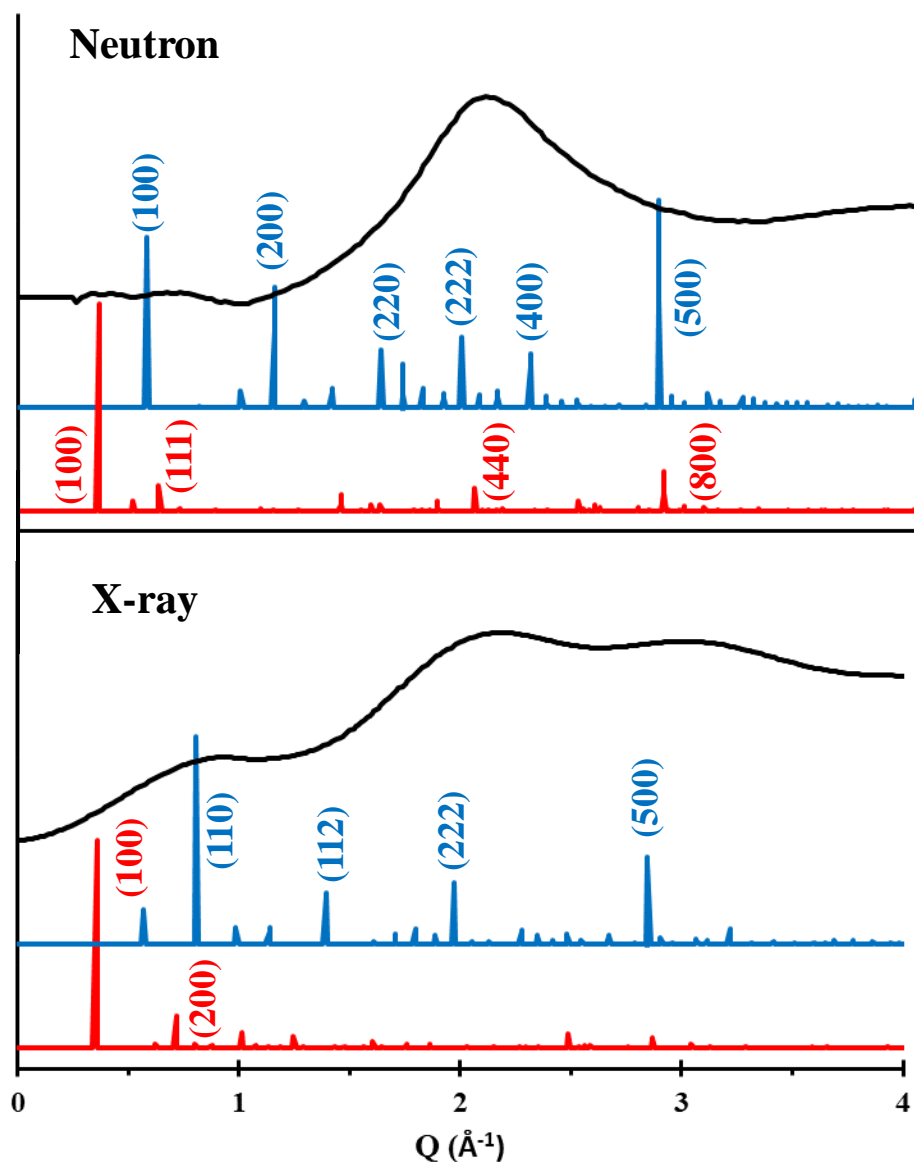


Figure 3.20 Experimental neutron and X-ray structure factor plots of the $R = 21$ aqueous zinc chloride (black) compared with the calculated powder diffraction patterns of the idealized CsCl- (blue) and NaCl-type (red) packing structures.

3.4.4 RMC modelling of the system

To further investigate the proposed CsCl- and NaCl-type structural models of the $R = 9$ solution, RMC modelling was utilized to fit the neutron scattering data. The calculated pair distribution functions and structure factors for the two structure types are given in Figures 3.21 and 3.22, respectively. Unit cells were constructed by taking the triclinic $R = 3$ unit cell,

expanding it to the experimentally measured density of the liquid $R = 9$ composition, and adjusting it to the cubic lattice parameters given above for the idealized cell models. A second hydration shell was then placed around the $\text{Zn}(\text{H}_2\text{O})_6^{2+}$ species. A simulation box was produced by using 64 of the $R = 9$ unit cells ($4 \times 4 \times 4$). An Excel macro was utilized to introduce disorder into the system by randomly rotating and translating each ion in the simulation box. Reverse Monte Carlo (RMC) modelling of the supercells was performed with intramolecular ion bond distances constrained to those of the above characterized $\text{Zn}(\text{D}_2\text{O})_6^{2+}$ and ZnCl_4^{2-} ions as well as the bond distances and angles of the water molecules.

The PDF of each of these simulations provides a remarkably good fit to the experimental PDF, as seen in Figure 3.21. While these simulated PDFs effectively replicate the local structure of the liquid, they do not provide sufficient detail to distinguish between the two idealized models.

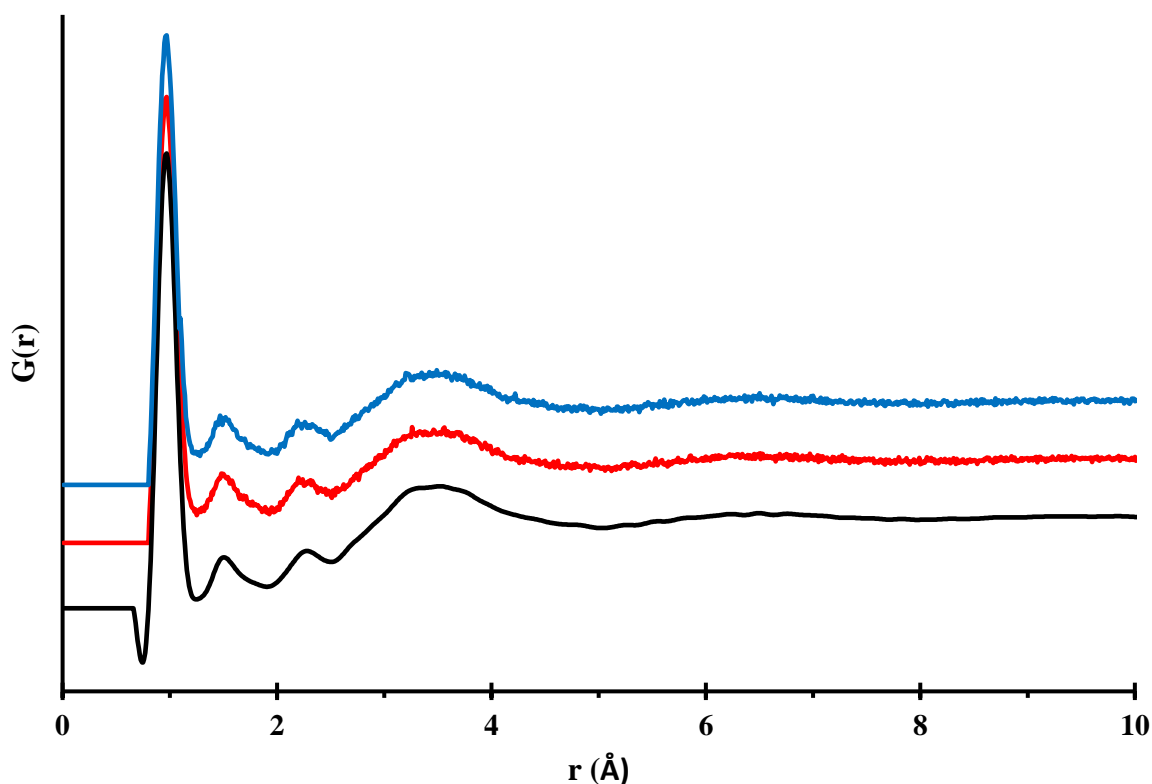


Figure 3.21 Pair distribution functions of the $R = 9$ zinc chloride solution obtained by neutron diffraction measurements (black) and RMC modelling of the idealized CsCl- (red) and NaCl-type (blue) supercells.

In the case of the $R = 9$ composition, the calculated structure factors, shown in Figure 3.21, also match the experimental data remarkably well with much more broadening than was observed for the modelling of the $R = 3$ composition in Chapter 2 and reference 33. The additional broadening here indicates a higher degree of disorder in the system, primarily due to the weaker constraints on the second-shell waters during the simulation. Additional disorder in the system likely results from the use of only neutron diffraction data in the simulation, which will result in a model more heavily weighted to the deuterium/water scattering. Thus, the heavier elements, such as the zinc centers of the molecular ions, will be more ordered than would be expected, while at the same time, the second hydration shell, of which the distances were not tightly constrained in the simulation, will be more disordered than anticipated. This is

experimentally observed in Figure 3.23, where the $\text{Zn}(\text{H}_2\text{O})_6^{2+}$ and ZnCl_4^{2-} ions are still close to being in separate planes, while the additional waters are observed to be much more disorganized. As a result, while the RMC modelling supports the existence of pseudo-cubic type packing in the $R = 9$ liquid, it cannot be determined at this time as to whether the CsCl- or NaCl-type structure is most likely to exist in the liquid. Inclusion of the X-ray diffraction data in future simulations will provide more weighting to the heavier elements, and will likely result in greater clarity as to the structure of the liquid. However, while the RMC modelling may be inconclusive as to the structure-type likely to occur in the $R = 9$ and $R = 21$ special compositions, the idealized powder patterns indicate that the CsCl-type structure more closely matches the experimental liquid scattering data.

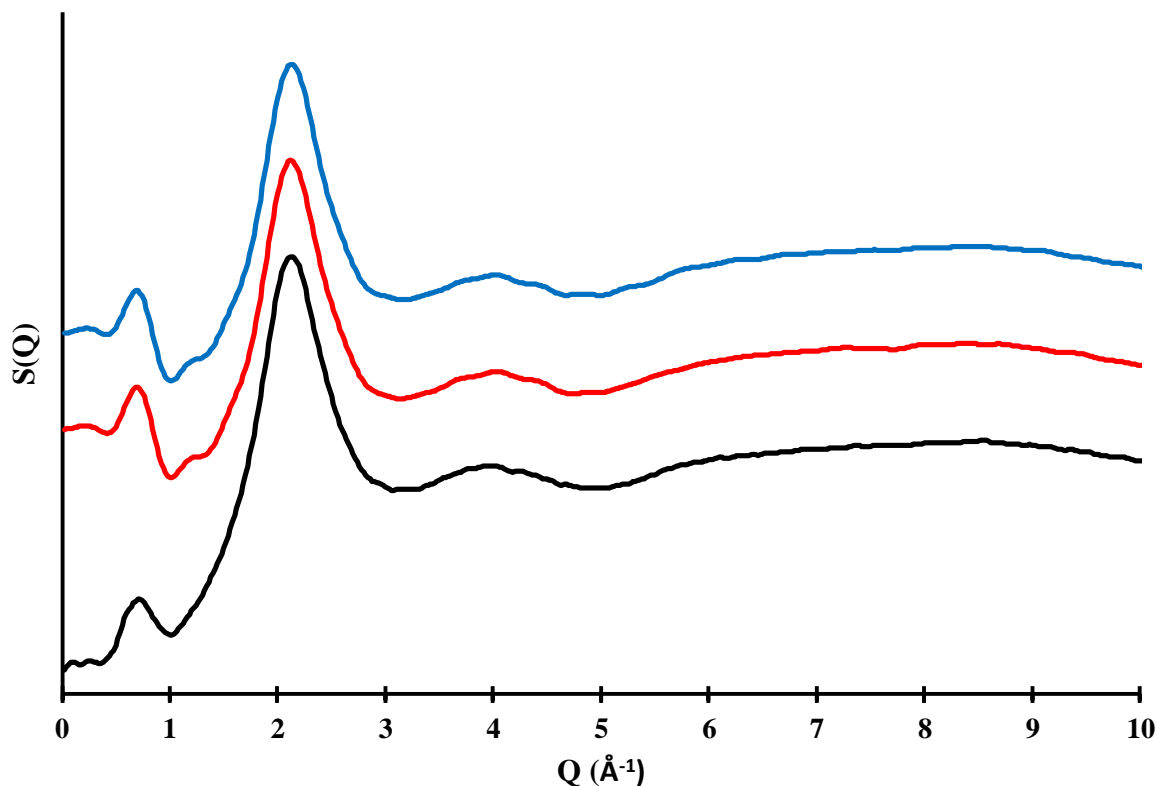


Figure 3.22 Structure factor plots of the $R = 9$ zinc chloride solution obtained by neutron diffraction measurements (black) and RMC modelling of the idealized CsCl- (red) and NaCl-type (blue) supercells.

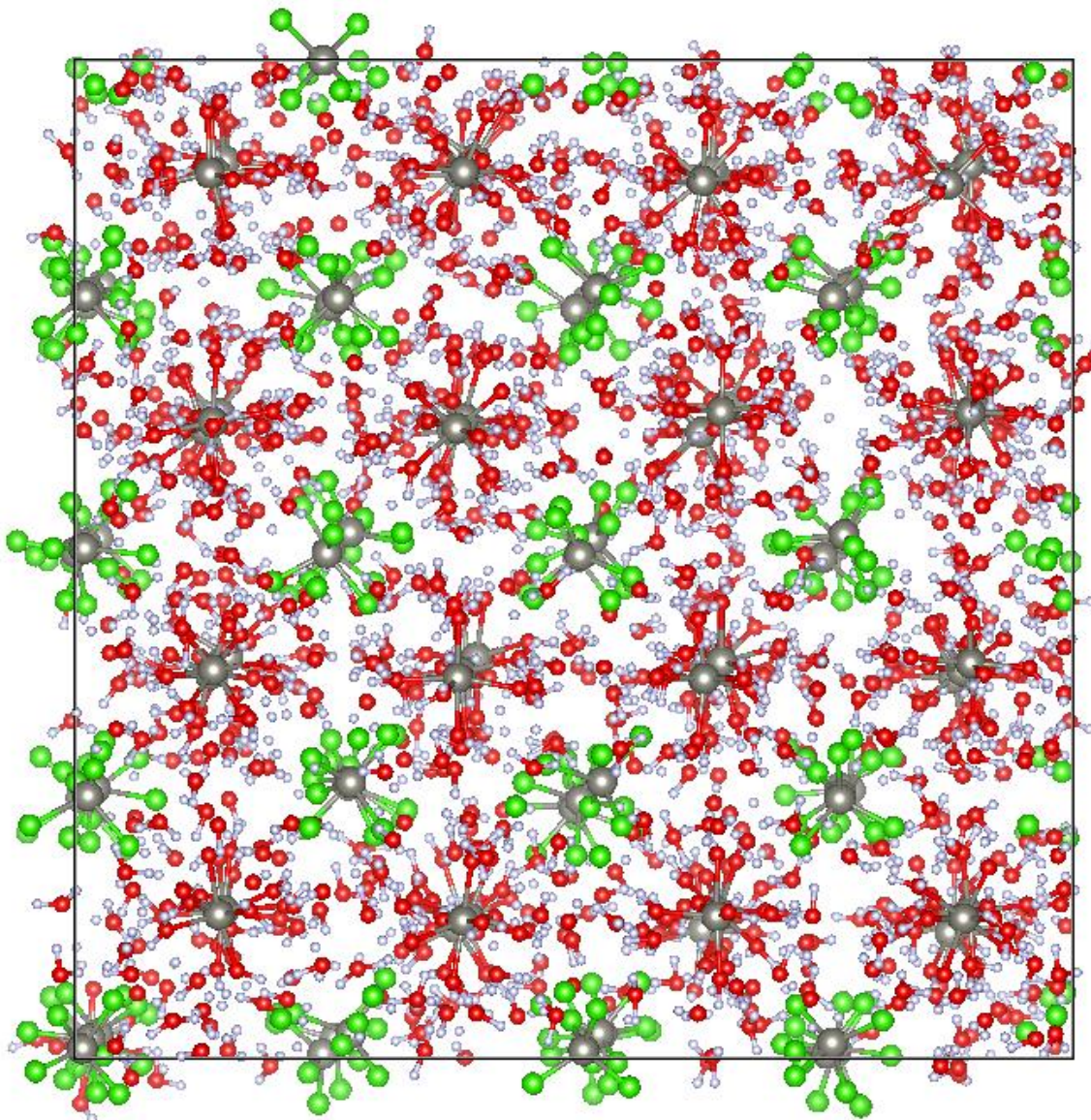


Figure 3.23 Ball-and-stick representation of the RMC simulation box of the idealized CsCl model of the $R = 9$ ZnCl_2 solution.

3.5 Conclusion

The analysis of PDF and Raman data for aqueous ZnCl_2 solutions of concentrations of $R > 3$ not only provides strong evidence for the persistence of the $\text{Zn}(\text{H}_2\text{O})_6^{2+}$ and ZnCl_4^{2-} ions but also strongly indicates the existence of a second hydration shell as well. Interestingly, it is in the compositional region of the second hydration shell, $4 < R < 10$, in which crystallization of the system was not observed via DSC (i.e. in the phase diagram) or low temperature neutron

diffraction. It is our proposal that the strength of the interaction between waters in the first and second hydration shells prevents phase segregation from occurring in the system thus resulting in glass formation upon cooling.

Analysis of the structure factor data from both X-ray and neutron diffraction combined with idealized models and RMC simulations provides evidence of up to three hydration shells in the aqueous ZnCl_2 system. Furthermore, it is found that intermediate range order (IRO) is maintained in the system with a CsCl-type packing of ions in solutions with completed second ($R = 9$) and third ($R = 21$) hydration shells.

3.6 References

1. Taylor, T. 1859.
2. Baik, D.; Fray, D., Electrodeposition of zinc from high acid zinc chloride solutions. *Journal of Applied Electrochemistry* **2001**, *31* (10), 1141-1147.
3. Beck, F.; Rüetschi, P., Rechargeable batteries with aqueous electrolytes. *Electrochimica Acta* **2000**, *45* (15), 2467-2482.
4. Marino, M.; Misuri, L.; Carati, A.; Brogioli, D., Proof-of-concept of a zinc-silver battery for the extraction of energy from a concentration difference. *Energies* **2014**, *7* (6), 3664-3683.
5. Fanglong, Q.; Jinhe, S.; Shaolei, X.; Chenglong, S.; Yongzhong, J., Preparation and Thermal Property of Ionic Liquid based on ZnCl₂/ChCl. *International Proceedings of Chemical, Biological and Environmental Engineering* **2015**, *90*, 70-75.
6. Jin, J.; Li, H.; Chen, C.; Zhang, B.; Xu, L.; Dong, B.; Song, H.; Dai, Q., Enhanced Performance of Perovskite Solar Cells with Zinc Chloride Additives. *ACS applied materials & interfaces* **2017**.
7. Barnes, H.; Rose, A., Origins of hydrothermal ores. *Science* **1998**, *279* (5359), 2064-2065.
8. Crerar, D.; Wood, S.; Brantley, S.; Bocarsly, A., Chemical controls on solubility of ore-forming minerals in hydrothermal solutions. *The Canadian Mineralogist* **1985**, *23* (3), 333-352.
9. Christianson, D. W., Structural biology of zinc. *Advances in protein chemistry* **1991**, *42*, 281-355.
10. Prasad, A. S., Zinc: the biology and therapeutics of an ion. *Annals of internal medicine* **1996**, *125* (2), 142-143.
11. Jentsch, T. J.; Stein, V.; Weinreich, F.; Zdebik, A. A., Molecular structure and physiological function of chloride channels. *Physiological reviews* **2002**, *82* (2), 503-568.
12. Babich, H.; Stotzky, G., Toxicity of zinc to fungi, bacteria, and coliphages: influence of chloride ions. *Applied and environmental microbiology* **1978**, *36* (6), 906-914.
13. Braunstein, J., Some aspects of solution chemistry in liquid mixtures of inorganic salts with water. *Inorganica Chimica Acta Reviews* **1968**, *2*, 19-30.
14. Harris, A.; Parton, H., The transport numbers of zinc chloride from emf measurements. *Transactions of the Faraday Society* **1940**, *36*, 1139-1141.

15. Foxton, F.; Shutt, W., The activity of zinc chloride in concentrated solution. *Transactions of the Faraday Society* **1927**, *23*, 480-488.
16. Robinson, R.; Stokes, R.; Wilson, J. M., A thermodynamic study of bivalent metal halides in aqueous solution. *Transactions of the Faraday Society* **1940**, *36*, 733-748.
17. Dunsmore, H. S.; Paterson, R., Re-determination of the standard electrode potential of zinc and mean molal activity coefficients for aqueous zinc chloride at 298.15 K. *Journal of the Chemical Society, Faraday Transactions 1: Physical Chemistry in Condensed Phases* **1976**, *72*, 495-503.
18. Goldberg, R. N., Evaluated activity and osmotic coefficients for aqueous solutions: Bi-univalent compounds of zinc, cadmium, and ethylene bis (trimethylammonium) chloride and iodide. *Journal of Physical and Chemical Reference Data* **1981**, *10* (1), 1-56.
19. Hittorf, W., Das Verhalten der Diaphragmen bei der Elektrolyse von Salzlösungen. *Zeitschrift für Physikalische Chemie* **1903**, *43* (1), 239-249.
20. Rabinowitsch, A., Über die anomale Dissoziation in wässrigen Lösungen. *Zeitschrift für Physikalische Chemie* **1921**, *99* (1), 338-360.
21. Mead, D. J.; Fuoss, R. M., Conductance and viscosity of concentrated solutions of calcium and zinc chlorides. *The Journal of Physical Chemistry* **1945**, *49* (5), 480-482.
22. Eastal, A.; Sare, E.; Moynihan, C.; Angell, C., Glass-transition temperature, electrical conductance, viscosity, molar volume, refractive index, and proton magnetic resonance study of chlorozinc complexation in the system $ZnCl_2 + LiCl + H_2O$. *Journal of solution chemistry* **1974**, *3* (11), 807-821.
23. Agnew, A.; Paterson, R., Transport in aqueous solutions of group IIB metal salts at 298.15 K. Part 6.—Irreversible thermodynamic parameters for zinc chloride and verification of Onsager's reciprocal relationships. *Journal of the Chemical Society, Faraday Transactions 1: Physical Chemistry in Condensed Phases* **1978**, *74*, 2896-2906.
24. Miller, D. G.; Rard, J. A., Generalized isothermal transport coefficients of $ZnCl_2-H_2O$ at 25° C. *Journal of Molecular Liquids* **1992**, *52*, 145-179.
25. Thomas, B.; Fray, D., The conductivity of aqueous zinc chloride solutions. *Journal of Applied Electrochemistry* **1982**, *12* (1), 1-5.
26. Nakamura, Y.; Shimokawa, S.; Futamata, K.; Shimoji, M., NMR relaxation study of water molecules in concentrated zinc chloride solutions. *The Journal of Chemical Physics* **1982**, *77* (6), 3258-3262.
27. Irish, D. E.; McCarroll, B.; Young, T. F., Raman Study of Zinc Chloride Solutions. *The Journal of Chemical Physics* **1963**, *39* (12), 3436-3444.

28. Mylius, F., Uber das Chlorzink. *Zeitschrift fur anorganische und allgemeine Chemie* **1905**, 44 (1), 209-220.
29. Angell, C.; Sare, E., Glass-Forming Composition Regions and Glass Transition Temperatures for Aqueous Electrolyte Solutions. *The Journal of Chemical Physics* **1970**, 52 (3), 1058-1068.
30. Yamaguchi, T.; Hayashi, S.; Ohtaki, H., X-ray diffraction and Raman studies of zinc(II) chloride hydrate melts, $ZnCl_2 \cdot rH_2O$ ($r = 1.8, 2.5, 3.0, 4.0, \text{ and } 6.2$). *The Journal of Physical Chemistry* **1989**, 93 (6), 2620-2625.
31. Follner, H.; Brehler, B., Die Kristallstruktur des $ZnCl_2 \cdot 4/3H_2O$. *Acta Crystallographica Section B* **1970**, 26 (11), 1679-1682.
32. Hennings, E.; Schmidt, H.; Voigt, W., Crystal structures of $ZnCl_2 \cdot 2.5H_2O$, $ZnCl_2 \cdot 3H_2O$ and $ZnCl_2 \cdot 4.5H_2O$. *Acta Crystallographica Section E* **2014**, 70 (12), 515-518.
33. Wilcox, R. J.; Losey, B. P.; Folmer, J. C. W.; Martin, J. D.; Zeller, M.; Sommer, R., Crystalline and Liquid Structure of Zinc Chloride Trihydrate: A Unique Ionic Liquid. *Inorganic Chemistry* **2015**, 54 (3), 1109-1119.
34. Desa, J. E.; Wright, A. C.; Wong, J.; Sinclair, R. N., A neutron diffraction investigation of the structure of vitreous zinc chloride. *Journal of non-crystalline solids* **1982**, 51 (1), 57-86.
35. Angell, C.; Wong, J., Structure and Glass Transition Thermodynamics of Liquid Zinc Chloride from Far-Infrared, Raman, and Probe Ion Electronic and Vibrational Spectra. *The Journal of Chemical Physics* **1970**, 53 (5), 2053-2066.
36. Aliotta, F.; Maisano, G.; Migliardo, P.; Vasi, C.; Wanderlingh, F.; Smith, G. P.; Triolo, R., Vibrational dynamics of glassy and molten $ZnCl_2$. *The Journal of Chemical Physics* **1981**, 75 (2), 613-618.
37. Van Uitert, L.; Wemple, S., $ZnCl_2$ glass: A potential ultralow-loss optical fiber material. *Applied Physics Letters* **1978**, 33 (1), 57-59.
38. Kirilenko, I., Glass formation in the $ZnCl_2$ - H_2O system. *Russian Journal of Inorganic Chemistry* **2013**, 58 (10), 1183-1186.
39. Nguyen-Trung, C.; Bryan, J. C.; Palmer, D. A., Crystal structure and thermogravimetric analysis of hexaaquazinc triflate. *Structural Chemistry* **2004**, 15 (2), 89-94.
40. Duhlev, R.; Macicek, J., Structure of magnesium zinc tetrachloride hexahydrate $MgZnCl_4 \cdot 6H_2O$. *Acta Crystallographica Section C: Crystal Structure Communications* **1991**, 47 (8), 1573-1575.

41. Powell, D. H.; Barnes, A. C.; Enderby, J. E.; Neilson, G. W.; Salmon, P. S., The hydration structure around chloride ions in aqueous solution. *Faraday Discussions of the Chemical Society* **1988**, 85 (0), 137-146.
42. Bergstroem, P. A.; Lindgren, J.; Kristiansson, O., An IR study of the hydration of perchlorate, nitrate, iodide, bromide, chloride and sulfate anions in aqueous solution. *The Journal of Physical Chemistry* **1991**, 95 (22), 8575-8580.
43. Van Der Vegt, N. F.; Haldrup, K.; Roke, S.; Zheng, J.; Lund, M.; Bakker, H. J., Water-mediated ion pairing: occurrence and relevance. *Chemical reviews* **2016**, 116 (13), 7626-7641.
44. Li, J.; Bian, H.; Chen, H.; Wen, X.; Hoang, B. T.; Zheng, J., Ion association in aqueous solutions probed through vibrational energy transfers among cation, anion, and water molecules. *The Journal of Physical Chemistry B* **2012**, 117 (16), 4274-4283.
45. Soniat, M.; Pool, G.; Franklin, L.; Rick, S. W., Ion association in aqueous solution. *Fluid Phase Equilibria* **2016**, 407, 31-38.
46. Ichihashi, M.; Wakita, H.; Masuda, I., Structure of iron (II) and cobalt (II) bromide complexes in aqueous solution by X-ray diffraction analysis. *Journal of solution chemistry* **1984**, 13 (7), 505-516.
47. Wakita, H.; Ichihashi, M.; Mibuchi, T.; Masuda, I., The structure of nickel (II) bromide in highly concentrated aqueous solution by X-ray diffraction analysis. *Bulletin of the Chemical Society of Japan* **1982**, 55 (3), 817-821.
48. Morris, D. F. C.; Short, E. L.; Waters, D. N., Zinc chloride and zinc bromide complexes—III: Structures of species in solution. *Journal of Inorganic and Nuclear Chemistry* **1963**, 25 (8), 975-983.
49. Maeda, M.; Ito, T.; Hori, M.; Johansson, G., The structure of zinc chloride complexes in aqueous solution. *Zeitschrift für Naturforschung A* **1996**, 51 (1-2), 63-70.
50. Parchment, O. G.; Vincent, M. A.; Hillier, I. H., Speciation in aqueous zinc chloride. An ab initio hybrid microsolvation/continuum approach. *The Journal of Physical Chemistry* **1996**, 100 (23), 9689-9693.
51. Enderby, J.; Cummings, S.; Herdman, G.; Neilson, G.; Salmon, P.; Skipper, N., Diffraction and the study of aqua ions. *Journal of Physical Chemistry* **1987**, 91 (23), 5851-5858.
52. Kanno, H.; Hiraishi, J., Raman spectroscopic study of glassy aqueous zinc halide solutions. *Journal of Raman Spectroscopy* **1980**, 9 (2), 85-89.

53. Mayanovic, R. A.; Anderson, A. J.; Bassett, W. A.; Chou, I., XAFS measurements on zinc chloride aqueous solutions from ambient to supercritical conditions using the diamond anvil cell. *Journal of synchrotron radiation* **1999**, *6* (3), 195-197.
54. Dagnall, S. P.; Hague, D. N.; Towl, A. D. C., X-ray diffraction study of aqueous zinc(II) nitrate. *Journal of the Chemical Society, Faraday Transactions 2: Molecular and Chemical Physics* **1982**, *78* (12), 2161-2167.
55. Kuzmin, A.; Obst, S.; Purans, J., X-ray absorption spectroscopy and molecular dynamics studies of hydration in aqueous solutions. *Journal of Physics: Condensed Matter* **1997**, *9* (46), 10065.
56. Pavlov, M.; Siegbahn, P. E.; Sandström, M., Hydration of beryllium, magnesium, calcium, and zinc ions using density functional theory. *The Journal of Physical Chemistry A* **1998**, *102* (1), 219-228.
57. Rudolph, W. W.; Pye, C. C., Zinc (II) hydration in aqueous solution. A Raman spectroscopic investigation and an ab-initio molecular orbital study. *Physical Chemistry Chemical Physics* **1999**, *1* (19), 4583-4593.
58. D'Angelo, P.; Barone, V.; Chillemi, G.; Sanna, N.; Meyer-Klaucke, W.; Pavel, N. V., Hydrogen and Higher Shell Contributions in Zn²⁺, Ni²⁺, and Co²⁺ Aqueous Solutions: An X-ray Absorption Fine Structure and Molecular Dynamics Study. *Journal of the American Chemical Society* **2002**, *124* (9), 1958-1967.
59. Fatmi, M. Q.; Hofer, T. S.; Randolph, B. R.; Rode, B. M., An extended ab initio QM/MM MD approach to structure and dynamics of Zn (II) in aqueous solution. *The Journal of Chemical Physics* **2005**, *123* (5), 054514.
60. Cauët, E.; Bogatko, S.; Weare, J. H.; Fulton, J. L.; Schenter, G. K.; Bylaska, E. J., Structure and dynamics of the hydration shells of the Zn²⁺ ion from ab initio molecular dynamics and combined ab initio and classical molecular dynamics simulations. *The Journal of Chemical Physics* **2010**, *132* (19), 194502.
61. Bock, C. W.; Markham, G. D.; Katz, A. K.; Glusker, J. P., The arrangement of first- and second-shell water molecules around metal ions: effects of charge and size. *Theoretical Chemistry Accounts* **2006**, *115* (2-3), 100-112.
62. Obst, S.; Bradaczek, H., Molecular dynamics simulations of zinc ions in water using CHARMM. *Journal of Molecular Modeling* **1997**, *3* (6), 224-232.
63. Rowlinson, J.; Curtiss, C., Lattice theories of the liquid state. *The Journal of Chemical Physics* **1951**, *19* (12), 1519-1529.
64. Barker, J. A., *Lattice theories of the liquid state*. Pergamon Press: 1963; Vol. 1.

65. Gaskell, P. H., Medium-range structure in glasses and low-Q structure in neutron and X-ray scattering data. *Journal of non-crystalline solids* **2005**, *351* (12), 1003-1013.
66. Soper, A., Partial structure factors from disordered materials diffraction data: An approach using empirical potential structure refinement. *Physical review B* **2005**, *72* (10), 104204.
67. Easteal, A.; Giaquinta, P.; March, N.; Tosi, M., Chemical effects in diffusion and structure of zinc chloride in aqueous solution. *Chemical Physics* **1983**, *76* (1), 125-128.
68. Cubiotti, G.; Bosi, P.; Menzinger, F.; Sacchetti, F., Some evidence for a structural transition in electrolyte solutions. *Journal of Physics C: Solid State Physics* **1980**, *13* (10), 1951.
69. Ribeiro, M. C., Intermediate-range order in aqueous solutions of salts: a systematic computer simulation study. *Journal of Physics: Condensed Matter* **2005**, *17* (3), 453.
70. Gaspar, A.; Marques, M. A.; Cabaço, M.; de Barros Marques, M.; Buslaps, T.; Honkimaki, V., X-Ray diffraction investigations of concentrated aqueous solutions of calcium halides. *Journal of Molecular Liquids* **2004**, *110* (1), 15-22.
71. Hammersley, A., FIT2D: an introduction and overview. *European Synchrotron Radiation Facility Internal Report ESRF97HA02T* **1997**.
72. Qiu, X.; Thompson, J. W.; Billinge, S. J. L., PDFgetX2: a GUI-driven program to obtain the pair distribution function from X-ray powder diffraction data. *Journal of Applied Crystallography* **2004**, *37* (4), 678.
73. Neuefeind, J.; Feygenson, M.; Carruth, J.; Hoffmann, R.; Chipley, K. K., The Nanoscale Ordered MATERIALS Diffractometer NOMAD at the Spallation Neutron Source SNS. *Nuclear Instruments and Methods in Physics Research Section B: Beam Interactions with Materials and Atoms* **2012**, *287*, 68-75.
74. Tucker, M. G.; Keen, D. A.; Dove, M. T.; Goodwin, A. L.; Hui, Q., RMCProfile: reverse Monte Carlo for polycrystalline materials. *Journal of Physics: Condensed Matter* **2007**, *19* (33), 335218.
75. Wilcox, R. J. Sorption to Dissolution: The Reactivity of Small Molecules with Condensed Phase Metal Halide Networks. North Carolina State University, Raleigh, 2009.
76. Fontana, M.; Maisano, G.; Migliardo, P.; Wanderlingh, F., Raman spectroscopy and local order in aqueous solutions of strong II-I electrolytes. *The Journal of Chemical Physics* **1978**, *69* (2), 676-683.

77. Quicksall, C. O.; Spiro, T. G., Raman spectra of tetrahalozincates and the structure of aqueous $ZnCl_4^{2-}$. *Inorganic chemistry* **1966**, *5* (12), 2232-2233.
78. Bulmer, J. T.; Irish, D. E.; Ödberg, L., The temperature dependence of raman band parameters for aquated Mg (II) and Zn (II). *Canadian Journal of Chemistry* **1975**, *53* (24), 3806-3811.
79. Dill, E. D.; Josey, A. A.; Folmer, J. C. W.; Hou, F.; Martin, J. D., Experimental Determination of the Crystallization Phase-Boundary Velocity in the Halozeotype CZX-1. *Chemistry of Materials* **2013**, *25* (20), 3932-3940.
80. Hillis, B. G.; Losey, B. P.; Weng, J.; Ghaleb, N.; Hou, F.; Martin, J. D., From Rate Measurements to Mechanistic Data for Condensed Matter Reactions: A Case Study Using the Crystallization of $[Zn(OH)_2]_6[ZnCl_4]$. *Crystals* **2016**, *7* (1), 11.
81. W. Rudolph, W.; C. Pye, C., Zinc(II) hydration in aqueous solution. A Raman spectroscopic investigation and an ab-initio molecular orbital study. *Physical Chemistry Chemical Physics* **1999**, *1* (19), 4583-4593.
82. McQuarrie, D. A.; Chemistry, J. P., *A Molecular Approach*. University Science Books: USA: 1997.
83. Angell, C.; Choi, Y., Crystallization and vitrification in aqueous systems. *Journal of microscopy* **1986**, *141* (3), 251-261.
84. Angell, C., Liquid fragility and the glass transition in water and aqueous solutions. *Chemical reviews* **2002**, *102* (8), 2627-2650.
85. Shalaev, E. Y.; Franks, F., Equilibrium phase diagram of the water-sucrose-NaCl system. *Thermochimica acta* **1995**, *255*, 49-61.
86. Vuillard, G. Contribution a l'etude de l'etat vitreux et de la cristallisation des solutions aqueuses. 1957.
87. Moran Jr, H., System lithium chloride–water. *The Journal of Physical Chemistry* **1956**, *60* (12), 1666-1667.
88. Andrić, J. M.; Janjić, G. V.; Ninković, D. B.; Zarić, S. D., The influence of water molecule coordination to a metal ion on water hydrogen bonds. *Physical Chemistry Chemical Physics* **2012**, *14* (31), 10896-10898.
89. Matsumoto, M.; Saito, S.; Ohmine, I., Molecular dynamics simulation of the ice nucleation and growth process leading to water freezing. *Nature* **2002**, *416* (6879), 409.
90. Moore, E. B.; Molinero, V., Structural transformation in supercooled water controls the crystallization rate of ice. *Nature* **2011**, *479* (7374), 506.

91. Soper, A. K., The radial distribution functions of water and ice from 220 to 673 K and at pressures up to 400 MPa. *Chemical Physics* **2000**, 258 (2–3), 121-137.
92. Fu, L.; Bienenstock, A.; Brennan, S., X-ray study of the structure of liquid water. *The Journal of Chemical Physics* **2009**, 131 (23), 234702.
93. Bol, W.; Gerrits, G. J. A.; Van Panthaleon Eck, C. L., The hydration of divalent cations in aqueous solution. An X-ray investigation with isomorphous replacement. *Journal of Applied Crystallography* **1970**, 3 (6), 486-492.
94. Munoz-Paez, A.; Pappalardo, R. R.; Sanchez Marcos, E., Determination of the Second Hydration Shell of Cr³⁺ and Zn²⁺ in Aqueous Solutions by Extended X-ray Absorption Fine Structure. *Journal of the American Chemical Society* **1995**, 117 (47), 11710-11720.
95. Arab, M.; Bougeard, D.; Smirnov, K. S., Molecular dynamics study of the structure and dynamics of Zn²⁺ ion in water. *Chemical Physics Letters* **2003**, 379 (3–4), 268-276.
96. Brancato, G.; Rega, N.; Barone, V., Microsolvation of the Zn(II) ion in aqueous solution: A hybrid QM/MM MD approach using non-periodic boundary conditions. *Chemical Physics Letters* **2008**, 451 (1–3), 53-57.
97. Mohammed, A. M.; Loeffler, H. H.; Inada, Y.; Tanada, K.-i.; Funahashi, S., Quantum mechanical/molecular mechanical molecular dynamic simulation of zinc(II) ion in water. *Journal of Molecular Liquids* **2005**, 119 (1–3), 55-62.
98. Huang, C.; Wikfeldt, K.; Nordlund, D.; Bergmann, U.; McQueen, T.; Sellberg, J.; Pettersson, L. G.; Nilsson, A., Wide-angle X-ray diffraction and molecular dynamics study of medium-range order in ambient and hot water. *Physical Chemistry Chemical Physics* **2011**, 13 (44), 19997-20007.
99. Neilson, G. W.; Howe, R. A.; Enderby, J. E., The quasi-lattice structure in concentrated aqueous solutions. *Chemical Physics Letters* **1975**, 33 (2), 284-285.

CHAPTER 4

Nuclear Magnetic Resonance Studies of the Concentration Dependence of Hydrogen Bonding Interactions in Aqueous Zinc Chloride Solutions

4.1 Introduction

Water is an essential part of life and aqueous solutions are important both in nature and for use in modern industry. As a result, extensive research has been conducted to characterize the structure of liquid water both as its pure melt and as a component of aqueous solutions.^{1,2} A deeper understanding of the structure/interactions of water in the presence of ions will result in greater control over reactions in aqueous media and solution properties. While disagreement remains as to the true structure of liquid water, the most commonly proposed structures include a tetrahedral network similar to that of hexagonal ice, and an icosahedral cluster type structure consisting of regions of higher and lower order.^{3,4,5} Both models propose a high degree of structural order in liquid water due to the hydrogen bonding network which has been shown to be sensitive to changes in both temperature and solute concentration.⁶

In Chapter 2 and reference 7, evidence was presented to suggest the formation of an octahedral hydration shell around half the zinc ions in the $R = 3$ zinc chloride hydrate. Furthermore, in Chapter 3, evidence based on neutron and X-ray diffraction data was presented which indicated the existence of multiple hydration shells in aqueous zinc chloride solutions more dilute than the $R = 3$ composition. ^1H NMR allows for the measurement of differences in the hydrogen environment between pure water and aqueous solutions containing unique regions of solvent around the ion also known as hydration shells. The most distinct region is that of the first solvation shell in which waters are bound directly to the ion. The direct interaction of water with the metal has a substantial effect on the electron density around the water hydrogen atoms

which results in a noticeable change in the chemical shift compared to that of pure water. Additionally, hydration shells of the 2nd, 3rd, or higher order, in which the waters are not directly bound to the ion, likely exist. The electron density of the hydrogen atoms on these water molecules will also be effected differently from those of pure water, resulting in additional unique chemical shift values.⁸ Finally, there is “bulk” water, the region in which the water is not significantly affected by the presence of an ion and maintains the hydrogen bonding structure observed in pure water. However, it is not clear at what concentration water begins to have a structure similar to that of the bulk. Thus, it is anticipated that ¹H NMR will aid in answering this question.

Past ¹H NMR investigations of aqueous electrolyte solutions have included variable temperature chemical shift experiments as well as magnetic relaxation and self-diffusion measurements.^{9,10} Researchers have made the assumption that a single hydration shell surrounds each ion in aqueous solutions while treating all other water as “bulk”, resulting in what is known as the two-state model.^{6, 9, 11-12} The two-state equation has been combined with variable temperature data and rearranged, making the assumption that solvating waters have no temperature dependence, to determine the number of waters associated with the solute, commonly referred to as the “effective hydration number”, in solution which includes the hydration around both cations and anions.¹³ Evidence from infrared photodissociation spectroscopy (IRPD) suggests that transition metal ions, including Zn²⁺, typically have 6 waters in their first hydration shell.¹⁴ However, some effective hydration numbers, for example in Al(NO₃)₃ solutions, have been found by NMR measurements to be as large as 13.4, indicating the existence of a second hydration shell around the cation.¹¹ Furthermore, spin-lattice (T₁) relaxation NMR and self-diffusion coefficients of aqueous zinc chloride solutions show a much

larger hindrance of translational motion at high concentrations indicating that the water molecules are more strongly affected by the presence of the ions and in fact could be forming a second hydration shell.¹⁵ Additionally, nuclear magnetic relaxation dispersion (NMRD) measurements also show evidence of at least two hydration shells around Cr^{3+} and Fe^{3+} ions.¹⁶ In combination with experimental measurements, density functional theory (DFT) calculations have been used to investigate the coordination environment of group 2 metal ions as well as Zn^{2+} and demonstrate that the binding energy of waters in the second shell are on the order of 3 times larger than the interaction energy between two isolated water molecules.¹⁷ The results of these DFT calculations indicate that strong water-water hydrogen bonding exists between the first two hydration shells of Be^{2+} , Mg^{2+} , Ca^{2+} and Zn^{2+} ions. Lastly, Car-Parrinello molecular dynamics (CPMD) calculations and infrared (IR) spectroscopy measurements of Al^{3+} , Cr^{3+} and Rh^{3+} ions support the existence of up to three hydration shells around these metal ions.^{18,19,20-21}

In this chapter, ^1H NMR measurements were taken of pure water and aqueous solutions of AlCl_3 , $\text{Al}_2(\text{SO}_4)_3$, CaCl_2 , MgCl_2 , MgSO_4 , NaCl , ZnCl_2 , and ZnSO_4 as a systematic study to gain better insight into the hydration of ions in aqueous solutions. The resulting chemical shift data was observed as a function of temperature and concentration. The aqueous ZnCl_2 data were then used to develop mathematical models to decompose the single measured peak into the various water environments in solution. It was ultimately found that five hydration shells were necessary to fully describe the zinc chloride data. The developed mathematical model was then applied to the additional aqueous salt solutions and it was determined that 2 – 4 hydration shells were required to describe the chemical shift data of these solutions.

4.2 Experimental Methods

4.2.1 Sample preparation

Zinc chloride, purchased from Sigma Aldrich (reagent grade $\geq 98\%$), was doubly sublimed under dynamic vacuum in Pyrex tubes at 450 °C. The material was transferred to a vial and stored under nitrogen atmosphere in a glovebox. ZnCl_2 aqueous solutions were prepared by measuring the appropriate amount of zinc chloride by mass in the glovebox followed by the addition of 18 M Ω water, obtained using a Millipore Synergy ultrapure water filtration system, on the benchtop using an Oxford 100 – 1000 μL micropipette. Additional aqueous solutions of NaCl, CaCl_2 , MgCl_2 , AlCl_3 , ZnSO_4 , MgSO_4 , and $\text{Al}_2(\text{SO}_4)_3$ were made in the same manner using as purchased material.

4.2.2 ^1H NMR measurements

NMR samples were prepared by placing approximately 0.25 mL of sample into a 5 mm NMR tube. An external lock of ^6d -acetone, obtained from Sigma Aldrich (99.9%), was used by placing a 3-mm diameter NMR tube containing the reference inside a 5-mm tube containing the sample. Chemical shift data were collected on a Varian Mercury 400 MHz spectrometer equipped with a 5 mm PFG gradient 4-nuclei probe. Variable temperature measurements were collected over a temperature range from -80 to 45 °C using a Varian Model L900 temperature controller. The data were processed using the ACD-NMR Processor and SpinWorks software packages to obtain the Fourier transform of the measured FID and perform a standard phase correction.^{22,23}

4.2.3 Hartree-Fock calculations

^1H NMR chemical shifts of water molecules complexed in octahedral geometry with Na^+ , Ca^{2+} , Mg^{2+} , Zn^{2+} , and Al^{3+} ions were calculated at the Hartree-Fock level of theory using Gaussian 09 software with a 6-31g basis set and the Gauge-Independent Atomic Orbital (GIAO)

method to calculate the NMR shielding tensor.²⁴ Calculations were performed for isolated hydrated ions with no polarizable continuum model (PCM). The calculated spectra are reported relative to tetramethylsilane (TMS).

4.3 Results

4.3.1 Concentration dependent ¹H NMR of zinc chloride solutions

In an attempt to differentiate the hydration shell environments in aqueous zinc chloride solutions, room temperature ¹H NMR measurements were performed on a series of solutions with concentrations from $R = 3$ to $R = 400$ where R is the number of molar equivalents of water in the solution. For all compositions, a single chemical shift was observed, albeit significantly dependent on the concentration of zinc chloride in solution. A plot of the room temperature chemical shift as a function of the mole % water is shown in Figure 4.1. Three distinct regions are observed, differentiated by changes in the slope of the data. The first region occurs at concentrations of $R < 9$ (< 90 % water) and displays an approximately linear trend as a function of mole % water with a slope of 3.00 (0.06). The second region, occurring for $9 < R < 100$ (90% to 99% water), also shows an approximately linear trend with a slope of 5.12 (0.05). The slope of these two lines appears to change abruptly at the concentration of $R = 9$. The steeper slope for the more dilute solutions ($R = 9$ to $R = 100$) indicates that the most dramatic change in chemical environment occurs in this concentration range. A third region is observed at even more dilute concentrations of $R > 100$, for which there is no statistically significant variation from the chemical shift of pure water, though a linear fit to this data suggests a slope of 2.2 (0.6). The variation in chemical shift for the $R = 100$ solution to that of pure water is less than 0.02 ppm. This plateau of the concentration dependent chemical shift in dilute aqueous solutions of $ZnCl_2$

has been previously reported and was proposed to be a result of the polarization of waters beyond the first hydration shell combined with the formation of ion pairs.²⁵

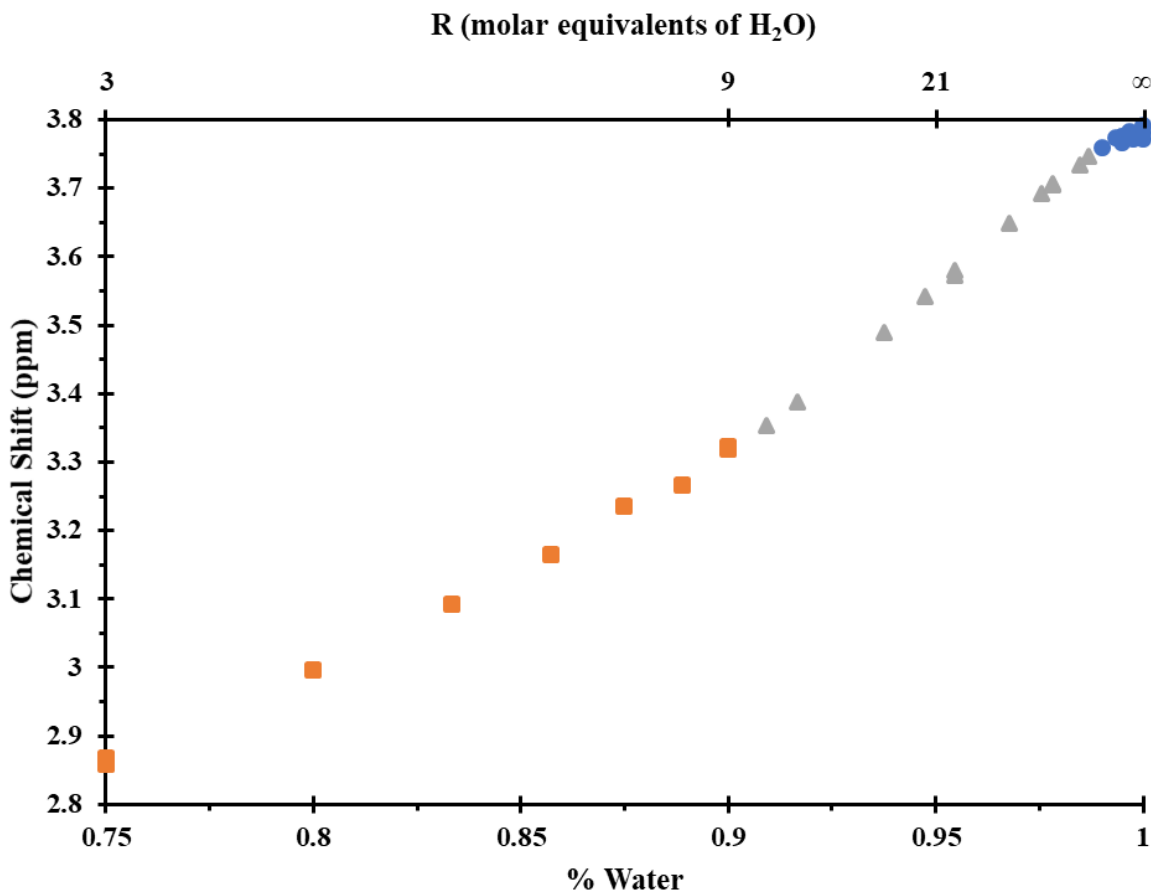


Figure 4.1 Concentration dependent ¹H NMR chemical shift of the zinc chloride aqueous solutions from R = 3 to R = 9 (squares), R = 9 to R = 100 (triangles), and R = 100 to pure water (circles).

In Chapter 2 and reference 7 it was demonstrated that in the R = 3 solution, the molecular ions $\text{Zn}(\text{H}_2\text{O})_6^{2+}$ and ZnCl_4^{2-} persist such that this solution is best described as an ionic liquid. To investigate whether the proton chemical shift dependence is a result of disproportionation of these molecular ions, a similar concentration dependent measurement of the Raman spectrum was performed since both of these molecular ions exhibit distinctive Raman signals. Remarkably, as shown in the concentration dependent plot of Figure 4.2, and discussed in Chapter 3, both of these species persist into high dilutions. If Cl^- would dissociate from the ZnCl_4^{2-} anion, the

Raman spectra would be expected to exhibit a relative decrease in the intensity of the 283 cm^{-1} peak and correspondingly increase in the 400 cm^{-1} peak characteristic of the hydrated zinc cation. This is not observed. Instead both species exhibit a comparable loss of intensity upon dilution. Thus, the ZnCl_4^{2-} anion appears to persist even to the highest levels of dilution studied.

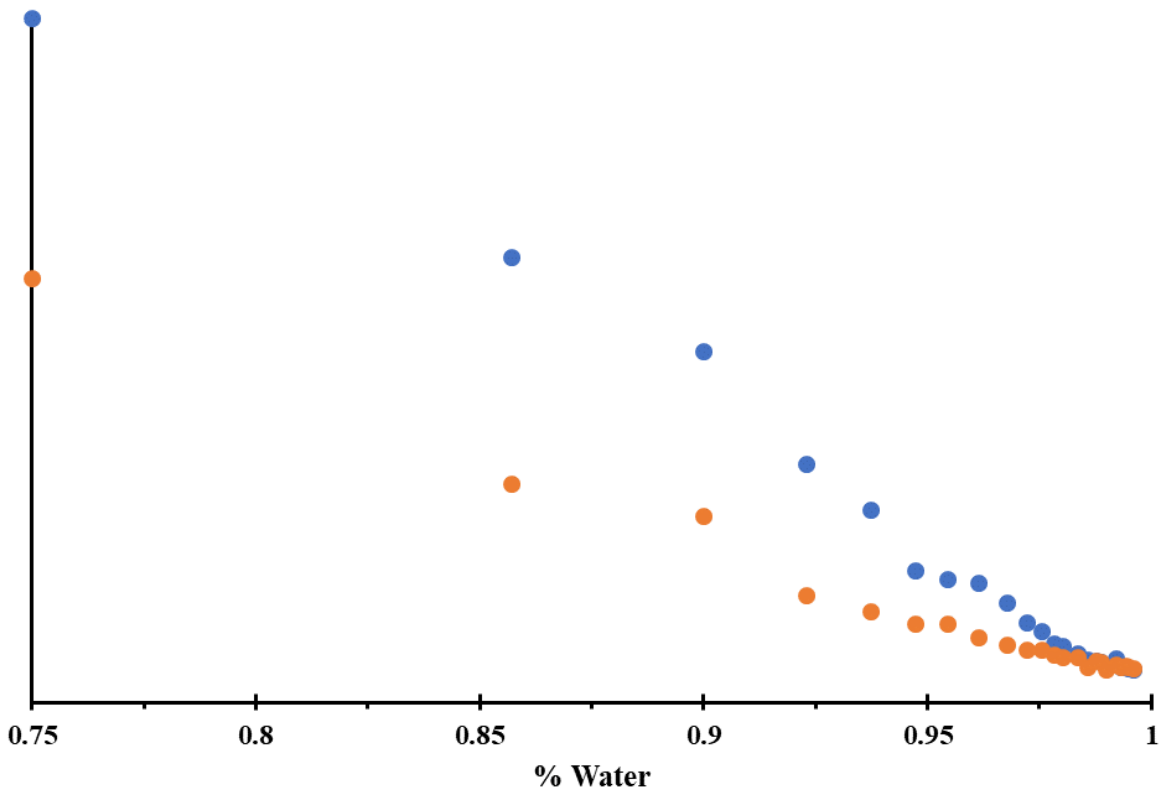


Figure 4.2 Peak intensities of the Raman peaks at 283 cm^{-1} (orange) and 400 cm^{-1} (blue) for aqueous zinc chloride as a function of percent water.

4.3.2 Measurements of different salts

Zinc chloride is one of the most soluble salts known, with 432 g ZnCl_2 dissolving in 100 g H_2O at $25\text{ }^\circ\text{C}$. Thus, while its solubilization characteristics are likely unique and played an important role in the development of mathematical fitting models, a systematic evaluation of the ^1H NMR spectra of other aqueous salt solutions for which the ions exhibit a range of solubilities, should provide an important check for validation of the proposed fitting model. Therefore, a

series of concentration dependent, room temperature ^1H NMR measurements were obtained for the following salts: NaCl, CaCl₂, MgCl₂, AlCl₃, ZnSO₄, MgSO₄, Al₂(SO₄)₃, and a 1:1 MgCl₂/ZnCl₂. The room temperature solubility of each of these materials is reported in Table 4.1.

Table 4.1 Values for the solubility of the salts examined in the aqueous solutions.

Salt	Solubility (g/100g H ₂ O at 20 °C)	Mole Ratio
Al ₂ (SO ₄) ₃	36.4	52.16
MgSO ₄	35.1	19.03
ZnSO ₄	53.8	16.66
AlCl ₃	45.8	16.16
MgCl ₂	54.6	9.68
NaCl	36.0	9.01
CaCl ₂	74.5	8.27
ZnCl ₂	395	1.91

The concentration dependent chemical shift measurements of the additional salts can be seen in Figure 4.3. It can be observed that the sulfate salts along with AlCl₃ all have down field shifts as a function of concentration relative to pure water. The additional chloride salts are all observed to have upfield chemical shifts relative to water. The magnitude of the concentration dependence appears to scale with the charge density of the cation which are given in Table 4.2.²⁶

Table 4.2 Values for the ionic radii given in angstroms and calculated charge density of the examined ions. Ref. 26^a

Ion	Radius	Charge Density
ZnCl ₄ ²⁻	3.06 ^a	0.017
Cl ⁻	1.81	0.04
SO ₄ ²⁻	2.18 ^a	0.046
Na ⁺	1.02	0.225
Ca ²⁺	1.00	0.478
Zn ²⁺	0.740	1.18
Mg ²⁺	0.720	1.28
Al ³⁺	0.535	4.67

Additionally, Hartree-Fock calculations, shown in Figure 4.4, of the hydrated cations show approximately the same trend in chemical shift as a function of charge density with the largest charge density ion, Al³⁺, resulting in a down field shift of the hydrating waters while the smallest charge density ion, Na⁺, results in the largest upfield chemical shift of the hydrating waters. Unlike the aqueous zinc chloride system, all of these salt solutions exhibit a much more linear trend in the concentration dependence of the water ¹H NMR chemical shift. However, the appearance of subtle discontinuities similar to those in the ZnCl₂ system will be addressed in the next section.

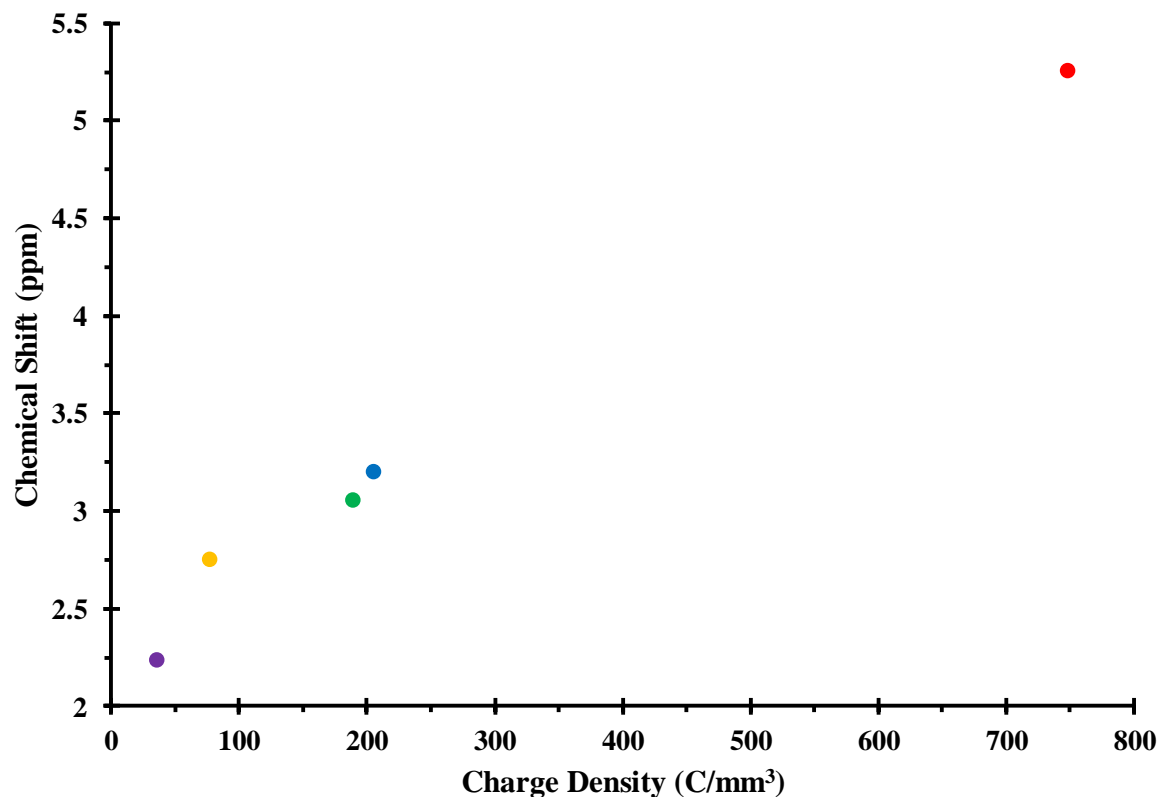


Figure 4.4 The calculated proton chemical shifts of sodium (purple), calcium (orange), zinc (green), magnesium (blue) and aluminum (red) ions hydrated by six water molecules.

4.3.3 Temperature dependent ^1H NMR of aqueous ZnCl_2

Variable temperature ^1H NMR experiments were conducted in an attempt to freeze out the signals of water molecules in distinct hydration shells from that of bulk water. A stack plot of the variable temperature ^1H NMR from 304 to 245 K for an $R = 21$ zinc chloride hydrate solution is given in Figure 4.5. For these measurements ^6d -acetone (sealed within the inner 3 mm NMR tube), which does not exhibit a substantive temperature dependence to its ^1H NMR chemical shift in the temperature range of the reported measurements, was used as a reference standard. A linear downfield shift of the water ^1H NMR signal from 3.44 ppm (304 K) to 4.00 ppm (250 K) with a slope of -9.25×10^{-3} (2.57×10^{-4}) upon decreasing temperature is readily apparent. Unlike the report of distinct ^1H NMR signals for coordinated water and bulk water

signals being frozen out by 220 K in aqueous $\text{Al}(\text{ClO}_4)_3$ solutions with stoichiometric amounts of urea or DMF,³³ at no temperature were multiple proton signals observed in the zinc chloride hydrates. Significant line broadening is observed at 245 K, which is also in the temperature range where ice crystallizes from $R = 21$, as was reported in Chapter 3 via low temperature neutron diffraction measurements.

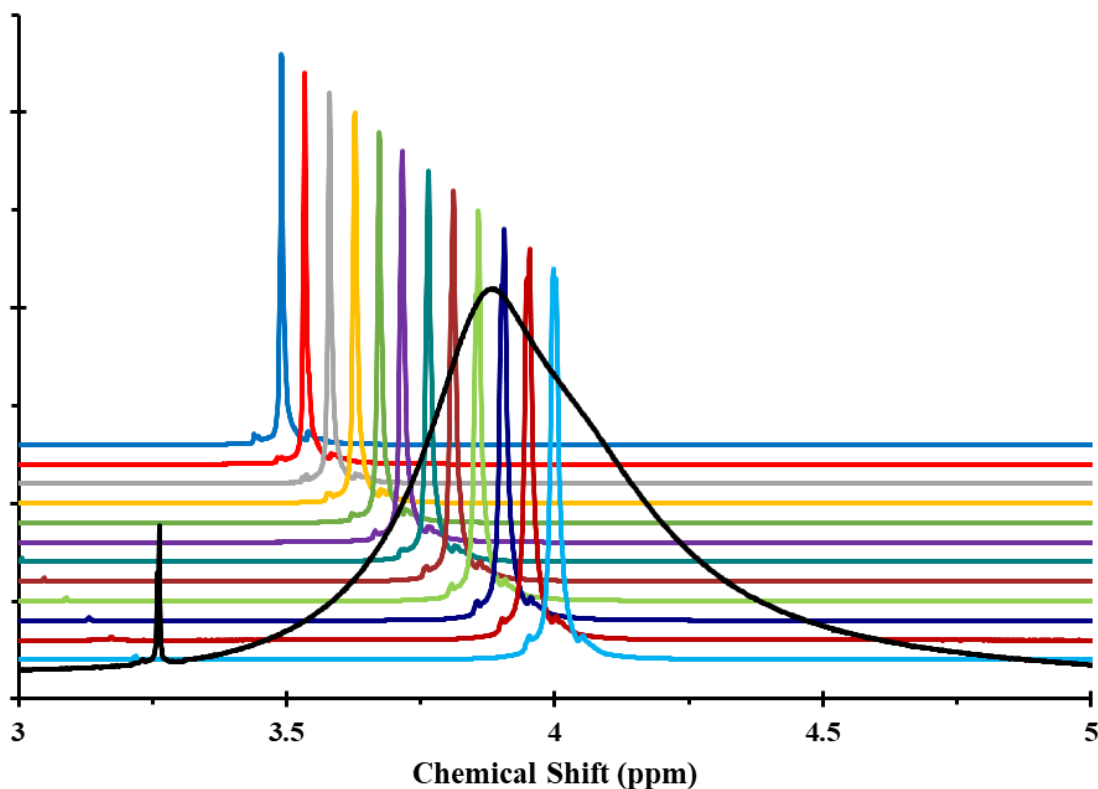


Figure 4.5 Variable temperature measurements for the $R = 21$ zinc chloride hydrate at 304 (blue), 300 (red), 297 (gray), 293 (orange), 290 (green), 284 (purple), 279 (teal), 273 (brown), 267 (light green), 262 (navy), 256 (dark red), 250 (light blue), and 245 (black) Kelvin.

While the water protons in the zinc chloride hydrate system are mobile on a time scale that is too fast for them to be resolved into distinct hydration shell environments by the ^1H NMR experiments, a significantly different temperature dependence of the ^1H NMR chemical shift, $d\delta/dT$, is observed as a function of the ZnCl_2 concentration. Temperature dependent chemical shift data in the range of 193 to 308 K for the special compositions $R = 3$ (75% water), 9 (90%

water), and 21 (95% water) is given in Figure 4.6. Furthermore, a comprehensive plot of the concentration dependence of $d\delta/dT$ is given in Figure 4.7. For all compositions investigated a linear upfield chemical shift is observed upon an increase in temperature. This trend is consistent with the temperature dependence of the ^1H NMR chemical shift observed for pure water that has been described as a result of the breakdown of water's hydrogen bonding network with increased temperature.²⁷⁻²⁸ However, there is a dramatic decrease in temperature dependence of the water chemical shift between pure water and the $R = 3$ zinc chloride hydrate as observed in Figures 4.6 and 4.7.

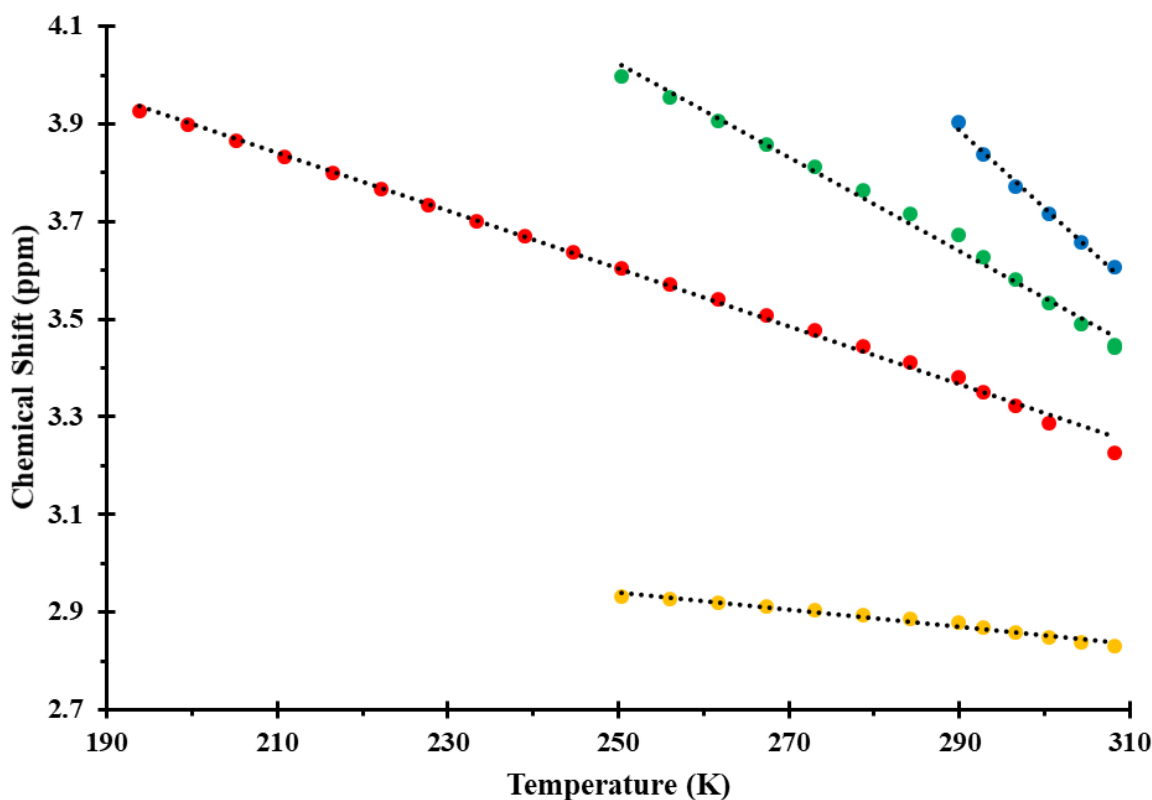


Figure 4.6 Temperature dependence of the ^1H NMR chemical shift of $R = 3$ (orange), $R = 9$ (red), $R = 21$ (green) aqueous zinc chloride solutions and pure water (blue) relative to ^6d -acetone.

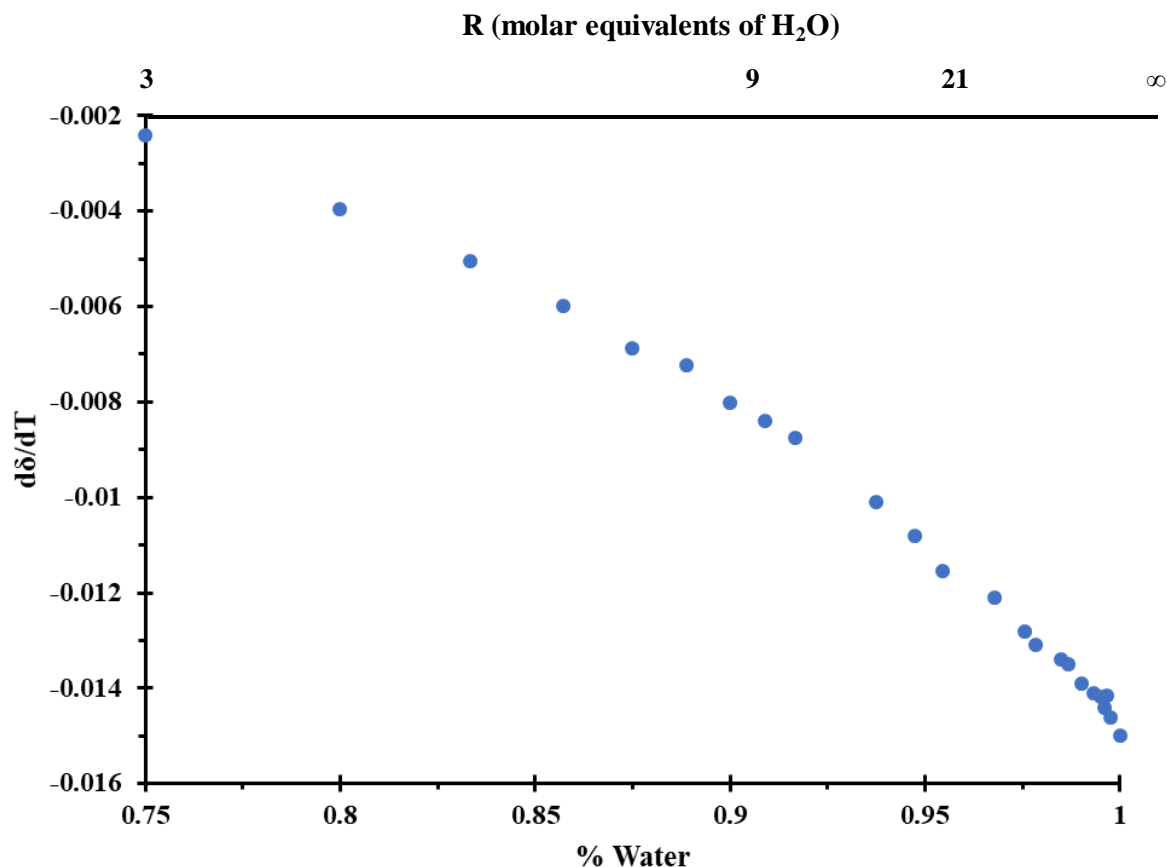


Figure 4.7 Dependence of the temperature variation as a function of % water in the aqueous zinc chloride solutions.

It is further interesting to note that, like the concentration dependent chemical shift (Figure 4.1) the temperature dependence ($d\delta/dT$) as a function of concentration, shown in Figure 4.7, also exhibits discontinuities. The overall trend seems to follow a relatively smooth curve, however, there appear to be significant changes in the concentration dependent trends at around $R = 9$ and $R = 100$ similar to the trend observed for the concentration dependent $ZnCl_2$ solutions.

4.4 Discussion

4.4.1 Temperature dependence of the 1H NMR spectra of aqueous $ZnCl_2$

As mentioned in the results section, the original purpose of the temperature dependent 1H NMR measurements was to resolve the different hydration shell environments. While separation

of the spectral peak was not observed at low temperature, important information can still be gleaned about the system based on the chemical shift dependence. As can be seen in Figures 4.6 and 4.7, pure water has a larger degree of change in its hydrogen environment as a function of temperature, observed as an upfield shift upon heating. It has been reported previously that the increase in electron density on the water hydrogens is associated with the breakdown of the hydrogen bonding network.²⁸ However, the diminished temperature dependence of the ^1H NMR chemical shift at high concentrations is indicative of stronger hydrogen bonding occurring between hydration shells. In particular, the discontinuity at $R = 9$ provides evidence of a distinct difference between the hydrogen bonding strength between the first and second hydration shells compared to others. As has been reported, based on ab initio calculations, the hydrogen bonding between the first and second shell is several times stronger than in pure water.²⁹ Additionally, while the temperature dependence as a function of concentration does increase at a faster rate at $R > 9$, it still does not equal the $d\delta/dT$ value of pure water, even at compositions of $R = 100$. This indicates that the Zn^{2+} ion continues to have a significant effect on the water beyond the second hydration shell.

4.4.2 Two-state model fit of concentration dependent ^1H NMR data from aqueous ZnCl_2 solutions

The existence of a single peak for the proton resonance, due to the fast exchange of protons compared to the timescale of the NMR measurement, makes direct observation of multiple hydrogen environments impossible.³⁰ However, a previous method for characterizing the ^1H NMR data has been to use what is known as the two-state model which proposes that the experimentally observed signal is a linear combination of chemical shifts from multiple different proton environments. To a first approximation, this model assumes that there are only two types

of water, those interacting with ions and bulk water. This leads to Equation 4.1 in which the total observed chemical shift, δ_{obs} , is determined as being the mole fraction weighted sum of the chemical shift of the hydrating waters and bulk water, δ_{solv} and δ_{bulk} , respectively.¹¹

$$\delta_{obs} = x_{solv}\delta_{solv} + x_{bulk}\delta_{bulk} \quad (4.1)$$

Past researchers have been unable to solve this equation directly due to the lack of knowledge regarding the value of δ_{solv} as well as the mole fraction of solvated water at a given concentration. However, because we know that all waters are bound directly to the zinc ion in the R = 3 hydrate, as discussed in Chapter 2 and reference 7, with six waters forming an octahedral complex around half of the zinc ions, giving us the hydration number as well as δ_{solv} , we can solve Equation 4.1 to determine the chemical shift at any given concentration. It is observed in Figure 4.8, however, that this two-state model provides a very poor fit to the experimentally measured data.

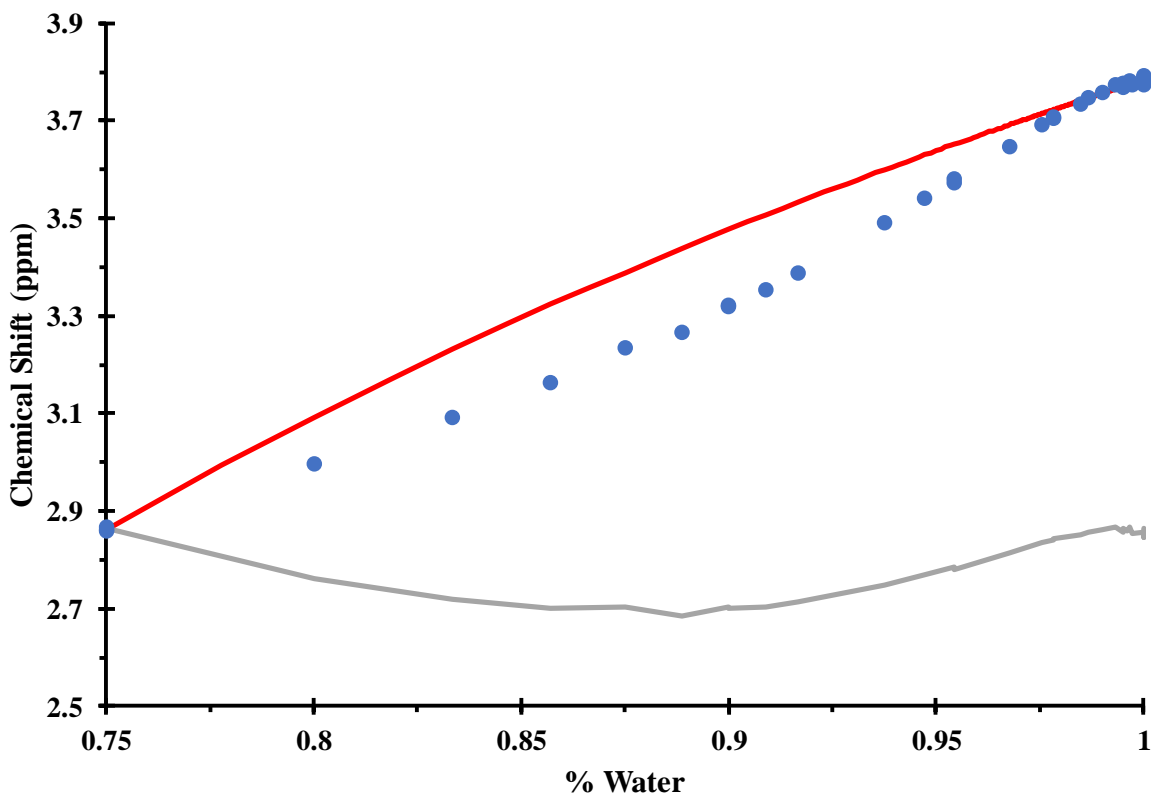


Figure 4.8 Fit of the ^1H NMR experimental data (blue) using the two-state model (red) along with the fit residuals (gray).

To investigate the extent of hydration utilizing two-state models^{6, 11}, it is assumed that the “effective” hydration number, that is the total number of waters with a chemical shift of δ_{solv} , can be determined through the measurement of the temperature dependent ^1H NMR. The determination of this effective hydration number is made possible by the rearrangement of Equation 4.1 in terms of the temperature derivative resulting in Equation 4.2 in which the mole fraction of solvated water is expressed in terms of the hydration number (h) and the molality (m).

$$\frac{d\delta_{\text{obs}}}{dT} = \left(\frac{hm}{55.55}\right) \frac{d\delta_{\text{solv}}}{dT} + \left(1 - \frac{hm}{55.55}\right) \frac{d\delta_{\text{bulk}}}{dT} \quad (4.2)$$

If it is then assumed that $d\delta_{\text{solv}}/dT = 0$, allowing for the removal of this term, Equation 4.3 is then obtained which can be easily solved for the hydration number.¹²

$$h = \frac{55.55}{m} \left[\frac{\frac{d\delta_{bulk}}{dT} \frac{d\delta_{obs}}{dT}}{\frac{d\delta_{bulk}}{dT}} \right] \quad (4.3)$$

However, a variation in chemical shift of -0.0017 ppm/°C is observed in the R = 3 aqueous ZnCl₂. Since all waters are solvating at this concentration this indicates a non-zero value for dδ_{solv}/dT, meaning that the above equation for effective hydration number does not hold for the zinc chloride system and a different means will need to be employed to determine the number and extent of waters interacting with the ions. Furthermore, it has been shown, both experimentally from incoherent quasi-elastic neutron scattering and computationally based on DFT calculations, that there are likely multiple water environments besides just bulk water and coordinated water around Zn²⁺ ions.^{31,32} Together these factors account for the poor fit of the above two-state model.

4.4.3 Multi-state model fit of concentration dependent ¹H NMR data from aqueous ZnCl₂ solutions

To address this issue, we have expanded Equation 4.1 to include additional water environments consisting of concentric hydration shells around the Zn²⁺ ion. The expansion of the two-state model can be seen in Equation 4.4 where multiple shells are proposed to hydrate the cation as has been previously suggested in the literature.²⁷

$$\delta_{obs} = x_1\delta_1 + x_2\delta_2 + \dots + x_{bulk}\delta_{bulk} \quad (4.4)$$

Next, we have to point out that there cannot be such a thing in the equation for the observed chemical shift as “third shell” water until an amount of water in the system, corresponding to a completely filled second shell, has been reached. This results in the total chemical shift of the system being described as a piecewise function of the following form:

$$\delta_{obs} = \begin{cases} \alpha\delta_1 + (1 - \alpha)\delta_2, & \text{if } 6 \leq R \leq 18 \\ \alpha\delta_1 + 2\alpha\delta_2 + (1 - 3\alpha)\delta_3, & \text{if } 18 < R \leq 42 \\ \alpha\delta_1 + 2\alpha\delta_2 + 4\alpha\delta_3 + (1 - 7\alpha)\delta_4, & \text{if } 42 < R \leq 90 \\ \alpha\delta_1 + 2\alpha\delta_2 + 4\alpha\delta_3 + 8\alpha\delta_4 + (1 - 15\alpha)\delta_5, & \text{if } 90 < R \leq 186 \\ \alpha\delta_1 + 2\alpha\delta_2 + 4\alpha\delta_3 + 8\alpha\delta_4 + 16\alpha\delta_5 + (1 - 31\alpha)\delta_6, & \text{if } 186 < R \end{cases} \quad (4.5)$$

Additionally, based on previous reports that the second hydration shell around zinc has twelve waters and, as was done for the diffraction fitting in Chapter 3, it is assumed that each hydration shell doubles the number of waters.³³ This means that the mole fraction in each shell can be defined in terms of the number of waters in the first hydration shell, which will be labeled as (h) and the value will be taken as 6 based on the data for the R = 3 hydrate. The value of (α) in Equation 4.5 can then be defined as:

$$\alpha = \frac{h-hx}{x} \quad (4.6)$$

Where (x) is related to the mole equivalents of water in the solution, as shown in Equation 4.7:

$$x = \frac{R}{1+R} \quad (4.7)$$

The first shell value, δ_1 , can be taken as the measured chemical shift for the R = 3 composition and the higher shell chemical shift values will become fitting parameters. Table 4.3 shows the number of waters used for each shell in the fitting model along with the calculated chemical shift values. Additionally, Figure 4.9 shows the fit of the data along with the residuals. While the overall better fit than the two-state model indicates that multiple hydration shells are necessary to describe the data, it is observed that beyond the second shell the calculated value for the chemical shift is close to that of pure water, experimentally found to be 3.784 ppm. This indicates that the most significant effect on water occurs in the first two hydration shells.

Table 4.3 Calculated fixed chemical shift values for the higher hydration shells along with the average experimentally measured chemical shift of the R = 3 hydrate.

Shell	Waters	Chemical Shift (ppm)
1 st	6	2.863
2 nd	12	3.515
3 rd	24	3.785
4 th	48	3.818
5 th	96	3.808
6 th	192	3.786

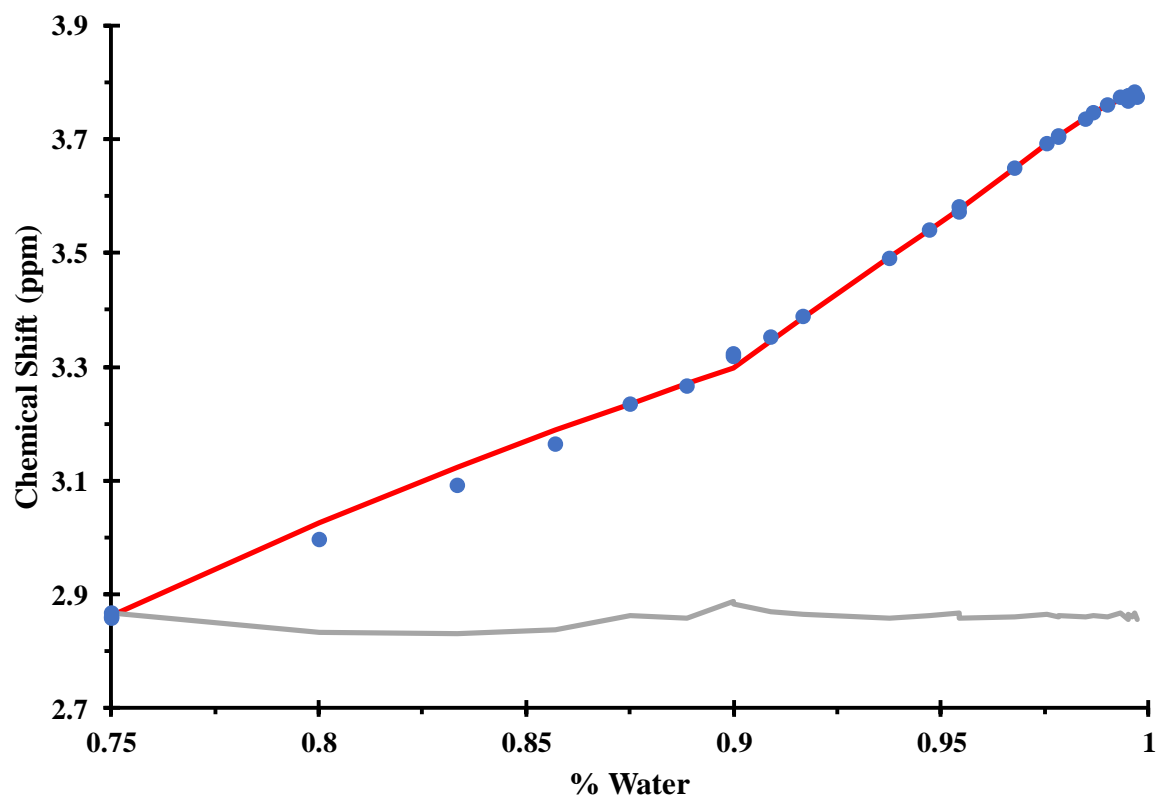


Figure 4.9 Fit of the ^1H NMR experimental data (blue) using the multi-state model with fixed chemical shift values (red) along with the fit residuals (gray).

Additionally, it should be pointed out that the piecewise function model provides a much better fit to the discontinuity in the data at R = 9, seen in Figure 4.9, than the previously described two-

state model. One justification for this is that the kink points observed in the mole fraction weighted data, which is not seen in the two-state fit, is a result of the addition of the term for the next hydration shell. In other words, below $R = 9$ there are only two terms in the equation corresponding to the first and second hydration shells. However, the kink at $R = 9$ in the experimental data is explained by the addition of a third term to the equation for calculating the observed chemical shift.

However, the fact that only a single proton peak, varying as a function of concentration, is observed in the solutions indicates that the hydrogen environment is highly sensitive to the composition of the sample. Thus, the chemical shift values assigned to each hydration shell will also likely vary as a function of concentration. In addition, the above mentioned two-state model, combined with a fixed-shell approximation, should be applicable with zinc chloride solutions between $R = 3$ and $R = 9$ because here we know the chemical shift of waters bound directly to the zinc and all additional waters should only be second shell. In this case, because we know the mole fractions for both proton environments, the two-state model should be able to be rearranged to solve for the chemical shift of the second shell waters. If the assumption that the chemical shift of waters in the different hydration shells do not change as a function of concentration were true, then the calculated value for the second shell chemical shift should be the same at each concentration between $R = 3$ and $R = 9$. The fact that this is not the case indicates that it is likely that the chemical shift value for each environment changes as a function of concentration. This would make sense given the fact that as the second shell is built up there is progressively more hydrogen bonding with the first shell. It has been suggested in the literature that the observed chemical shift of a sample is actually a complex summation of hydrogen bond breaking, structure directing, polarization, and electrostatic field interactions.³⁴

The complexities involved in deriving each of these terms from experimentally measured data are very difficult. However, an approximation can be reached in which the observed change in the chemical shift in each shell is calculated from the experimental data as a function of concentration. One thing that might support the need to have the chemical shift of the shells changing as a function of concentration is the temperature derivative data for the $R = 3$ hydrate which indicates that even when bound to the metal the electron density on the water hydrogens is still susceptible to changes whether it is from a change in temperature or the intermolecular interactions with other waters. Furthermore, there is computational evidence, utilizing the MP2/def2-QZVP method, that the hydrogen bonding interactions between first and second shells are stronger than in pure water which means that this should be even more likely to result in a noticeable change in chemical shift.²⁹ Water in the first shell is interacting directly with the ion which has much more of an effect on the polarization of the water.³⁵ Shown in Figure 4.10, is an idealized model of a zinc ion with three complete hydration shells around it, this would correspond to the $R = 21$ solution. With the help of this model we can begin to understand the shape of the variation in chemical shift in each hydration shell. As the second shell (blue) builds up around the first shell (red) upon dilution the direct hydrogen bonding between these two shells is expected to have a significant effect on the isolated first shell chemical shift, which is observed in the measurement of the $R = 3$ hydrate. However, once the second shell is complete, it effectively shields the first shell from interactions with higher hydration shells such as the third shell (green). This results in much less significant change in the chemical shift of the first shell at dilutions past the concentration at which the second shell is complete, in the case of our system this is proposed to occur at $R = 9$.

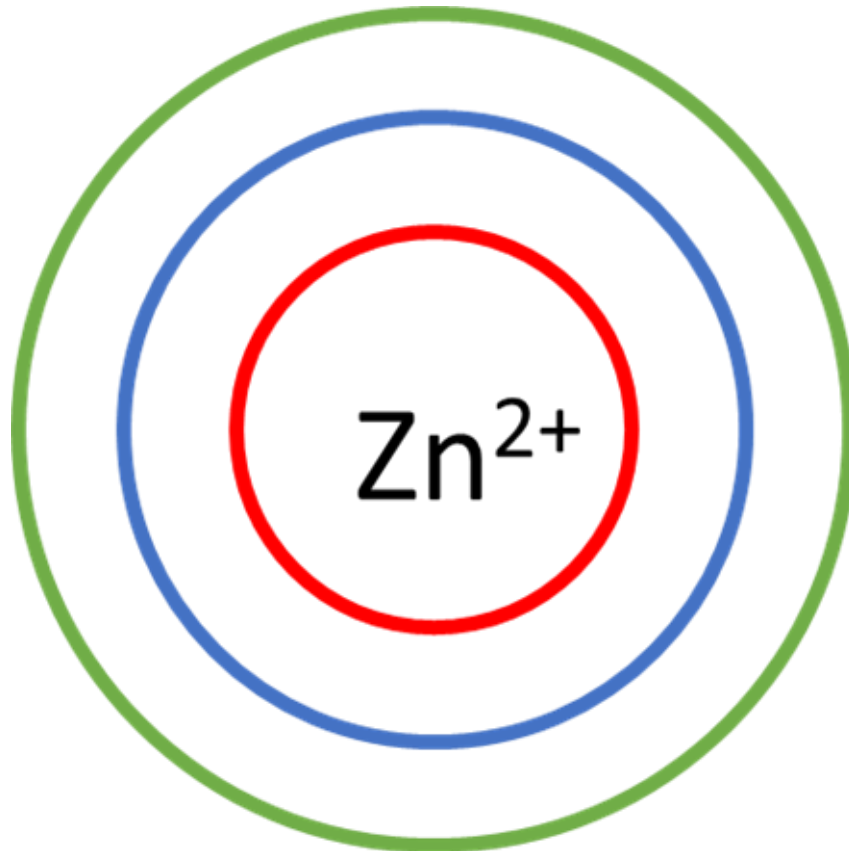


Figure 4.10 Simple concentric circular model displaying the increasing shell idea with the first hydration shell in red, second in blue and third in green.

To model this behavior an exponential function of the type $1 - e^{-kx}$ is found to be ideal because it allows for the magnitude of change to be significant when adjacent shells are being filled while decaying to very minimal change when higher shells are being filled. As can be observed in Figure 4.11, the function changes rapidly at lower values followed by much less change at higher values. This is the kind of behavior that is proposed for the waters in a specific hydration shell as the subsequent shell begins to form. This behavior is not unprecedented as it is similar to what is known to occur for electronic double layers. That is to say that the effect of an electrode surface on ions in solution decays exponentially with each successive layer of ions at the electrode surface.³⁶

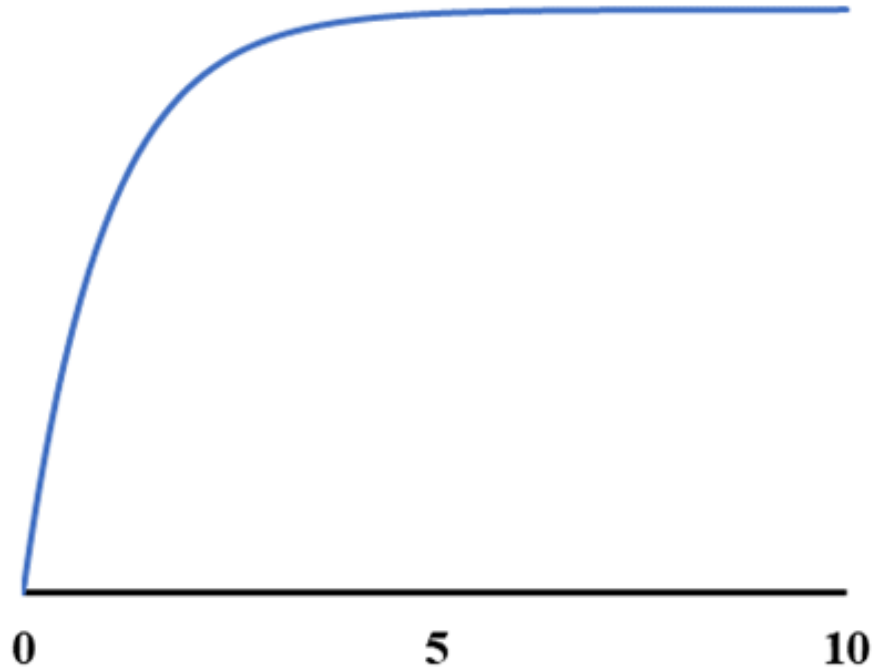


Figure 4.11 Plot of the exponential function $1 - e^{-kx}$ where $k = 1$.

Thus, the following exponential equations are proposed to determine the chemical shift of waters in each hydration shell as a function of concentration.

$$\delta_1 = \delta_{f_1} - (\delta_{f_1} - \delta_{i_1})e^{-k_1(R-h)} \quad (4.8)$$

$$\delta_2 = \delta_{f_2} - (\delta_{f_2} - \delta_{i_2})e^{-k_2(R-h-1)} \quad (4.9)$$

$$\delta_3 = \delta_{f_3} - (\delta_{f_3} - \delta_{i_3})e^{-k_3(R-3h-1)} \quad (4.10)$$

$$\delta_4 = \delta_{f_4} - (\delta_{f_4} - \delta_{i_4})e^{-k_4(R-7h-1)} \quad (4.11)$$

$$\delta_5 = \delta_{f_5} - (\delta_{f_5} - \delta_{i_5})e^{-k_5(R-15h-1)} \quad (4.12)$$

$$\delta_6 = \delta_{f_6} - (\delta_{f_6} - \delta_{i_6})e^{-k_6(R-31h-1)} \quad (4.13)$$

where

$$R = \left(\frac{x}{1-x} \right) \quad (4.14)$$

Notice that we now have unique equations in which δ_n is the chemical shift of the n^{th} hydration shell. Within each shell the chemical shift value for the first and last waters to be added are given by δ_i and δ_f , respectively. The magnitude of the change in the chemical shift value as waters are added is represented by the k parameter. The parameters for each of the hydration shells can be seen in Table 4.4.

Table 4.4 Calculated parameters for the exponential fit equations of the first four hydration shells.

Shell	Waters	δ_i	δ_f	k
1 st	6	2.863	2.998	0.626
2 nd	12	3.031	3.548	0.181
3 rd	24	3.553	3.777	0.077
4 th	48	3.741	3.811	0.037
5 th	96	3.774	3.816	0.010
6 th	192	3.784	3.778	0.001

Using these parameters, the observed chemical shift can be calculated and compared with the experimentally measured values. As can be seen in Figure 4.12, the residuals of these fit values are much more randomized, indicated that this model describes the experimental data over the entire measured range much better than the previously proposed two-state or fixed-shell models.

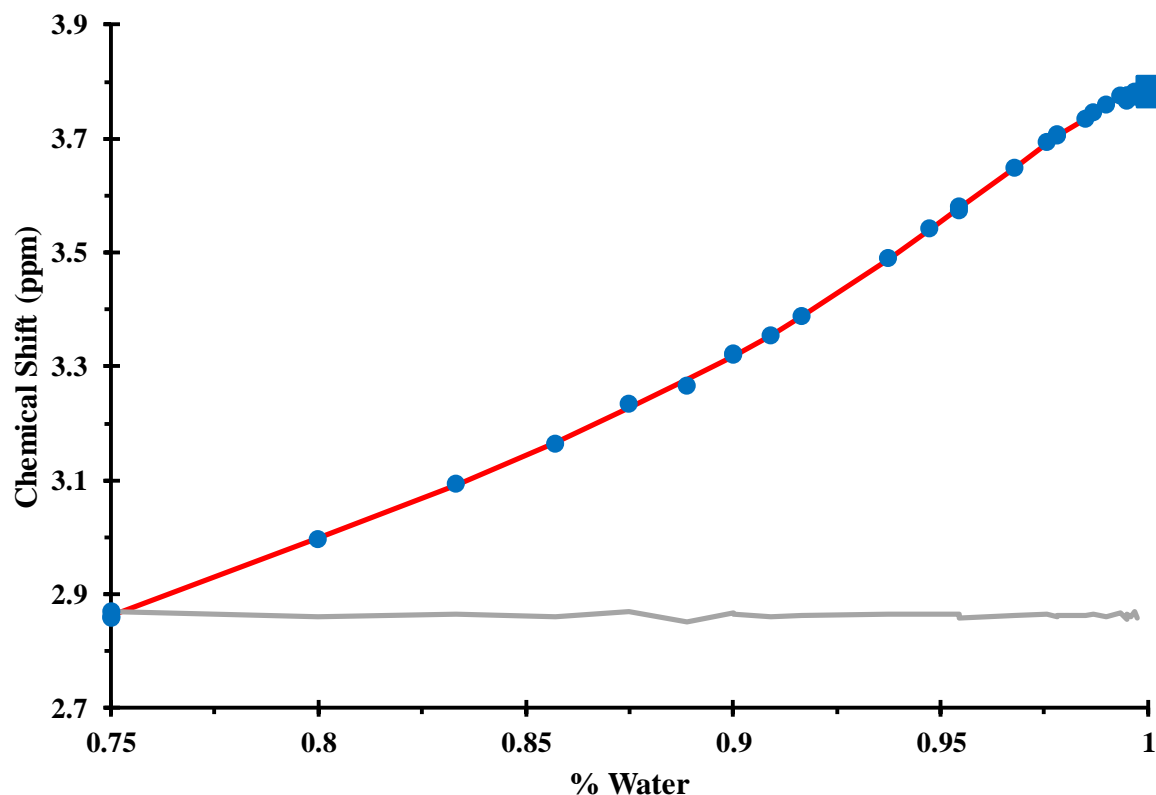


Figure 4.12 Fit of the ^1H NMR experimental data (blue) using the multi-state model with exponentially varying chemical shift values (red) along with the fit residuals (gray).

As with the fixed-shell model, when the third hydration shell is completed the calculated values for higher shells are close to the measured value for pure water. Even though the third shell ends with a value similar to that of pure water it was found that it was necessary to have up to six shells in order to properly fit the plateau that is observed in the experimental data in solutions more dilute than $R = 100$.

4.4.4 Multi-State fitting model applied to the ^1H NMR data of additional ionic salt solutions

The multi-state fitting model was also applied to eight additional salts, NaCl , CaCl_2 , MgCl_2 , AlCl_3 , $\text{Mg}(\text{SO}_4)$, $\text{Zn}(\text{SO}_4)$ and $\text{Al}_2(\text{SO}_4)$ as well as a 1:1 mixture of $\text{ZnCl}_2/\text{MgCl}_2$. Unlike the aqueous zinc chloride system in which information can be obtained regarding the first hydration shell, which was shown to be necessary for the multi-shell fitting model, the solubility

limit of the remaining salts examined, shown in Table 4.1, prohibits the obtaining of such information about their first hydration shells. However, the successful fitting of the zinc chloride data can be used as a template for fitting the remaining salts. In each of these cases there were assumed to be six hydrating waters around the cation and the anion was not explicitly considered. The experimental data along with the calculated fit can be seen for the sulfate salts as well as AlCl_3 in Figure 4.13 and for the remaining chloride salts in Figure 4.14. The hydration numbers used in each fit are shown in Table 4.5 and the fitting parameters can be found in Table A.1 (Appendix A). It is observed that, in both AlCl_3 and $\text{Al}_2(\text{SO}_4)_3$, four shells were necessary to fit the data where as MgSO_4 and ZnSO_4 only required two shells. This is in contrast to the larger numbers of shells needed for the MgCl_2 and ZnCl_2 solutions as well as the $\text{ZnCl}_2/\text{MgCl}_2$ mixture.

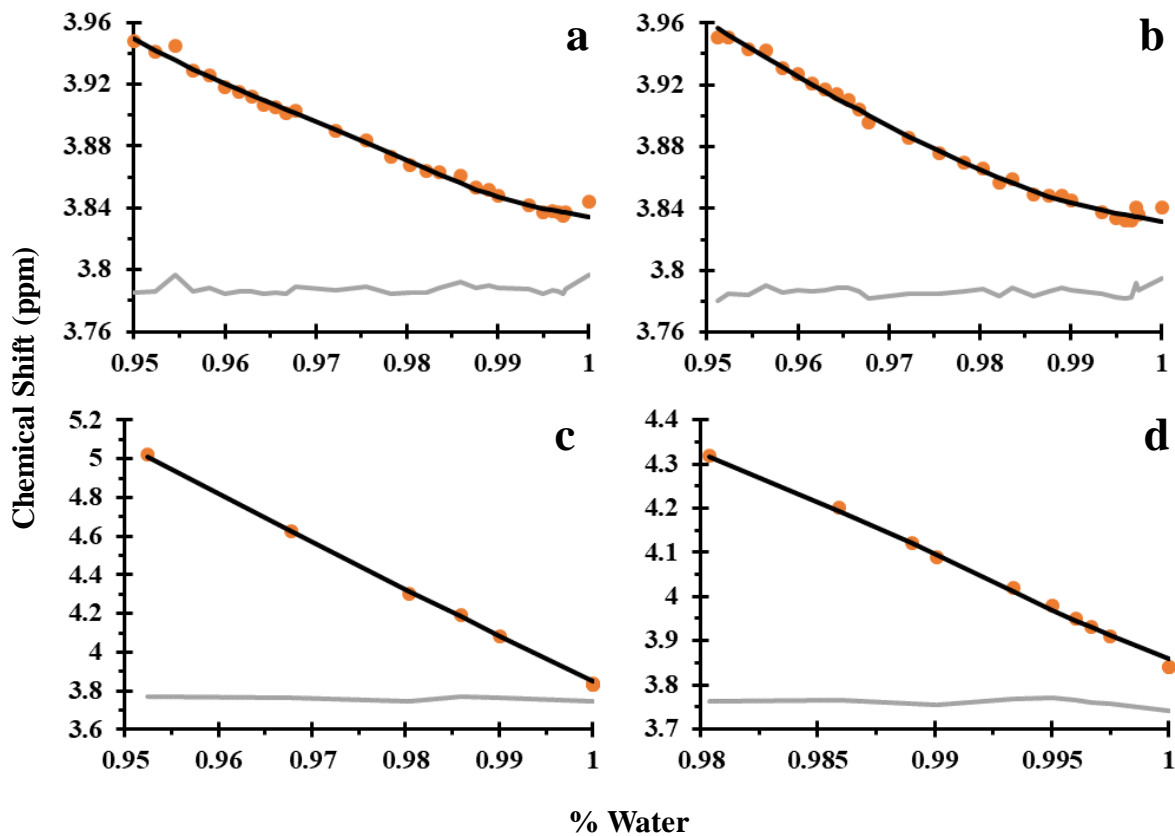


Figure 4.13 The calculated chemical shift (black) obtained from the application of the multi-state fitting model to the experimental data (orange) of a) Zn(SO₄), b) Mg(SO₄), c) AlCl₃ and d) Al₂(SO₄) along with the fit residuals (gray).

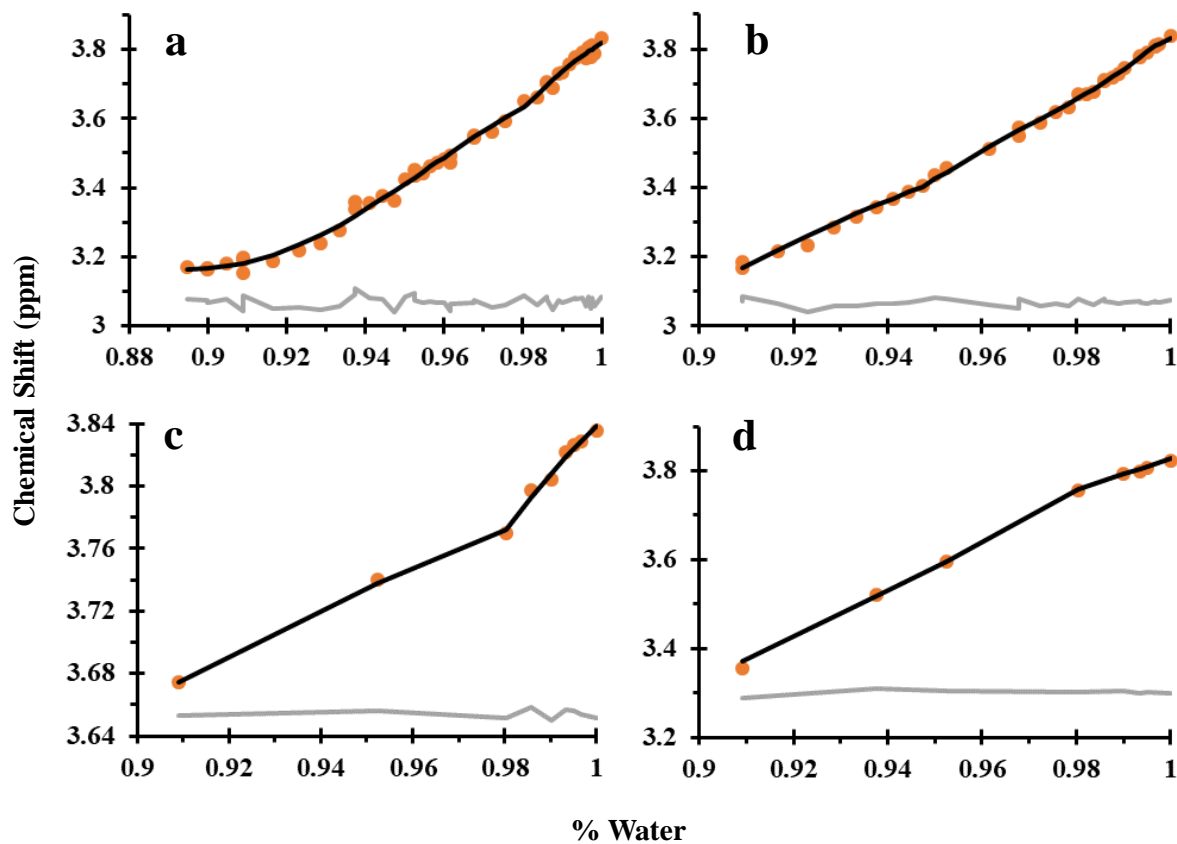


Figure 4.14 The calculated chemical shift (black) obtained from the application of the multi-state fitting model to the experimental data (orange) of a) CaCl₂, b) NaCl, c) MgCl₂ and d) 1:1 mixture of ZnCl₂/MgCl₂ along with the fit residuals (gray).

Table 4.5 The number of hydration shells that were necessary to sufficiently fit each of the additional salts examined.

Salt	Number of Hydration Shells
NaCl	3
CaCl ₂	4
MgCl ₂	4
AlCl ₃	4
Zn(SO ₄)	2
Mg(SO ₄)	2
Al ₂ (SO ₄) ₃	4
ZnCl ₂ /MgCl ₂	4

The low number of hydration shells needed to fit the ZnSO_4 and MgSO_4 solutions is likely associated with the increased water-water hydrogen bonding due to the higher structure making capability of sulfate relative to chloride.³⁷ Whereas the higher charge density of the aluminum ion results in the formation of additional hydration shells. When compared to literature values, each of these cations are observed to have higher than predicted hydration. Calcium and magnesium ions have been reported to have up to two hydration shells.¹⁷ Whereas Al^{3+} has been reported to have three hydration shells.¹⁹ Lastly, Na^+ has been proposed to only have a single hydration shell in aqueous solutions.³⁸

While both AlCl_3 and $\text{Al}_2(\text{SO}_4)_3$ have strong linear trends, the additional salts can be seen to deviate from this. The ZnSO_4 , MgSO_4 , and CaCl_2 have more polynomial shapes whereas the NaCl , MgCl_2 and $\text{ZnCl}_2/\text{MgCl}_2$ mixtures show evidence of distinct discontinuities. Additional investigation will be necessary to confirm the trends as well as to begin to understand the true structural features of the solutions resulting in their manifestations. However, despite the differences in shape, each of these datasets are well fit by the multi-state exponential model.

4.5 Conclusion

The fitting of the proton chemical shift shows strong evidence that several layers of hydration shells exist around the hydrated zinc ion. Additionally, it was found that to properly describe the ^1H NMR data the change in water chemical shift as a function of hydration shell filling needed to be accounted for via an exponential expression. Lastly, the newly developed fitting method is shown to be applicable to multiple salt solutions in which it predicts a higher degree of hydration than previously reported.

4.6 References

1. Amann-Winkel, K.; Bellissent-Funel, M.-C.; Bove, L. E.; Loerting, T.; Nilsson, A.; Paciaroni, A.; Schlesinger, D.; Skinner, L., X-ray and Neutron Scattering of Water. *Chemical reviews* **2016**, *116* (13), 7570-7589.
2. Smith, D. E.; Haymet, A., Structure and dynamics of water and aqueous solutions: the role of flexibility. *The Journal of Chemical Physics* **1992**, *96* (11), 8450-8459.
3. Wernet, P.; Nordlund, D.; Bergmann, U.; Cavalleri, M.; Odelius, M.; Ogasawara, H.; Näslund, L.-Å.; Hirsch, T.; Ojamäe, L.; Glatzel, P., The structure of the first coordination shell in liquid water. *Science* **2004**, *304* (5673), 995-999.
4. Kühne, T. D.; Khaliullin, R. Z., Nature of the asymmetry in the hydrogen-bond networks of hexagonal ice and liquid water. *Journal of the American Chemical Society* **2014**, *136* (9), 3395-3399.
5. Chaplin, M., A proposal for the structuring of water. *Biophysical chemistry* **2000**, *83* (3), 211-221.
6. Malinowski, E. R.; Knapp, P. S.; Feuer, B., NMR Studies of Aqueous Electrolyte Solutions. I. Hydration Number of NaCl Determined from Temperature Effects on Proton Shift. *The Journal of Chemical Physics* **1966**, *45* (11), 4274-4279.
7. Wilcox, R. J.; Losey, B. P.; Folmer, J. C. W.; Martin, J. D.; Zeller, M.; Sommer, R., Crystalline and Liquid Structure of Zinc Chloride Trihydrate: A Unique Ionic Liquid. *Inorganic Chemistry* **2015**, *54* (3), 1109-1119.
8. Wright, M. R., *An introduction to aqueous electrolyte solutions*. John Wiley & Sons: 2007.
9. Knapp, P. S.; Waite, R. O.; Malinowski, E. R., NMR Studies of Aqueous Electrolyte Solutions. III. Hydration of Sodium Perchlorate, Hydrochloric Acid, and Perchloric Acid from Temperature Effects on Proton Shifts. *The Journal of Chemical Physics* **1968**, *49* (12), 5459-5463.
10. Van der Maarel, J.; Lankhorst, D.; De Bleijser, J.; Leyte, J., Water dynamics in aqueous electrolyte solutions from proton, deuterium and oxygen-17 nuclear magnetic relaxation. *The Journal of Physical Chemistry* **1986**, *90* (7), 1470-1478.
11. Malinowski, E. R.; Knapp, P. S., NMR Studies of Aqueous Electrolyte Solutions. II. Hydration of Al(NO₃)₃ Determined from Temperature Effects on Proton Shift. *The Journal of Chemical Physics* **1968**, *48* (11), 4989-4991.
12. Vogrin, B. F. J.; Knapp, P. S.; Flint, W. L.; Anton, A.; Highberger, G.; Malinowski, E. R., NMR Studies of Aqueous Electrolyte Solutions. IV. Hydration Numbers of Strong

- Electrolytes Determined from Temperature Effects on Proton Shifts. *The Journal of Chemical Physics* **1971**, *54* (1), 178-181.
13. Creekmore, R. W.; Reilley, C. N., Nuclear magnetic resonance determination of hydration numbers of electrolytes in concentrated aqueous solutions. *The Journal of Physical Chemistry* **1969**, *73* (5), 1563-1568.
 14. O'Brien, J. T.; Williams, E. R., Coordination numbers of hydrated divalent transition metal ions investigated with IRPD spectroscopy. *The Journal of Physical Chemistry A* **2011**, *115* (51), 14612-14619.
 15. Nakamura, Y.; Shimokawa, S.; Futamata, K.; Shimoji, M., NMR relaxation study of water molecules in concentrated zinc chloride solutions. *The Journal of Chemical Physics* **1982**, *77* (6), 3258-3262.
 16. Bertini, I.; Fragai, M.; Luchinat, C.; Parigi, G., Solvent ¹H NMRD study of hexaquo chromium (III): inferences on hydration and electron relaxation. *Inorganic chemistry* **2001**, *40* (16), 4030-4035.
 17. Pavlov, M.; Siegbahn, P. E.; Sandström, M., Hydration of beryllium, magnesium, calcium, and zinc ions using density functional theory. *The Journal of Physical Chemistry A* **1998**, *102* (1), 219-228.
 18. Beret, E. C.; Galbis, E.; Pappalardo, R. R.; Sanchez Marcos, E., Opposite effects of successive hydration shells on the aqua ion structure of metal cations. *Molecular Simulation* **2009**, *35* (12-13), 1007-1014.
 19. Bergstroem, P. A.; Lindgren, J.; Read, M.; Sandstroem, M., Infrared spectroscopic evidence for second-sphere hydration in aqueous solutions of aluminum (3+), chromium (3+) and rhodium (3+). *The Journal of Physical Chemistry* **1991**, *95* (20), 7650-7655.
 20. Stangret, J.; Gampe, T., Ionic hydration behavior derived from infrared spectra in HDO. *The Journal of Physical Chemistry A* **2002**, *106* (21), 5393-5402.
 21. Waluyo, I.; Huang, C.; Nordlund, D.; Bergmann, U.; Weiss, T. M.; Pettersson, L. G.; Nilsson, A., The structure of water in the hydration shell of cations from x-ray Raman and small angle x-ray scattering measurements. *The Journal of Chemical Physics* **2011**, *134* (6), 064513.
 22. *ACD/NMR Processor Academic Edition*, 12.01; Advanced Chemistry Development, Inc.: Toronto, ON, Canada, 2010.
 23. *SpinWorks*, 4.2.3.0; Kirk Marat: Winnipeg, MB, 2016.

24. Frisch, M.; Trucks, G.; Schlegel, H.; Scuseria, G.; Robb, M.; Cheeseman, J.; Scalmani, G.; Barone, V.; Mennucci, B.; Petersson, G., Gaussian 09, Revision A. 1 [computer software]. Wallingford, CT, USA: *Gaussian* **2009**.
25. Shoolery, J. N.; Alder, B. J., Nuclear Magnetic Resonance in Concentrated Aqueous Electrolytes. *The Journal of Chemical Physics* **1955**, *23* (5), 805-811.
26. Roobottom, H. K.; Jenkins, H. D. B.; Passmore, J.; Glasser, L., Thermochemical radii of complex ions. *J. Chem. Educ* **1999**, *76* (11), 1570.
27. Modig, K.; Halle, B., Proton magnetic shielding tensor in liquid water. *Journal of the American Chemical Society* **2002**, *124* (40), 12031-12041.
28. Modig, K.; Pfrommer, B. G.; Halle, B., Temperature-dependent hydrogen-bond geometry in liquid water. *Physical review letters* **2003**, *90* (7), 075502.
29. Andrić, J. M.; Janjić, G. V.; Ninković, D. B.; Zarić, S. D., The influence of water molecule coordination to a metal ion on water hydrogen bonds. *Physical Chemistry Chemical Physics* **2012**, *14* (31), 10896-10898.
30. Kauzmann, W.; Eisenberg, D., *The structure and properties of water*. Clarendon Press: 1969.
31. Salmon, P.; Bellissent-Funel, M.-C.; Herdman, G., The dynamics of aqueous Zn²⁺ solutions: a study using incoherent quasi-elastic neutron scattering. *Journal of Physics: Condensed Matter* **1990**, *2* (18), 4297.
32. Bock, C. W.; Markham, G. D.; Katz, A. K.; Glusker, J. P., The arrangement of first- and second-shell water molecules around metal ions: effects of charge and size. *Theoretical Chemistry Accounts* **2006**, *115* (2-3), 100-112.
33. W. Rudolph, W.; C. Pye, C., Zinc(II) hydration in aqueous solution. A Raman spectroscopic investigation and an ab-initio molecular orbital study. *Physical Chemistry Chemical Physics* **1999**, *1* (19), 4583-4593.
34. Hindman, J. C., Nuclear Magnetic Resonance Effects in Aqueous Solutions of 1-1 Electrolytes. *The Journal of Chemical Physics* **1962**, *36* (4), 1000-1016.
35. Cauët, E.; Bogatko, S.; Weare, J. H.; Fulton, J. L.; Schenter, G. K.; Bylaska, E. J., Structure and dynamics of the hydration shells of the Zn²⁺ ion from ab initio molecular dynamics and combined ab initio and classical molecular dynamics simulations. *The Journal of Chemical Physics* **2010**, *132* (19), 194502.
36. Stojek, Z., The electrical double layer and its structure. In *Electroanalytical methods*, Springer: 2010; pp 3-9.

37. Tobias, D. J.; Hemminger, J. C., Getting specific about specific ion effects. *Science* **2008**, *319* (5867), 1197-1198.
38. Mancinelli, R.; Botti, A.; Bruni, F.; Ricci, M. A.; Soper, A. K., Hydration of Sodium, Potassium, and Chloride Ions in Solution and the Concept of Structure Maker/Breaker. *The Journal of Physical Chemistry B* **2007**, *111* (48), 13570-13577.

CHAPTER 5

Analysis of the Waters of Hydration in Aqueous Zinc Chloride Solutions Via Vibrational Spectroscopy

5.1 Introduction

Water and aqueous solutions are ubiquitous in nature as well as industrial applications. Not only have decades of research been focused on understanding the structure of pure water¹⁻³ but much work has also been done on understanding the interactions of pure water with dissolved ions (i.e. aqueous solutions).⁴⁻⁶ Experimental studies have included X-ray⁷⁻¹¹ and neutron diffraction¹¹⁻¹⁴, Raman¹⁵⁻¹⁸ and IR¹⁹⁻²² spectroscopy as well as NMR²³⁻²⁶ and EXAFS²⁷⁻²⁹ investigating water and solution structure. Additionally, computational work has also been performed utilizing bulk methods like molecular dynamics (MD) and Monte Carlo (MC) simulations to examine both pure water³⁰⁻³⁴ and aqueous solutions, including those of zinc chloride.³⁵⁻³⁶ Lastly, electronic structure calculations such as Density functional theory (DFT) have been used to investigate the formation and stability of molecular complexes and the hydration of individual ions in aqueous solutions.³⁷⁻³⁹ However, despite all of this work there is still much disagreement in the literature, not only about the structure of pure water but also about aqueous solutions. Some of the more important questions yet to be resolved are, to what distance does an ion effect the structure (i.e. hydrogen bonding network) of pure water and how many hydration shells form around ions in solution. Past researchers have utilized infrared and Raman spectroscopy to examine the temperature⁴⁰⁻⁴¹, pressure⁴²⁻⁴³ and ion concentration^{17-18, 44-45} dependence of the vibrational modes of water. From these examinations it has been found that the vibrational modes of water are very sensitive to the hydrogen bonding environment as well as the hydration shell structure of ions based on the change in peak frequency, width and shape in

the spectrum. Thus, vibrational spectroscopy is well suited to investigate the questions regarding solution structure outlined above.

Despite the decades of work, there is still a substantial amount of disagreement about the origin of the peaks observed in the vibrational spectrum of liquid water. A single water molecule has C_{2v} symmetry resulting in two symmetric (one stretching and one bending) and one asymmetric (stretching) vibrational modes. In the gas phase, these vibrational modes are clearly observed at 3652 and 3756 cm^{-1} for the symmetric and asymmetric stretching modes, respectively and 1595 cm^{-1} for the HOH bending mode. In liquid water excitations occur at 1645, 3277 and 3490 cm^{-1} which have been assigned, by some researchers, as belonging to the same C_{2v} modes observed in gas phase water, albeit shifted due to the formation of hydrogen bonding.⁴⁶⁻⁴⁷ In the case of liquid water, the symmetric and asymmetric stretching modes result in a broad stretching band feature which is reported to also contain the first overtone of the water bending mode.⁴⁶⁻⁴⁷ In keeping with the molecular interpretation, there have also been reports of clear evidence of the influence of intermolecular coupling (i.e. hydrogen bonding) on the overall spectrum as well as the role of Fermi resonance between the bending overtone and the symmetric stretching modes playing a significant role in the complex stretching band region of the liquid water spectrum.^{40, 45, 48-50} However, other literature reports claim that the complexity of the stretching band region results from varying degrees of hydrogen bonding between water molecules with the lower frequency peaks ($\sim 3200 \text{ cm}^{-1}$) corresponding to the stronger hydrogen bonding while the higher frequency region ($\sim 3600 \text{ cm}^{-1}$) are very weakly hydrogen bonded or what some label as “free water”.^{15, 51-54}

Attempts to deduce the effects of ions on the structure of water using vibrational spectroscopy have been made through the use of factor analysis (FA)^{21, 55-56}, multivariate curve

resolution (MCR)^{17, 57-59}, difference spectroscopy^{22, 51, 60-61}, ratiometric Raman¹⁸ and deconvolution of the stretching band profile through Gaussian fitting.⁶²⁻⁶⁵ Each of these methods were used in an attempt to determine the fundamental components of the measured spectra in order to better understand the true nature of aqueous solutions. Previous vibrational studies have proposed that there are only two “types” of water in aqueous solutions, those bound directly to the ions and bulk-type water.^{21, 55-56, 66-67} This is supported by additional studies that have shown that the vibrational spectra of pure water is unaffected past the first hydration shell. For example, it has been reported, from diffraction measurements of sodium and potassium halides as well from femtosecond pump-probe spectroscopy of Mg(ClO₄)₂, NaClO₄, and Na₂SO₄, that the “ice-like” structure of pure water is unaffected beyond the first hydration shell of these ions.^{28, 68-69} However, while features similar to those of pure water can be seen in both the PDF and structure factor data of diffraction measurements on aqueous solutions⁶⁸; it is unclear as to whether these features indicate the presence of the “pure” water structure on an intermediate range scale within the solution or if these features in the diffraction pattern correspond primarily to the local environment around each water molecule arranged in multiple layers of hydration shells surrounding the ions. It has recently been reported, based on femtosecond elastic second harmonic scattering (fs-ESHS) measurements of multiple electrolytes, that ions can effect water structure to concentrations as low as 10 μM.⁷⁰

In addition to understanding pure liquid water, much work has also been done to understand how water molecules interact directly with ions. Neutron and X-ray diffraction methods have been heavily utilized for examining the direct coordination of water to ions such as for Zn²⁺ in which octahedral coordination has been reported with an M-O distance of 2.17 Å.⁸ Additionally, Raman spectroscopy has been utilized to investigate the hydration of Zn²⁺ and also

proposed an octahedral coordination with Zn-O stretching frequency of 390 cm^{-1} .⁷¹ Furthermore, variable temperature NMR has been utilized to determine the nature of hydration in aqueous NaCl solutions and found that Na^+ ions were coordinated by four water molecules.²⁶ However, while most researchers assume only a single hydration shell around ions, molecular dynamics^{27, 71-72}, EXAFS⁷³ and XRD⁷⁴ have shown the existence of a second hydration shell around Zn^{2+} with an M-O distance of $\sim 4.2\text{ \AA}$. Furthermore, vibrational spectroscopic studies of alkali salts^{59, 61} as well as Al^{3+} , Cr^{3+} and Rh^{3+} have also suggested the existence of a second hydration shell.²² Lastly, there have even been reports, based on electronic structure calculations, that have proposed up to three hydration shells being observed for Ca^{2+} and Zn^{2+} .^{37, 75}

As reported in the preceding chapters, the remarkably high solubility of zinc chloride, 432 g/100 mL of H_2O at $25\text{ }^\circ\text{C}$, allows for the unique situation in which solvated water can be directly measured. Here we performed ATR-IR as well as isotropic and polarized Raman spectroscopy to examine the water bending and stretching mode regions as a function of zinc chloride concentration. By utilizing the high solubility of ZnCl_2 the two-state model of vibrational spectra was tested, and it was found that to properly fit the data multiple hydration shells were required indicating that the effects of the ions on the water structure extend further than many previous reports have claimed.

5.2 Experimental Methods

5.2.1 Materials and synthesis

Reagent grade zinc chloride was obtained from Aldrich and doubly sublimed at $400\text{ }^\circ\text{C}$ for approximately 24 hours under dynamic vacuum. Following sublimation, the material, analyzed via powder X-ray diffraction (XRD) and differential scanning calorimetry (DSC), was confirmed to be $\delta\text{-ZnCl}_2$ (m.p. $317\text{ }^\circ\text{C}$), which has been previously reported to be the most anhydrous phase.⁷⁶

The sublimed ZnCl_2 was stored under nitrogen atmosphere in a glovebox. Aqueous zinc chloride solutions were then made on the benchtop using 18 M Ω H_2O , obtained from a Millipore Synergy ultrapure water filtration system.

5.2.2 Raman spectroscopy

Raman solutions were made by first making an $R = 3$ (75% water) solution. This solution was then diluted in-situ to obtain the additional desired sample concentrations. This method was confirmed to be valid in a separate set of experiments in which samples of $R = 3, 9,$ and 21 were made $2, 24,$ and 48 hours prior to analysis as well as an additional sample prepared immediately before being placed in the instrument. Examination of these samples confirmed that there was no statistically significant difference between them and thus the in-situ dilution method was confirmed to be valid with no significant aging of the samples necessary. Using the above-mentioned method, three separate sets of Raman measurements were taken in the spectral region of 60 to 2200 cm^{-1} , two of which ranged in concentration from $3 \leq R \leq 250$ while the third ranged from $3 \leq R \leq 100$. Two data series ranging in concentration from $3 \leq R \leq 100$ and $2.75 \leq R \leq 845$ were made for measurements in the spectral region of 1800 to 4000 cm^{-1} . In each case toluene was used as a calibration standard. Raman spectra of the aqueous zinc chloride solutions were collected using a Coherent Ar/Kr laser operating at 488 nm with a power of 30 A . A PIXIS charge coupled device (CCD) detector was used.

5.2.3 Infrared spectroscopy

A set of infrared spectra were collected in the concentration range of $2.03 \leq R \leq 229.38$ in the spectral range of 0 to 7900 cm^{-1} using a Digilab FTS-3000 Fourier transformed infrared (FT-IR) spectrometer with a mounted crystalline germanium, attenuated total internal reflection (ATR) sampling attachment (Pike Technologies inc., MIRacle™ Single Reflection ATR). A second set

of IR measurements were taken in the range of $3 \leq R \leq 275$ in a spectral range of 400 to 4000 cm^{-1} using a Shimadzu IRPrestige-21 (FT-IR) spectrometer also with a germanium ATR attachment (Pike Technologies inc., GladiATR). In each case a droplet of aqueous zinc chloride or pure water was pipetted onto the ATR crystal. The infrared light was focused onto the photodiode of a liquid nitrogen-cooled, narrow band mercury-cadmium-telluride (MCT) (Digilab) or a standard DLATGS (Shimadzu) detector. In the case of the Digilab FTS-3000, the spectrometer was purged with dry nitrogen, which reduces atmospheric water or CO_2 contamination in the spectral beam path. However, for the Shimadzu IRPrestige-21 no instrument purge was performed. Spectra were recorded at room temperature, approximately $23 (0.5)^\circ\text{C}$ with a resolution of 1 cm^{-1} (Digilab) and 2 cm^{-1} (Shimadzu). The spectra were converted into absorbance units by taking the negative of the log ratio of a sample spectrum to that of an empty crystal.

5.3 Results

5.3.1 Examination of the 2800 to 4000 cm^{-1} spectral region

Raman and IR measurements of the stretching modes of water have been analyzed in past studies of multiple aqueous solutions^{19, 51, 53, 65} including those of zinc chloride^{63, 77} across a wide range of concentrations. The “stretching” mode actually consisting of a complex band profile in the frequency region of 2800 to 4000 cm^{-1} which has been proposed to consist of the vibrational features attributed to C_{2v} water, namely the first overtone of the bending mode combined with the symmetric and asymmetric stretching modes.⁴⁶ However, others have proposed that the stretching band features arise from the stretching modes of water molecules in different hydrogen bonding environments.⁵¹ Not only has there been disagreement about the true identity of these modes in pure water but there have also been various proposals about how the features in this region are effected by the presence of ions in solution.^{17, 46, 53, 55, 65-66, 78-79} Here we have examined the

stretching mode of water in aqueous zinc chloride solutions from a concentration of $R = 2.75$ (73% water) to that of pure water via ATR-IR spectroscopy as well as isotropic and polarized Raman spectroscopy.

Isotropic Raman data were collected for aqueous zinc chloride solutions in the spectral region from 2300 to 4000 cm^{-1} . Two separate dilution series were prepared, (D1) in the concentration range of 3 (75% water) $\leq R \leq 100$ (99% water) and (D2) across the concentration range 2.75 (73% water) $\leq R \leq 845$ (99.9% water). Both sets of dilutions were prepared via the iterative dilution scheme outlined in section 5.2.2.

Representative Raman spectra from dilution series (D1), $3 \leq R \leq 100$, plus that of pure water are shown in Figure 5.1 in the spectral region of 2800 to 4000 cm^{-1} . The major features of the spectra consist of a strong absorption in the region of $\sim 3400 \text{ cm}^{-1}$ with weaker peaks occurring at approximately 3200 and 3600 cm^{-1} . The main peak, observed at $\sim 3490 \text{ cm}^{-1}$ for the $R = 3$ hydrate, blue shifts to $\sim 3510 \text{ cm}^{-1}$ for the $R = 6$ composition, as shown in Figure 5.2. At concentrations more dilute than $R = 6$ the main peak red shifts with an approximate linear trend having a slope of -632 (30). Both the 3200 and 3600 cm^{-1} peaks are observed to diminish in intensity upon addition of zinc chloride to pure water.

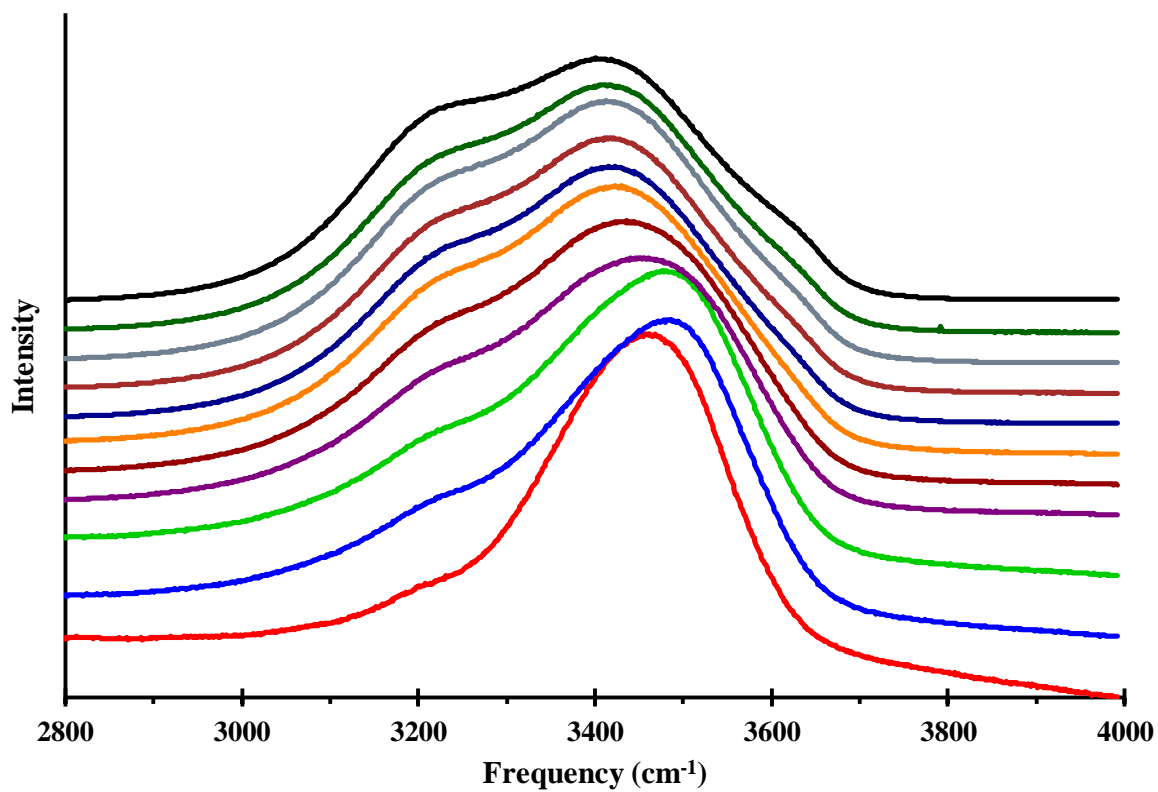


Figure 5.1 Isotropic Raman spectra of aqueous zinc chloride solutions of composition R = 3 (red), R = 6 (blue), R = 9 (green), R = 15 (purple), R = 21 (dark red), R = 35 (orange), R = 45 (dark blue), R = 60 (brown), R = 80 (gray), R = 100 (dark green) and pure water (black).

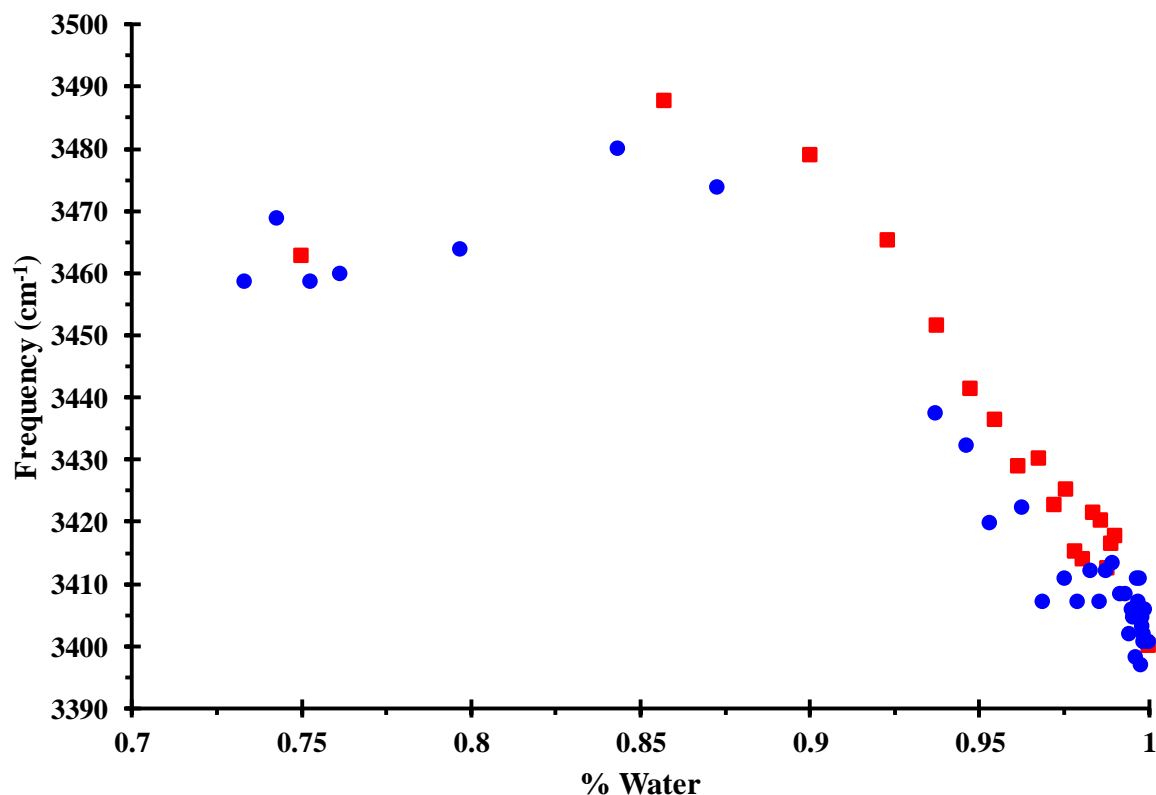


Figure 5.2 Concentration dependence of the main spectroscopic feature for dataset D1 (red) and D2 (blue).

In addition to the Raman measurements, two separate sets of IR data were also collected. Because of the smaller sample size required for ATR-IR measurements compared to that of the Raman experiments, solutions for each dilution series were prepared fresh at each composition. The first dataset (A1) was in the concentration range 2.03 (67% water) $\leq R \leq 229.38$ (99.57% water) and were collected over a spectral range from 0 to 7900 cm^{-1} . The second set (A2) was from $3 \leq R \leq 275$ (99.64% water) and collected in the spectral range of 400 to 4000 cm^{-1} .

Shown in Figure 5.3 is the IR spectra of the dilution series (A1), $2.03 \leq R \leq 229.38$, along with pure water. The main peak is observed at $\sim 3400 \text{ cm}^{-1}$ with an intense shoulder at 3200 cm^{-1} and a very weak shoulder at approximately 3600 cm^{-1} . When compared to the Raman data, Figure 5.1, the shoulder at 3200 cm^{-1} is noticeably more intense in the IR spectra. As with the Raman

data, the main peak in the IR data has an initial blue shift of $\sim 10 \text{ cm}^{-1}$ upon dilution, shown in Figure 5.4, with its highest frequency value occurring at a composition of $\sim R = 5$. Upon further dilution there is a linear trend from $5 \leq R \leq 9$ with a slope of $-437 (20)$. Unlike the Raman data, however, there is a distinct change in slope to $-347 (52)$ past the $R = 9$ composition. It can also be observed in Figure 5.3 that the 3200 and 3600 cm^{-1} peaks both are greatly diminished in intensity upon addition of zinc chloride.

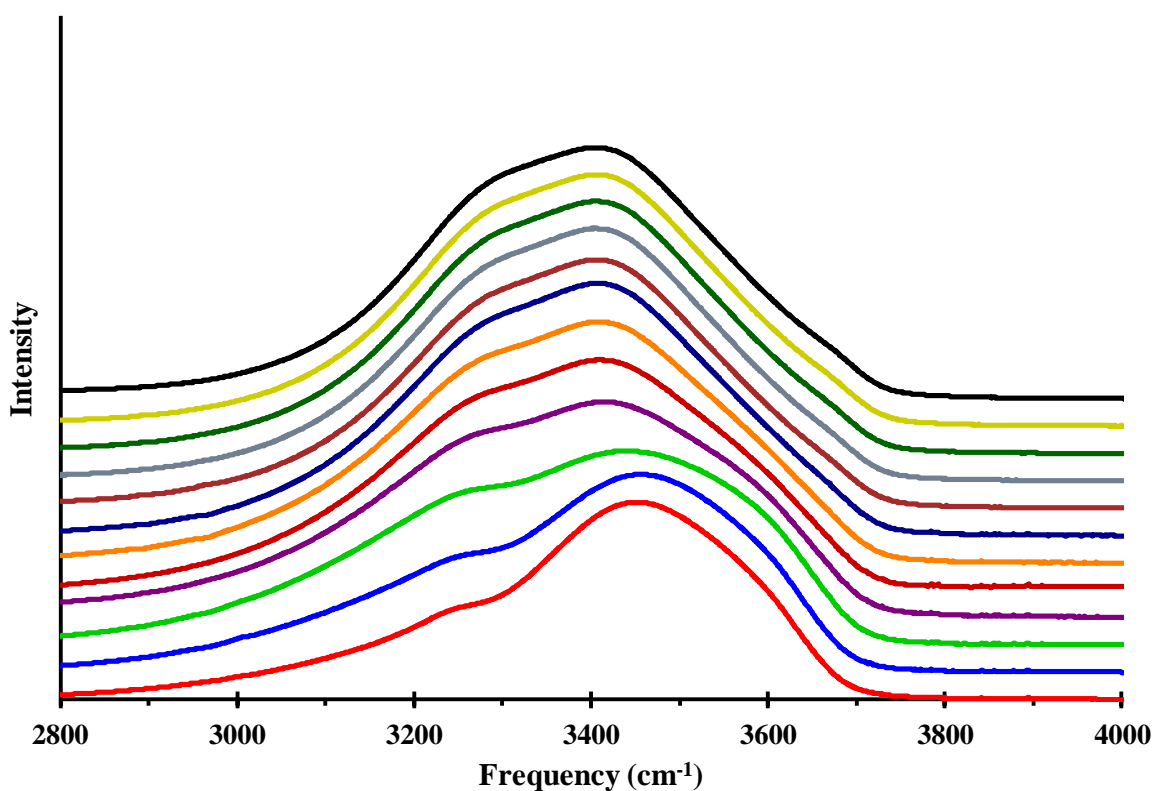


Figure 5.3 ATR-IR spectra of aqueous zinc chloride solutions of composition $R = 2.03$ (red), $R = 3.09$ (blue), $R = 5.99$ (green), $R = 9.96$ (purple), $R = 14.63$ (dark red), $R = 20.69$ (orange), $R = 37.71$ (dark blue), $R = 57.58$ (brown), $R = 87.01$ (gray), $R = 120.67$ (dark green), $R = 229.38$ (yellow) and pure water (black).

likely the symmetric and asymmetric water stretching modes, respectively. Evidence of this is also observed in the apparent depolarization ratio of this peak which is much less than 0.75. This is because the peak in the parallel spectrum is a combination peak, whereas the perpendicular peak consists of only the depolarized asymmetric mode. Lastly, the shoulder at round 3600 cm^{-1} is also observed to be a depolarized mode.

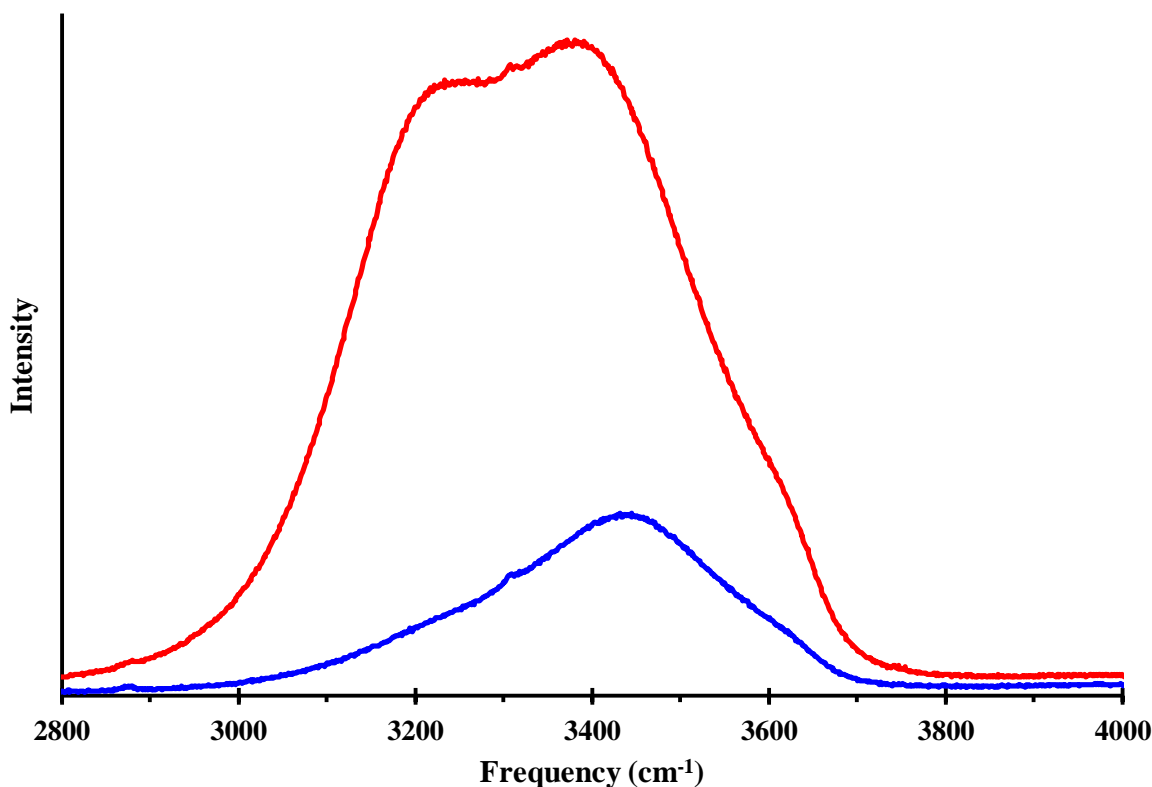


Figure 5.5 Polarized Raman spectra of pure water. Parallel alignment (red) and perpendicular alignment (blue).

5.3.2 Examination of the $1500\text{ to }1800\text{ cm}^{-1}$ spectral region

The water bending mode has been previously investigated both in pure water⁸⁰⁻⁸² and in aqueous solutions.^{59, 83-85} Of particular interest is the connection of the bending mode to the stretching band region in the form of the first overtone ($2\nu_2$) and the potential Fermi resonance between this mode and the fundamental transition of the symmetric stretching mode (ν_1).^{40, 45, 48-}

^{50, 86} Here we have examined the water bending mode region, from 1500 to 1800 cm^{-1} , using ATR-IR and isotropic Raman spectroscopy in the concentration range from $R = 2.75$ to that of pure water.

In the region of the water bending mode, isotropic Raman spectra were collected for three unique dilution series of aqueous zinc chloride solutions, two (B1 and B2) in the concentration range 3 (75% water) $\leq R \leq 250$ (99.6% water) and one (B3) across the concentration range $3 \leq R \leq 100$ (99.0% water). As with the Raman measurements performed in the water stretching band region, the series were prepared using the in-situ dilution scheme outlined in section 5.2.2. Raman data were collected from 60 to 2200 cm^{-1} , however, the region from 1500 to 1800 cm^{-1} is examined here to look at the water bending mode.

Representative Raman spectra from dilution series B1, $3 \leq R \leq 250$, plus that of pure water are shown in Figure 5.6 across the entire measured spectral range. The low frequency features of the spectra at approximately 290 and 390 cm^{-1} correspond to the ZnCl_4^{2-} and $\text{Zn}(\text{H}_2\text{O})_6^{2+}$ symmetric stretching modes, respectively, which were discussed in Chapter 3. Additionally, in the low frequency region, between approximately 200 cm^{-1} and the low wavenumber instrumental limit, significant Rayleigh scattering is observed. Of interest here is the peak at ~ 1640 cm^{-1} which is observed to be very weak due to the strong luminescent background which is increasingly dominant at higher wavenumbers. The lower intensity features at approximately 1100 cm^{-1} , 800 cm^{-1} and below 500 cm^{-1} have been discussed as being characteristic absorptions of the water librational modes.⁴⁶ These lower frequency excitations become more apparent at compositions $R \geq 21$, however, additional focus will not be given to these features here due to the low signal-to-noise ratio in this region, particularly at higher concentrations.

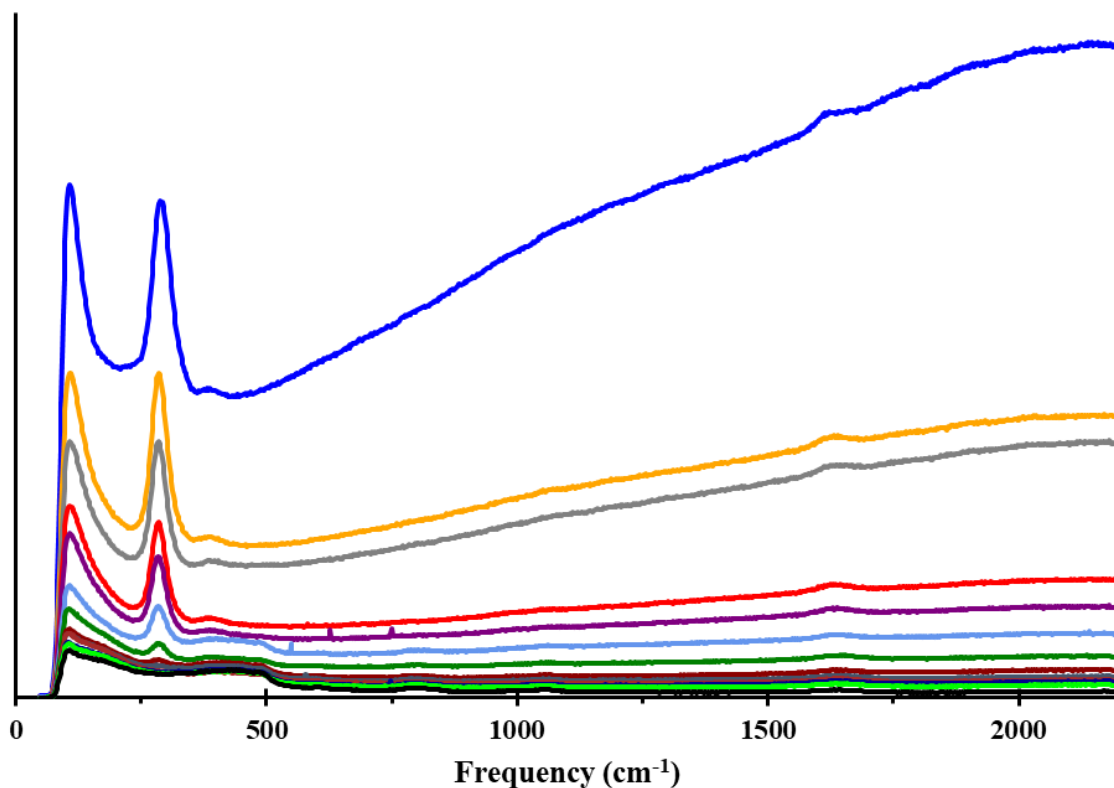


Figure 5.6 Raman spectra of the zinc chloride hydrates for dilution series D1 R = 3 (blue), R = 6 (orange), R = 9 (gray), R = 12 (red), R = 15 (purple), R = 21 (light blue), R = 40 (green), R = 60 (dark red), R = 80 (blue-gray), R = 100 (brown), R = 175 (dark blue), R = 250 (light green), and pure H₂O (black).

Due to the intense luminescent background, particularly in the higher concentration samples, singular value decomposition (SVD) was applied independently to each of the three dilution series in the spectral region of 1500 to 1800 cm⁻¹. The methods utilized for SVD analysis have been previously described in Chapter 3 and reference 87. The Raman spectra of each series were aggregated into an $\mathbf{m} \times \mathbf{n}$ data matrix \mathbf{A} , where \mathbf{m} is the number of frequency values in each spectrum and \mathbf{n} is the number of measured spectra. These concentration-dependent data were deconvoluted into two sets of orthonormal basis functions according to Equation 5.1

$$\mathbf{A} = \mathbf{U}\mathbf{\Sigma}\mathbf{V}^T \quad (5.1)$$

where the left singular matrix \mathbf{U} corresponds to the concentration-independent basis vectors (i.e., components of the total data), the right singular matrix \mathbf{V}^T corresponds to their concentration dependence and $\mathbf{\Sigma}$ is composed of singular values (i.e., weighting factors) that describe the contribution of the corresponding singular vectors and are sorted in decreasing magnitude. The first two components, \mathbf{u}_1 and \mathbf{u}_2 , respectively represent approximately 97% and 2% of the original \mathbf{A} matrix. The remaining 1% of the data is spread across 21 and 17 additional basis vectors for datasets (B1 and B2) and (B3), respectively. These basis vectors have no apparent physical interpretation (i.e. noise). Shown in Figure 5.7 are the first two SVD components along with their respective loadings for all three datasets. Component 1 is observed to have a single peak present at $\sim 1625 \text{ cm}^{-1}$ with the corresponding loadings indicative of diminished peak intensity upon dilution. Furthermore, observed in this component is the luminescent background which increases at higher wavenumber as seen in the raw spectra. Component 2 contains a peak at $\sim 1645 \text{ cm}^{-1}$ with its corresponding loadings indicating that this feature increases in intensity upon dilution. Based on the peak positions in each component along with the observation of the luminescent background in component 1, it can be surmised that component 1 corresponds to the high concentration spectra (primarily the $R = 3$ hydrate) and component 2 corresponds to the spectrum of pure water.

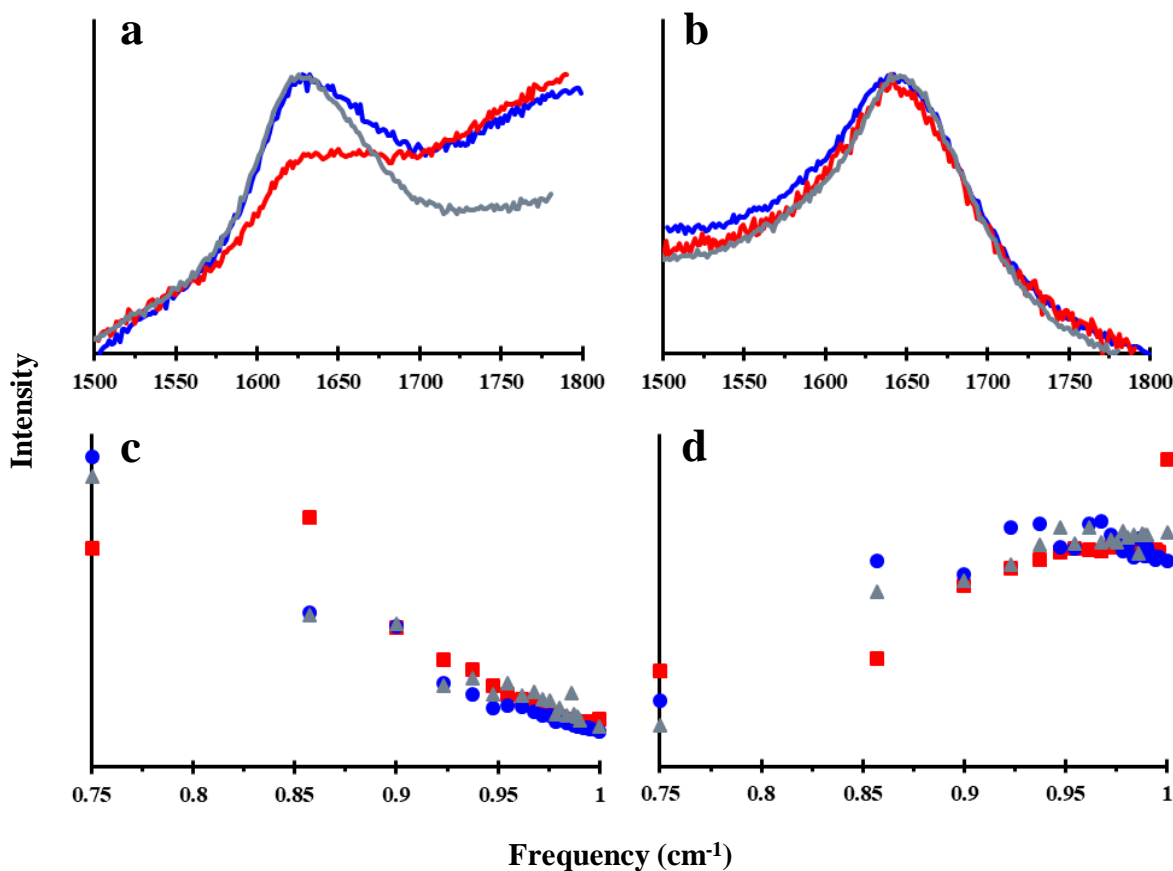


Figure 5.7 SVD of the Raman data in the water bending mode region for a) u_1 , b) u_2 , c) v_1 and d) v_2 . Dilution series are represented as B1 (blue), B2 (red) and B3 (gray).

ATR-IR measurements were taken over a broader spectral range than the Raman measurements. Thus, the data series introduced in section 5.3.1 for the water stretching band region, (A1) and (A2), were the same data sets examined for the IR analysis of the bending mode region.

Shown in Figure 5.8 are selected IR spectra of the dilution series (A1), $2.03 \leq R \leq 229.38$, along with pure water. There is observed to be a single sharp peak in the $R = 2.03$ composition at $\sim 1615 \text{ cm}^{-1}$ that blue shifts to a value of $\sim 1640 \text{ cm}^{-1}$ for pure water, as shown in Figure 5.9, with an approximate linear trend containing a slope of 96 (5). Additionally, the peak can be seen to be significantly more narrow in the $R = 2.03$ composition and broaden upon dilution from a value of

42 to 82 cm^{-1} , as seen in Figure 5.10. As with the frequency shift the broadening has an approximately linear trend with a slope of 117 (5).

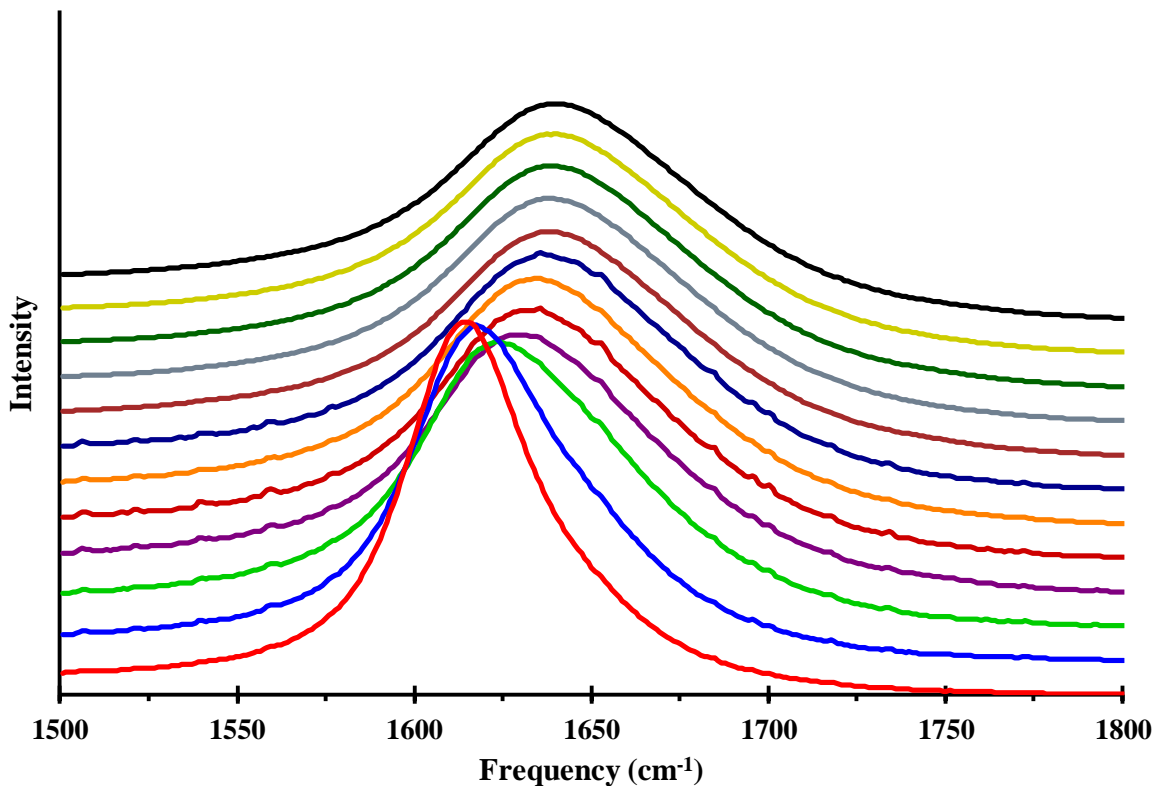


Figure 5.8 ATR-IR spectra of the water bending mode in aqueous zinc chloride solutions of composition $R = 2.03$ (red), $R = 3.09$ (blue), $R = 5.99$ (green), $R = 9.96$ (purple), $R = 14.63$ (dark red), $R = 20.69$ (orange), $R = 37.71$ (dark blue), $R = 57.58$ (brown), $R = 87.01$ (gray), $R = 120.67$ (dark green), $R = 229.38$ (yellow) and pure water (black).

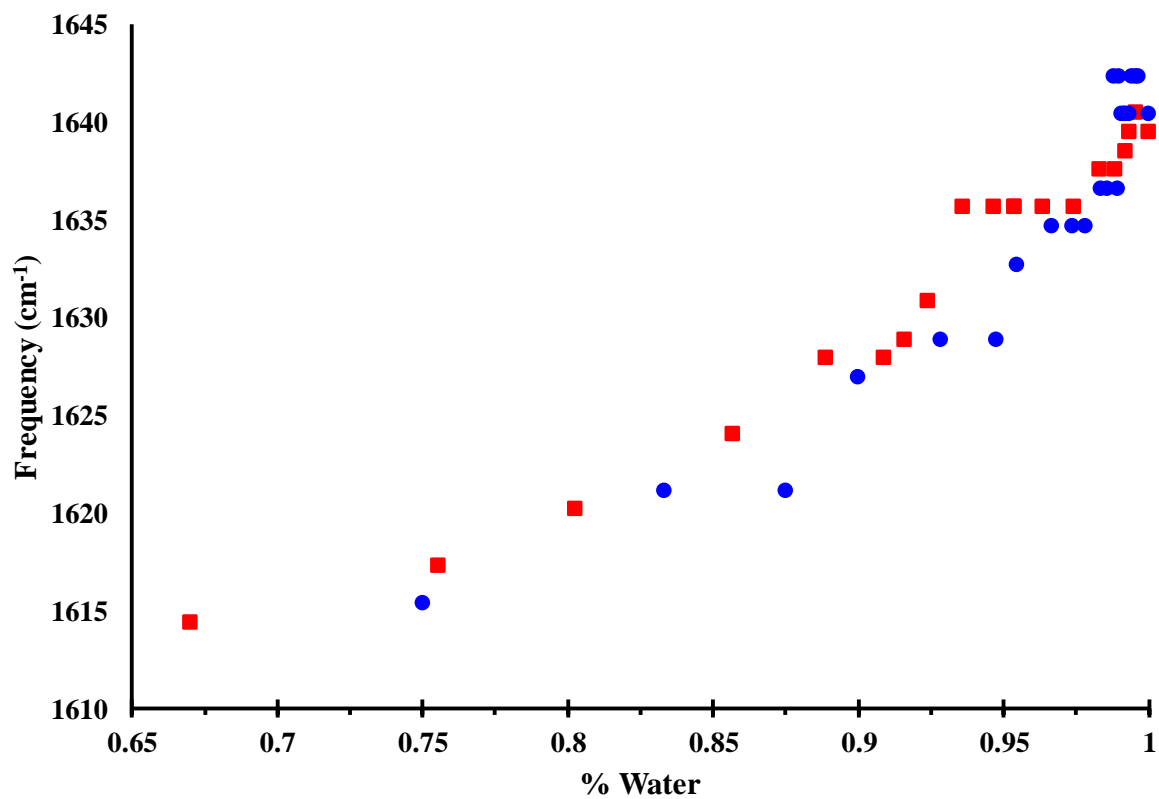


Figure 5.9 Concentration dependence of the frequency of the water bending peak in the IR data for A1 (red) and A2 (blue).

solutions. This has resulted in the proposal of numerous fitting equations to try and understand measured spectra. An example of such an equation, proposed by Dillon et. al.⁶⁶ is shown below:

$$I_{soln} = \beta \{ \alpha I_{water} + (1 - \alpha) I_{electrolyte} \} \quad (5.2)$$

in which I_{soln} is the experimentally measured solution spectrum, I_{water} is the spectrum of pure water and $I_{electrolyte}$ is the spectrum of waters bound directly to the ions. The parameters α and β are utilized in this case to scale the proportion of the water “types” and the overall intensity, respectively. In these studies, however, the authors point out that the spectra of the solvated water cannot be experimentally measured because it lies beyond the solubility limit of the salts being examined. To circumvent this issue researchers have developed multiple different methods, such as utilizing factor analysis (FA), to determine a hypothetical spectrum of solvated water employed in the calculation of spectra.^{19, 21, 55-56} However, in the zinc chloride system the spectrum of solvated water can be measured directly in the R = 3 hydrate. As was stated in the NMR analysis in Chapter 4, the possession of this solvated spectrum allows us to test the two-state model. Utilizing the experimental Raman and IR spectra of the R = 3 zinc chloride hydrate and pure water from data series (D1) and (A1), respectively, along with Equation 5.2, theoretical spectra were calculated for each measured concentration. Shown in Figures 5.11 and 5.12 are selected spectra along with their fits and residuals for the Raman and IR measurements, respectively.

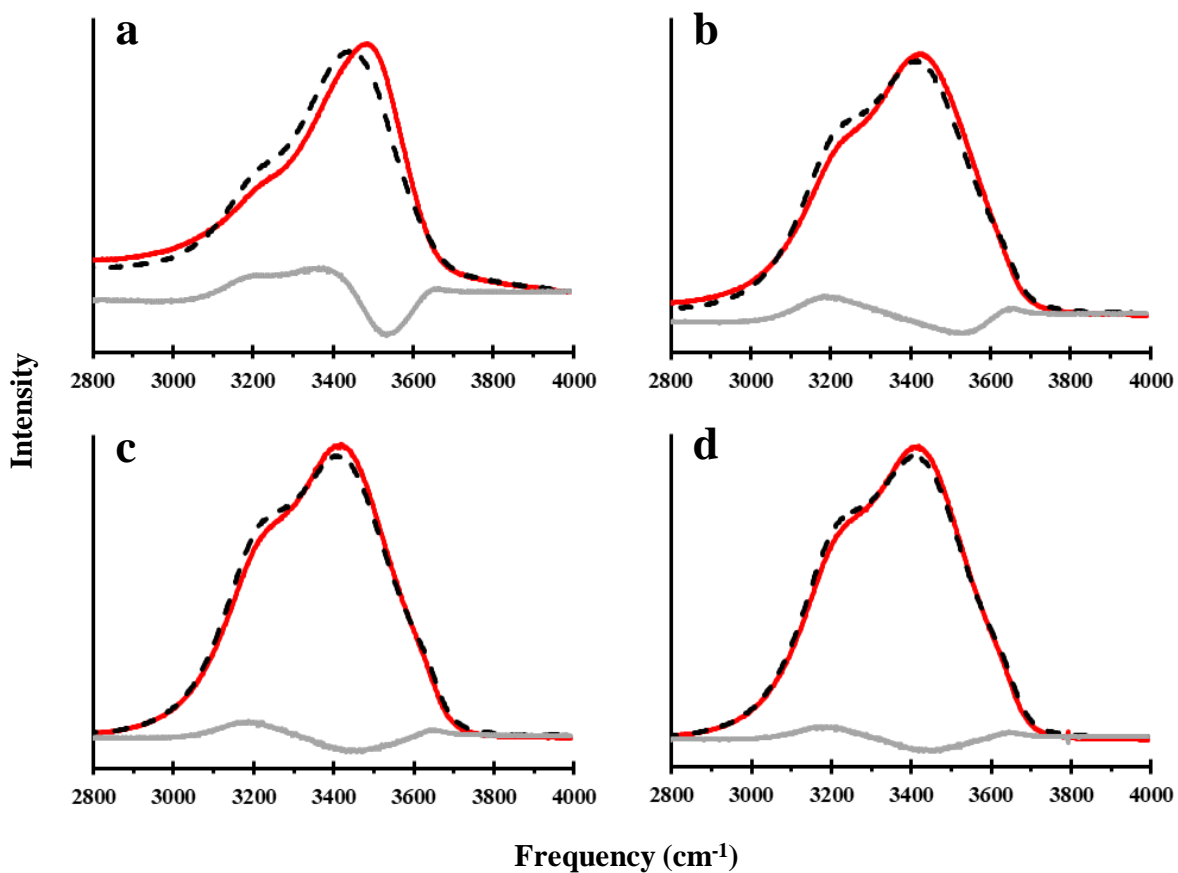


Figure 5.11 Raman spectra from data series (D1) for compositions of a) R = 6, b) R = 35, c) R = 70 and d) R = 100. The experimental data (red) are shown along with the two-state fitting model (black) and residuals (gray) for each composition.

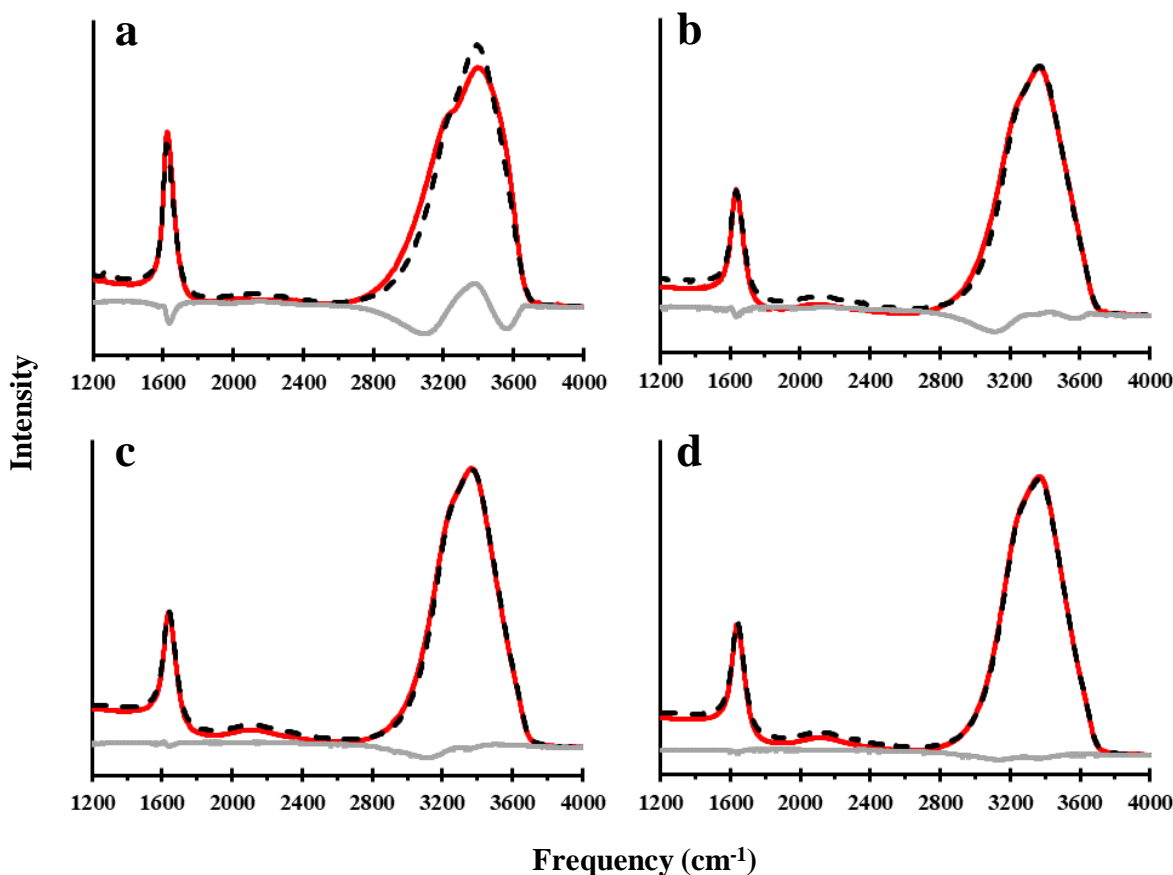


Figure 5.12 ATR-IR spectra from data series (A1) for compositions of a) $R = 6$, b) $R = 27$, c) $R = 58$ and d) $R = 229$. The experimental data (red) are shown along with the two-state fitting model (black) and residuals (gray) for each composition.

It can be observed in both cases, based on the residual plots, that the higher concentration region is not fit as well as the more dilute region. This seems logical because at higher dilutions the pure water spectrum becomes more dominant. However, it should be noted that even in the most dilute solutions shown, there is still not a good fit. If the two-state model were correct, then the spectrum at any concentration (R) should be obtained from a linear combination of the pure water and $R = 3$ spectra with $\alpha = 1 - 3/R$. While this method results in composition dependent spectra that are close to matching the measured data, there are still noticeable differences, not only in peak shape but also intensity. The lack of fit observed in the two-state model indicates that

there are likely more than two water environments in aqueous zinc chloride solutions, thus a more extensive fitting model is required.

5.4.2 Utilization of multi-shell fitting models to vibrational spectroscopic data

The previously reported analysis of our diffraction and NMR data, discussed in Chapters 3 and 4, respectively, indicate that there exist water environments in aqueous solution beyond that of pure water and “solvated” water bound directly to the ion. It is our proposal based on the lack of fit of the two-state model that introduction of several layers of different “types” of hydration shell water would give a better fit. Not only does the zinc chloride system allow for the direct measurement of the solvated-water spectrum at the $R = 3$ composition, but the water spectra in higher hydration shells can also be determined. For example, by assuming that the second shell contains 12 water molecules as a result of each first shell water having two hydrogen bonds⁷⁴, the second shell would be complete at a composition of $R = 9$. The experimental spectrum can then be reproduced by the following linear combination:

$$I_{soln} = \alpha I_1 + (1 - \alpha)I_2 \quad (5.3)$$

in which I_{soln} is the experimentally measured spectrum for the $R = 9$ aqueous zinc chloride solution. The spectra I_1 and I_2 correspond to those of water molecules in the first and second hydration shells, respectively. In the case of the zinc chloride system, the first shell spectrum is equivalent to the experimentally measured $R = 3$ spectrum. The parameter α corresponds to the mole fraction water in the first hydration shell, which in this case is 0.33 (i.e. 3/9). Equation 5.3 can then be rearranged to solve for the spectrum of I_2 . Additionally, this method can be expanded further to solve for the spectra of multiple hydration shells. Shown in Equations 5.4 – 5.7 is the expansion and rearrangement of Equation 5.3 to solve for the vibrational spectra of hydration shells 2 - 5:

$$I_2 = \frac{\{I_{soln} - \alpha I_1\}}{(1 - \alpha)} \quad (5.4)$$

$$I_3 = \frac{\{I_{soln} - \alpha_1 I_1 - \alpha_2 I_2\}}{(1 - \sum_1^{n-1} \alpha_n)} \quad (5.5)$$

$$I_4 = \frac{\{I_{soln} - \alpha_1 I_1 - \alpha_2 I_2 - \alpha_3 I_3\}}{(1 - \sum_1^{n-1} \alpha_n)} \quad (5.6)$$

$$I_5 = \frac{\{I_{soln} - \alpha_1 I_1 - \alpha_2 I_2 - \alpha_3 I_3 - \alpha_4 I_4\}}{(1 - \sum_1^{n-1} \alpha_n)} \quad (5.7)$$

In this case we are continuing the assumption of doubling the number of waters in each successive hydration shell thus the parameter α_n is determined for the n^{th} hydration shell as shown in Table 5.1. Shown in Figures 5.13 and 5.14 are the calculated spectra for hydration shells 2 through 5 plus that of the experimentally measured $R = 3$ which corresponds to the first hydration shell for the Raman and IR data, respectively.

Table 5.1 Equations used to calculate the mole fraction of waters in each hydration shell based on the solution concentration given in R (α) and mole fraction (α').

n	1	2	3	4	5
α	3/R	6/R	12/R	24/R	48/R
α'	(3/x)-3	(6/x)-6	(12/x)-12	(24/x)-24	(48/x)-48

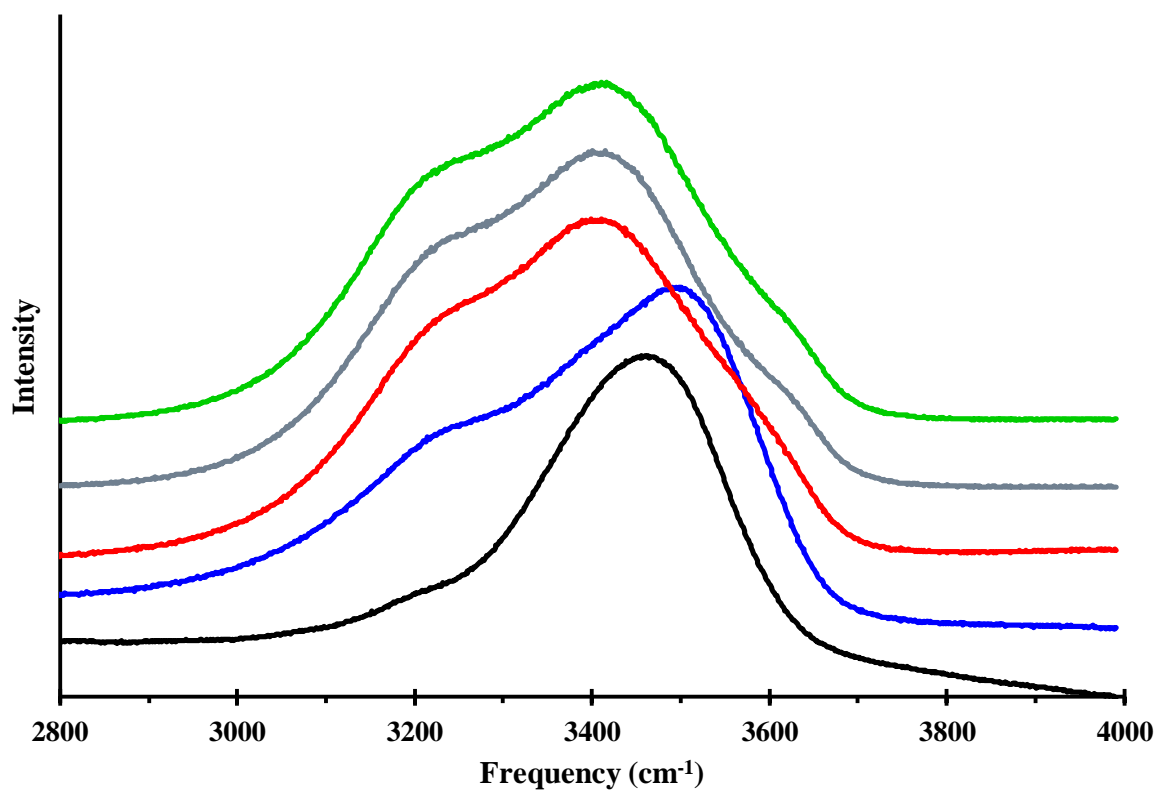


Figure 5.13 The measured spectrum of the $R = 3$ hydrate (black) corresponding to the first hydration shell plus the calculated spectra of the second (blue), third (red), fourth (gray) and fifth (green) hydration shells.

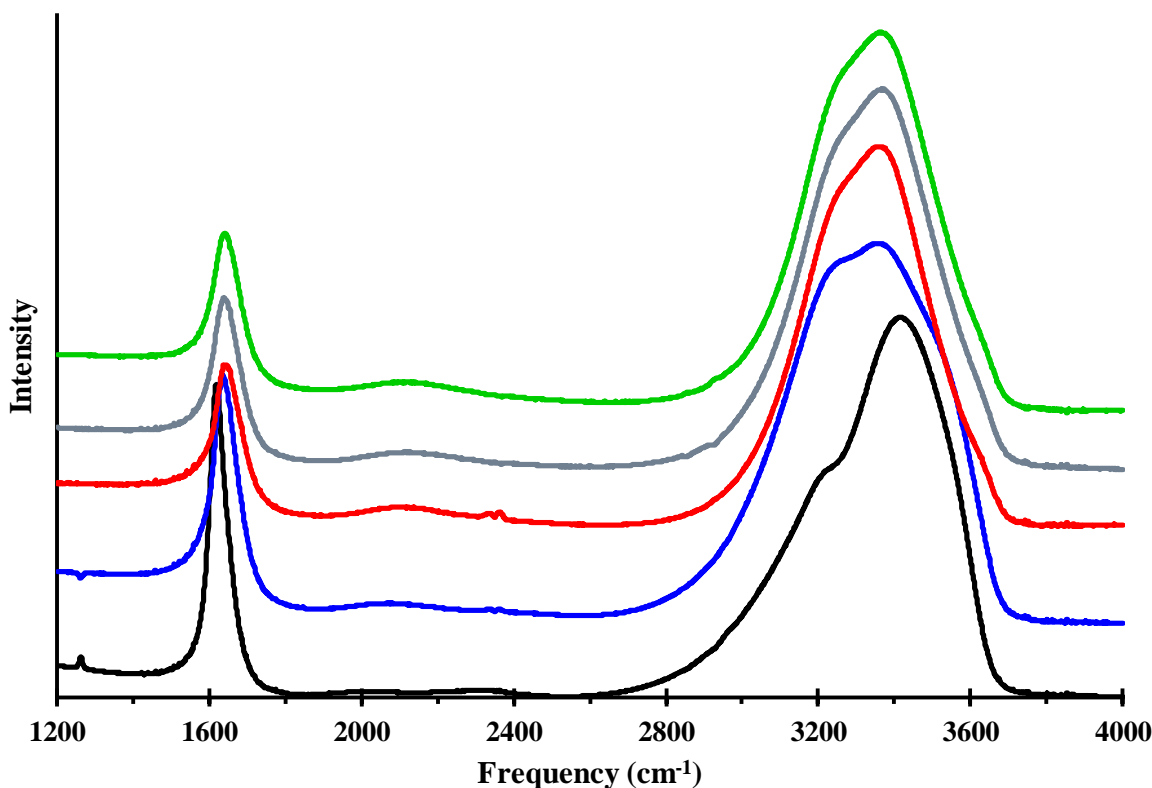


Figure 5.14 The measured spectrum of the $R = 3$ hydrate (black) corresponding to the first hydration shell plus the calculated spectra of the second (blue), third (red), fourth (gray) and fifth (green) hydration shells.

It can be seen in the Raman spectra, Figure 5.13, that the $\sim 3400\text{ cm}^{-1}$ peak blue shifts from a value of 3470 cm^{-1} in the 1st shell to a value of 3495 cm^{-1} in the 2nd shell followed by a red shift to a value of 3420 cm^{-1} in the higher shells after which its frequency value stays constant. Additionally, the 3200 cm^{-1} peak is much stronger in the 2nd shell spectrum and by the 3rd shell is almost at a constant value. Lastly, the 3600 cm^{-1} peak does not become noticeable until the 3rd shell spectrum. In contrast, the 3400 cm^{-1} peak in the 2nd shell spectrum of the IR broadens significantly to include a shoulder at $\sim 3600\text{ cm}^{-1}$. Additionally, a very strong peak at $\sim 3200\text{ cm}^{-1}$ is observed in the 2nd shell IR spectrum. The 3400 cm^{-1} mode also red shifts in the IR. Lastly, the bending mode broadens and blue shifts from shell 2-5.

Care must be exercised in the interpretation of the “shell spectra” themselves because they do get effected by the fit. For example, the large peak at 3200 cm⁻¹ in the 2nd shell spectra of the IR is diminished in intensity in higher calculated shell spectra due to the fitting method being a summation in which the intense 3200 cm⁻¹ is accounted for in the 2nd shell. However, the “shell” in which a feature is seen strongest/first corresponds to the concentration region where that feature begins to appear and in the case of the 3200 cm⁻¹ mode means that it is at high concentration that this mode begins to contribute significantly to the IR spectrum.

Using the calculated spectra for the multiple hydration shells the following equation can then be utilized to fit the experimental data corresponding to the water stretching band profile of the Raman data and the broader region which includes the water bending mode for the IR data:

$$I_{soln} = \beta\{\alpha_1 I_1 + \alpha_2 I_2 + \dots + (1 - \sum_1^{n-1} \alpha_n) I_{water}\} \quad (5.8)$$

in which all parameters are the same as outline above with the addition of the β parameter as an intensity scaling factor. Utilizing Equation 5.8, the fitting procedure was again performed on the data series (D1) and (A1) for the Raman and IR spectra, respectively. Shown in Figure 5.15 are selected fits of the Raman data from $6 \leq R \leq 100$ and shown in Figure 5.16 are selected IR fits in the concentration range of $6 \leq R \leq 229$. Through the examination of the residuals of successive fits for both the Raman and IR data utilizing increasing numbers of hydration shells, it was found that the best fits came at a value of five hydration shells.

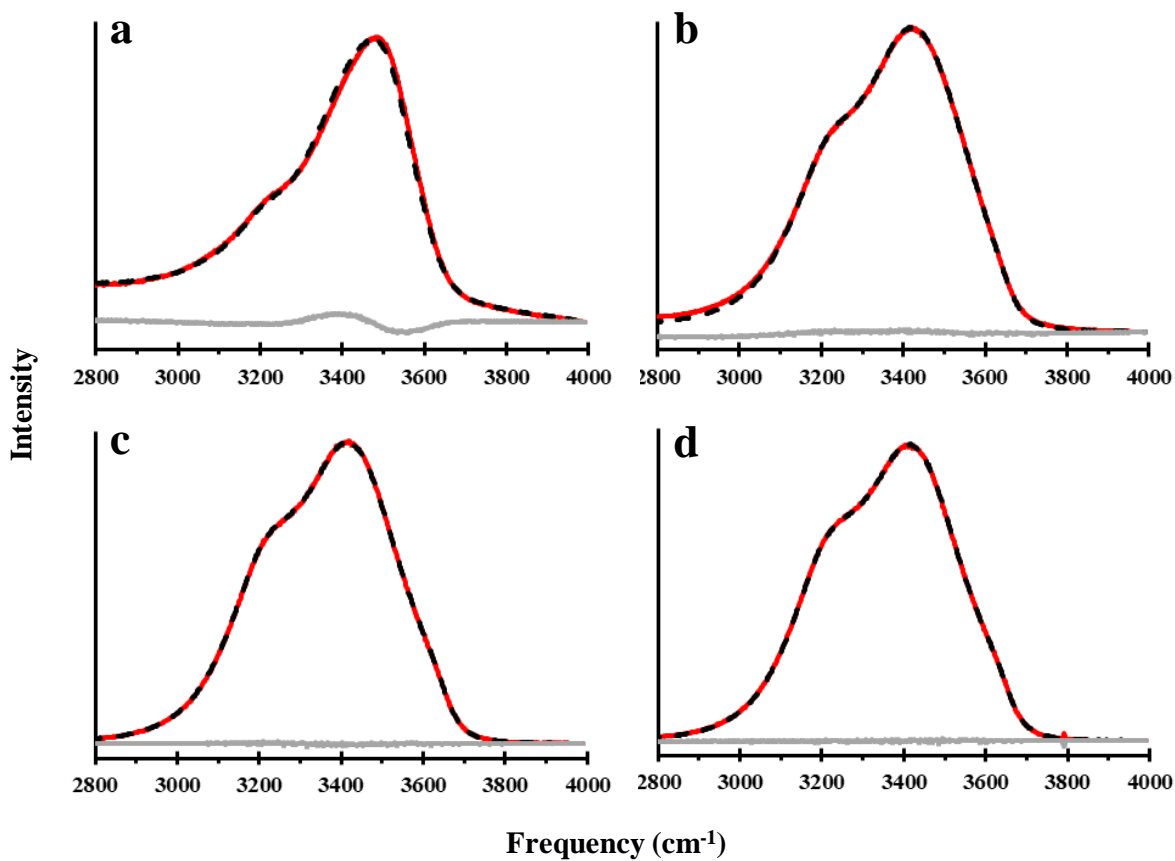


Figure 5.15 Raman spectra from data series (D1) for compositions of a) $R = 6$, b) $R = 35$, c) $R = 70$ and d) $R = 100$. The experimental data (red) are shown along with the multi-shell fitting model utilizing five hydration shells (black) and residuals (gray) for each composition.

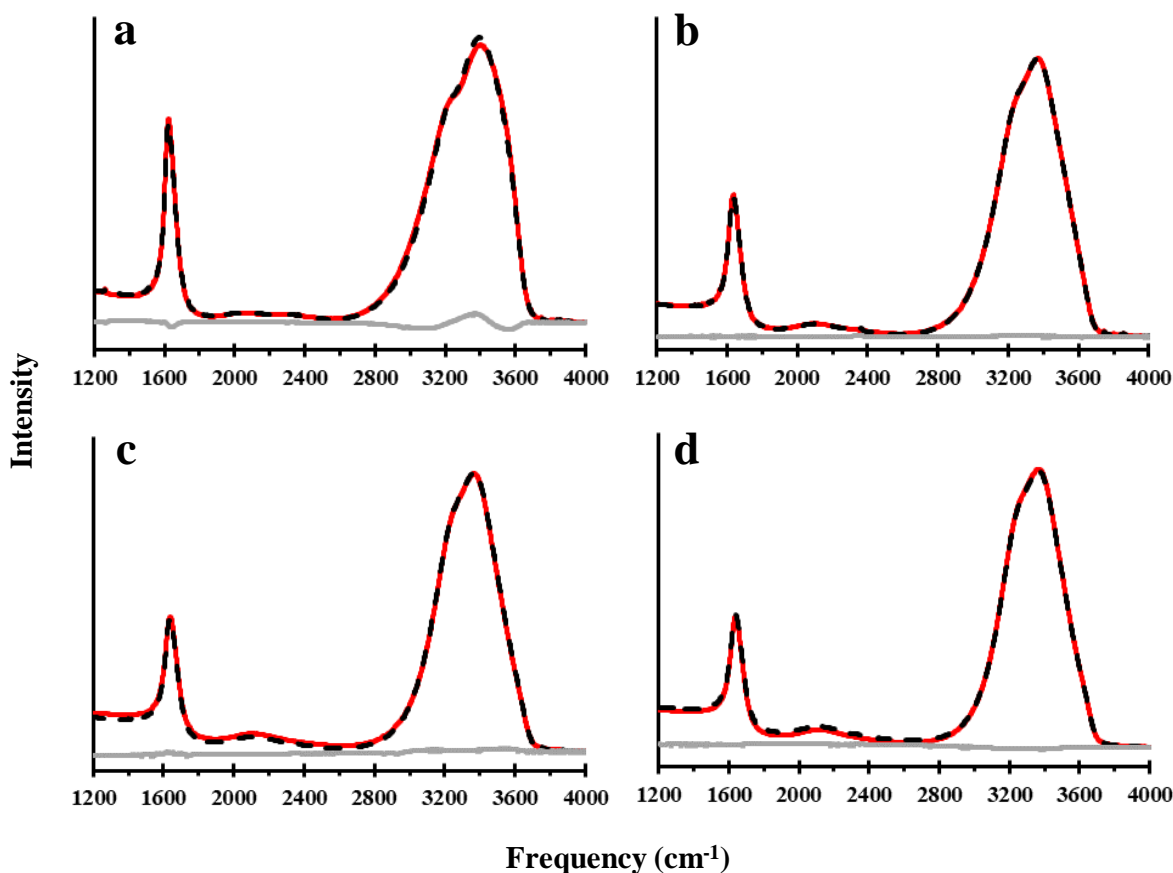


Figure 5.16 ATR-IR spectra from data series (A1) for compositions of a) $R = 6$, b) $R = 27$, c) $R = 58$ and d) $R = 229$. The experimental data (red) are shown along with the multi-shell fitting model utilizing five hydration shells (black) and residuals (gray) for each composition.

In both the IR and Raman cases the fits show remarkably better residuals than those of the two-state model. However, the high concentration data is still not well fit, which is likely due to the assumption of a combination of 1st and 2nd shell water to describe a situation in which the second shell will not have fully formed (i.e. $R < 9$). However, the improved residuals in this region over those of the two-state model indicate that the water in this region is closer to that of the calculated 2nd shell than that of pure water.

5.4.3 Insight into the nature of pure water gained through the study of aqueous $ZnCl_2$

There is much disagreement about the true identity of the modes observed in liquid water compared to those of the gas phase in which excitations occur at 1595, 3652 and 3756 cm^{-1} for

the bending, symmetric and asymmetric stretching modes, respectively. Interpretations of the spectrum of liquid water include a simplistic molecular point of view in which the stretching region consists of the bending overtone plus the symmetric and asymmetric stretching modes.⁴⁶⁻

⁴⁷ Expansion of this view point is done by the inclusion of intermolecular coupling and Fermi resonance to produce a more complex stretching band profile which results in multiple levels of splitting of the unperturbed OH stretching modes.^{40, 45, 48-50} Lastly, there have been proposals that the stretching band region consists of different hydrogen bonding environments ranging from strongly hydrogen bonded in the low frequency region at $\sim 3200\text{ cm}^{-1}$ to much weaker hydrogen bonding in the 3600 cm^{-1} region.

Additionally, these modes have many interpretations in the context of aqueous solutions such as the direction of the energy shift upon addition of a solute being reflective of the structure making/breaking nature of the ions, that is to say if the ion strengthens/weakens the hydrogen bonding network of water.^{4, 88} In many cases these interpretations cannot be directly tested because it is unknown with a high degree of accuracy what species are present in solution. However, the R = 3 zinc chloride hydrate system provides a unique platform from which to begin to understand water structure both in solutions and pure liquid. As was reported in chapter 2 and reference 89, the R = 3 hydrate contains all waters bound directly to the zinc ion which, because it is highly electron withdrawing, results in the OH bond being very activated and these waters being strong hydrogen bond donors. Furthermore, there is evidence that the waters in the R = 3 are not strongly interacting with the ZnCl_4^{2-} anion. First off, as was discussed in chapter 2, the loss of hydrogen bonding in the R = 3 system results in a red shift in the water bending mode and a blue shift in the water stretching mode. Additionally, the bending peak is observed to be significantly narrowed in the R = 3 spectrum, the narrowing of the bending mode has been

reported in the literature as resulting from the loss of the intermolecular coupling as the hydrogen bonding network of pure water is lost.^{58, 90-91} As shown in Figure 5.10 the FWHM has essentially a linear trend, broadening from 42 to 82 cm^{-1} upon dilution. This trend reflects the building up of the hydrogen bonding network and intermolecular coupling in the shell structure of water. Lastly, it can be seen that the 3200 and 3600 cm^{-1} modes are significantly weakened in the $R = 3$ spectrum.

Upon dilution the 3200 cm^{-1} mode is observed to grow back in much more intensely and at higher concentration in the IR spectra than in the Raman spectra which is observed in both the experimental data as well as the calculated hydration shell spectra. The observed difference is due to the different ways in which the dipole moment and polarizability are affected. When bound directly to the zinc both the dipole moment and polarizability are heavily affected due to the heavy withdrawing of electron density off of the water through the oxygen atom. It has been reported based on molecular dynamics simulations that the dipole moment in the first hydration shell of Zn^{2+} is 25% (3.4 D) larger than that of pure water (2.73 D).²⁷ However, upon addition of waters to the system which begin to build up hydration shells, the waters in the second shell do not have their dipole moments affected nearly as much as the first shell since they are not interacting directly with the metal ion. The second shell has a value only 2.6% (2.8 D) larger compared to bulk water.²⁷ The much larger dipole moment in the first shell means that there will be less change in dipole moment upon excitation. The polarizability though is going to be more of a collective phenomenon in the hydration shells and the second hydration shell is still going to be very different from pure water which means that the Raman spectra are still very different.

While the polarized Raman spectrum of water, shown in Figure 5.5, does indicate that the 3200 cm^{-1} mode has the same symmetry as the water bending mode, the disappearance of this

mode in the concentrated solutions, as opposed to the bending mode which sharpens and becomes more intense, indicates that the 3200 cm^{-1} mode is at the very least not entirely a result of the bending overtone. It has been shown in the literature that there is a connection between the breadth of the bending mode and the peak at 3200 cm^{-1} which becomes stronger as there is more intermolecular coupling and Fermi resonance.^{40, 45, 48-50, 58} The trend in the SVD loadings of the Raman bending mode, seen in Figure 5.7, is likely also reflective of the increase/decrease of hydrogen bonding and intermolecular coupling upon dilution. The fact that this comes out in the SVD is further evidence that the change in intermolecular coupling plays a significant role in the system. In addition to the broadening of the bending mode upon dilution, there is also an accompanying blue shift in the frequency which is characteristic of the hindrance of the bending motion due to the formation of hydrogen bonding.

The 3600 cm^{-1} mode also disappears in the $R = 3$ hydrate and grows back in upon dilution. However, polarized Raman reveals that this mode is not of the same symmetry as the bending mode and thus the same intermolecular coupling and Fermi resonance responsible for the 3200 cm^{-1} peak is not what causes the change in this peak. However, both the 3200 and 3600 cm^{-1} modes are observed to disappear in high temperature spectra of pure water due to the loss of hydrogen bonding which indicates that both peaks are connected to the hydrogen bonding network of the system.⁴⁰⁻⁴¹ The fact that both of these modes grow in past a certain concentration and do not change in frequency much upon additional dilution indicates that these peaks are more connected to the hydrogen bonding network. However, the continued change in frequency of the bending and stretching modes indicate that these are looking at different aspects of water from the 3200 and 3600 peaks and that even in the most dilute samples examined the solutions are not like pure water even though the multi-shell model indicates that regions of pure

water begin to exist past $R = 93$. The 3600 mode disappears in the $R = 3$ while a small amount of the 3200 mode remains, this is likely due to the bending mode overtone.

5.5 Conclusion

Utilizing experimental data to validate the two-state modelling scheme, it was shown that the solution spectra were not fully reproduced. However, the addition of multiple water environments into the model resulted in dramatically better fits giving evidence for the existence of multiple hydration shells and indicating that, in the case of zinc chloride, the Zn^{2+} ion has a significant effect on the water structure well beyond the first hydration shell.

Additionally, the aqueous zinc chloride system allows for a better understanding of the vibrational spectrum of pure water by providing information about the peaks and their evolution from the $R = 3$ hydrate, where the hydrogen bonding network of pure water does not exist, to that of pure water. Evidence suggests that the molecular modes of water are observed at $\sim 1600\text{ cm}^{-1}$ for the bending mode along with a combination peak of the symmetric and asymmetric stretching modes at $\sim 3450\text{ cm}^{-1}$ while the peaks observed at 3200 and 3600 cm^{-1} are representative of the hydrogen bonding network of the system while some amount of the 3200 cm^{-1} peak is due to the bending overtone.

5.6 References

1. Chadwell, H. M., The Molecular Structure of Water. *Chemical reviews* **1928**, 4 (4), 375-398.
2. Pople, J. A. In *Molecular association in liquids II. A theory of the structure of water*, Proc. R. Soc. Lond. A, The Royal Society: 1951; pp 163-178.
3. Kauzmann, W.; Eisenberg, D., *The structure and properties of water*. Clarendon Press: 1969.
4. Marcus, Y., Effect of ions on the structure of water: structure making and breaking. *Chemical reviews* **2009**, 109 (3), 1346-1370.
5. Smith, J. D.; Saykally, R. J.; Geissler, P. L., The effects of dissolved halide anions on hydrogen bonding in liquid water. *Journal of the American Chemical Society* **2007**, 129 (45), 13847-13856.
6. Tielrooij, K.; Garcia-Araez, N.; Bonn, M.; Bakker, H., Cooperativity in ion hydration. *Science* **2010**, 328 (5981), 1006-1009.
7. Fu, L.; Bienenstock, A.; Brennan, S., X-ray study of the structure of liquid water. *The Journal of Chemical Physics* **2009**, 131 (23), 234702.
8. Dagnall, S. P.; Hague, D. N.; Towl, A. D. C., X-ray diffraction study of aqueous zinc(II) nitrate. *Journal of the Chemical Society, Faraday Transactions 2: Molecular and Chemical Physics* **1982**, 78 (12), 2161-2167.
9. Kruh, R.; Standley, C., An X-ray diffraction study of aqueous zinc chloride solutions. *Inorganic chemistry* **1962**, 1 (4), 941-943.
10. Gaspar, A.; Marques, M. A.; Cabaço, M.; de Barros Marques, M.; Buslaps, T.; Honkimaki, V., X-Ray diffraction investigations of concentrated aqueous solutions of calcium halides. *Journal of Molecular Liquids* **2004**, 110 (1), 15-22.
11. Amann-Winkel, K.; Bellissent-Funel, M.-C.; Bove, L. E.; Loerting, T.; Nilsson, A.; Paciaroni, A.; Schlesinger, D.; Skinner, L., X-ray and Neutron Scattering of Water. *Chemical reviews* **2016**, 116 (13), 7570-7589.
12. Neilson, G.; Enderby, J., Aqueous solutions and neutron scattering. *The Journal of Physical Chemistry* **1996**, 100 (4), 1317-1322.
13. Enderby, J. E.; Howells, W. S.; Howe, R. A., The structure of aqueous solutions. *Chemical Physics Letters* **1973**, 21 (1), 109-112.

14. Soper, A. K., The radial distribution functions of water and ice from 220 to 673 K and at pressures up to 400 MPa. *Chemical Physics* **2000**, 258 (2–3), 121-137.
15. Sun, Q., The Raman OH stretching bands of liquid water. *Vibrational Spectroscopy* **2009**, 51 (2), 213-217.
16. Carey, D. M.; Korenowski, G. M., Measurement of the Raman spectrum of liquid water. *The Journal of Chemical Physics* **1998**, 108 (7), 2669-2675.
17. Perera, P. N.; Browder, B.; Ben-Amotz, D., Perturbations of water by alkali halide ions measured using multivariate Raman curve resolution. *The Journal of Physical Chemistry B* **2009**, 113 (7), 1805-1809.
18. Wang, Y.; Zhu, W.; Lin, K.; Yuan, L.; Zhou, X.; Liu, S., Ratiometric detection of Raman hydration shell spectra. *Journal of Raman Spectroscopy* **2016**, 47 (10), 1231-1238.
19. Max, J.-J.; Gessinger, V.; van Driessche, C.; Larouche, P.; Chapados, C., Infrared spectroscopy of aqueous ionic salt solutions at low concentrations. *The Journal of Chemical Physics* **2007**, 126 (18), 184507.
20. Stangret, J.; Gampe, T., Ionic hydration behavior derived from infrared spectra in HDO. *The Journal of Physical Chemistry A* **2002**, 106 (21), 5393-5402.
21. Larouche, P.; Max, J.-J.; Chapados, C., Isotope effects in liquid water by infrared spectroscopy. II. Factor analysis of the temperature effect on H₂O and D₂O. *The Journal of Chemical Physics* **2008**, 129 (6), 064503.
22. Bergstroem, P. A.; Lindgren, J.; Read, M.; Sandstroem, M., Infrared spectroscopic evidence for second-sphere hydration in aqueous solutions of aluminum (3+), chromium (3+) and rhodium (3+). *The Journal of Physical Chemistry* **1991**, 95 (20), 7650-7655.
23. Zhu, X.; Zhang, H.; Li, H., The structure of water in dilute aqueous solutions of ionic liquids: IR and NMR study. *Journal of Molecular Liquids* **2014**, 197, 48-51.
24. van Der Maarel, J. R. C., A H, D, and 17O Nuclear magnetic relaxation study on the structure and dynamics of water in concentrated ZnCl₂. *Journal of Magnetic Resonance (1969)* **1989**, 81 (1), 92-103.
25. Nakamura, Y.; Shimokawa, S.; Futamata, K.; Shimoji, M., NMR relaxation study of water molecules in concentrated zinc chloride solutions. *The Journal of Chemical Physics* **1982**, 77 (6), 3258-3262.
26. Malinowski, E. R.; Knapp, P. S.; Feuer, B., NMR Studies of Aqueous Electrolyte Solutions. I. Hydration Number of NaCl Determined from Temperature Effects on Proton Shift. *The Journal of Chemical Physics* **1966**, 45 (11), 4274-4279.

27. Cauët, E.; Bogatko, S.; Weare, J. H.; Fulton, J. L.; Schenter, G. K.; Bylaska, E. J., Structure and dynamics of the hydration shells of the Zn²⁺ ion from ab initio molecular dynamics and combined ab initio and classical molecular dynamics simulations. *The Journal of Chemical Physics* **2010**, *132* (19), 194502.
28. Brancato, G.; Rega, N.; Barone, V., Microsolvation of the Zn(II) ion in aqueous solution: A hybrid QM/MM MD approach using non-periodic boundary conditions. *Chemical Physics Letters* **2008**, *451* (1–3), 53-57.
29. D'Angelo, P.; Barone, V.; Chillemi, G.; Sanna, N.; Meyer-Klaucke, W.; Pavel, N. V., Hydrogen and Higher Shell Contributions in Zn²⁺, Ni²⁺, and Co²⁺ Aqueous Solutions: An X-ray Absorption Fine Structure and Molecular Dynamics Study. *Journal of the American Chemical Society* **2002**, *124* (9), 1958-1967.
30. Rahman, A.; Stillinger, F. H., Molecular dynamics study of liquid water. *The Journal of Chemical Physics* **1971**, *55* (7), 3336-3359.
31. Willow, S. Y.; Salim, M. A.; Kim, K. S.; Hirata, S., Ab initio molecular dynamics of liquid water using embedded-fragment second-order many-body perturbation theory towards its accurate property prediction. *Scientific reports* **2015**, *5*, 14358.
32. Luzar, A.; Chandler, D., Effect of environment on hydrogen bond dynamics in liquid water. *Physical review letters* **1996**, *76* (6), 928.
33. Lie, G. C.; Clementi, E.; Yoshimine, M., Study of the structure of molecular complexes. XIII. Monte Carlo simulation of liquid water with a configuration interaction pair potential. *The Journal of Chemical Physics* **1976**, *64* (6), 2314-2323.
34. Barker, J.; Watts, R., Structure of water; A Monte Carlo calculation. *Chemical Physics Letters* **1969**, *3* (3), 144-145.
35. Arab, M.; Bougeard, D.; Smirnov, K. S., Molecular dynamics study of the structure and dynamics of Zn²⁺ ion in water. *Chemical Physics Letters* **2003**, *379* (3–4), 268-276.
36. Rowley, C. N.; Roux, B. t., The solvation structure of Na⁺ and K⁺ in liquid water determined from high level ab initio molecular dynamics simulations. *Journal of chemical theory and computation* **2012**, *8* (10), 3526-3535.
37. Lei, X.; Pan, B., Structures, Stability, Vibration Entropy and IR Spectra of Hydrated Calcium Ion Clusters [Ca (H₂O)_n]²⁺(n= 1– 20, 27): A Systematic Investigation by Density Functional Theory. *The Journal of Physical Chemistry A* **2010**, *114* (28), 7595-7603.
38. Pavlov, M.; Siegbahn, P. E.; Sandström, M., Hydration of beryllium, magnesium, calcium, and zinc ions using density functional theory. *The Journal of Physical Chemistry A* **1998**, *102* (1), 219-228.

39. Wang, Y.-L.; Wang, Y.; Yi, H.-B., High-Order Ca (II)–Chloro Complexes in Mixed CaCl₂–LiCl Aqueous Solution: Insights from Density Functional Theory and Molecular Dynamics Simulations. *The Journal of Physical Chemistry A* **2016**, *120* (28), 5635-5648.
40. Zhelyaskov, V.; Georgiev, G.; Nickolov, Z., Temperature study of intra-and inter-molecular coupling and Fermi resonance constants in the Raman spectra of liquid water using Fourier deconvolution. *Journal of Raman Spectroscopy* **1988**, *19* (6), 405-412.
41. Smith, J. D.; Cappa, C. D.; Wilson, K. R.; Cohen, R. C.; Geissler, P. L.; Saykally, R. J., Unified description of temperature-dependent hydrogen-bond rearrangements in liquid water. *Proceedings of the National Academy of Sciences of the United States of America* **2005**, *102* (40), 14171-14174.
42. Kawamoto, T.; Ochiai, S.; Kagi, H., Changes in the structure of water deduced from the pressure dependence of the Raman OH frequency. *The Journal of Chemical Physics* **2004**, *120* (13), 5867-5870.
43. Okada, T.; Komatsu, K.; Kawamoto, T.; Yamanaka, T.; Kagi, H., Pressure response of Raman spectra of water and its implication to the change in hydrogen bond interaction. *Spectrochimica Acta Part A: Molecular and Biomolecular Spectroscopy* **2005**, *61* (10), 2423-2427.
44. Lin, Y.-S.; Auer, B.; Skinner, J., Water structure, dynamics, and vibrational spectroscopy in sodium bromide solutions. *The Journal of Chemical Physics* **2009**, *131* (14), 144511.
45. Zhelyaskov, V.; Georgiev, G.; Nickolov, Z.; Miteva, M., Concentration Raman study of intramolecular, intermolecular and Fermi resonance interactions in the OH stretching spectra of dilute solutions of HDO in D₂O using Fourier deconvolution technique. *Molecular Physics* **1988**, *64* (6), 1133-1144.
46. Walrafen, G. E., Raman Spectral Studies of the Effects of Electrolytes on Water. *The Journal of Chemical Physics* **1962**, *36* (4), 1035-1042.
47. Walrafen, G. E., Raman Spectral Studies of Water Structure. *The Journal of Chemical Physics* **1964**, *40* (11), 3249-3256.
48. Sceats, M. G.; Stavola, M.; Rice, S. A., On the role of Fermi resonance in the spectrum of water in its condensed phases. *The Journal of Chemical Physics* **1979**, *71* (2), 983-990.
49. Sokołowska, A.; Kęcki, Z., Inter-and intra-molecular coupling and Fermi resonance in the Raman spectra of liquid water. *Journal of Raman Spectroscopy* **1986**, *17* (1), 29-33.
50. Wójcik, M. J.; Rice, S. A., The vibrational spectrum of the water dimer: some model based predictions. *The Journal of Chemical Physics* **1986**, *84* (6), 3042-3048.

51. Schmidt, D. A.; Miki, K., Defective Continuous Hydrogen-Bond Networks: An Alternative Interpretation of IR Spectroscopy. *ChemPhysChem* **2008**, *9* (13), 1914-1919.
52. Cooper, R. J.; Chang, T. M.; Williams, E. R., Hydrated Alkali Metal Ions: Spectroscopic Evidence for Clathrates. *The Journal of Physical Chemistry A* **2013**, *117* (30), 6571-6579.
53. Kitadai, N.; Sawai, T.; Tonoue, R.; Nakashima, S.; Katsura, M.; Fukushi, K., Effects of ions on the OH stretching band of water as revealed by ATR-IR spectroscopy. *Journal of solution chemistry* **2014**, *43* (6), 1055-1077.
54. Sun, Q., Raman spectroscopic study of the effects of dissolved NaCl on water structure. *Vibrational Spectroscopy* **2012**, *62*, 110-114.
55. Max, J.-J.; Chapados, C., IR spectroscopy of aqueous alkali halide solutions: pure salt-solvated water spectra and hydration numbers. *The Journal of Chemical Physics* **2001**, *115* (6), 2664-2675.
56. Max, J.-J.; Blois, S. d.; Veilleux, A.; Chapados, C., IR Spectroscopy of aqueous alkali halides. Factor analysis. *Canadian Journal of Chemistry* **2001**, *79* (1), 13-21.
57. Matt, S. M.; Ben-Amotz, D., Influence of Intermolecular Coupling on the Vibrational Spectrum of Water. *The Journal of Physical Chemistry B* **2018**.
58. Ahmed, M.; Namboodiri, V.; Singh, A. K.; Mondal, J. A., On the intermolecular vibrational coupling, hydrogen bonding, and librational freedom of water in the hydration shell of mono- and bivalent anions. *The Journal of Chemical Physics* **2014**, *141* (16), 164708.
59. Besemer, M.; Bloemenkamp, R.; Ariese, F.; Manen, H.-J. v., Identification of Multiple Water-Iodide Species in Concentrated NaI Solutions Based on the Raman Bending Vibration of Water. *The Journal of Physical Chemistry A* **2016**, *120* (5), 709-714.
60. Dubessy, J.; Lhomme, T.; Boiron, M.-C.; Rull, F., Determination of chlorinity in aqueous fluids using Raman spectroscopy of the stretching band of water at room temperature: application to fluid inclusions. *Applied spectroscopy* **2002**, *56* (1), 99-106.
61. Bergstroem, P. A.; Lindgren, J.; Kristiansson, O., An IR study of the hydration of perchlorate, nitrate, iodide, bromide, chloride and sulfate anions in aqueous solution. *The Journal of Physical Chemistry* **1991**, *95* (22), 8575-8580.
62. Schmidt, D. A.; Miki, K., Structural correlations in liquid water: A new interpretation of IR spectroscopy. *The Journal of Physical Chemistry A* **2007**, *111* (40), 10119-10122.
63. Aliotta, F.; Fontana, M.; Maisano, G.; Migliardo, P.; Wanderlingh, F., Coexistence of structures in electrolytic solutions investigated by Raman scattering. *Journal of Modern Optics* **1980**, *27* (7), 931-938.

64. Li, R.; Jiang, Z.; Shi, S.; Yang, H., Raman spectra and ^{17}O NMR study effects of CaCl_2 and MgCl_2 on water structure. *Journal of molecular structure* **2003**, *645* (1), 69-75.
65. Li, R.; Jiang, Z.; Guan, Y.; Yang, H.; Liu, B., Effects of metal ion on the water structure studied by the Raman O-H stretching spectrum. *Journal of Raman Spectroscopy* **2009**, *40* (9), 1200-1204.
66. Dillon, S. R.; Dougherty, R. C., Raman studies of the solution structure of univalent electrolytes in water. *The Journal of Physical Chemistry A* **2002**, *106* (34), 7647-7650.
67. Woutersen, a.; Emmerichs, U.; Bakker, H., Femtosecond mid-IR pump-probe spectroscopy of liquid water: Evidence for a two-component structure. *Science* **1997**, *278* (5338), 658-660.
68. Soper, A. K.; Weckström, K., Ion solvation and water structure in potassium halide aqueous solutions. *Biophysical Chemistry* **2006**, *124* (3), 180-191.
69. Mancinelli, R.; Botti, A.; Bruni, F.; Ricci, M.; Soper, A., Perturbation of water structure due to monovalent ions in solution. *Physical Chemistry Chemical Physics* **2007**, *9* (23), 2959-2967.
70. Chen, Y.; Okur, H. I.; Gomopoulos, N.; Macias-Romero, C.; Cremer, P. S.; Petersen, P. B.; Tocci, G.; Wilkins, D. M.; Liang, C.; Ceriotti, M., Electrolytes induce long-range orientational order and free energy changes in the H-bond network of bulk water. *Science advances* **2016**, *2* (4), e1501891.
71. Rudolph, W. W.; Pye, C. C., Zinc (II) hydration in aqueous solution. A Raman spectroscopic investigation and an ab-initio molecular orbital study. *Physical Chemistry Chemical Physics* **1999**, *1* (19), 4583-4593.
72. Mohammed, A. M.; Loeffler, H. H.; Inada, Y.; Tanada, K.-i.; Funahashi, S., Quantum mechanical/molecular dynamic simulation of zinc(II) ion in water. *Journal of Molecular Liquids* **2005**, *119* (1-3), 55-62.
73. Munoz-Paez, A.; Pappalardo, R. R.; Sanchez Marcos, E., Determination of the Second Hydration Shell of Cr^{3+} and Zn^{2+} in Aqueous Solutions by Extended X-ray Absorption Fine Structure. *Journal of the American Chemical Society* **1995**, *117* (47), 11710-11720.
74. Bol, W.; Gerrits, G. J. A.; Van Panthaleon Eck, C. L., The hydration of divalent cations in aqueous solution. An X-ray investigation with isomorphous replacement. *Journal of Applied Crystallography* **1970**, *3* (6), 486-492.
75. Cooper, T. E.; O'Brien, J. T.; Williams, E. R.; Armentrout, P. B., Zn^{2+} has a primary hydration sphere of five: IR action spectroscopy and theoretical studies of hydrated Zn^{2+} complexes in the gas phase. *The Journal of Physical Chemistry A* **2010**, *114* (48), 12646-12655.

76. Wilcox, R. J. Sorption to Dissolution: The Reactivity of Small Molecules with Condensed Phase Metal Halide Networks. North Carolina State University, Raleigh, 2009.
77. Wall, T. T.; Hornig, D. F., Raman spectra of water in concentrated ionic solutions. *The Journal of Chemical Physics* **1967**, *47* (2), 784-792.
78. Nickolov, Z. S.; Miller, J., Water structure in aqueous solutions of alkali halide salts: FTIR spectroscopy of the OD stretching band. *Journal of colloid and interface science* **2005**, *287* (2), 572-580.
79. Li, R.; Jiang, Z.; Chen, F.; Yang, H.; Guan, Y., Hydrogen bonded structure of water and aqueous solutions of sodium halides: a Raman spectroscopic study. *Journal of molecular structure* **2004**, *707* (1), 83-88.
80. Imoto, S.; Xantheas, S. S.; Saito, S., Molecular origin of the difference in the HOH bend of the IR spectra between liquid water and ice. *The Journal of Chemical Physics* **2013**, *138* (5), 054506.
81. Larsen, O. F.; Woutersen, S., Vibrational relaxation of the H₂O bending mode in liquid water. *The Journal of Chemical Physics* **2004**, *121* (24), 12143-12145.
82. Ashihara, S.; Huse, N.; Espagne, A.; Nibbering, E.; Elsaesser, T., Vibrational couplings and ultrafast relaxation of the O–H bending mode in liquid H₂O. *Chemical Physics Letters* **2006**, *424* (1-3), 66-70.
83. Piatkowski, L.; Bakker, H., Vibrational dynamics of the bending mode of water interacting with ions. *The Journal of Chemical Physics* **2011**, *135* (21), 214509.
84. Yan, C.; Xue, Z.; Zhao, W.; Wang, J.; Mu, T., Surprising Hofmeister effects on the bending vibration of water. *ChemPhysChem* **2016**, *17* (20), 3309-3314.
85. Li, J.; Bian, H.; Chen, H.; Wen, X.; Hoang, B. T.; Zheng, J., Ion association in aqueous solutions probed through vibrational energy transfers among cation, anion, and water molecules. *The Journal of Physical Chemistry B* **2012**, *117* (16), 4274-4283.
86. Ahmed, M.; Singh, A. K.; Mondal, J. A.; Sarkar, S. K., Water in the hydration shell of halide ions has significantly reduced Fermi resonance and moderately enhanced Raman cross section in the OH stretch regions. *The Journal of Physical Chemistry B* **2013**, *117* (33), 9728-9733.
87. Dill, E. D.; Josey, A. A.; Folmer, J. C. W.; Hou, F.; Martin, J. D., Experimental Determination of the Crystallization Phase-Boundary Velocity in the Halozeotype CZX-1. *Chemistry of Materials* **2013**, *25* (20), 3932-3940.

88. Mancinelli, R.; Botti, A.; Bruni, F.; Ricci, M. A.; Soper, A. K., Hydration of Sodium, Potassium, and Chloride Ions in Solution and the Concept of Structure Maker/Breaker. *The Journal of Physical Chemistry B* **2007**, *111* (48), 13570-13577.
89. Wilcox, R. J.; Losey, B. P.; Folmer, J. C. W.; Martin, J. D.; Zeller, M.; Sommer, R., Crystalline and Liquid Structure of Zinc Chloride Trihydrate: A Unique Ionic Liquid. *Inorganic Chemistry* **2015**, *54* (3), 1109-1119.
90. Kabisch, G., Intermolecular coupling of bending vibrations in liquid water. *Journal of molecular structure* **1981**, *77* (3-4), 219-226.
91. Falk, M., Frequencies of H-O-H, H-O-D and D-O-D bending fundamentals in liquid water. *Journal of Raman Spectroscopy* **1990**, *21* (9), 563-567.

CHAPTER 6

Conclusion

The solution of the zinc chloride trihydrate ($R = 3$) crystal structure, discussed in Chapter 2, revealed two unique zinc environments in the solid state, those being the $\text{Zn}(\text{H}_2\text{O})_6^{2+}$ and ZnCl_4^{2-} ions. Analysis of the liquid phase diffraction combined with RMC modelling and Raman spectroscopy revealed that not only do these ions persist upon melting but that the CsCl-type packing observed in the crystal persists into the liquid state as well. This not only put to rest decades of uncertainty about the species present in the $R = 3$ but also showed the existence of a unique fully inorganic ionic liquid. Furthermore, knowledge of the $R = 3$ liquid structure proved to be invaluable in the examination of a broader concentration range of aqueous zinc chloride solutions.

Additional analysis of X-ray and neutron diffraction as well as Raman and DSC measurements of compositions of $R > 3$ show strong evidence of a second hydration shell tightly bound to the first shell of $\text{Zn}(\text{H}_2\text{O})_6^{2+}$ upon dilution. The vibrational spectroscopy shows that in the $R = 3$ the hydrogen bonding network of water is completely broken down. Upon dilution this network begins to build back up in the hydration shells, however, at concentrations of $R \leq 9$ the waters are bound tightly into the second shell, having very strong interactions with the first shell which prevents there from being any crystallization in this region of the phase diagram. The existence of a second shell is observed in the PDF via the presence of the Zn-O_{II} contact at 4.2 Å. Furthermore, the unique solubility of ZnCl_2 , resulting in the observation of ^1H NMR and vibrational spectra of waters bound to Zn^{2+} , allowed for the development of mathematical models to predict the extent of hydration shells in the system as a function of concentration. The calculated shells in both the NMR and vibrational spectroscopy also show that second shell is

very different from pure water. The fitting models of both the NMR and vibrational spectroscopy as well as the X-ray PDF indicate that at $R > 9$ the hydration shell waters locally organize similar to pure water. This manifests in the phase segregation and crystallization of ice at dilutions past $R = 9$. Moreover, examination of the structure factor data with respect to idealized crystalline models and RMC simulations indicate that solutions of compositions $R = 9$ and $R = 21$, having completed second and third hydration shells, display a CsCl-type packing in the liquid state.

Additionally, the aqueous zinc chloride system allows for a better understanding of the vibrational spectrum of pure water by providing information about the peaks and their evolution from the $R = 3$ hydrate, where the hydrogen bonding network of pure water does not exist, to that of pure water. Evidence suggests that the molecular modes of water are observed at $\sim 1600 \text{ cm}^{-1}$ for the bending mode along with a combination peak of the symmetric and asymmetric stretching modes at $\sim 3450 \text{ cm}^{-1}$ while the peaks observed at 3200 and 3600 cm^{-1} are representative of the hydrogen bonding network of the system while some amount of the 3200 cm^{-1} peak is due to the bending overtone.

Lastly, applying the mathematical model developed for the ^1H NMR data of zinc chloride to multiple other aqueous salt solutions resulted in the prediction of multiple hydration shells which indicates that these solutions are more ordered than previously thought. Together the evidence for the high degree of order not only in the ZnCl_2 system but also in additional sulfate and chloride salts of Al^{3+} , Mg^{2+} , Ca^{2+} and Na^+ indicates that there is a degree of intermediate range order in multiple aqueous salt solutions. Better understanding of this ordering could

APPENDICES

Appendix A

Table A.1 Determined fitting parameters for the additional salt solutions investigated via ^1H HMR and fit with the multi-shell exponential model.

Salt	Shell	Waters	δ_i	δ_r	k
NaCl	1 st	6	2.747	3.256	0.110
	2 nd	12	3.516	3.575	0.054
	3 rd	24	3.729	3.832	0.016
CaCl ₂	1 st	6	3.164	3.164	0.000
	2 nd	12	3.172	3.693	0.163
	3 rd	24	3.703	3.814	0.025
	4 th	48	3.805	3.819	0.037
MgCl ₂	1 st	6	3.549	3.703	0.148
	2 nd	12	3.757	3.762	0.207
	3 rd	24	3.756	3.791	0.031
	4 th	48	3.820	3.838	0.041
AlCl ₃	1 st	6	6.289	6.611	0.107
	2 nd	12	4.570	4.300	0.055
	3 rd	24	3.914	3.851	0.045
	4 th	48	3.884	3.908	0.020
Zn(SO ₄)	1 st	6	4.741	4.021	0.196
	2 nd	12	3.927	3.834	0.042
Mg(SO ₄)	1 st	6	4.432	4.013	0.101
	2 nd	12	3.929	3.832	0.049
Al ₂ (SO ₄) ₃	1 st	6	7.155	5.899	0.094
	2 nd	12	4.755	4.627	0.148
	3 rd	24	4.003	3.859	0.040
	4 th	48	3.838	3.856	0.033
ZnCl ₂ /MgCl ₂	1 st	6	3.164	3.409	0.136
	2 nd	12	3.344	3.742	0.205
	3 rd	24	3.778	3.834	0.113
	4 th	48	3.822	3.828	0.057